CTH-RF-43

JET-JB2-9008

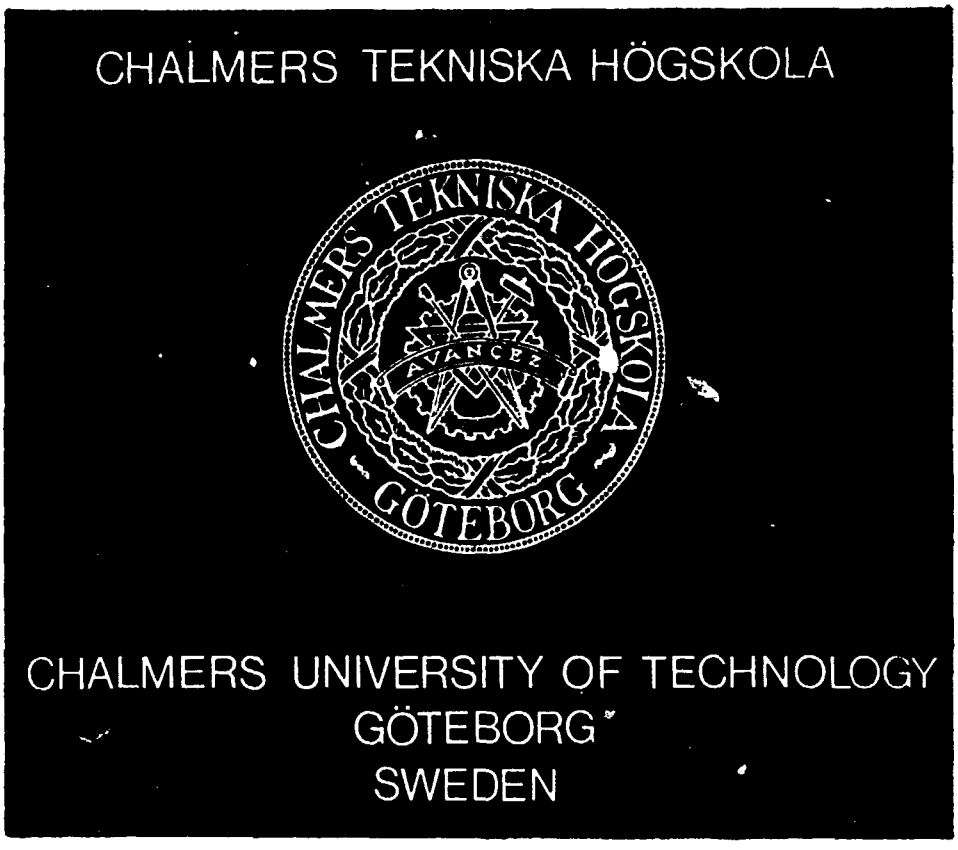

CTH-RF-43

Combined Proton-Recoil and Neutron Time-of-Flight Spectrometer for 14 MeV Neutrons

by

Gudmar Grosshoeg (project leader),

and

Dan Aronsson, Erik Arvidsson, Klaes-Håkan Beimer,
Lars-Olof Pekkari , Ryszard Rydz,
and Nils G. Sjöstrand.

ISSN 99-0358116-5

Department of Reactor Physics.

May 1983

Design Study of Neutron Diagnostic System for JET

JET Contract Number: JB2/9008.

Combined Proton-Recoil and Neutron Time-of-Flight Spectrometer for 14 MeV Neutrons

by

Gudmar Grosshoeg (project leader),

and

Dan Aronsson, Erik Arvidsson, Klaes-Håkan Beimer, Lars-Olof Pekkari[1], Ryszard Rydz, and Nils G. Sjöstrand.

Department of Reactor Physics.
Chalmers University of Technology.
S-412 96 Gothenburg, Sweden.

[1] Institute for Electromagnetic Field Theory and Plasma Physics.

ISSN 99-0358116-5 May 31, 1983

Contents

List of figures

List of tables

Summary

The purpose of the neutron diagnostic systems is to provide information about the plasma behaviour. The energy distribution of the neutrons emerging from the plasma depends on the plasma temperature and the methods used to heat the plasma. A simple relation, equation 1.4, exists between the width of the neutron energy-distribution peak and the plasma temperature for a plasma in equilibrium[1]. From this we find that a neutron spectrometer for plasma diagnostics should have an energy resolution of 100 keV. The efficiency of the spectrometer is determined by the requirement that it should be possible to evaluate a spectrum for each shot[2]. As a preliminary design parameter a neutron flux density at the foil of 10^9 n/cm^2,s was used. Combining this with an efficiency of 10^{-6} counts/s per n/cm^2,s we obtain a counting rate of 1000 counts/s. Thus, 10^4 events are collected during a 10-second long shot.

The proton recoil method[3] has been used as a tool for fast neutron spectroscopy since the middle of the fifties. The resolution obtained using only proton energy detection is about a few per cent. The resolution depends essentially on the variation of the angle between the initial-neutron and the recoil-proton paths, and on the slowing down of the proton in the scattering material. Therefore, the resolution of a system utilizing only proton-detection can be improved by a decrease of the angular variation and a decrease of the maximum slowing down in the scatterer. Both the methods lead to a decreased efficiency.

The decrease of the angular variation is limited by the divergence of the incoming neutron beam. However, the angular variation can be compensated by a measurement of the energy of the scattered neutron. The purpose of this work is to study this proton-neutron coincidence method and its possibilities as a tool for plasma diagnostics at JET.

The spectrometer design contains several parameters. Therefore, a reference design, TANSY[4], is used through the whole report as a base for the discussion of the various parameters. We do not consider TANSY to be the final solution. Other aspects not covered in this report should be considered for the final determination of the parameters.

The available amount of neutrons[5] depends on the plasma conditions and on the transfer of neutrons from the plasma to the scattering foil. The transfer depends on the amount of plasma seen by the foil. The transfer is lower than preliminarily assumed. Therefore, during some phases of the D-T operation of JET the full opening of the torus vacuum-vessel port may be used. However, we emphasize that the plasma is exposed to various heating schemes, the effect of which can be studied by neutron spectrometry[6]. Therefore, it is worthwhile to use the maximum possible neutron transfer combined with an efficiency as large as possible. Thus, we need a large foil area, which is most readily obtained using an annular foil.

The theoretical base for the method[7] is the neutron-proton scattering model using classical mechanics and equal masses for the proton and the neutron. Thus, the energy of the initial neutron can be calculated from the two measured quantities, the proton energy and the time difference between detection time of the proton and the scattered neutron.

Relativistic effects[8] and the fact that the masses of the proton and the neutron are not equal give a small correction for the angle between the scattered neutron and the recoil proton. This can easily be corrected for by an adjustment of the position of the neutron detectors. The evaluation of the inital-neutron energy can be done using classic mechanics and equal

---

1) Paragraph 1.1, »Design criteria.», page 11.

2) A further requirement is the measurement of the time dependent variation of the neutron spectrum during one shot. However, this possibility has not been considered in this work.

3) Chapter 2, »Previous designs.», page 23.

4) Paragraph 1.3, »TANSY, a reference design.», page 15.

5) Chapter 3, »The JET plasma as a neutron source.», page 29.

6) Paragraph 3.3, »Miscellaneous plasma neutrons.», page 31.

7) Paragraph 4.2, »The measurement method.», page 36.

8) Paragraph 4.3, »Relativistic and mass-difference effects.», page 37.

masses of the proton and the neutron. Corrections are necessary only at very extreme angles.

A polyethylene foil scatters the neutrons by the carbon nuclei as well as by the hydrogen nuclei[1]. The carbon scattered neutrons do not enter into the coincidence spectrum. However, they give an additional amount of background counts in the proton detector as well as in the neutron detectors. The load, relative to the hydrogen scattered neutrons, is 20% for the neutron detectors and 140% for the proton detector.

Several combinations of proton-detector and neutron-detector shapes and positions[2] have been studied. The best choice, in our opinion, is an annular foil scatterer, an annular neutron detector system, and a central proton detector[3]. Most of the work presented in this report is based on that solution.

The recoil-protons created in the scattering foil[4] lose energy during the passage out of the foil. This energy loss can not be predicted for a single proton and, therefore, it gives an energy uncertainty in the measured energy of the proton. The energy loss is a quantum-mechanical slowing-down process. It has two side effects, energy straggling and angular straggling. The energy straggling[5] gives a further spread of the proton energy. The spread is small as compared to the spread caused by the slowing down from different positions in the foil. The angular spread[6] causes a loss of coincidences, which for TANSY is estimated at 10% if the full range of coincidences is used.

Both the efficiency and the energy spread of the protons leaving the scattering foil are proportional to the thickness of the foil. We have tried to find a method counter-acting the decreased precision caused by a thick foil. Two methods have been studied[7]. The first one is based on the unfolding method used for gaseous proton-recoil spectrometers. We show that, from the theoretical point of view, the method works well and provides the same mean energy distribution as a thin foil. However, the standard deviation of the single points of the distribution are always larger than the corresponding standard deviation of a distribution from a thin foil. Therefore, the increased amount of data collected by this method can not be used in order to increase the precision.

The other method is based on the idea of using a scintillator as a scatterer. The amount of light created during the slowing down of the proton in the scintillator is proportional to the energy loss. However, the light transfer in the foil depends on the position of the scattering event. Therefore, the method can not be used for this application.

In the neutron-proton scattering there is an equally large probability to find a proton recoil at any energy below the energy of the initial neutron. The proton detector selects[8] a part of this distribution. The selected part depends on the position of the proton-detector relative to the scattering foil and on the dimensions of the foil and the detector. For large distances between the foil and the detector the energy width, the difference between the highest and lowest energy of the selected protons relative to the initial-neutron energy, is inversely proportional to the squared foil-detector distance, equation 6.14. The same is true for the proton detection sensitivity, equation 6.16. Combining these we find that the sensitivity[9] is proportional to the energy width. Therefore, a spectrometer using only proton detection will lose sensitivity when the resolution is improved.

In the proposed spectrometer the proton energy width is not constrained by the resolution requirements in the same way as in the only-proton spectrometer. A rich variety of proton energy spectra[10] can be considered. The limitations are set by the neutron detection.

Three types of neutron detectors[11] have been considered. The neutron glass scintilla-

---

1) Paragraph 4.4, »Neutron-carbon scattering.», page 38.
2) Paragraph 4.5, »Exploitation possibilities.», page 39.
3) Figure 32, »An annular scatterer.», page 57.
4) Chapter 5, »The scattering material.», page 59.
5) Paragraph 5.2, »Energy straggling.», page 60.
6) Paragraph 5.3, »Angle straggling.», page 61.
7) Paragraph 5.4, »Thick foil scatterer.», page 63.
8) Chapter 6, »Proton detection.», page 75.
9) Paragraph 2.1, »Definition of resolution, sensitivity, and efficiency.», page 23.
10) Paragraph 6.2, »Energy distribution.», page 77.
11) Chapter 7, »Neutron detection.», page 91.

tors have a too low sensitivity[1] for this application. The liquid scintillator[2] offers the possibilities of gamma background reduction by the use of pulse shape discrimination. However, it gives a complicated design, both mechanically and electronically. The most straightforward choice is the plastic scintillator. It offers good timing properties, a relatively high sensitivity, ard can easily be machined to complex shapes.

The drawback of the plastic scintillator is the low light output[3] for protons as compared to the light output for electrons. This gives a high gamma background sensitivity. Therefore, a high bias must be used which results in a blocking-out of low-energy neutrons. Therefore, neutron scattering angles[4] of about 75 degrees[5] must be used[6]. However, at these angles the neutron energies are about 1 MeV, which implies a long distance between the foil and the neutron-detectors in order to keep a resonable resolution of the time-of-flight measurement. This is one aspect of the resolution-efficiency dilemma[7]. Another aspect is the thickness of the foil. An increased foil thickness gives an increased efficiency but a worsened energy resolution.

An optimization of the system using the method of trial and error has given the parameters for TANSY[8]. Thereby, we have taken the shape of the scattered-neutron energy distribution[9] into account. A peaked distribution gives a more efficient use of the neutron detectors, which shall be as small as possible because of the gamma sensitivity problem.

The nstrument will work with a high counting rate[10]. An analysis of the deadtime effects[11] shows that the dynamic range is one or at most two decades[12]. Therefore, the neutron-flow into the spectrometer should be controlled by some other means. One possibility[13] is the use of the diaphragm placed close to the torus. However, an inspection of a possible beam shaping system[14][15] shows that the diaphragm as well as the collimator must be changed for the adjustment of the neutron-flow.

The measured data are collected[16] using the list mode. The collected data may contain too few events for the investigation of the time-dependent neutron-spectrum for a single shot. However, using data from several shots the mean time-dependency can be obtained.

Some tests[17] have been done in order to obtain information about the behaviour of a semi-conductor detector in a neutron field. The tests show that the disturbancies caused by neutron reactions in the silicon normally give pulses with amplitudes lower than the proton-recoil pulses.

The conclusion[18] of this work is that a spectrometer with the desired properties can be made. No physical obstructions have been found. The difficulties foreseen are of a technical nature and can be overcome by some further developments[19]. The cost[20] of the hardware of the instrument has been estimated at about 300,000 GBP. This does not include the neutron beam shaping system.

---

1) Figure 55, »Li-glass coincidence probability.», page 109.
2) Paragraph 7.2, »Liquid scintillators.», page 91.
3) Figure 51, »Light response for a plastic scintillator.», page 95.
4) Figure 56, »Pilot U coincidence probability.», page 110.
5) Figure 58, »Coincidence probability in TANSY.», page 112.
6) Chapter 8, »Characteristics of the detection method.», page 99.
7) Paragraph 8.3, »The resolution-efficiency dilemma.», page 103.
8) Table 2, »Efficiency parameters.», page 104.
9) Figure 58, »Coincidence probability in TANSY.», page 112
10) Table 4, »Rates of events at 10^9 n/cm^2,s.», page 108.
11) Chapter 8 4, »The dynamic range.», page 104.
12) Figure 73, »Detection rate, with background.», page 127.
13) Chapter 9, »Neutron beam shaping.», page 131.
14) Figure 77, »A 1400 cm^2 beam shaping system.», page 135.
15) Figure 78, »A 324 cm^2 beam shaping system.», page 136.
16) Chapter 10, »Data acquisition.», page 139.
17) Chapter 11, »Test measurements.», page 145.
18) Chapter 14, »Conclusions.», page 157.
19) Chapter 13, »Developments required.», page 155.
20) Chapter 12, »Cost estimates.», page 153.

1 Introduction

The proton-recoil method has for many years been a tool for fast neutron spectrometry. The neutron-proton collision is unique in the respect that it gives the highest possible transfer-of-energy from the neutron to the recoiling nucleus. Actually, for a head-on collision, the whole neutron energy is transferred to the proton. Therefore, it is the optimal reaction to use in order to transfer energy from a neutron to a charged particle. The accuracy of a measurement will mainly depend on the problems encountered in the proton-energy measurement.

The fundamental dilemma of this method is the range of scattering angles involved. A narrow range gives a high precision but low efficiency and conversely. Expressed in another way, efficiency costs precision.

One way to overcome, or at least to partly solve the problem, is to measure not only the proton energy but also the energy of the scattered neutron. Using scattering events with the proton in the forward direction will turn the neutron measurement into a correction term measurement.

This idea was put forward by Lorenzen and Elevant {1,2} leading to the proposal for this work. We have tried to find a report about an instrument using this method in the literature but not found any. However, complex instruments with low counting rates have been used in astronomy measurements {77}.

Here, we will first look upon the relation between the plasma parameters and the neutron energy distribution (1.1). We show that the neutron energy peak shift is very small. It is of the order of a few tens of keV for a plasma temperature below 20 keV. The Doppler effect gives a broadening of the neutron peak. The width, measured as the full width at half maximum, goes from 160 keV at a plasma temperature of 1 keV to 730 keV at 20 keV.

Next, we consider the possibility to measure these quantities (1.2). From the statistical point of view, we find that only a few counts are needed in order to determine the neutron energy mean value. The accuracy is limited by the resolution of the instrument.

For a determination of the broadening we need an energy-resolution better than half the width of the peak. The accuracy is then determined by the number of accumulated events. 1000 counts give an accuracy of 4%.

Our conclusion is that the resolution of the instrument should be of the order of 100 keV. The number of accumulated events should be 1000 or more for each determination of the width.

A design named TANSY, which might fulfil these requirements, is presented in 1.3.

1.1 Design criteria

This spectrometer is intended to be a tool for plasma diagnostics, during the D-T phase of JET. In article 3.2 of the contract for this work {5} it is stated that the system should be optimized to work with neutron energies peaked at 14.06 MeV. Furthermore, it is pointed out that the expected Doppler broadening amounts to up to 950 keV. The neutral beam injection gives an increased broadening.

Williams {3} has found that the Doppler shift of the mean energy is very small. He uses a cross-section σ in the Gamow form {4} , i.e.

$$\sigma(E_o) = \frac{\sigma}{E_o} e^{-b/\sqrt{E_o}} \qquad (1.1)$$

where b is estimated at 32. This gives a mean energy of the neutrons

$$\bar{E} \approx \lambda Q + \frac{3 m_n kT}{2(m_d + m_t)} + \lambda \left(\frac{kTb}{2}\right)^{2/3} \qquad (1.2)$$

where

m_n = the neutron mass

m_d = the deuteron mass

m_t = the triton mass

λ = the neutron energy to the total energy ratio

Q = reaction energy

kT = the plasma temperature

This shift is small. For a plasma temperature of 5 keV it is 16 keV, for 10 it is 27 keV , and for 20 keV it is 44 keV.

Williams gives also the relative dispersion,

$$D = \sqrt{\frac{4 m_a kTQ}{(m_d + m_t)}} \qquad (1.3)$$

Assuming a Gaussian peak, Elevant {26} has calculated the FWHM-value to

$$\Delta E = 177\sqrt{kT} \qquad (1.4)$$

where ΔE and kT are given in keV[1]. For a plasma temperature range of 1 to 20 keV we obtain an energy spread from 163 to 729 keV.

Therefore, the energy range of the spectrometer is set to 4 MeV, from 12 to 16 MeV. This gives some margin to the values calculated.

The resolution should be good enough for a determination of the FWHM value of the peak. However, it should also open up the possibility to study the details of the peak, which we at this point do not know very much about.

1.2 Channel width and count rate

The measurement gives a neutron energy distribution from which we may extract a mean energy value and a measure of the distribution width. At this point we will estimate the channel width and number of events needed in order to determine these parameters.

We assume that after the evaluation of the energy of each recorded neutron, we have a distribution P_i, where i is the channel number. Each channel has a corresponding mean energy E. Thus, there is a linear relationship between the channel number and the energy. From the measured distribution we estimate the mean energy,

$$\bar{E} = \frac{\Sigma P_i E_i}{\Sigma P_i} \qquad (1.5)$$

[1] Actually, Elevant gives here a coefficient of 198, which seems us to be somewhat too high.

We assume the contents in the channels to be independent (VAR(P) = P) and estimate the standard deviation of the mean value.

$$\sigma_E = \frac{\sqrt{\Sigma P_i (E_i - \bar{E})^2}}{\Sigma P_i} = \sqrt{\frac{\bar{E^2} - \bar{E}^2}{\Sigma P_i}} \tag{1.6}$$

This standard deviation gives the accuracy of the estimated mean value. The standard deviation related to the plasma temperature is given by {26}

$$\sigma_m = \sigma_E \sqrt{\Sigma P_i} \tag{1.7}$$

Now, we assume that the neutron energy distribution can be approximated with a normal distribution.

$$P_i = \frac{N}{\sigma_m \sqrt{2\pi}} e^{-\frac{(E_i - \bar{E})^2}{2\sigma_m^2}} \Delta E = N f_i \Delta E \tag{1.8}$$

where

N is the total number of recorded events, and

ΔE is the channel width.

Thus, the full width at half maximum is

$$\Delta E = \sigma_m \sqrt{8 \ln 2} \tag{1.9}$$

From chapter 1.1, »Design criteria.», we have

$$(\Delta E)_P = 177 \sqrt{kT} \tag{1.10}$$

for a D-T plasma. Thus

$$\sigma_m = 75 \sqrt{kT} \tag{1.11}$$

The variance of the standard deviation is

$$VAR(\sigma_m) = \frac{[\Sigma P_i][\Sigma P_i (E_i - \bar{E})^4] - [\Sigma P_i (E_i - \bar{E})^2]^2}{4[\Sigma P_i]^2 [\Sigma P_i (E_i - \bar{E})^2]} \tag{1.12}$$

from which we get the relative standard deviation as

$$\sigma_\sigma = \frac{\sigma_m}{2\sqrt{\Sigma P_i}} \sqrt{\frac{[\Sigma P_i][\Sigma P_i (E_i - \bar{E})^4]}{[\Sigma P_i (E_i - \bar{E})^2]^2} - 1} \tag{1.13}$$

Using equation 1.8 , the equations 1.6 and 1.13 can be rewritten

$$\sigma_{\bar{E}} = \frac{1}{\sqrt{N}} \frac{\sqrt{\Sigma f_i (E_i - \bar{E})}}{\Sigma f_i} \tag{1.14}$$

$$\sigma_\sigma = \frac{\sigma_m}{2\sqrt{N}} \sqrt{\frac{\Sigma f_i (E_i - \bar{E})^4}{\left[\Sigma f_i (E_i - \bar{E})^2\right]^2} - 1} \tag{1.15}$$

Now, in the limit of zero channel width

$$\int_{-\infty}^{\infty} f_i \, dE = 1 \qquad \int_{-\infty}^{\infty} (E_i - \bar{E})^2 f_i \, dE = \sigma_m^2$$

$$\int_{-\infty}^{\infty} (E_i - \bar{E})^4 f_i \, dE = 3\sigma_m^4$$

Thus,

$$\sigma_{\bar{E}} = \frac{\sigma_m}{\sqrt{N}} \tag{1.16}$$

$$\sigma_\sigma = \frac{\sigma_m}{\sqrt{2N}} \tag{1.17}$$

which transformed by equation 1.11 gives

$$\sigma_{\bar{E}} = \frac{75\sqrt{kT}}{\sqrt{N}} \tag{1.18}$$

$$\sigma_{kT} = \sqrt{\frac{2}{N}} \, kT \tag{1.19}$$

According to the formula 1.18, we need ten events for a plasma temperature of 10 keV in order to get a standard deviation of the mean value, which is less than 100 keV. The plasma temperature is determined from the width of the peak. 100 counts give an accuracy of 14% and 1000 counts give an accuracy of 4%.

The measured standard deviation contains both the width of the plasma peak and the spectrometer resolution. We have above treated them together. O.N. Jarvis[1] has investigated the effect of the mixed widths. He finds that the spectrometer can be used down to the resolution of the spectrometer. The necessary number of events at this point is estimated at 1000 counts. This number decreases with increasing plasma temperature. However, the final resolution will depend on the evaluation process used, tails of the distribution, background effects, et cetera.

The influence of the number of channels used is illustrated in figure 1, »Mean neutron-energy determination.», and 2, »Neutron peak width determination.». Equations 1.6 and 1.13 are used together with an integer value distribution from equation 1.8. The fraction part of the numbers in equation 1.8 is randomized in the rounding off operation in order to somewhat simulate a statistical distribution.

[1] Private communication.

Both the calculations indicate that the result is independent of the channel width up to a width corresponding to about half the FWHM-value. At about three quarter of the FWHM-value the analysis begins to break down. All energy moments tend to zero, which makes the standard deviation indeterminable. Note that the standard deviation is decreasing. Actually, in the limit, all information is collected in one channel. The accuracy is then the channel width, but no further information is collected about the precision of the measurement.

In conclusion we find that the channel width should not be larger than half the FWHM-value. For a plasma temperature of 1 keV this gives about 100 keV channel width. The corresponding value for 5 keV is about 200. However, we will neither lose, nor gain any accuracy by using the 100 keV channel width even here.

1.3 TANSY, a reference design

The design of a spectrometer using both neutron and proton detection involves several parameters. It is very difficult to find an algorithm for a simultaneous optimization of all these parameters. Therefore, we are forced to use the trial-and-error method.

Here, we present one set of possible parameters. They define a reference design, which we call TANSY. The effect of altering single parameters or a subset of parameters will be discussed at appropriate places in this document.

TANSY has an annular polyethylene foil. This has a mean radius of 8 cm, a width of 2 cm, and a thickness of 1.2 mg/cm^2. Thus, the inner diameter is 7 cm and the outer is 9 cm. The area is 100.57 cm^2.

As proton-detector we use a 2-mm-thick silicon semiconductor. It has a radius of 1 cm and is placed on the central axis, 29.94 cm from the foil.

32 Pilot U plastic neutron detectors form a ring around the central axis. The mean radius perpendicular to the central axis is 100 cm and the foil-detector distance along the axis is 25 cm. The width of the detectors is 8 cm and the thickness is 2 cm.

Several quantities can be derived from the parameters defined above. The mean classic design angles are 15 and 75 degrees for the proton path and the neutron path, respectively. The relativistic angle correction is 0.2 degrees for the neutron detector and 0.05 degrees for the proton detector. Thus, the corrected angles are 74.80 and 14.95 degrees, respectively. The mean distance between the foil and the neutron-detector, that is the mean flight path for the neutron, is 95.33 cm.

The sensitivity of TANSY at 14 MeV is estimated at 10^{-8} counts per neutron reaching the foil. This corresponds to an efficiency of 10^{-6} counts/(n/cm^2). The resolution is about 100 keV.

The geometrical parameters of TANSY are summarized in figure 3. A sketch of the neutron and proton coincidence paths is given in figure 4. Preliminary lay-outs of the proton-detection and the complete system are given in the figures 5 and 6. However, it will be seen in chapter 9 that larger dimensions are needed in order to avoid neutron scattering from the collimator, the chamber walls et cetera, see the figures 77 and 78.

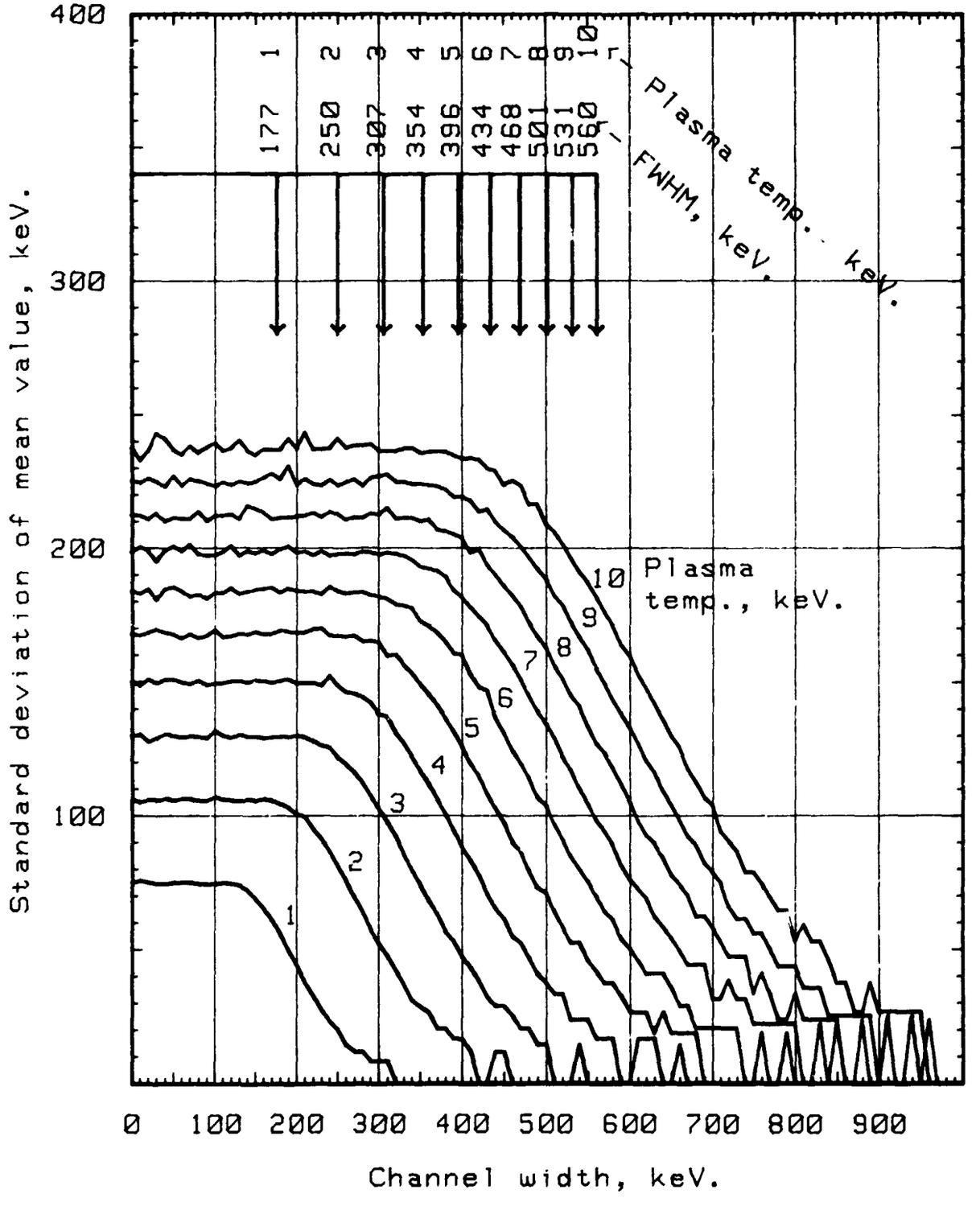

Figure 1. Mean neutron-energy determination.

The standard deviation is calculated by equation 1.6. The calculation is done for 1000 events but the result is normalized to 1 event.

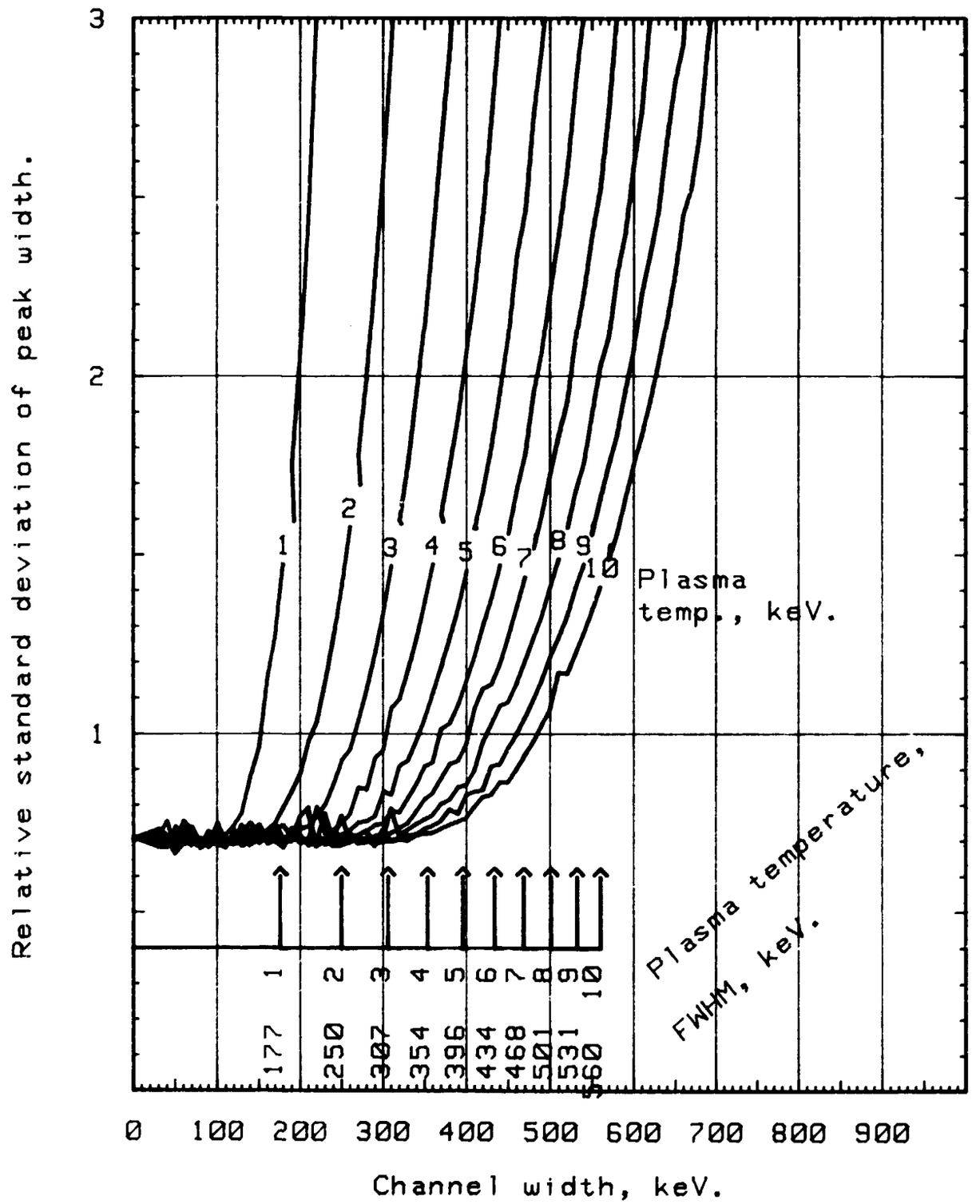

Figure 2. Neutron peak width determination.

The standard deviation of the peak width is calculated from equation 1.13. The calculation is done for 1000 events but the result is normalized to 1 event.

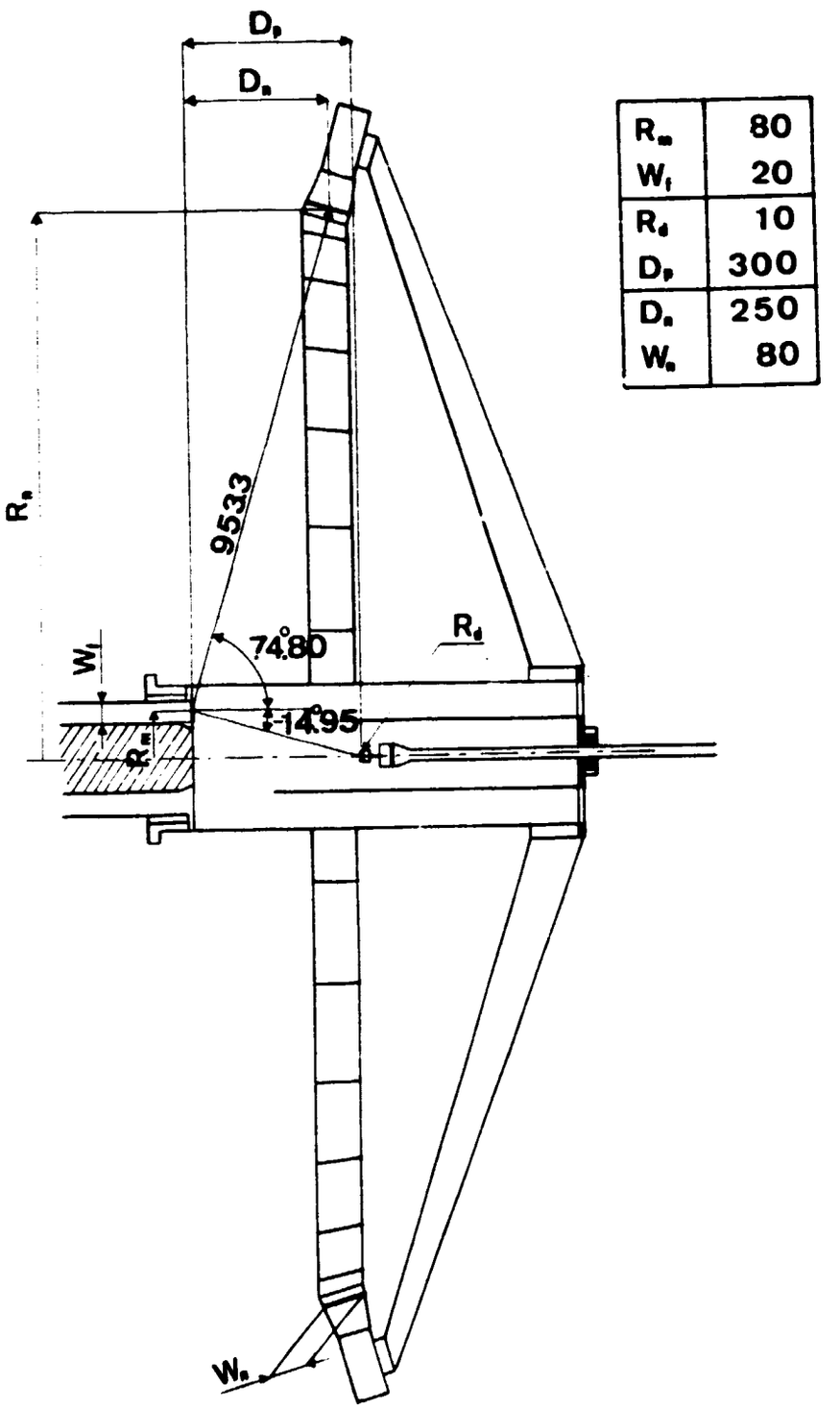

R_m	80
W_t	20
R_d	10
D_p	300
D_a	250
W_a	80

Figure 3. Geometrical definitions of TANSY.

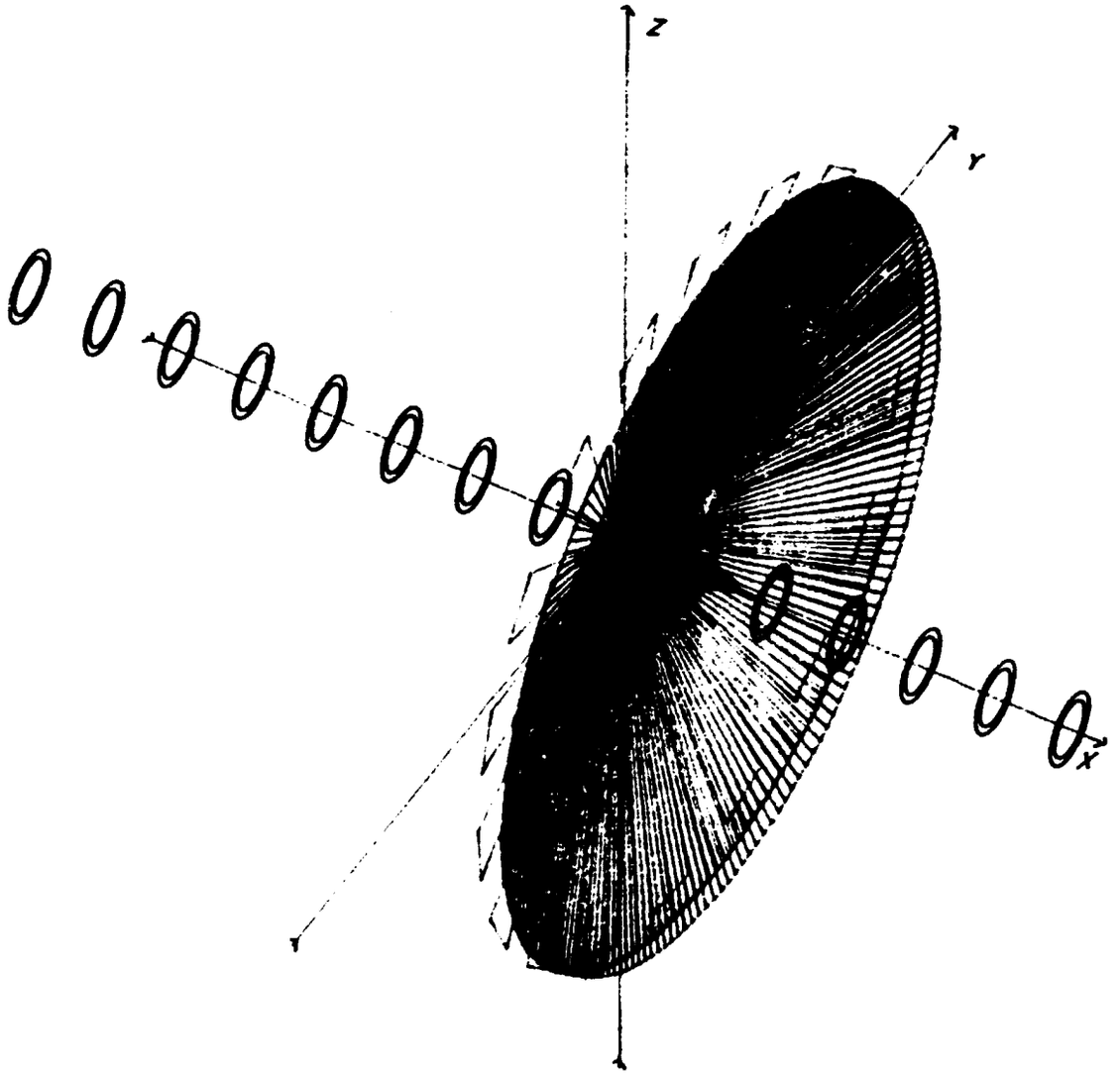

Figure 4. The neutron- and proton-coincidence paths in TANSY.

The collimated neutron beam enters along the x-axis. The recoil-proton paths form a cone topped by the proton detector. The neutron-paths go outwards from the centrally placed scattering foil.

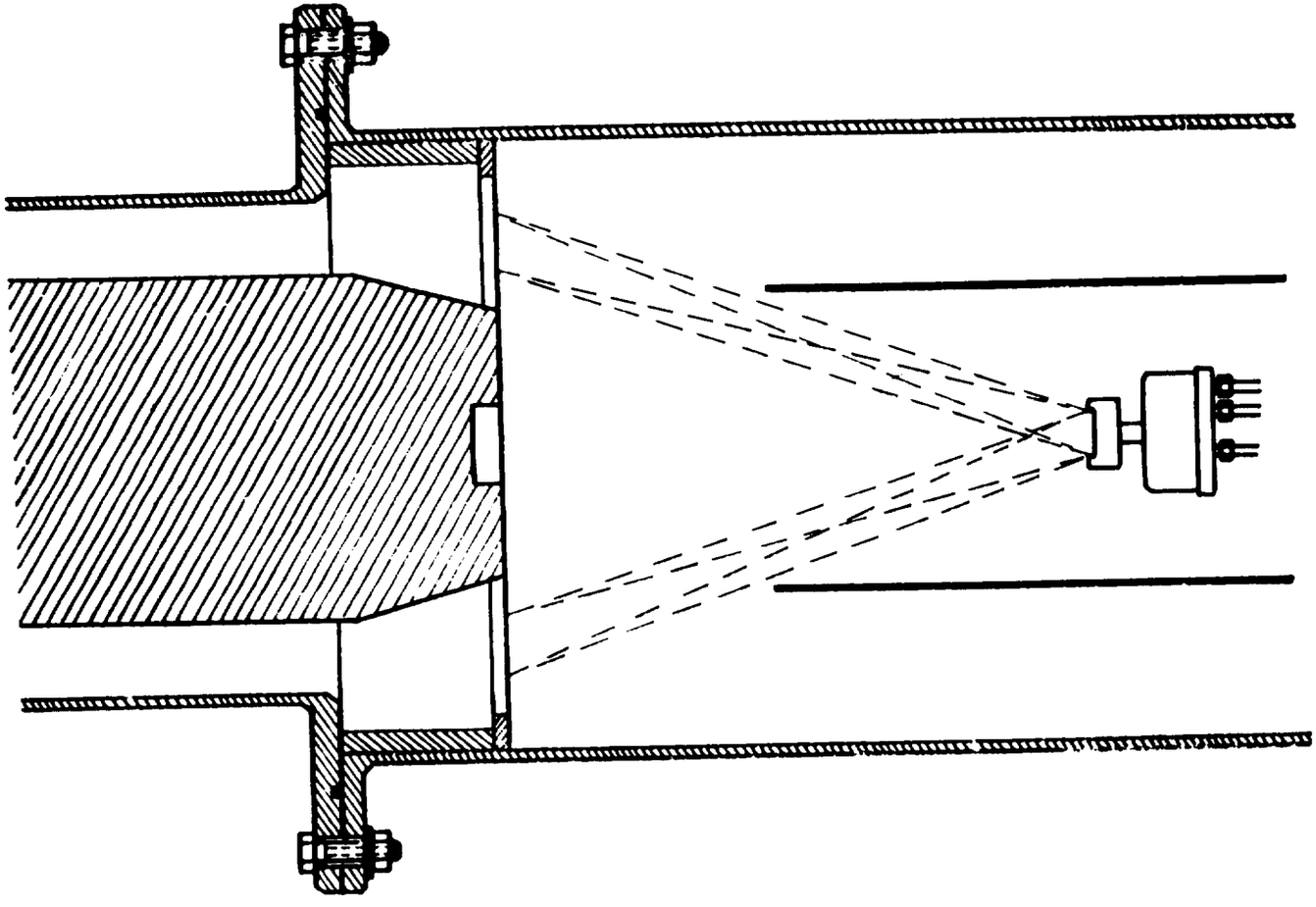

Figure 5. Proton detection lay-out.

The amount of protons reaching the proton detector is limited by tantalum shields. The incoming beam must never touch any surface seen by the proton detector, see chapter 9.

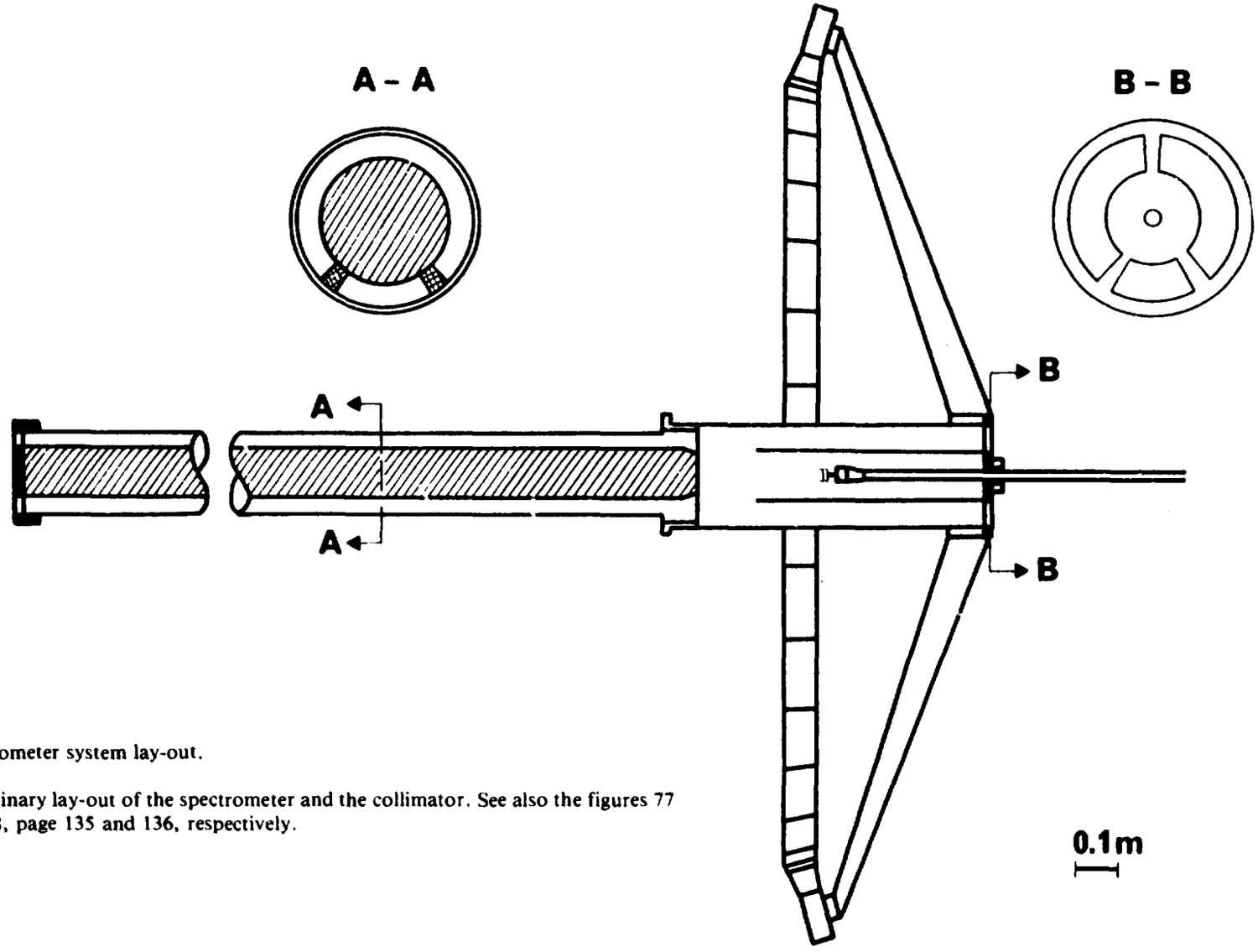

Figure 6. Spectrometer system lay-out.

Preliminary lay-out of the spectrometer and the collimator. See also the figures 77 and 78, page 135 and 136, respectively.

2 Previous designs

The first proton-recoil spectrometers usable at energies around 14 MeV where developed during the fifties. Since then, the semiconductor detector has been developed and has been used for proton-recoil measurements. However, only a few reports have appeared in the open literature until the latest years when high energy neutron sources and fusion diagnostics have created a renewed interest.

Here, we do not intend to make a complete review of the proton-recoil method. The purpose of this paragraph is to pick up those developments and ideas, which might be of interest for the design of the proposed spectrometer. Further information and a more complete reference list is given in the references 6, 7, 8, and 9.

2.1 Definition of resolution, sensitivity, and efficiency

The two most important design characteristics of a neutron spectrometer are the efficiency and the resolution. These may be defined in different ways depending on the application. Marion and Fowler {6} use a point source in the definition of the efficiency. In our case, with an almost parallel beam, it is more convenient to use the foil as a starting point for the definition.

- We define the efficiency as the number of recorded events/s per neutron flux density unit at the scattering foil.
- We define the sensitivity as the number of counts per neutron reaching the foil.
- We define the resolution as the full width at half maximum of a recorded energy spectrum created by a monoenergetic neutron source.

2.2 The liquid scintillator NE213

In a liquid scintillator like NE213, the whole energy is absorbed in the scintillator. The result is a proton-energy distribution, which must be unfolded in order to obtain the neutron-energy spectrum. This unfolding procedure is in principle a differentiation, which means that many events must be accumulated in order to get sufficient statistics in the evaluated spectrum. Morgan and England {10} describe a neutron spectrometer for the ORMAK facility at ORNL. They use a NE213 proton-recoil detector, 4.65 cm in diameter and 4.60 cm in length, and pulse shape discrimination for neutron selection.

The photomultiplier, RCA8850, is shielded by a magnetic shield and the entire spectrometer is surrounded by a 0.7 cm thick lead shield. A test of the magnetic shield shows that the gain shift is not higher than 2% during the shots.

A measurement of the neutron distribution gave a considerably broader peak than expected from the detector resolution, which was about 20% at this energy. This broadening of the peak as well as a slight shift towards lower energies are attributed to multiple elastic scattering in the material surrounding the plasma.

A second peak found at 1 MeV was assumed to come from inelastic scattering in the aluminium of the coil supports, torus wall, and outer vessel.

Slaughter {11} has tested NE213 combined with the RCA8850 photomultiplier in a high counting rate range. He claims that magnetic fields up to 0.01 T have no effect on a photomultiplier tube enclosed in 1-mm-thick shields. However, higher fields saturate the shield. Transistor-stabilized voltage-divider chain is used and the linear signal is derived from dynode 10 in order to avoid saturation effects from the 14 MeV neutrons generated by the LLL Rotating Target Neutron Source.

For the three scintillator diameters 1, 2, and 4.5 cm he got the resolutions 1000, 650, and 830 keV, respectively, at a count rate of 0.5×10^6 counts per second. He states that the dynamic range of the spectrometer is small. At counting rates exceeding 0.6 to 0.7×10^6 the pulse-height spectra are significantly degraded. On the other hand, because about 10^5 recoil proton events are required for the analysis, low counting rates must continue over several plasma pulses.

Chatelier et al. {12} give a review of the types of neutron spectrometers used in fusion research so far. They stress that

> *»The ideal spectrometer, i.e. that spectrometer which has a high counting rate together with a high resolution and which can explore a wide energy range, does not exist since those features do not jointly exist. Consequently a choice must be made between those characteristics.»*

The NE213-scintillator is viewed by the XP2020 photomultiplier. The dynode chain is zener diod stabilized and the tube is shielded by an outer 0.8-cm-thick iron shield and an inner 0.8-mm-thick μ-metal one against the 20 G magnetic field.

Four spectra can be achieved within a single shot at TFR. The unfolding can be made between two successive discharges with help of a simplified code. The resolution at 2.5 MeV is 10%.

2.3 Two scintillators

With two scintillators one has the possibility to select a band of scattering angles and thereby avoid the unfolding. Some examples of such instruments are given in the references 13, 14, and 15. As long as amplitude measurements from scintillation detectors are used for the energy determination, these instruments do not give any significant improvements. However, a useful spectrometer may be achieved and used in neutron time-of-flight spectrometer mode {1,2}.

A modern spectrometer using two detectors for proton-recoil measurements is described by Geller et al. {16} (figure 7). The scatterer is a thin stilbene scintillator followed by a semiconductor. Actually, it is a telescope with a correction measurement for the proton-energy losses in the scatterer. It is of great interest for this work and we will discuss it further in chapter 5, »The scattering material.». The authors have found that the resolution is better than 5% for neutron energies above 10 MeV.

2.4 Proton-recoil telescopes

The classic proton-recoil telescope design is described by Johnson and Trail {17}. With five polyethylene foils of different thicknesses, the spectrometer covers the energy range 2 to 20 MeV. The recoiling protons pass through two proportional counters and terminate in a Na(Tl) crystal.

A foil having a thickness of 15 mg/cm^2 and an area of 1.98 cm^2 gives a resolution of 5.3%, a sensitivity of 3.6×10^{-6}, and an efficiency of 7.1×10^{-6} counts/(n,cm^{-2}). The contributing factors to the resolution are 4% radiator thickness, 1.6% geometric spread, 1.5% channel width, 1.5% neutron energy spread, and about 4% spread due to the crystal[1)].

[1)] The authors do not explain how these figures shall be combined into a total resolution.

The scatterer should contain as much hydrogen per volume-unit as possible. Takenoto and Hirato {18} have used a liquid scatterer. The proton energy loss in the window was 200 keV and the total energy resolution using a CsI(Tl) scintillator was about 20%.

Cambiaghi et al. {19} have used a combination of a dE- and an E-detector in order to measure the scattered protons. They claim that a resolution of 100 keV may be obtained but they take neither geometric nor stopping power effects into account. No efficiency is given. Therefore, the report is of limited value.

The telescope described by Ryves {20} is designed for neutron flux measurements (figure 8). The 0.5 mm[1] thick polyethylene foil gives an energy resolution of about 11% as estimated from his figures. However, the author gives an interesting discussion about some practical problems.

Particle identification is obtained by using a 250-micrometer-thick silicon dE-detector and a 2-mm-thick silicon E-detector. Combined with two proportional-counters, these give a fourfold coincidence for the detection of the protons.

Tantalum is used in an aperture between the silicon detectors. It is also used as backing material for the foil. Originally, a thin graphite backing was used, but this produced several per cent of lower energy particles due to neutron inelastic and elastic scattering. The thin tantalum backing was found to produce negligible background and furthermore, it degraded the high energy background protons produced in the steel front window of the telescope.

Finally, the telescope was lined with 2-mm-thick graphite. Graphite has high thresholds for the (n,p) and (n,alfa) reactions.

Morgan et al. {21} have used an unusal scattering foil. It is a sandwich of two polyethylene foils separated by an aluminium proton-absorber. The neutrons reached first a 2.03 mg/cm^2-thick polyethylene foil. The aluminium was 6.9 mg/cm^2 thick, it stopped protons whose energy was less than 1.5 MeV. The thickness of the second polyethylene foil was 0.65 mg/cm^2.

The idea with the sandwich is to obtain an efficiency compensation at higher energies. At low energies only protons from the thinner foil reach the Si-detector, at higher energies both the foils give contributions. The efficiency for the thin foil is 2.32×10^{-8} times the cross-section, which varies from about 4 barns at 1 MeV to about 1.6 at 5 MeV. Both the polyethylene foils provide together a factor of about 4 higher efficiency.

Two peaks appear in the medium energy range, i.e. around 3 MeV. The background from the aluminium is low at this energy. Only an E-detector is used. The peak widths are about 0.5 MeV.

Tantalum is used for the entrance and exit windows to the vacuum chamber.

2.5 Designs with annular scattering foils

The efficiency of a recoil neutron spectrometer is directly proportional to the amount of material used as scatterer. However, in order to have a good resolution, the thickness must be small and the scattering angle almost constant. A barrel-like scatterer {22,24} has been used in order to fulfil these demands, figure 9. We will use a barrel-like scatterer in some tests described in chapter 11, »Test measurements.», page 145. However, the method is not usable for a parallel beam of neutrons, so we can not use it in the final design.

Keith Furr and Runyon {23} have used an annular scattering foil and an axial silicon proton detector (figure 10), a method which will be adopted in this work. The distance between the foil and the detector in the design by Keith Furr and Runyon is 8.43 cm, the detector has a radius of 0.51 cm, and the foil has an inner radius of 1.27 cm and an outer radius of 2.06 cm. The efficiency is 5.70×10^{-6} times the scattering cross-section in barns for a 2.89 mg/cm^2-thick polyethylene foil. Thus, the foil area is 8.26 cm^2 and the sensitivity 0.69×10^{-6} times the cross-section. At 14 MeV this gives a sensitivity of 0.48×10^{-6}, which is somewhat too low for our purpose. However, this spectrometer is optimized for the energy range 2 to 5 MeV. The geometric resolution is 4.12%.

[1] 50 mg/cm^2.

The silicon detector is shielded for direct neutron and gamma radiation by lucite and lead. The whole spectrometer is inserted into a cylindrical collimator in the biological shield of a reactor.

Sidhu and Czirr {25} have used an annular radiator and axial recoil detector (figure 11) for monitoring purposes at the LLL linac. They used 3.3 and 0.3 mg/cm^2 polyethylene foils as scatterer. The Pb-shield for the silicon detector is 45 cm long. The collimated beam has an outer radius of 6.35 and an inner radius of 3.18 cm.

The background-to-signal ratio at 14 MeV is about 3%. The authors note that few-nanoseconds timing can be done quite easily.

A fast spectrometer with high detection efficiency has been developed by Chung {78}. Coneshaped horizontal detectors are used in addition to ring-shaped vertical radiatiors. Fast neutron-induced background is suppressed by a factor of more than 20 with Ge(Li) detectors in comparison with Si(Li) detectors. The measured spectrum of 15.1 MeV neutrons has an energy resolution of approximately 5% and detection efficiency of $1x10^{-4}$ when 20 mg/cm^2 polyethylene radiatiors are used. High purity Ge surface barrier detectors further suppress the neutron-induced background with a peak-to-background ratio of 44:1 at a neutron energy of 15.1 MeV. No detoriation of spectrometer characteristics are found with high purity Ge detectors during recycling from room temperature to liquid nitrogen temperature.

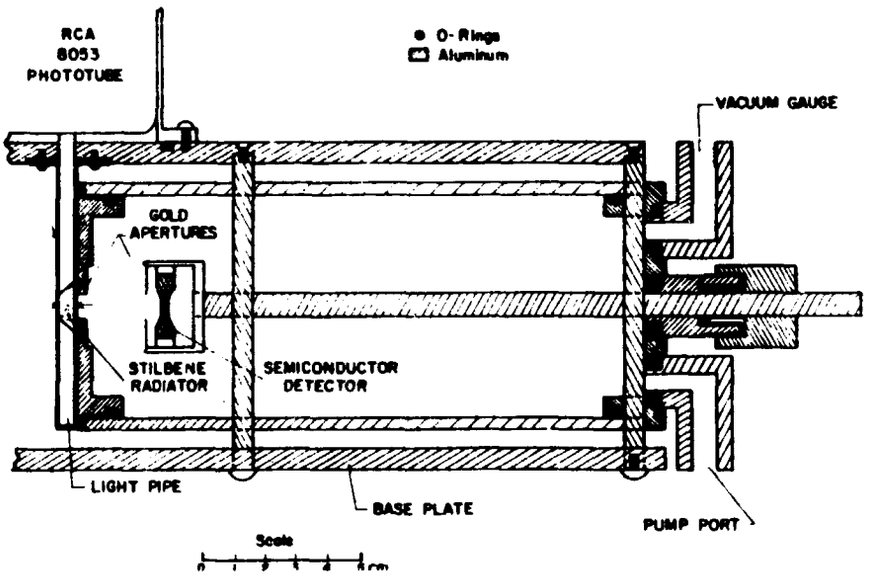

Figure 7. A telescope made by Geller et al.

Reproduced from reference 16.

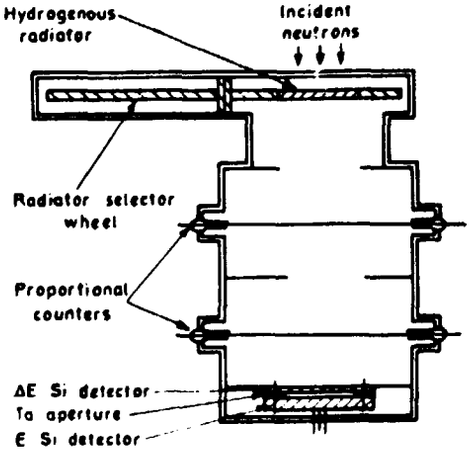

Figure 8. The Ryves proton-recoil telescope.

Reproduced from reference 20.

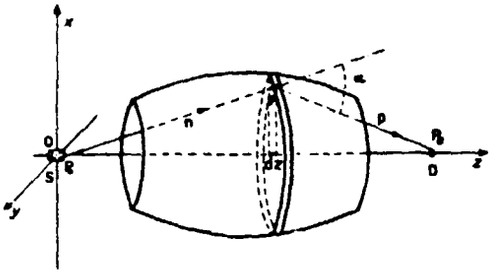

Figure 9. A barrel-like scatterer.

Reproduced from reference 22.

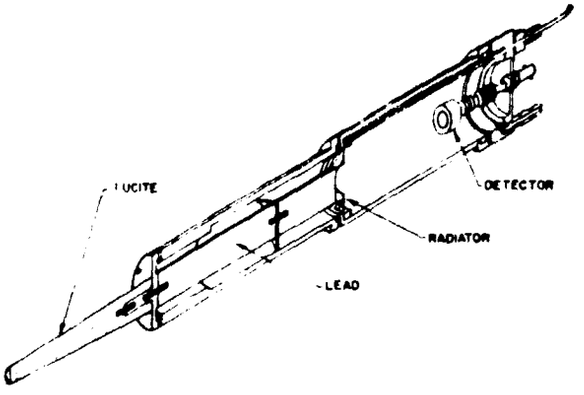

Figure 10. A spectrometer according to Keith Furr and Runyon.

Reproduced from reference 23.

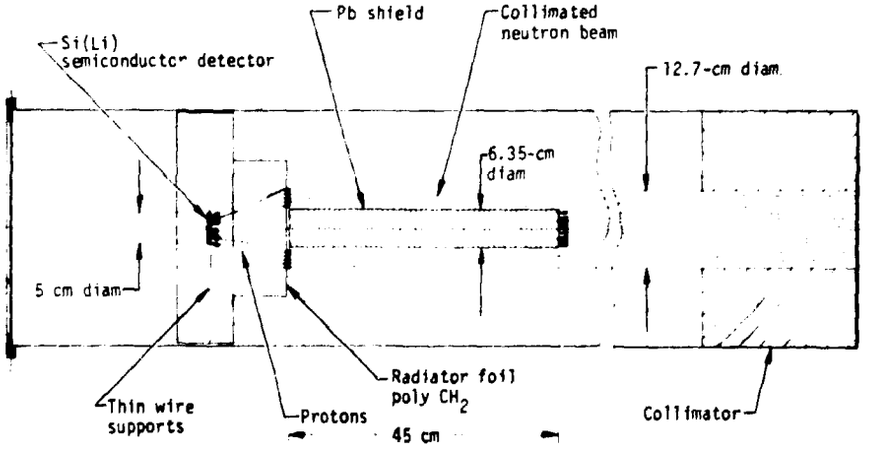

Figure 11. Fast-neutron monitor made by Sidhu and Czirr.

Reproduced from reference 25.

3 The JET plasma as a neutron source

The phase III of JET operation will involve a deuterium and tritium plasma in the temperature range 5 to 20 keV. The total number of neutrons emerging from the plasma during a single 10 s pulse, a shot, is estimated at 10^{18} to 10^{20} neutrons.

The neutron energy distribution reflects the properties of the plasma. The purpose of the neutron diagnostics is to pick up this information, store it and display it in an understandable way. The peak shape, energy displacement, symmetry, width, and tails of the neutron energy spectrum are properties which directly give a qualitative information about the plasma. However, for quantitative measurements we need some models connecting the ion movements and the neutron spectrum. These models are different for different processes in the plasma and are so far only partly known.

The interpretation of the neutron spectrum and the extraction of valuable parameters are not a part of this work. However, we need some knowledge about the spectrum as a background for a proper design of the spectrometer.

The most important sources of neutrons are the thermonuclear reaction, paragraph 3.1, and the beam-plasma reaction, paragraph 3.2. Some other effects will be discussed in paragraph 3.3.

In spite of the fact that JET will be one of the most powerful neutron sources on earth, it will be difficult to extract a sufficient amount of undisturbed neutrons for spectrometry. We will need the largest possible opening of the radial view port of the vacuum vessel in order to enable the collection of 1000 events per second, paragraph 3.4.

3.1 Thermonuclear fusion neutrons

The thermonuclear reaction will dominate at plasma temperatures higher than 10 keV. It is caused by reacting ions in equilibrium with a Maxwellian velocity distribution. The neutron production rate per unit volume for a two component plasma, deuterium and tritium, is given by

$$R = n_D \, n_T \, \langle \sigma v \rangle \tag{3.1}$$

where

n_D = deuterium ion density,

n_T = tritium ion density, and

$\langle \sigma v \rangle$ = the reactivity.

The reactivity is a mean value in the velocity space over the product of the cross-section and the normalized ion velocity distributions, $\sigma(v)$ and f(v). Thus, it is given by

$$\langle \sigma v \rangle = \int d^3 v_D \, d^3 v_T \sigma(v) \, v \, f_D(\mathbf{v}_D) f_T(\mathbf{v}_T) \tag{3.2}$$

$$v = |\mathbf{v}_D - \mathbf{v}_T|$$

A good approximation of the reactivity {66} is

$$\langle \sigma v \rangle = 10^{-10} \exp\left[\frac{a_1}{(kT)^r} + \sum_{i=0}^{4} a_{i+2} (kT)^i\right] \qquad (3.3)$$

where $r = 0.2935$ and the constants are -21.38, -25.20, -7.101×10^{-2}, 1.938×10^{-4}, 4.925×10^{-6}, and -3.984×10^{-8}, respectively. Here, the plasma temperature shall be given in keV in order to obtain the reactivity in $cm^{-3}s^{-1}$.

The emerging neutron energy spectrum will be a peaked distribution {67,3,68,26} with the peak mean energy very close to 14.06 MeV. The fwhm-value and the dispersion of the peak are given by the equations 1.4 and 1.3, respectively. The evaluation of the peak can be done using either of these equations. Both are related to the plasma temperature.

The dispersion, defined directly from the moments of the distribution, is from the statistical point of view the best choice. However, other plasma-related effects such as beam-plasma interaction and tails in the distribution influence the dispersion and make the interpretation uncertain. Background events must be carefully removed, since any remainder will disturb the result.

The fwhm-value is not so well-defined as the dispersion. The evaluation is somewhat subjective. However, for a complicated peak it is more readily extracted and interpreted than the dispersion.

3.2 Beam-plasma induced neutrons

The beam-plasma neutrons are caused by reactions between the thermal ion distribution and the neutral beam injected ions. They will dominate the measured neutron energy distribution at plasma ion temperatures lower than about 5 keV.

The velocity distribution {69,70} is of the type

$$f(v) \sim (v^3 - v_c^3)^{-1} \qquad v \leq v_o \qquad (3.4)$$

$$f(v) \sim (v^3 - v_c^3)^{-1} e^{-\frac{m}{2kT}(v^3 - v_o^3)} \qquad v > v_o \qquad (3.5)$$

where

v_c is the critical velocity, the velocity where ion drag = electron drag, and

v_o is the velocity of the injected ions.

The neutron energy distribution is illustrated in figure 12. The width of the distribution is the sum of the energy of the injected ions and the plasma temperature measured in energy units {72}. The energy of the injected ions is the dominating part. It is about 160 keV as compared to 15 keV or less for the plasma. Therefore, the plasma properties will show up in the slopes of the neutron distribution. An increasing plasma temperature will give an increasing broadening of the peak and a decreasing relative derivative of the slope.

The spectrometer sees a large part of the plasma. Therefore, we do not expect any shift of the neutron-spectrum mean energy. The neutron energy distribution will be symmetric around 14.06 MeV.

The widths calculated by Towner and Jassby {72} go from 13 to 15 MeV. From this we have determined the energy range for the spectrometer. The interval 12 to 16 MeV gives some margin for unexpected deviations.

3.3 Miscellaneous plasma neutrons

To the two principal sources of neutrons, the thermonuclear and the beam-plasma reactions, can be added the beam-beam reactions. However, we expect only a negligible neutron output from these reactions.

Of greater interest are those test schemes which will be developed at JET. The neutron diagnostics will play a significant role in the evaluation of these tests, some of which (hopefully) are not predictable. As an example, the simple picture of neutron production will be modified in case of significant ion-tail enhancement with extensive use of rf-heating {71}. The ion-tail enhancement may be increased by the use of the energy-clamping scheme, i.e. tuning the rf-heating in resonance with the injected ions {73}.

The enhanced ion-tails will significantly change both the total yield and the energy distribution of the fusion neutrons. Therefore, the energy range and the dynamic range should be kept as wide as possible.

3.4 Neutron yields for TANSY

The total neutron flow into the foil of TANSY has been estimated using the equations 3.1 to 3.3. The foil is placed 20 m from the torus centre. A primary shield, a diaphragm for neutrons, is placed 6 m from the torus centre, see figure 13. The shield is considered totally absorbing and the aperture totally transparent, i.e. no account is taken for the absorption in the radial view port. The maximal opening is assumed to be 70x20 = 1400 cm^2 and it is assumed that this area can be reduced by some kind of plugs in order to adjust the neutron-flow to a proper value. The collimator is considered designed so that all points of the foil can see the whole aperture.

The total neutron flow for different apertures is shown in figure 14. The TANSY sensitivity is 10^{-8} giving a wanted flow of 10^{11} neutrons per second, a flow which we reach at 6 keV with the largest aperture. A not perfect but still usable spectrum of about 1000 counts can be collected at 3 keV.

It is difficult to get an exact estimate of the neutron flow, since several for us unpredictable parameters are involved. The sight line passes the plasma twice, see figure 13. Therefore, parameters, such as the mean radius and the width of the plasma, affect the neutron flow. These and other parameters vary during a shot. The measured neutron distribution is a time mean value over the entire shot. It is important to adjust the neutron flow, with the aperture, so that the peak neutron flow does not override the upper limit of the dynamic range, see paragraph 8.4, page 104.

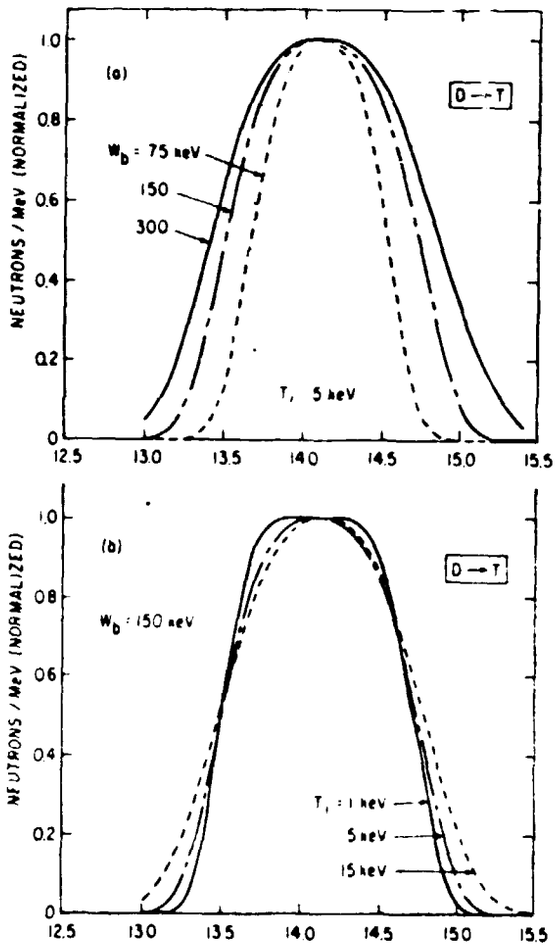

Figure 12. Beam-plasma reactions.

Calculated neutron spectra for beam-plasma reactions. The upper figure shows the distributions for a plasma temperature of 5 keV and injection energies of 75, 150, and 300 keV. The lower figure shows the distributions for an injection energy of 150 keV and plasma temperatures of 1, 5, and 15 keV. Reproduced from reference 72.

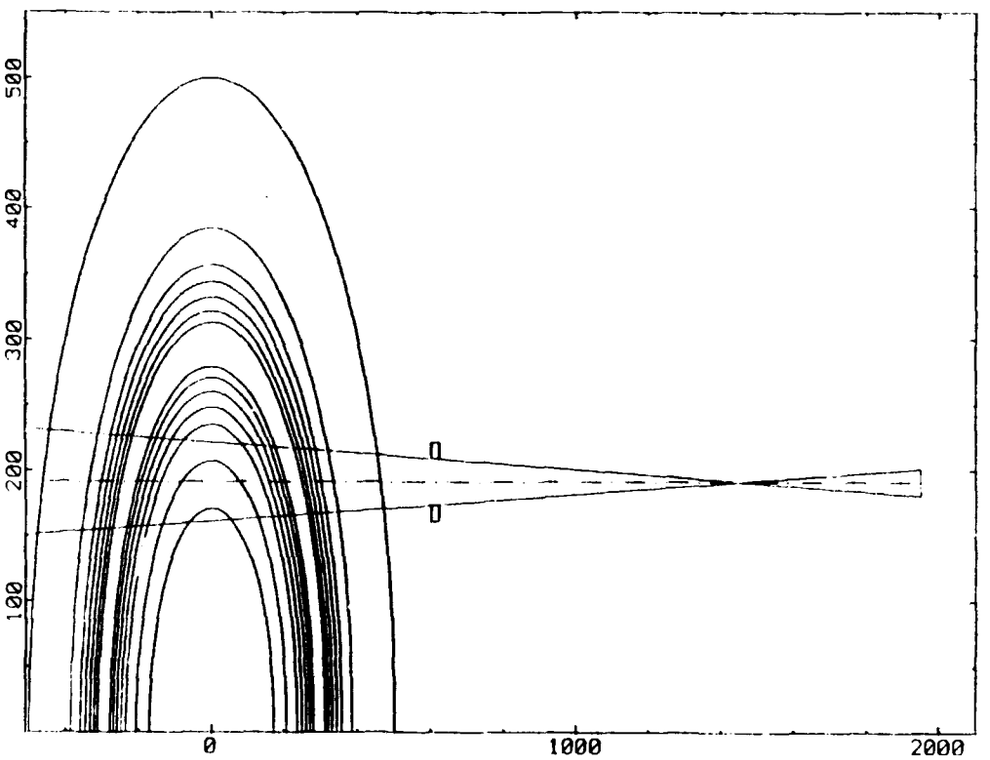

Figure 13. Sight lines in the plasma.

The sight lines are determined by the foil and aperture sizes and positions. The sight lines pass twice through the plasma. The distances are given in cm.

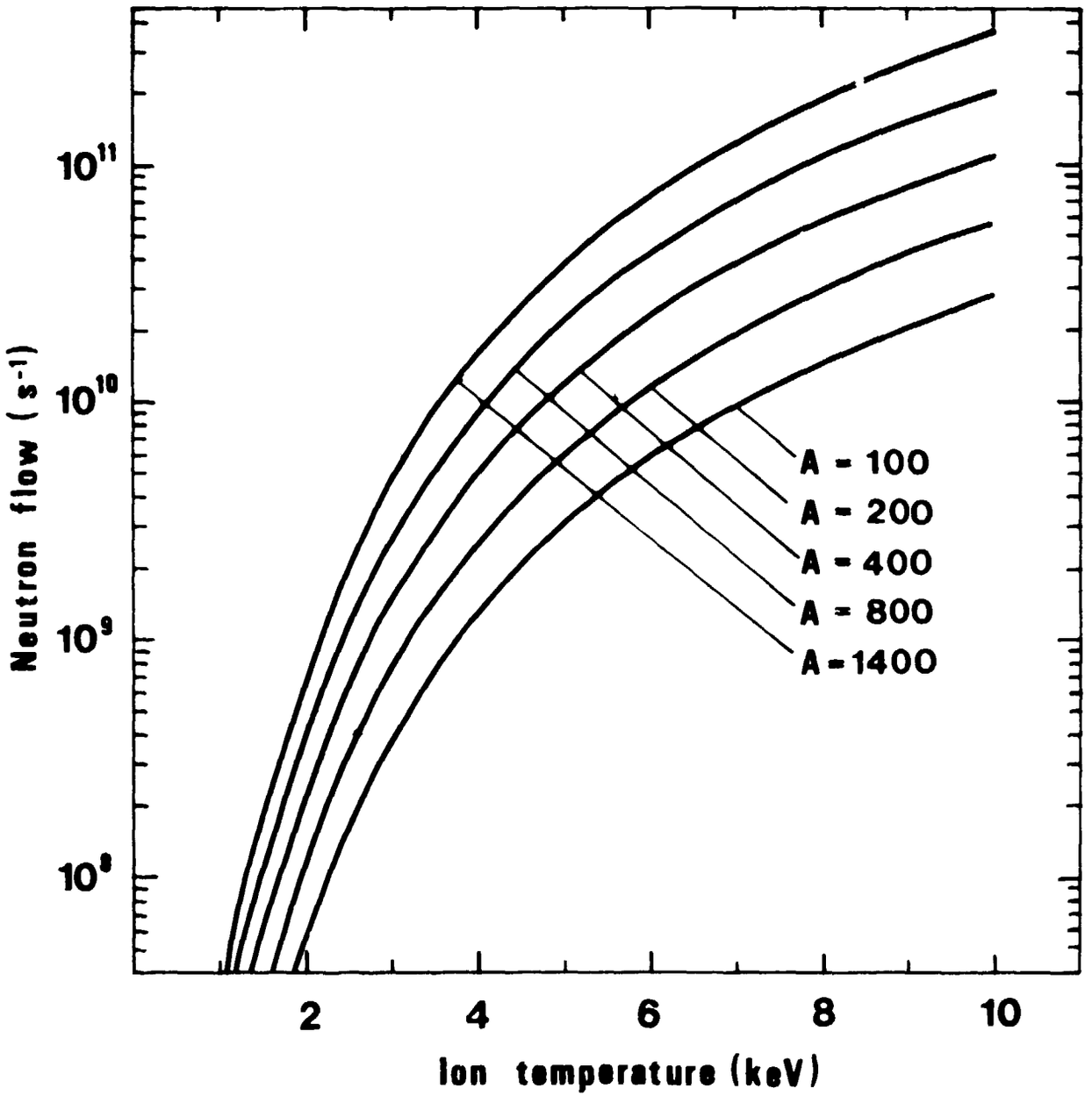

Figure 14. Neutron flow.

The total neutron flow into the foil for different apertures A in cm^2. The neutron flux density at the foil is the neutron flow divided by the foil area, i.e. 100 times lower than the given values. The spectrometer sensitivity is 10^{-8} and the efficiency 10^{-6} cm^2.

4 Neutron scattering

The basic idea of this spectrometer is a simultaneous measurement of the energies of the neutron and the proton emerging from a neutron-proton scattering process. The proton energy is measured directly by a silicon detector. The neutron energy is derived from the time difference between the signals from the proton-detector and a neutron-detector. Using classic mechanics the initial-neutron energy can be calculated by one single formula, equation 4.6.

An analysis with relativistic mechanics in which we take the neutron-proton mass difference into account shows that the equation 4.6 gives sufficient accuracy for most of the usable scattering angles. However, small proton-recoil angles must be avoided. A small correction must be done for the detector positions. The angle between the scattered neutron and the proton is slightly less than 90 degrees.

The use of a polyethylene scatterer gives parasitic neutron-carbon scattering. The relative amount of these neutrons is about 20% for TANSY. They have an average energy of 12.5 MeV.

During the course of this work we have considered several possible neutron-detector, proton-detector, and scatterer combinations. We present some of these ideas in the figures 27 to 32.

4.1 Classic neutron-proton scattering

The classic model for neutron-proton scattering is very simple. The neutron mass and the proton mass are considered to be equal, which means that there is a right angle between the paths of the recoiling proton and the scattered neutron. The energy of the neutron or the proton is given by the same formula,

$$E = E_o \cos^2\theta \tag{4.1}$$

where E_0 is the initial neutron energy and θ is the scattering or the recoil angle.

We may convert this equation into a velocity equation,

$$v = c\sqrt{\frac{2E_o}{m}}\cos\theta \tag{4.2}$$

where c is the light velocity and the mass m is measured in energy units.

Gammel (in reference 6, page 2209) gives an empirical formula for the total scattering cross section

$$\sigma_s(E) = 3\pi\,[1.206E + (-1.86 + 0.09415E + 0.0001306E^2)^2]^{-1} + \pi\,[1.206E + (0.4223 + 0.13E)^2]^{-1} \tag{4.3}$$

where E is given in MeV. A more recent formula is given by Hopkins and Breit {27}. However, the difference in the 14 MeV range is small. We will use the above formula, which for 14 MeV neutrons gives a cross section of 0.69 barns.

The angular variation of the cross section is small[1]. Therefore, this variation will be neglected. Thus, we write the scattering cross-section per unit solid angle in the laboratory system as

$$\sigma_H(\theta) = \frac{\sigma_s(E)}{4\pi} \, 4\cos\theta \tag{4.4}$$

These four equations are the base for our analysis. They are always used unless otherwise stated. All deviations, relativistic effects etc., will be considered to be corrections to these formulae.

4.2 The measurement method

The energy of the proton can be measured with high accuracy. The resolution of a silicon detector is only a few tens of keV. The most accurate method to measure the neutron energy is the time-of-flight method. The resolution depends on the accuracy of the flight-path-length determination and the timing characteristics of the detectors. Here we will combine these two methods.

The timing and energy characteristics of the scattering process are illustrated in figure 15. The energy of the incoming neutron is distributed on the scattered neutron and the recoiling proton. It is favourable to use a small proton recoil angle. The proton will then pick up most of the initial-neutron energy and the proton flight time will be short. At 15 degrees the proton energy is 13 MeV and the neutron energy is 1 MeV. Therefore, the accuracy requirement of the neutron energy measurement is about ten times lower than the requirement of the proton energy measurement.

The time difference between the detection of the proton and the neutron is

$$t = \frac{l_n}{c}\sqrt{\frac{m_n}{2E_n}} - \frac{l_p}{c}\sqrt{\frac{m_p}{2E_p}} \tag{4.5}$$

where

l is the flight-path length

E is the particle energy

m is the particle mass in energy units

n,p are indexes for neutron and proton, respectively.

We combine this with the fact that the initial neutron energy is the sum of the neutron and the proton energy. Then we have

$$E_o = E_p + \frac{m_n l_n^2}{2\left(ct + l_p\sqrt{\frac{m_p}{2E_p}}\right)^2} \tag{4.6}$$

[1] See reference 7 for further references.

This equation is illustrated for TANSY in the figures 70 and 71 in chapter 8, »Characteristics of the detection method.». The flight times are of the order of 6 ns for the proton and 80 ns for the neutron. The second term of equation 4.6 is then of the order of 1 MeV, i.e. 8% of the first term. Therefore, the time measurement may be looked upon as a correction term measurement.

It should be pointed out that the determination of the energy depends only on the time delay and the proton energy. It does not depend on the scattering angle. From this point of view there is no requirement for collimators or other methods for scattering angle limitations. However, the accuracy of the measurement depends on the scattering angle. Therefore, rather serious limitations will appear later on.

4.3 Relativistic and mass-difference effects

14 MeV neutrons are weakly relativistic. They have a velocity, which is 17% of the vacuum light velocity. The use of classic mechanics in the conversion between energy and velocity gives about 1% deviation from the correct value. This is in the same range as the wanted resolution of the spectrometer. Therefore, it is necessary to study this effect although it is normally not taken into account in this energy range {30}.

Another problem that often is neglected {28} is the mass difference between the neutron and the proton. The mass of the proton is about 0.14% lower than the neutron mass. The difference is small but it gives some effects that can not be realized from the equal-mass model. The effects are in some cases much bigger than might be expected.

We will treat these two effects together and calculate corrections to the classical equal-mass model. The formalism is somewhat too extensive to be included here. However, it is a straight forward relativistic formalism as described by e.g. Baldin et al. {29}. Only three input constants are needed. We have used {31}:

proton rest mass = 938.2592 MeV
neutron rest mass = 939.5527 MeV and
light vacuum velocity = 2.9979245×10^8 m/s.

The formalism is readily explained by using the concept of the impulse ellipse. It is defined as the locus of the points given by the scattered-neutron momentum-vector in the laboratory system (figure 16). Normally, the recoil particle is heavier than the neutron. The origin is then inside the impulse ellipse; there is only one momentum-vector for each angle. However, in the case of a recoil particle lighter than the neutron, the origin will be outside the impulse ellipse. Then the neutron momentum-vector has two values for a given scattering angle. Only a limited range of scattering angles is allowed. The largest angle is defined by that momentum-vector, which is a tangent to the impulse ellipse. In the case of classic equal-mass scattering, the impulse ellipse is a circle going through the origin.

The neutron-proton impulse ellipse is shown in figure 17. Very high neutron energies are needed in order to give a visible deviation from a circle. However, an enlargement of the area around the origin (figure 18) shows that there is a critical scattering angle. It shows up at 86.993 degrees. It has the dignity of a law-of-nature. It is constant through all incoming neutron energies. It depends only on the ratio of the proton mass to the neutron mass.

$$\sin(\theta_{critical}) = \frac{m_p}{m_n} \tag{4.7}$$

In this method we measure the energy of the proton with a silicon detector. This is the real proton energy including relativistic effects. The neutron energy is given by a time-of-flight measurement, which depends on the relativistic effects. However, the neutron energy measurement is limited to large scattering angles, small energies, by the uncertainty of the time-of-flight method. No corrections are needed at energies of 1 to 2 MeV. However, we must be a little careful here. The energies versus the scattering angle are shown in figure 19. The classic equal-mass model gives too high values below 87 degrees and breaks down above this angle. No neutrons will be scattered to angles larger than 87 degrees.

The differential neutron scattering cross-section is shown in figure 20 and 21. A very thin peak appears at the critical angle. Below this there are two branches, one for the low energy neutrons and one for the high energy neutrons. The upper curve converges rapidly towards the classic distribution. The fraction of low energy neutrons is small and can be neglected below 85 degrees.

The angle between the scattered neutron and the recoiling proton is 90 degrees, a value which is independent of the initial-neutron energy as long as we use the classic equal-mass model. This may be deduced from the impulse ellipse, which is a circle in this case. In figure 22 we show that the correct value is somewhat less than 90 degrees. The mean correction in TANSY is 0.25 degrees. This can be corrected for by an adjustment of the neutron-detector position.

The variation with the initial-neutron energy is small, about 0.05 degrees in TANSY. It is not possible to correct for this variation. However, it is small and will be neglected. It will lead to a minor loss of coincidences, and there will be a negligible correction to the energy dependent sensitivity.

In figure 23 and 24 the corrections are separately given for the neutron and the proton. From the figures we see that the 0.25 degrees total correction depends mostly on the neutron scattering angle. The correction is 0.20 degrees for the neutron- and 0.05 degrees for the proton-angle. At low initial-neutron energies the unequal-mass effect appears only for the neutron.

In conclusion we find that there will be a few millimeter correction of the neutron detector-position. Beyond that no corrections are necessary. The classic equal-mass model will give sufficient accuracy for the evaluation of the measured data.

4.4 Neutron-carbon scattering

The most popular scattering foil material is polyethylene. It contains two hydrogen atoms for each carbon atom. The neutrons scattered by carbon do not fulfil the coincidence criterion. However, they create false coincidences.

The differential cross-section, in the center-of-mass system, for carbon depends on the scattering angle {32}. It is often represented by a Legendre polynomial expansion. The equation corresponding to equation 4.4 may be written {33}

$$\sigma_c(\theta) = \frac{\sigma_s(E)}{4\pi}\, C(\theta) \sum_{\nu=0}^{6} (2\nu+1)\, f_\nu P_\nu(\cos\Psi) \qquad (4.8)$$

where

ψ is the centre-of-mass scattering angle

P_ν is the Legendre polynomial

θ is the laboratory-system scattering angle.

The relation between θ and ψ is given by

$$\Psi = \theta + \sin^{-1}\left(\frac{m_n}{m_c}\sin\theta\right) \qquad (4.9)$$

and the factor

$$C(\theta) = \frac{\left[\cos(\theta) + \sqrt{\left(\frac{m_c}{m_n}\right)^2 - \sin^2(\theta)}\,\right]^2}{\left(\frac{m_c}{m_n}\right)\sqrt{\left(\frac{m_c}{m_n}\right)^2 - \sin^2(\theta)}} \qquad (4.10)$$

The ratio of the number of neutrons scattered by carbon nuclei to those scattered by hydrogen nuclei is then

$$R(\theta)\,d\theta = \frac{\sigma_C(\theta)\,d\theta}{2\sigma_H(\theta)} \tag{4.11}$$

This function is plotted in figure 25. Fortunately (for TANSY) the lowest value, about 20%, appears around 75 degrees.

The energy of the scattered neutrons is given by

$$E_c = E_o \left(\frac{m_n}{m_n+m_c}\right)^2 \left[\cos\theta + \left[\left(\frac{m_c}{m_n}\right)^2 - \sin^2\theta\right]^{1/2}\right]^2 \tag{4.12}$$

It is drawn in figure 26. For TANSY the energy is about 12.5 MeV. This means that about 80% may be removed by an upper discriminator. The maximum carbon-recoil energy is 2 MeV. Therefore, carbon recoils are easily removed by a lower discriminator in the proton-detector signal-line.

4.5 Exploitation possibilities

Three elements are involved in the measurement. They are the scatterer, the proton detector, and the neutron detector. The shapes of these are constrained by the coincidence condition. The proton-detector, a semi-conductor because of the resolution requirements, is normally circular. Then a point-scatterer and a parallel incoming neutron beam will create an ellipse-like neutron detector as illustrated in figure 27.

The shape of the neutron-detector will depend on the position of the proton-detector in relation to the neutron beam. If, as an extreme case, we place the proton-detector on the central axis, the neutron-detector will be ring-shaped, figure 28.

The use of a finite disc-shaped scattering foil will increase the number of possible scattering angles, figure 29. Each point of the foil shall be combined with all points of the proton-detector. This means that the scattered neutrons will be more spread out than in the point scatterer case. In figure 30 the appropriate neutron detector shape is shown as a function of the azimuth angle.

It is possible to use a thick scatterer. In figure 31 we consider a hydrogen gas scatterer. The stopping power for protons in hydrogen gas is low, about 7 keV per cm at normal pressure and temperature. A protected p-type proton-detector[1)] may be used in the gas in order to avoid a window. The scattering volume is defined by the neutron beam and some apertures for the protons.

One of two methods may be used in order to increase the efficiency of a system with a scattering foil. One may use an annular proton-detector or an annular scattering foil. The resolution of a silicon detector decreases with increasing surface area. Moreover, a semiconductor will have a limited life-time and a cost which dramatically increases with surface area and complexity. Therefore, we prefer an annular scatterer, figure 32, in spite of the fact that complications will arise in the construction of the collimator.

1) E.g. the »Ruggedized» R-type surface barrier detector from Ortec.

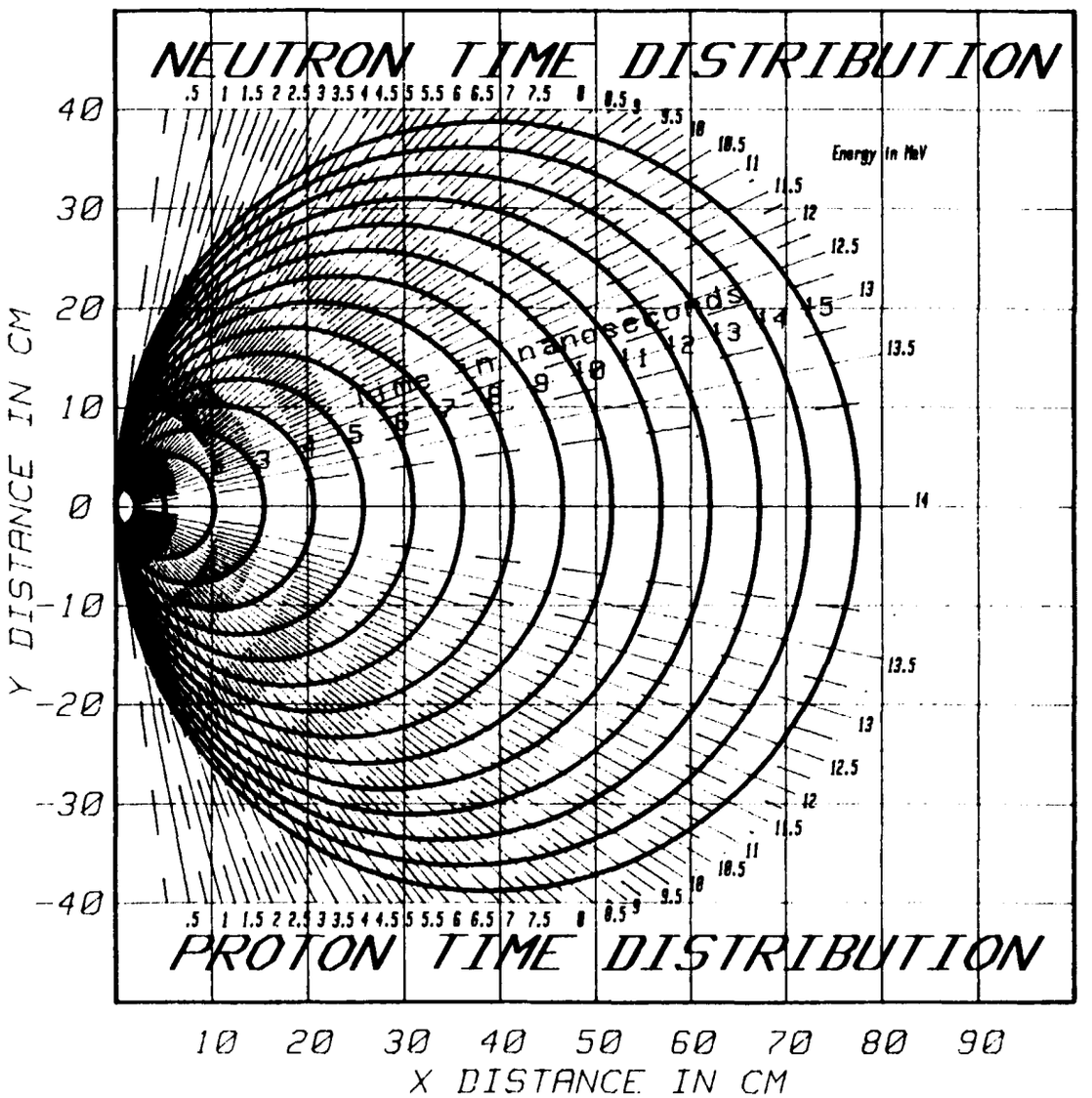

Figure 15. Classic neutron-proton scattering chart.

The angle between the neutron-path and the proton-path is always 90 degrees. Place a set square on the diagram with the 90 degree corner at the zero-point. Read arrival times, space coordinates, and energies for the particles along the legs of the set square.

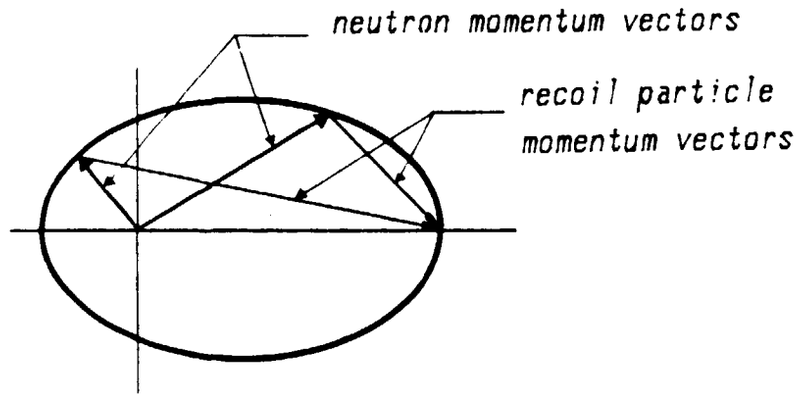

The impulse ellipse for a heavy scatterer.

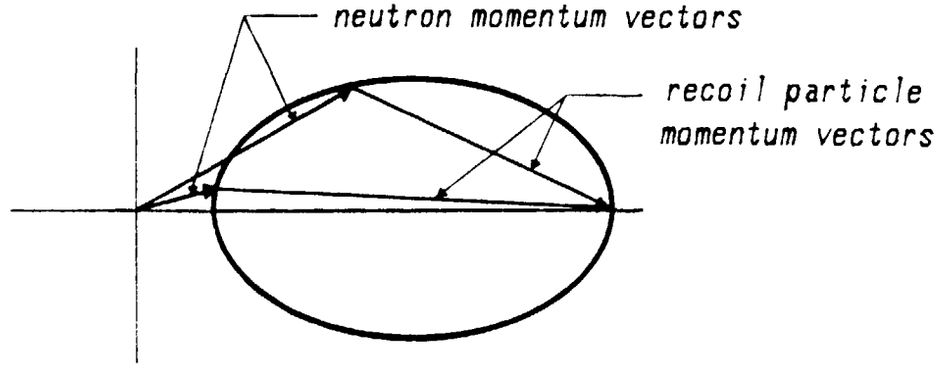

The impulse ellipse for a light scatterer.

Figure 16. Principles of the impulse ellipse.

The impulse ellipse is the locus of the points defined by the momentum-vector of the scattered neutron.

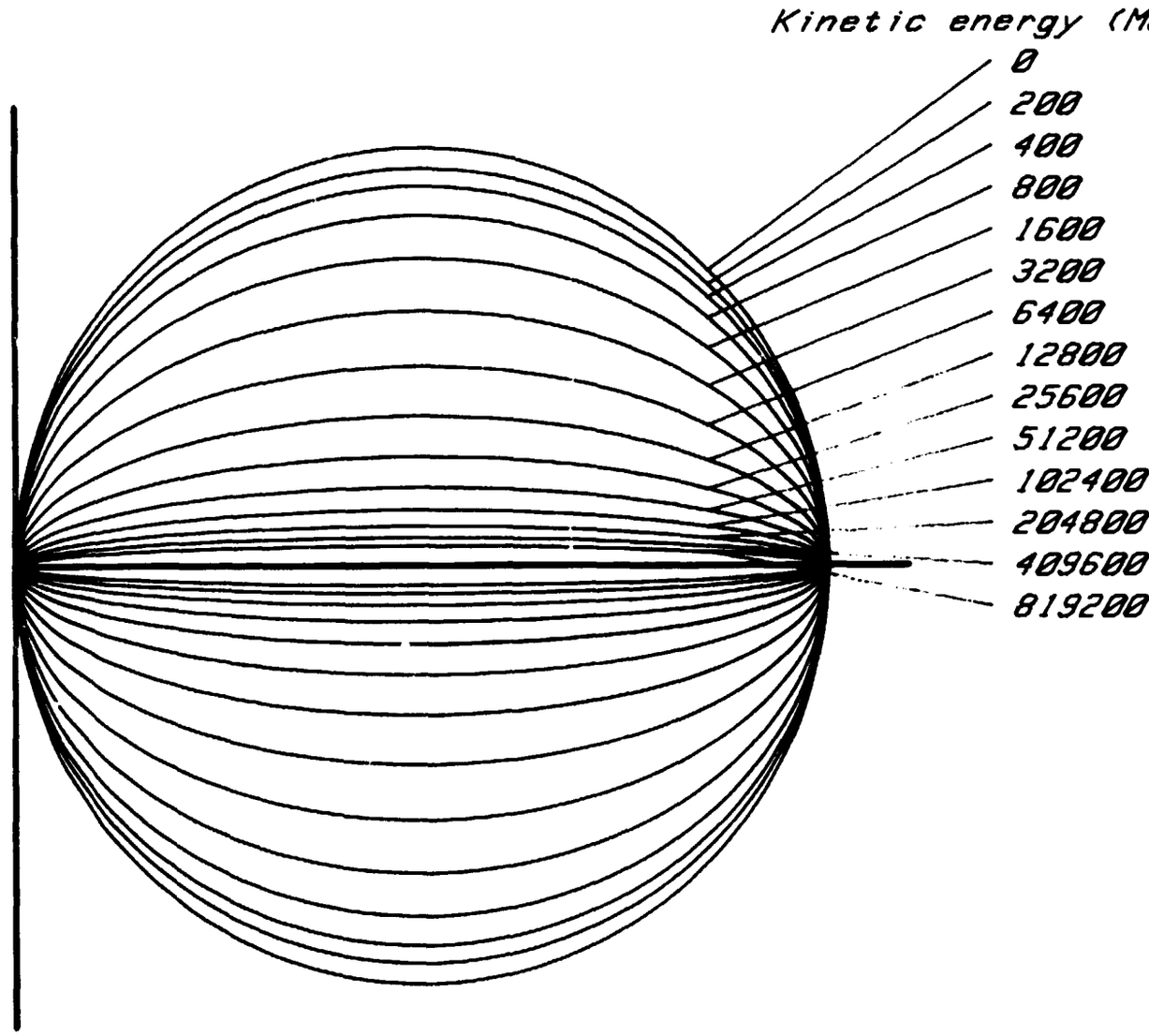

Figure 17. The neutron-proton scattering impulse ellipse.

The classic equal-mass model gives a circle. Deviations from the circle are visible only for high energies of the initial-neutrons.

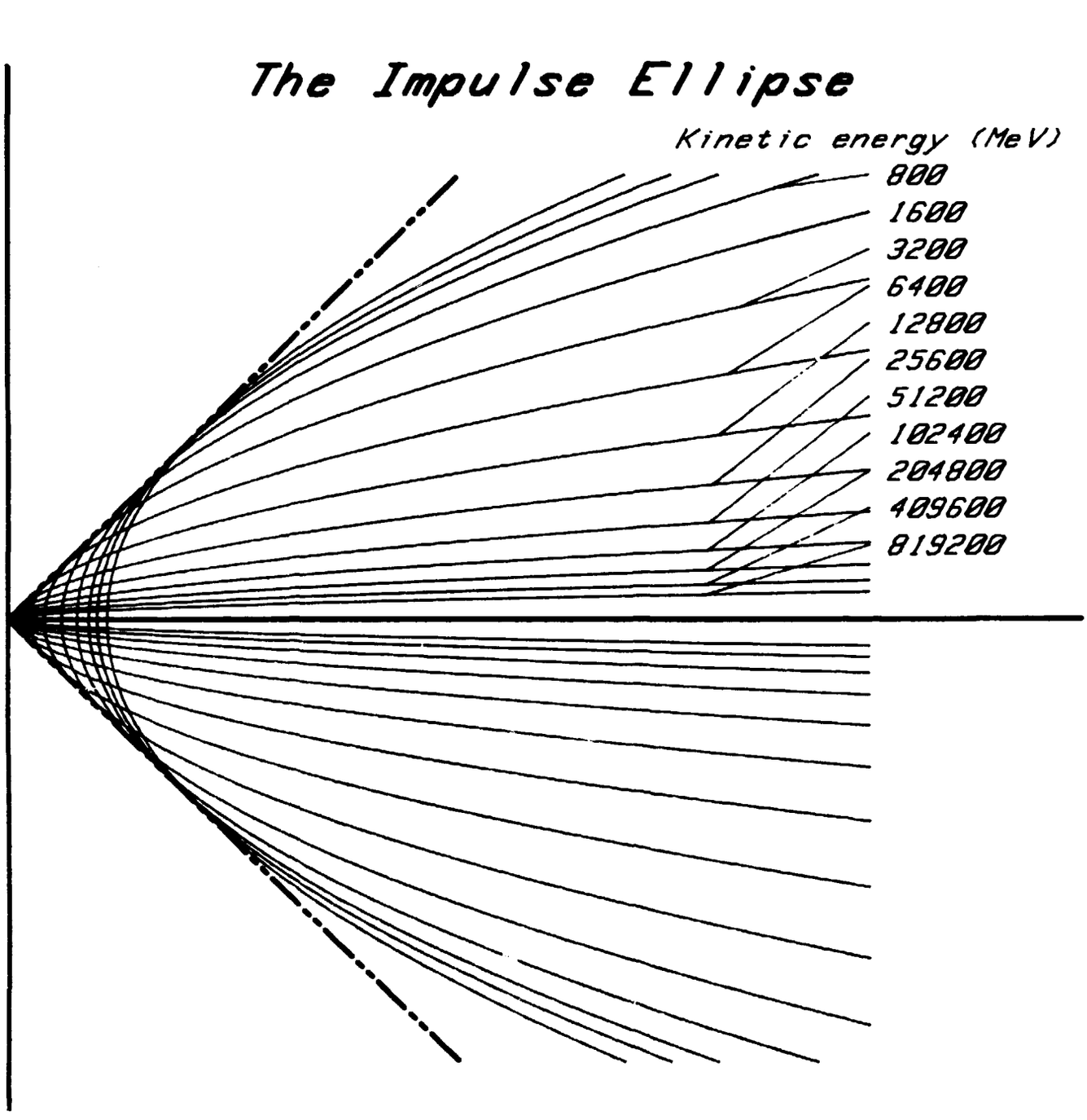

Figure 18. The critical angle.

Enlargement of figure 17 shows that there is a critical angle, which is independent of the initial-neutron energy.

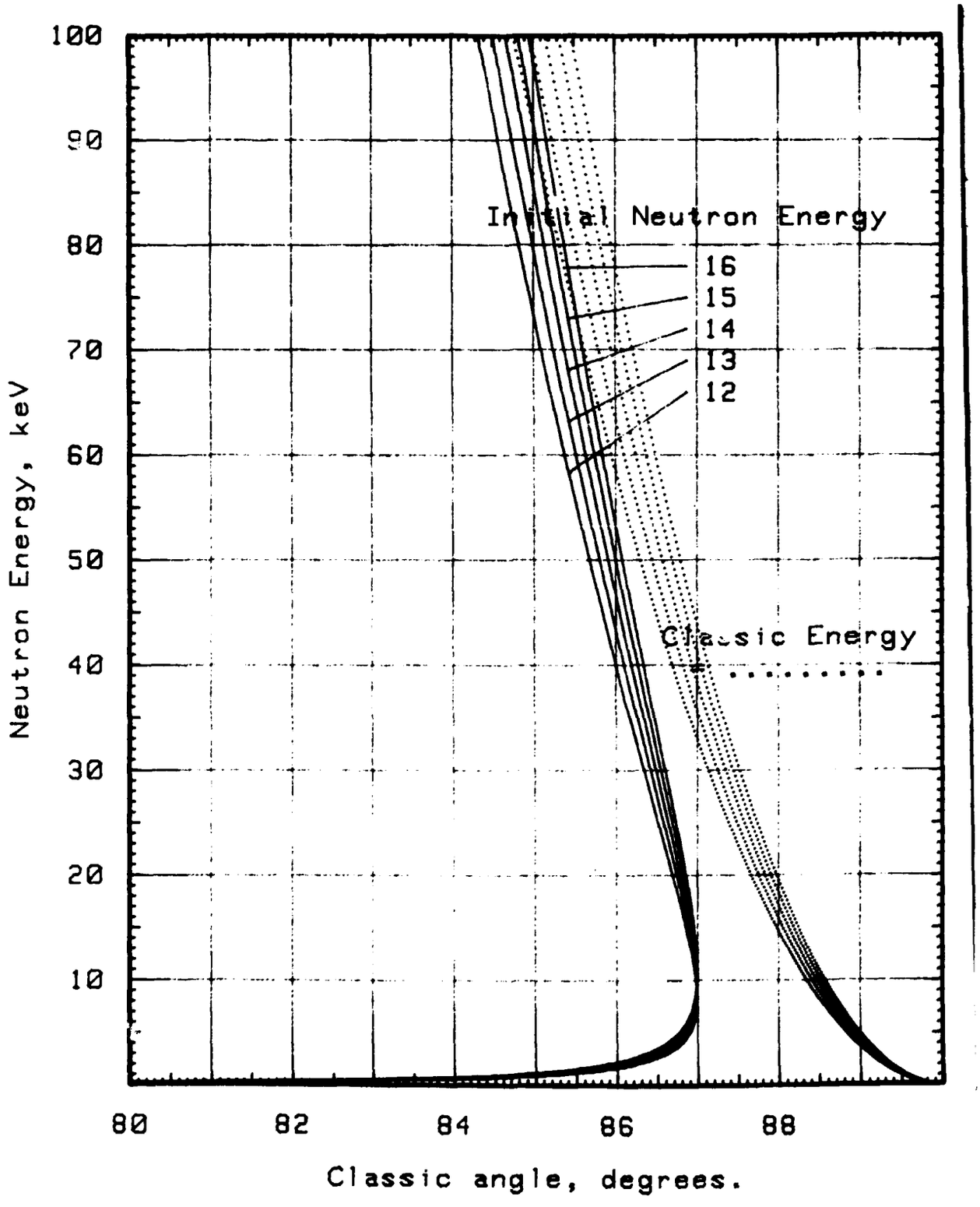

Figure 19. The kinetic energy of the neutron.

The energy is two-valued.

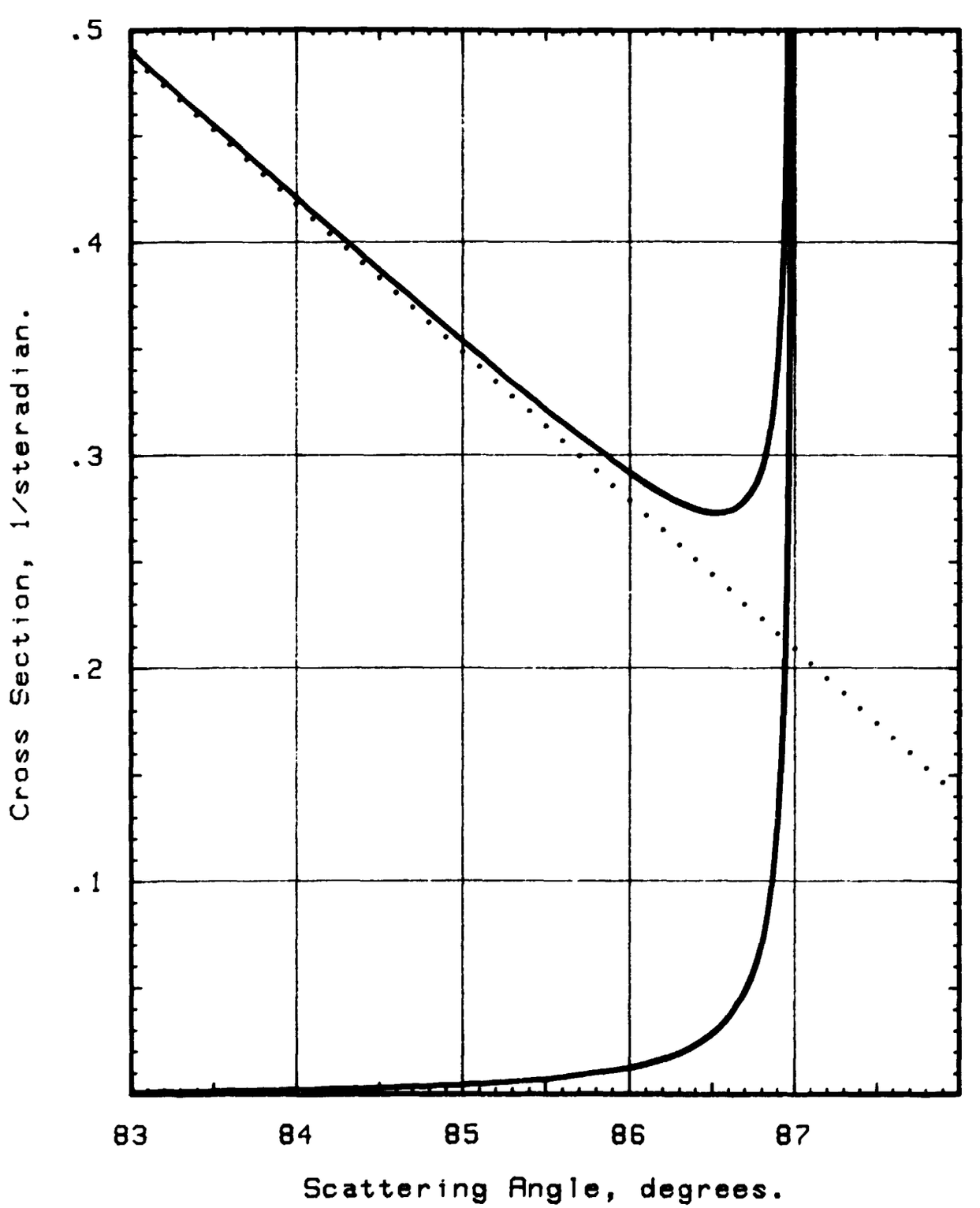

Figure 20. The differential neutron cross-section.

The dotted line represents the classic cross-section. The peak has an infinite magnitude but a finite area.

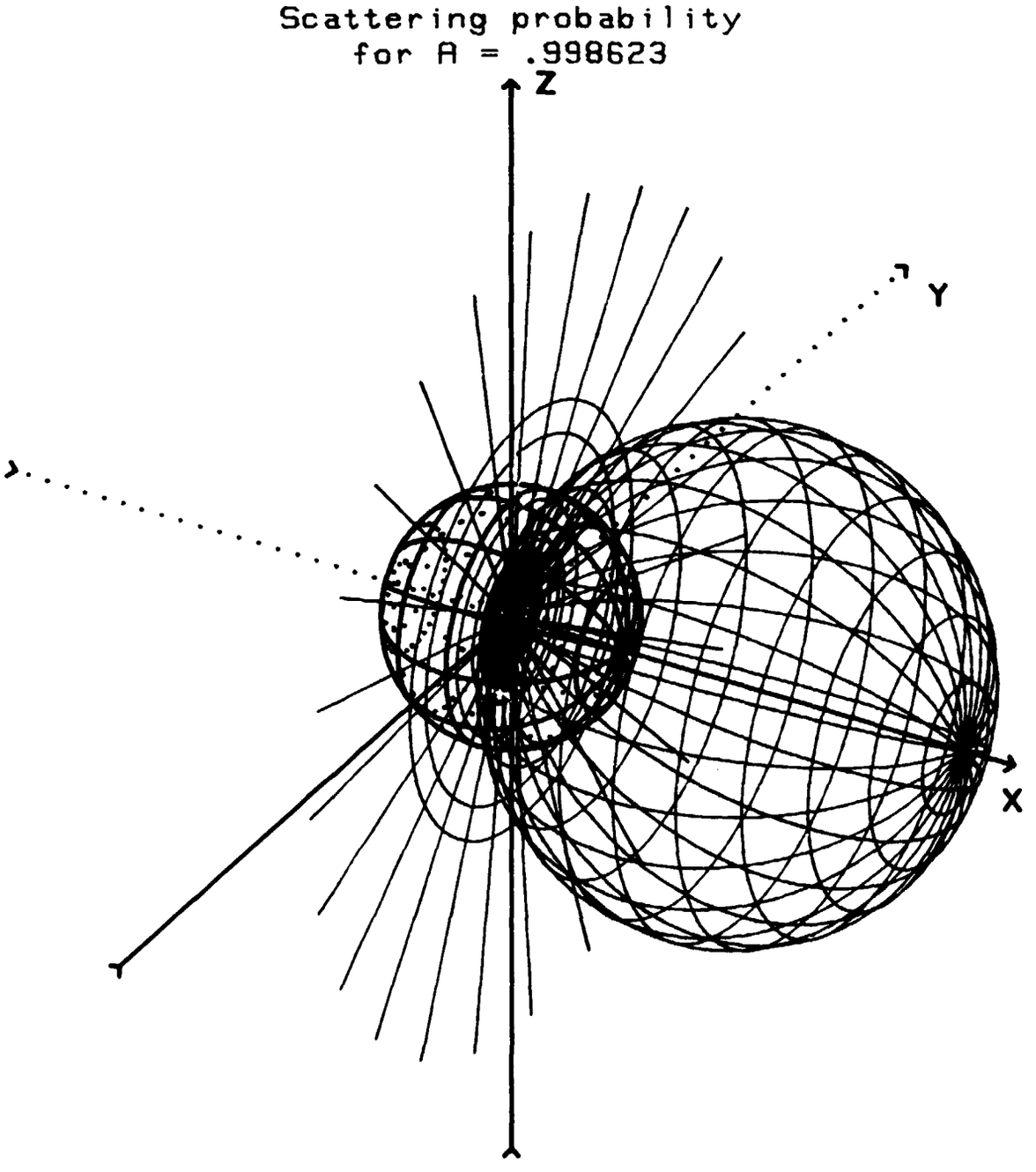

Figure 21. A three-dimensional view of the cross-section.

The cross-section is represented by the vector from the origin of the coordinate axes to the shown surface. The small sphere represents isotropic scattering, i.e. scattering against a heavy nucleus.

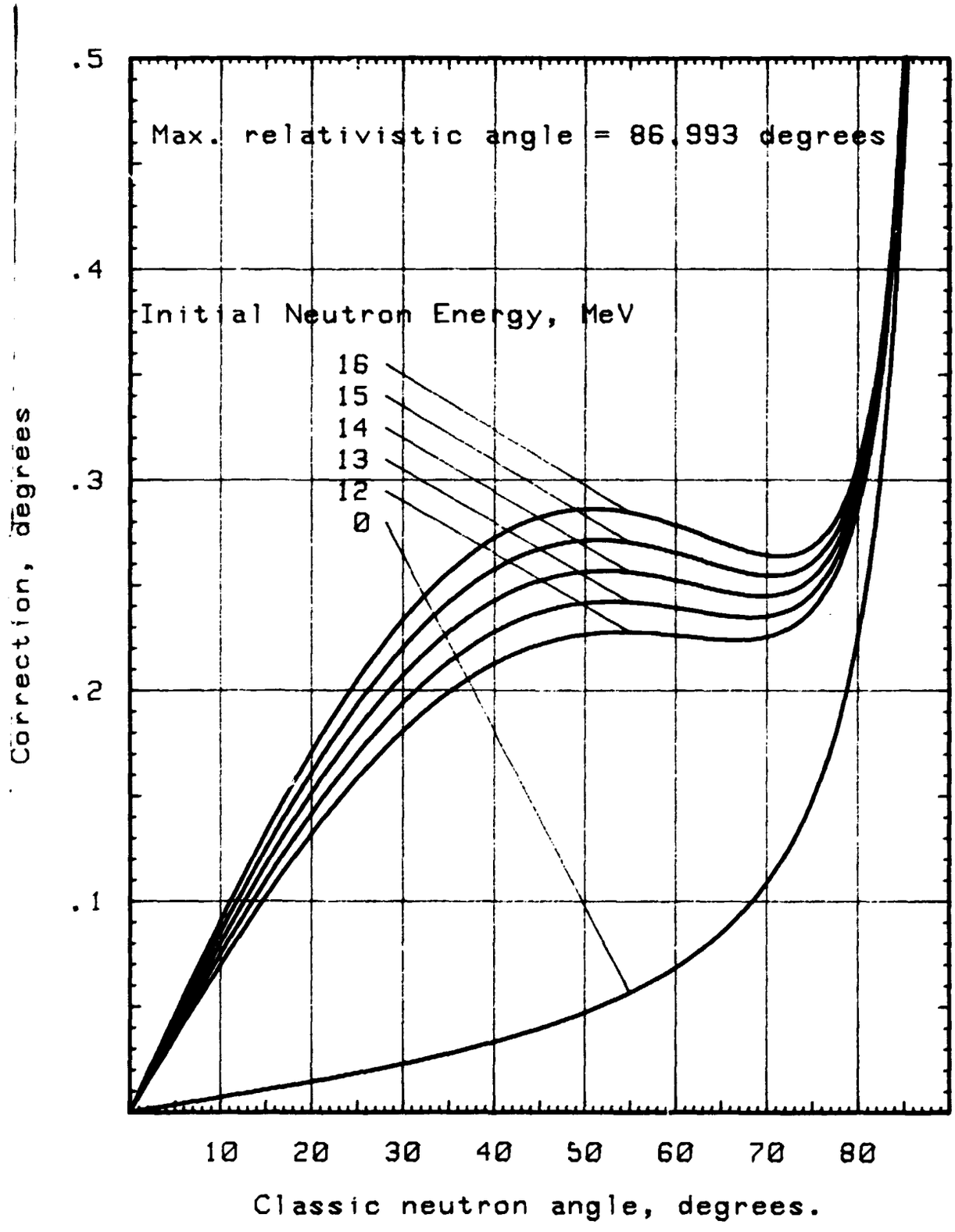

Figure 22. The angle between the neutron- and the proton-path.

Relativistic angle = 90 - correction

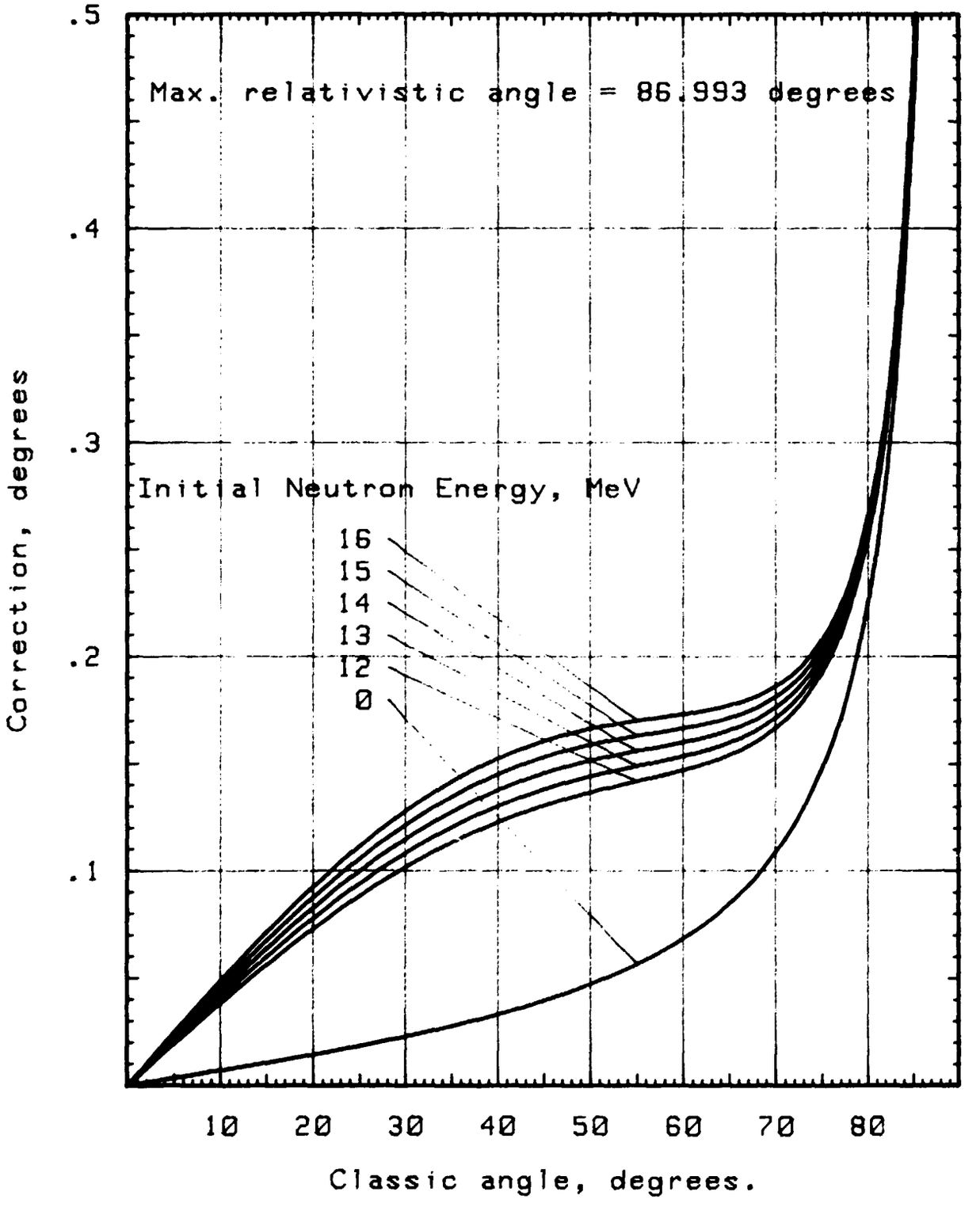

Figure 23. The neutron scattering angle.

Relativistic angle = classic - correction.

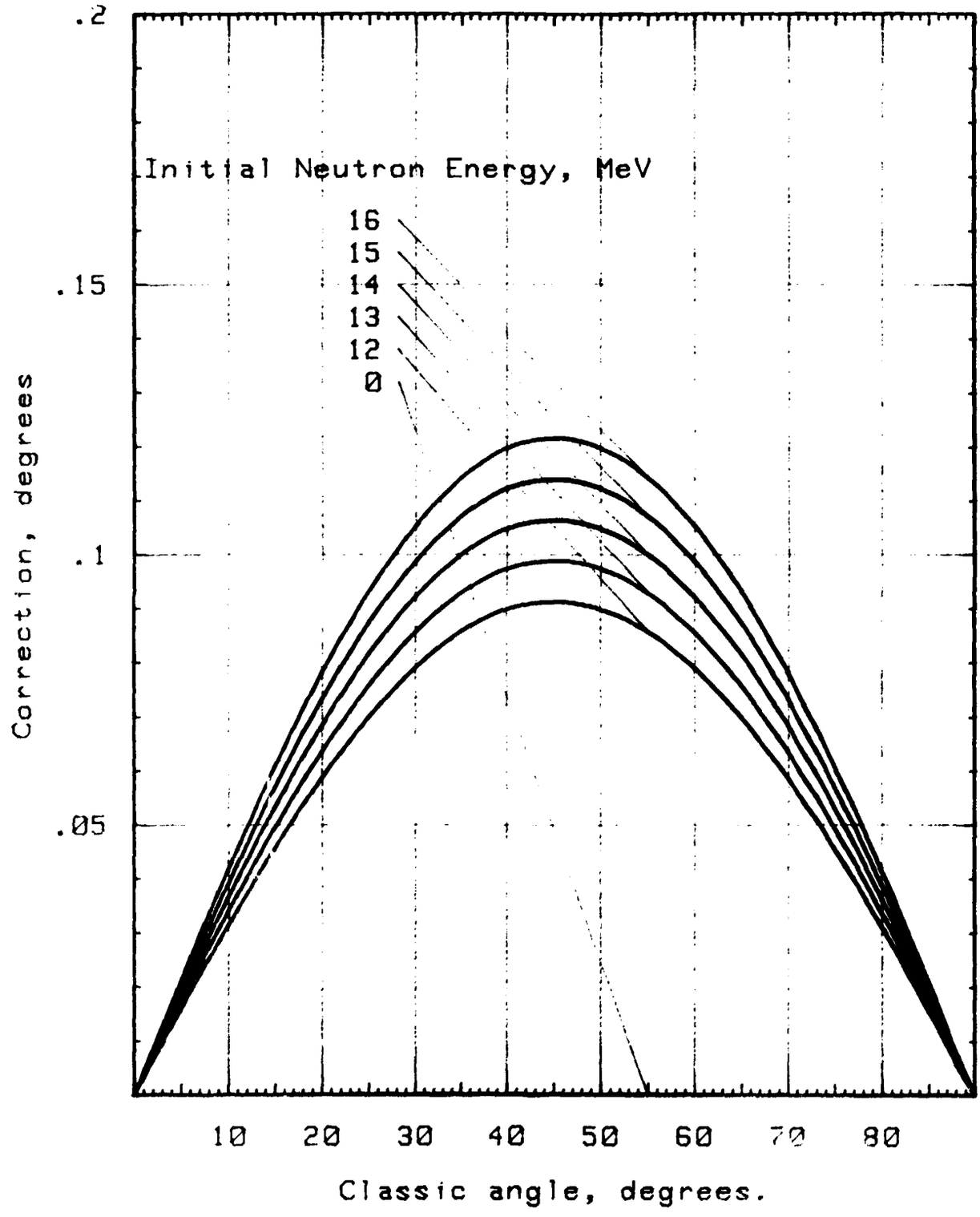

Figure 24. The proton scattering angle.

Relativistic angle = classic - correction.

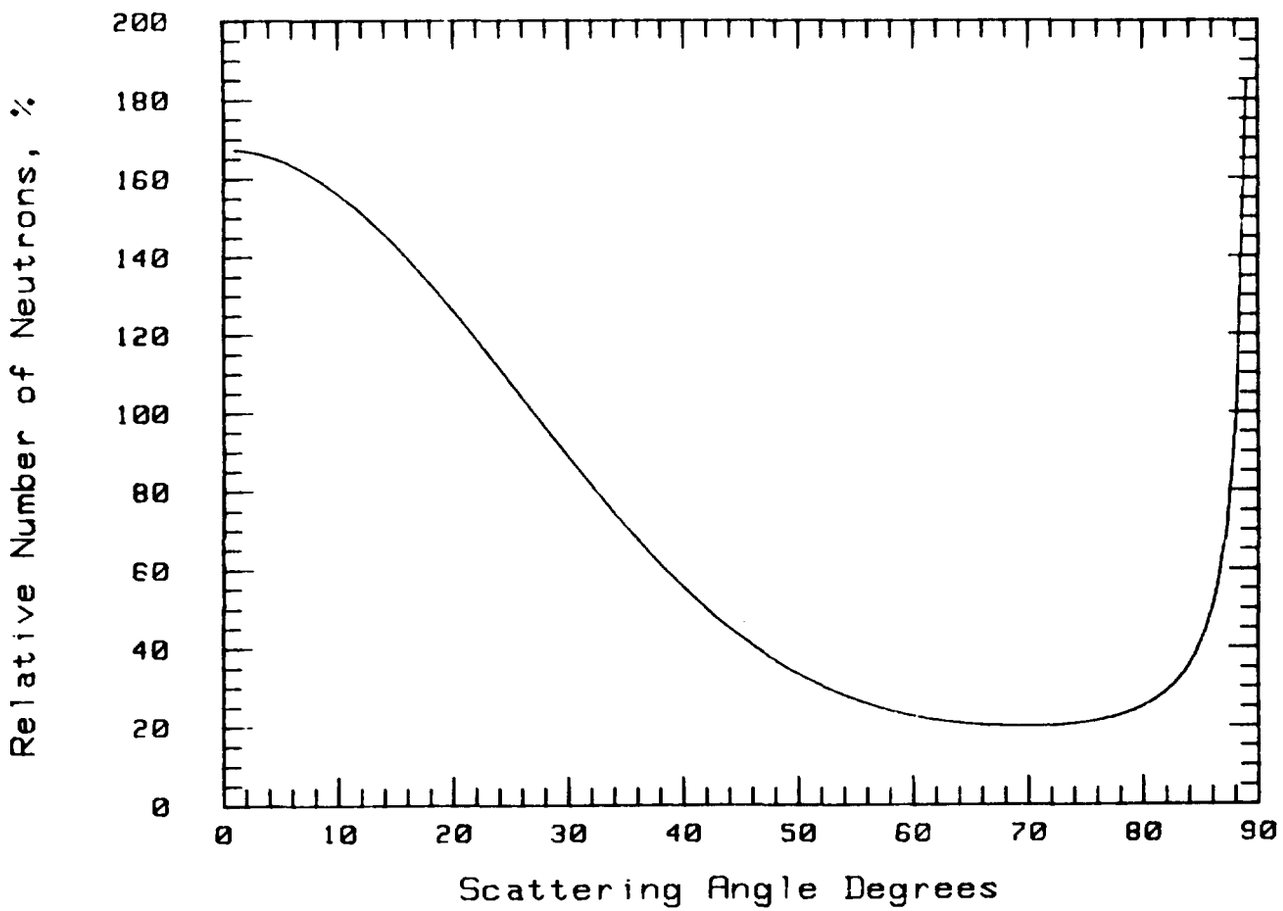

Figure 25. Carbon scattered neutrons.

The number of neutrons from carbon scattering in a polyethylene foil relative to the number of neutrons from proton scattering. The energy of the incoming neutrons is 14 MeV.

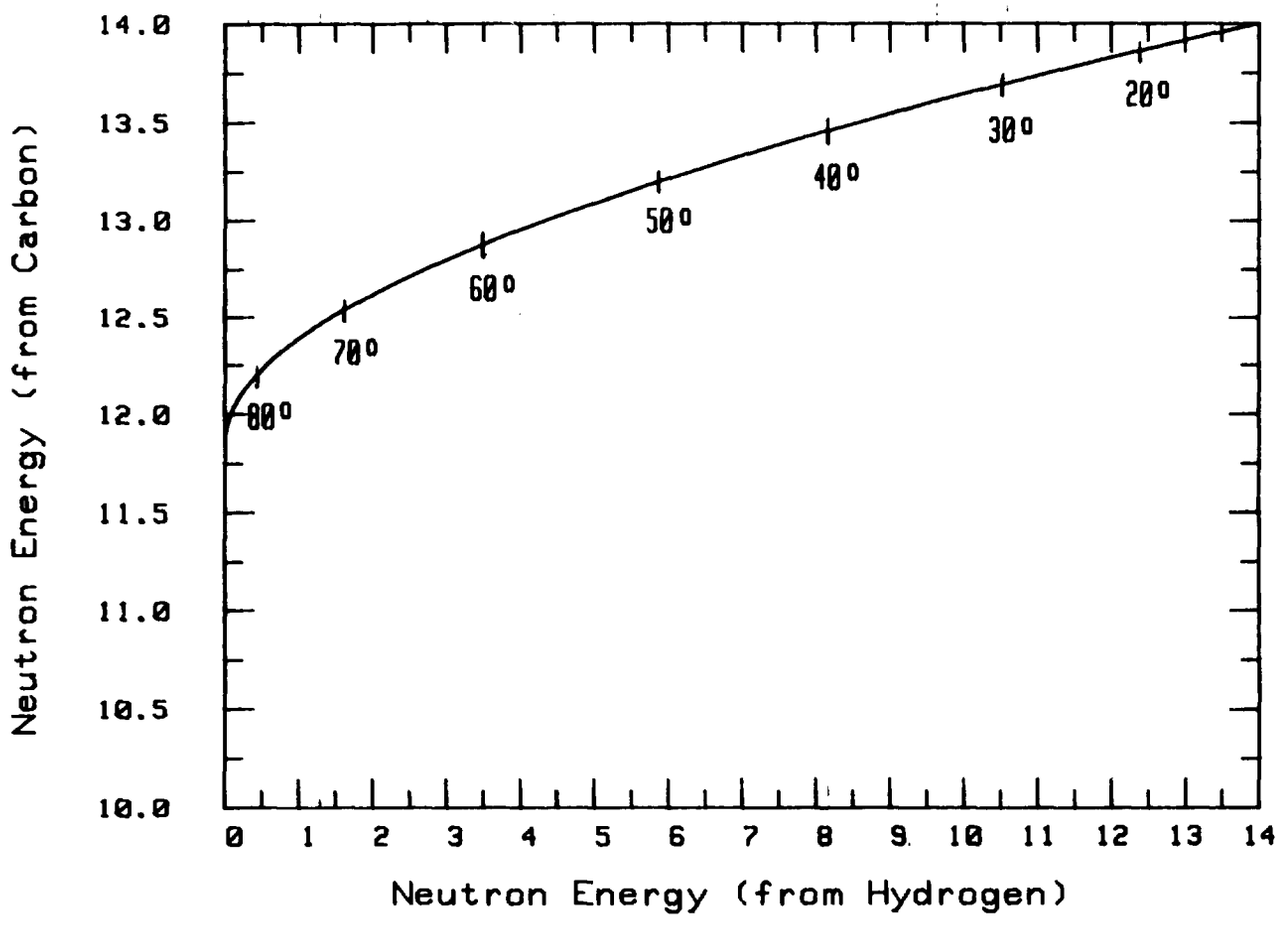

Figure 26. The energy of carbon-scattered neutrons.

The energy of the carbon recoils = 14 - (the energy of the scattered neutrons), MeV.

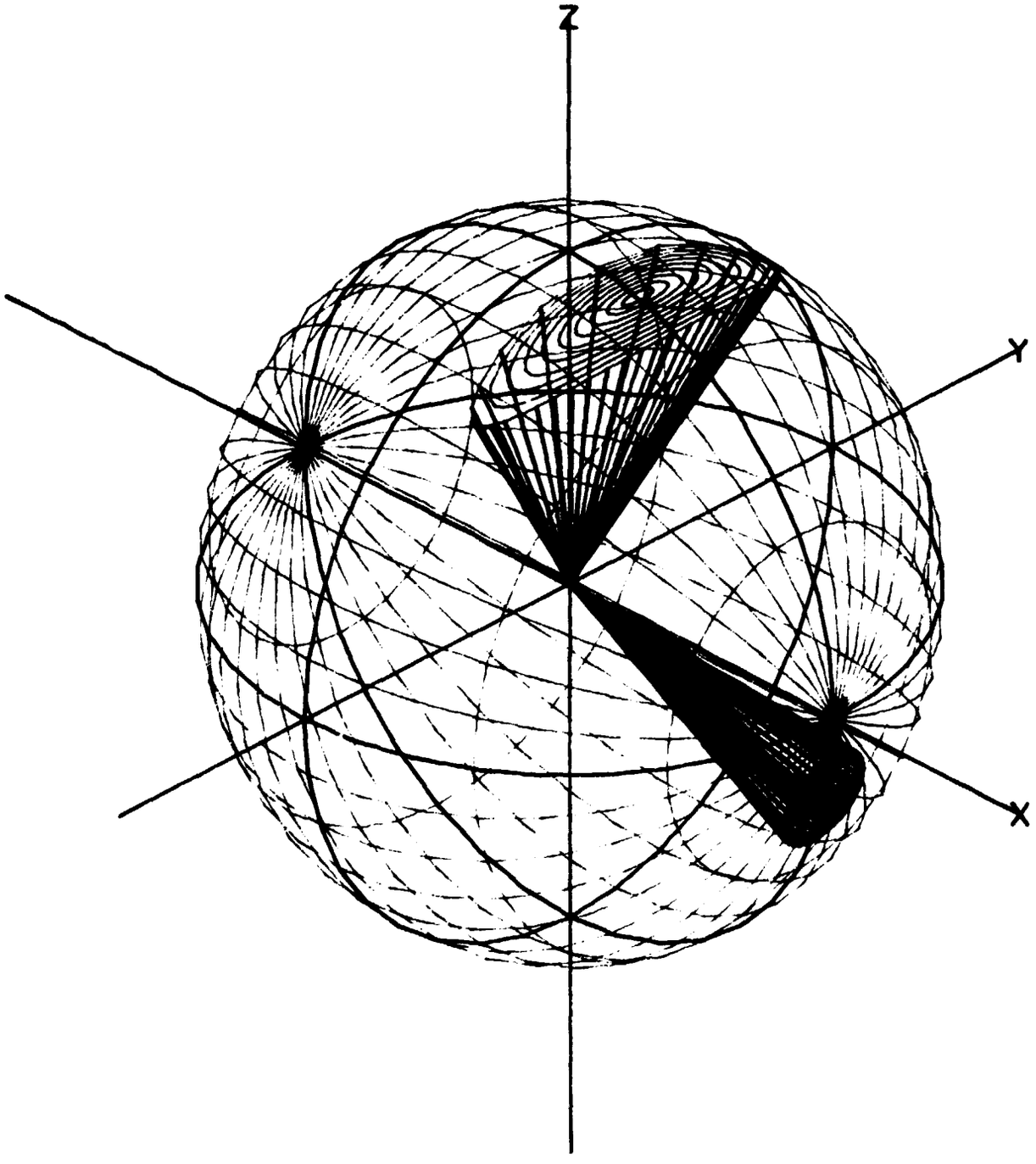

Figure 27. A point scatterer.

The neutron beam comes from the left and is scattered at the origin. Coincidence neutrons upwards and protons askew downwards.

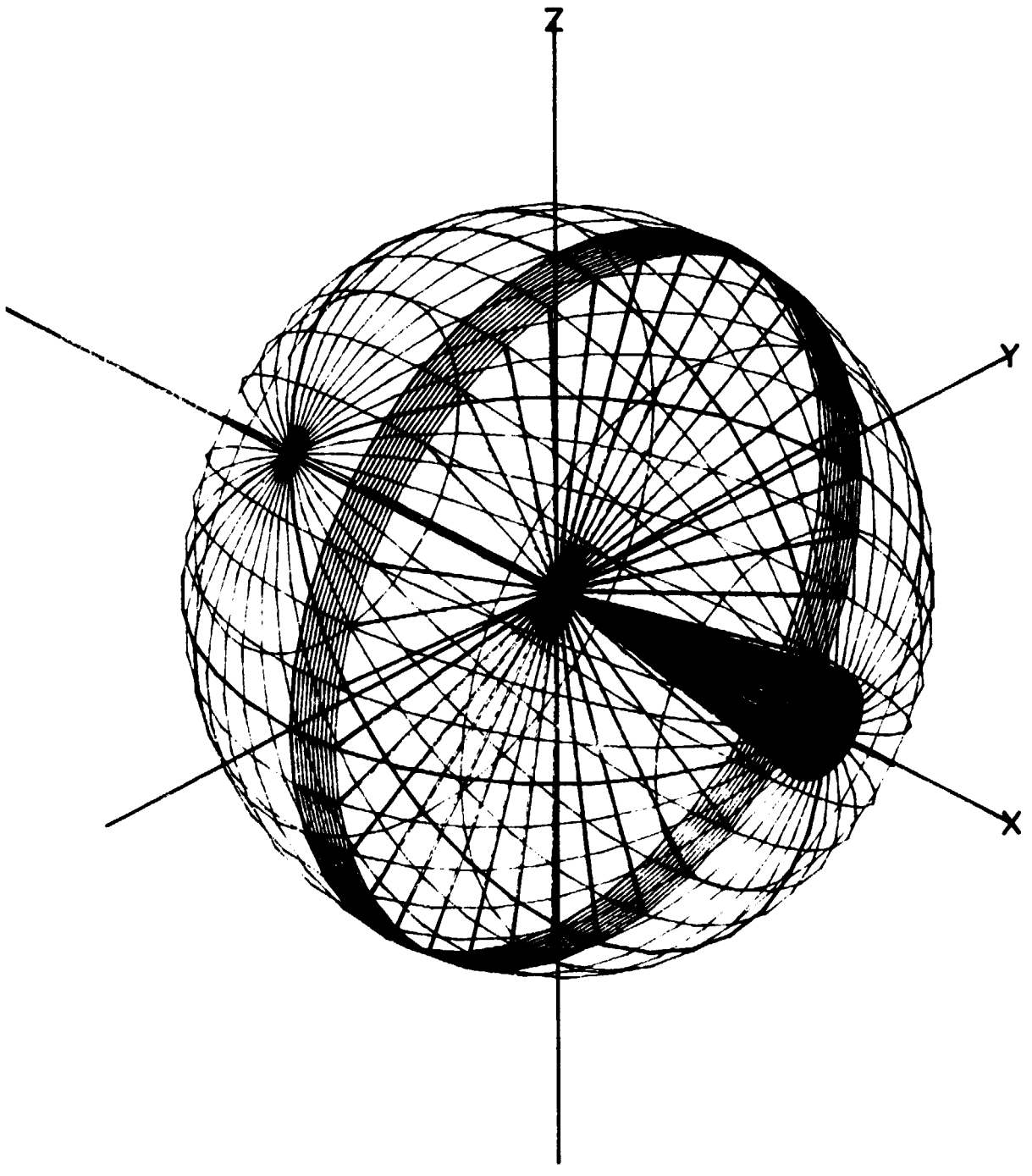

Figure 28. Scatterer and proton-detector on the central axis.

The proton-detector is in the neutron beam and will be burned out very fast. However, remove the central part. Then the figure illustrates an annular proton-detector.

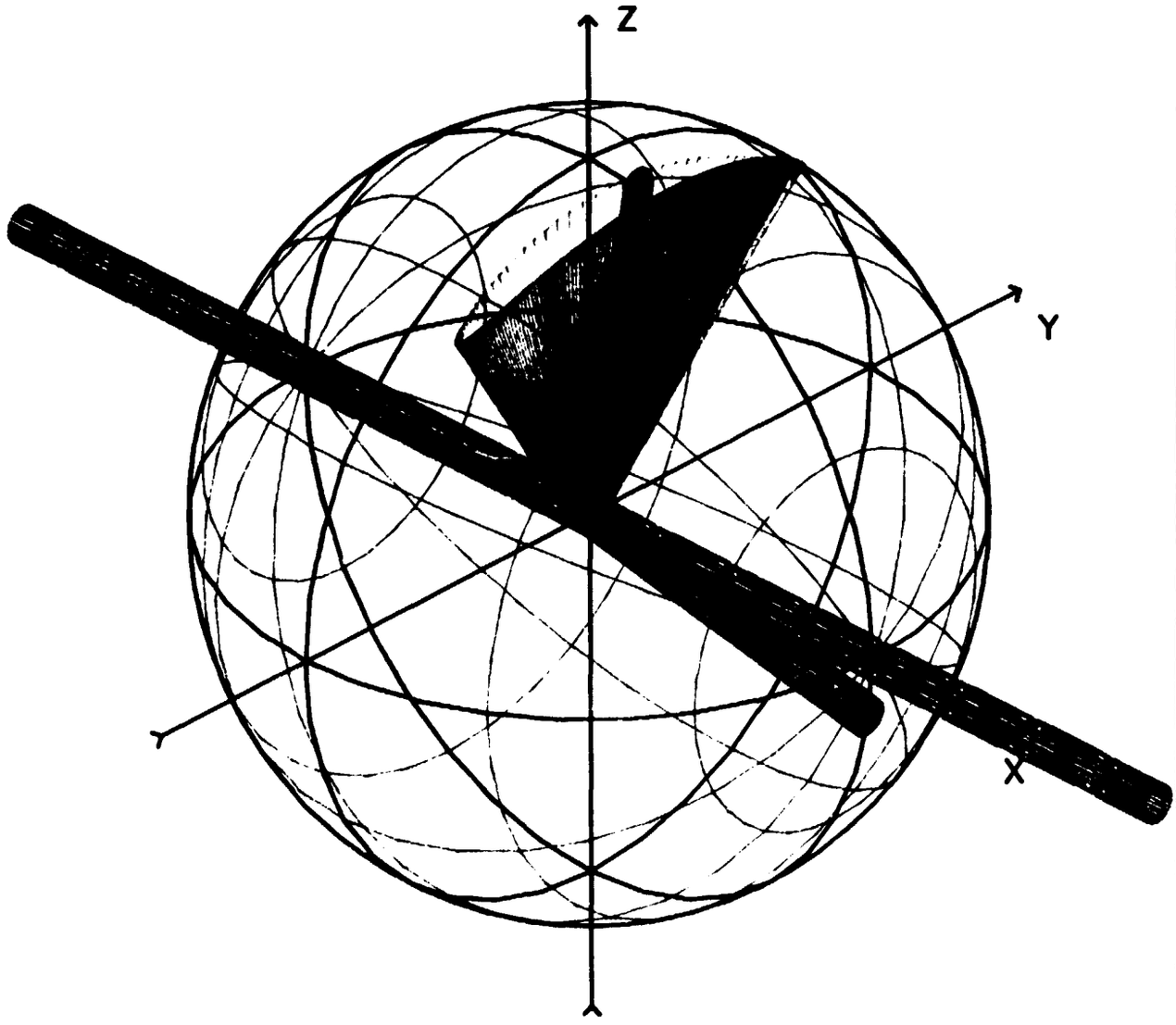

Figure 29. A foil scatterer.

The neutron paths will spread out when we use a foil. The parallel neutron paths are shown in the centre of the neutron-path-cone.

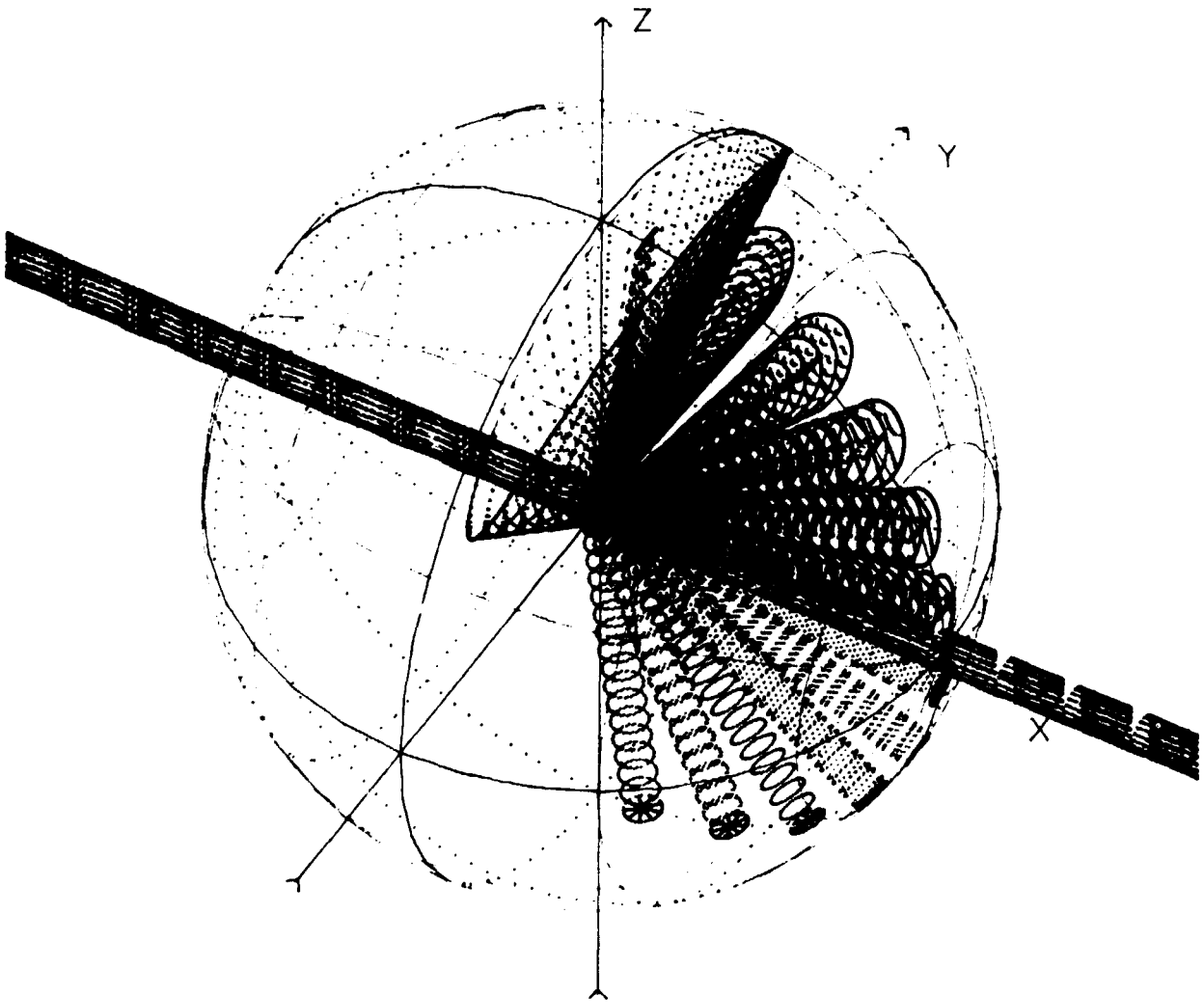

Figure 30. The neutron-detector shape for different angles.

The downward tubes show different positions of the proton-detector. The spreading out of the neutron-paths is most striking for large neutron-scattering angles.

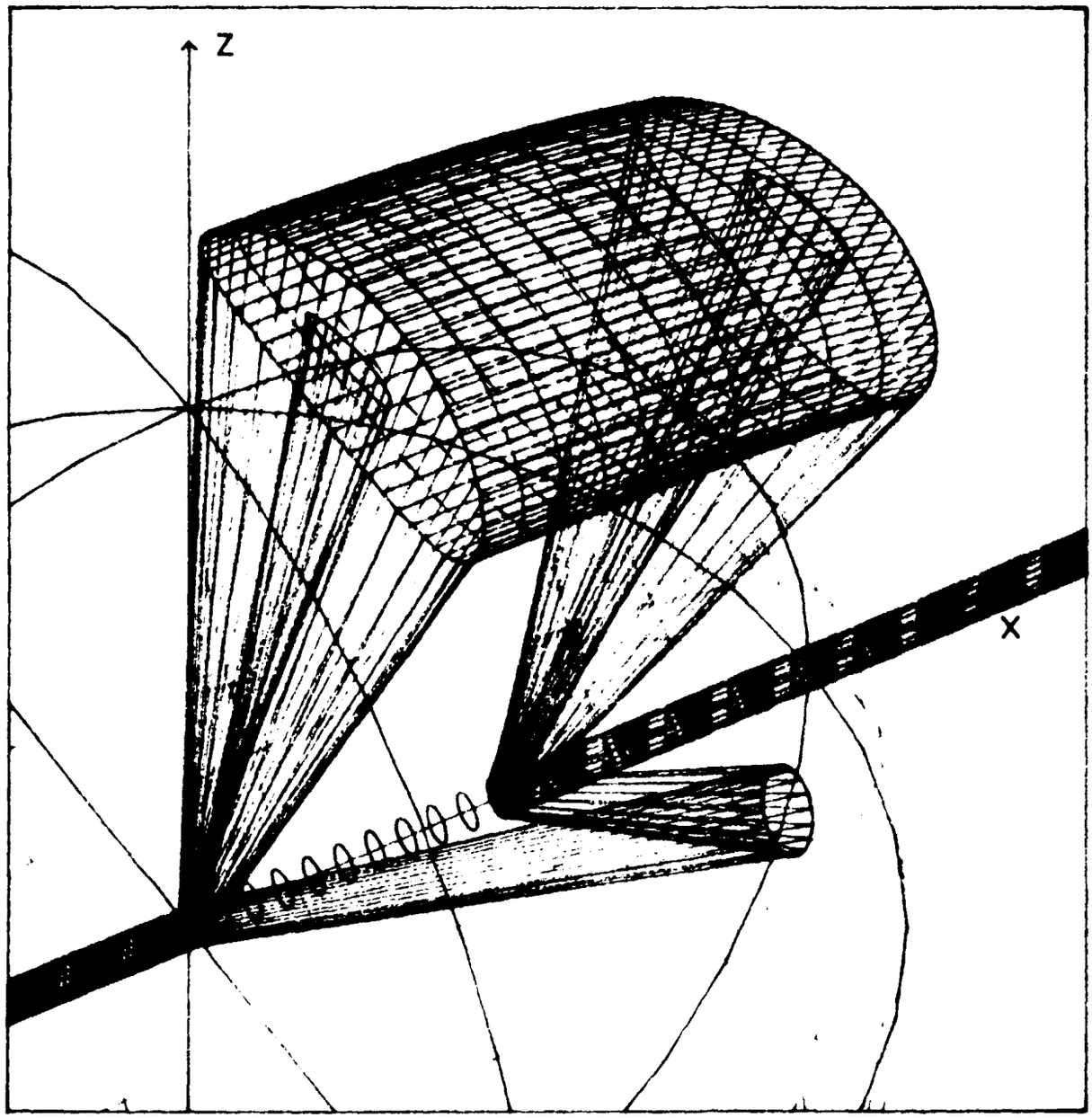

Figure 31. A hydrogen gas scatterer.

Hydrogen gas may be used as a scatterer. No window can be used but it is possible to find a proton semi-conductor detector which can work in the gas. The figure shows the neutron and proton paths for the outermost parts of the scatterer. The efficiency of this system can be controlled by the gas pressure.

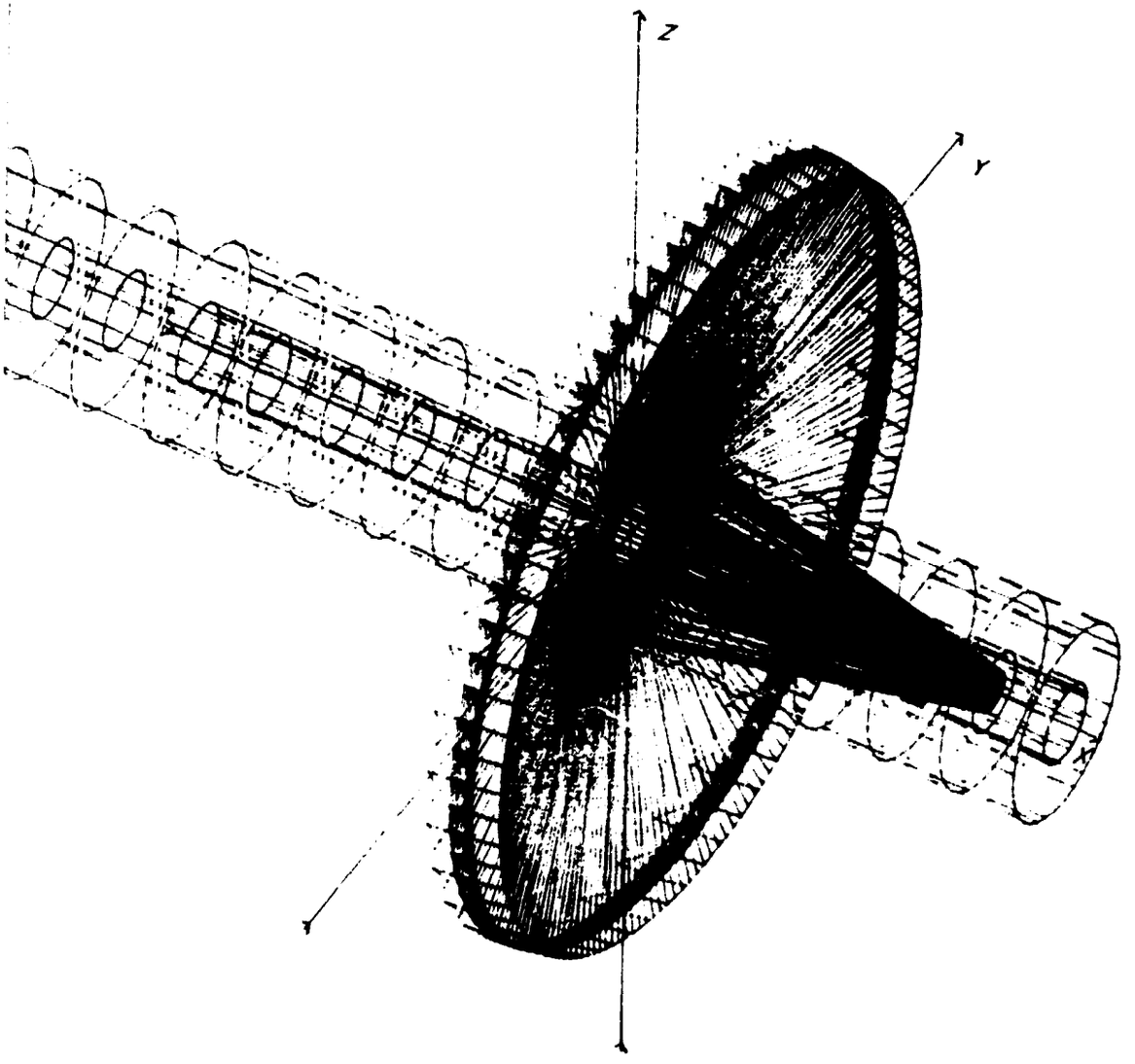

Figure 32. An annular scatterer.

The cheapest way to increase the efficiency is the use of an annular scatterer. See also TANSY, figure 4.

5 The scattering material

The recoil protons are created inside the scattering material (5.1). On their way out they lose energy, an energy loss that is approximately proportional to the flight path length in the foil. This is a process obeying the laws of quantum mechanics leading to a variation of energy and angle. The variation is called straggling. The energy straggling (5.2) gives an increased uncertainty in the proton measurement, the angular straggling (5.3) gives losses of proton-neutron coincidences.

We show that for TANSY the mean energy loss is 24 keV and that the maximum energy loss is 70 keV. A direct calculation from the stopping power gives 23 and 46 keV respectively.

The angular straggling in TANSY leads to a coincidence loss of about 10% if we use all angles defined by the proton-detector. Actually, the neutron detector is somewhat smaller. Therefore, the losses are limited to about 5%.

We consider two methods to increase the thickness of the scatterer. The first is an unfolding method (5.4) corresponding to the methods used in connection with gas-chamber neutron detectors. We show that this method works correctly. However, the standard deviation of the unfolded data is always higher than the standard deviation of the direct data from a thin foil. The thin foil is the optimal solution.

The other method uses an organic scintillator as scatterer (5.5). Again we find problems that we are unable to solve. The position-dependence of the weak light-source gives an unacceptable variation of the signal from the photomultiplier.

Finally, we make a survey over possible scattering materials (5.6). We find, in agreement with all other telescope makers, that polyethylene is the optimal choice. However, we emphasize that pure hydrogen has the lowest stopping power counted per hydrogen content unit. Therefore, this should be the optimal choice if the practical problems connected with a gas scatterer could be solved.

5.1 Stopping power

The recoil protons lose energy in the scattering foil essentially by two types of interactions, elastic nuclear collisions and Coulomb interaction.

The elastic nuclear collision is a scattering process leading to large energy losses and deflections in each interaction. The process was extensively discussed by Bohr {34}. More recently Bohr's ideas have been developed and refined by Lindhard et al. {35}. They show that the probability of nuclear collision is comparable with the probability of Coulomb interaction for energies below 25 keV. However, the nuclear collision probability decreases with increasing proton energy. Perkins and Cullen {36} find that the nuclear collision is less than one per mille of the Coulomb interaction at 14 MeV. In their work they have included the interference between the two processes.

The large deflection in each collision means that the coincidence criterion normally is not fulfilled for protons deflected by nuclear scattering. Therefore, the process will lead to a sensitivity loss. However, the loss is small and will be neglected.

The Coulomb interaction gives energy losses by ionization and excitation of the atoms. Several processes contribute and therefore Bichsel {37} finds it convenient to use three energy intervals with the limits 100 keV and 940 MeV. He and Fano {38} use a quantum-mechanical model of interaction, which in the mean interval has a sufficient accuracy for our purpose[1]. Their model contains corrections for the inner shells and high ionization density. Both these effects are small at 14 MeV. Thus, we neglect them. For protons we then have

[1] A more exact formula is given by Janni {41}.

$$-\frac{dE}{\rho\, dx} = \frac{4\pi N_0 e^4 Z}{M\beta^2 m_e}\left[\ln\left(\frac{2m_e\beta^2}{1-\beta^2}\right) - \beta^2 - \ln I\right] \qquad (5.1)$$

where

ϱ = density

N_0 = Avogadros number

Z = atomic number

M = mol weight of the stopping material

β = velocity of proton relative to the velocity of light

I = average excitation potential per electron

m_e = rest mass of electron in energy units.

The result is plotted in figure 34. From this it can be seen that the variation of the stopping power in the range 12 to 16 MeV is small. Therefore, a second order power expansion based on numerical values from equation 5.1 gives sufficient accuracy in this range.

$$-\frac{dE}{\rho\, dx} = 37.6 - 2.28(E-14) + 0.146(E-14)^2 \qquad (5.2)$$

Here, E shall be given in MeV.

At 14 MeV the stopping power is 38 keV/(mg/cm^2). This means that the thickness of the foil is limited to about 1 mg/cm^2 giving some room for other uncertainties.

5.2 Energy straggling

The stopping power formula (equation 5.1) gives the average energy loss for the protons. The energy loss varies around the average value due to unequal energy losses, fluctuations of the number and kind of collisions during the slowing down. We assume that the total energy loss has a Gaussian distribution around the average value. The energy distribution then takes the form {34}

$$P(E, E_0(x)) = \frac{dE}{\sqrt{2\pi}}\sqrt{\frac{M}{0.157\, Zx}} \cdot \exp\left[-\frac{(E-E_0)^2}{2}\sqrt{\frac{M}{0.157\, Zx}}\right] \qquad (5.3)$$

where

E_0 = the average energy in MeV from eq. 5.1 or 5.2,

x = the penetrated distance.

Fano {38} presents a more accurate formula but although the above expression is an approximation the results agree very well with experiments.

Equation 5.3 gives the distribution for one given penetration distance. However, in our case the protons are created inside the foil with a probability, which is independent of the distance between the collision point and the surface of the foil. Therefore, the energy distribution of the neutrons emerging from the foil is a folding of distributions with penetration distances varying from zero to the thickness of the foil.

$$P(E)\,dE = \int_0^{x} P(E, E_o(x))\,dx \tag{5.4}$$

The proton energy distribution is drawn in figure 36. The influence of the straggling effect can easily be seen. The straggling gives a slope in the curves. The distribution, disregarding the energy straggling, is rectangular. For example, the energy distribution for 1.24 mg/cm^2 has a cut-off at 47 keV if we neglect the straggling. However, the figure shows that the proton may lose up to 70 keV.

The conclusion for TANSY is that the energy loss has a mean value of 24 keV, a minimum value of 0 keV, and a maximum value of 70 keV. Only about 10% of the protons lose more than 46 keV.

5.3 Angle straggling

The second effect of the Coulomb interaction is the deflection of the protons. The repeated small angle deflections will spread up a parallel beam of protons. This effect is neglected in telescopes using only the protons. The reason is that the protons lost in one angle interval will be compensated for by other protons scattered into the interval. This statement is also true in a neutron-proton coincidence instrument as long as the angle is far from the angle boundaries defined by the detectors. However, in the neighbourhood of the boundaries, the coincidence condition will cause losses. The protons deflected from inside to outside the boundaries will not give signals in the proton detector. The protons deflected from outside to inside do not have corresponding signals in the neutron-detector.

We will here use the Moliere theory {40} of multiple scattering. The distribution function, the relative number of protons scattered to an angle element $d\theta$ in a cone with the top angle 2θ, is given by

$$f(\theta, x)\,d\theta = \vartheta\,d\vartheta \sum_{i=0}^{\infty} B^{-i} f^{i}(\vartheta) \tag{5.5}$$

The variable ϑ is a function of the distance x. It is given by

$$\vartheta = \theta \left[B \frac{0.178 \cdot 10^{-6} (1-\beta^2)\, Z\,(Z+1)\, x}{\beta^4 M} \right]^{-\frac{1}{2}} \tag{5.6}$$

and the coefficient B by

$$B - \ln B = \ln \left[\frac{6680 x\,(Z+1)\, Z^{1/3}}{\beta^2 M\,(1+3.34\,(Z/137\beta)^2)} \right] \tag{5.7}$$

The first three functions in the series are

$$f^{\circ}(\vartheta) = 2e^{-\vartheta^2}$$

$$f^{1}(\vartheta) = 2e^{-\vartheta^2}\left[-(\vartheta^2-1)\Psi(1) + \int_0^1 \frac{dt}{t^2}\left[(1-t)\,e^{t\vartheta^2} - 1 - t(\vartheta^2-1)\right]\right]$$

$$f^{2}(\vartheta) = 2e^{-\vartheta^2}\left[\left(\frac{\vartheta^4}{2} - 2\vartheta^2 + 1\right)\left[\Psi^2(2) + \Psi'(2)\right] + 2\int_0^1 \frac{dt}{t^3}\left[\ln\frac{t}{(1-t)} - \Psi(2)\right]\left[(1-t)^2 e^{t\vartheta^2} - 1 - (\vartheta^2-2)\,t - \left(\frac{\vartheta^4}{2} - 2\vartheta^2 + 1\right)t^2\right]\right]$$

where

$\psi(1) = 0.4228$

$\psi(2) = 0.9228$

$\psi'(2) = 0.3949$

Finally, we integrate equation 5.5 over all distances in the foil and obtain the angle distribution

$$P_a(\theta)\,\theta\,d\theta = K\int_0^{x} f(\theta, x)\,\theta\,d\theta\,dx \qquad (5.8)$$

where K is a normalization constant. The angle straggling is illustrated in figure 37 and 38.

An exact calculation of the losses in TANSY is rather complicated. It involves a calculation of the losses for all possible angles and scattering positions. We will limit the work to an estimate of the magnitude of the losses.

First, we assume that the detectors cover the same angles as defined by the classic coincidence condition. The distance from the mean point of the foil radii and the proton detector is 31 cm. From the figures 37 and 38 we find that there is a significant deflection up to 0.2 degrees, which gives a length on the detector of 1 mm. This means that there is a significant effect on a 2 mm strip at the detector boundary. The detector has a radius of 10 mm. There-

fore, the affected area is about 40% of the total area. Now, at the boundary about half the protons are deflected inwards. The loss is 50%. Assuming a linear dependence with the radius with zero loss at 8 mm gives the loss 0.40x(2x5/2)/(2x10) = 0.10 i.e. 10%.

Now, we have made the neutron detector smaller than defined by the proton-detector[1]. The neutron detector defines the outermost angles for about half the boundaries. Therefore, the angle straggling losses will be reduced to about 5%.

In conclusion we estimate the losses caused by angle straggling in TANSY at 5%.

5.4 Thick foil scatterer

The number of protons reaching the detector is proportional to the number of scattering nuclei in the foil. An increased foil thickness will give an increased detection probability. However, the protons lose energy in the foil. This may be taken into account by an unfolding technique.

The unfolding technique has been developed for proton-recoil gas-chambers and scintillator detectors {7,8}. In principle it should work even in this case, i.e. there should be a possibility to make a measurement with a thick scatterer and afterwards unfold the spectrum in order to improve the resolution.

We will show that it is possible to use an unfolding scheme in order to extract a high precision energy distribution. However, the statistical errors will be greater than those obtained with a thin foil of a thickness corresponding to the wanted resolution.

We will use a simplified spectrometer model for the investigation of the unfolding method. We use only head-on neutron-proton collisions, we neglect the absorption and outscattering of neutrons, and we assume that the stopping power is constant in the energy region of interest.

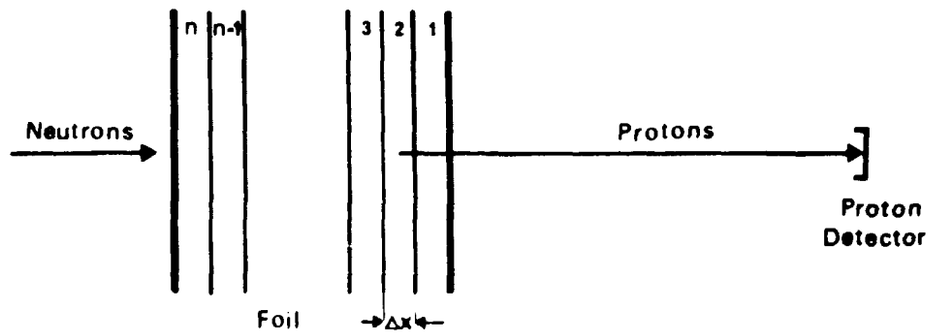

Figure 33. Unfolding geometry.

We divide the foil into subregions Δx. For convenience we choose the energy intervals in the proton detection system to be proportional to the subregion thickness times the stopping power. The n foil subregions are numbered from the detector-side of the foil and the energy intervals are numbered beginning at the highest energy (figure 33). The same energy intervals are used for both neutrons and protons; as only head-on collisions are utilized the neutron energy spectrum and the initial proton spectrum coincide. We use the notation {42}

$$F_{1,2} = (f_1, f_2, f_3, \ldots, f_k) \tag{5.9}$$

for the normalized initial proton vector.

[1] See chapter 8, »Characteristics of the detection method.».

The protons are slowed down in the foil and reach ultimately the proton detector. The recorded, normalized proton spectrum vector is

$$G_{1,k} = (g_1, g_2, g_3, \ldots, g_k) \tag{5.10}$$

There is a linear relationship between the two vectors

$$G_{k,1} = T_{k,k} \cdot F_{k,1} \tag{5.11}$$

Now, a measurement gives a result

$$P_{1,k} = (P_1, P_2, P_3, \ldots, P_k) \tag{5.12}$$

from which we may get the estimates

$$\hat{F}_{1,k} = (\hat{f}_1, \hat{f}_2, \hat{f}_3, \ldots, \hat{f}_k) \tag{5.13}$$

by

$$\hat{F}_{k,1} = T^{-1}_{k,k} \cdot G_{k,1} \tag{5.14}$$

The variance-covariance matrix for the estimated proton- (or neutron-) spectrum is then

$$M_{\hat{f}} = \varepsilon [\hat{F}, \hat{F}'] = T^{-1} M (T^{-1})' \tag{5.15}$$

where the prim denotes a transposed matrix.

The elements of **T** may be written

$$t_{i,j} = \sum_{l=0}^{n-1} \delta_{i,j+l} \tag{5.16}$$

which gives the elements of the inverse

$$t^{-1}_{i,j} = \sum_{l=0}^{\infty} (\delta_{i,j+l_n} - \delta_{i+1,j+l_n}) \tag{5.17}$$

The elements of the observation vector **P** are independent, moreover, they obey Poisson statistics. Therefore, the variance-covariance matrix **M** has non-zero elements only in the diagonal, the values of which are equal to the corresponding elements of **P**.

Thus, the elements of **M** are

$$m_p = P_i \delta_{i,j} \tag{5.18}$$

from which we get the elements of $M_{\hat{f}}$,

$$m_{\hat{f}} = [\delta_{i,j}(P_{i+\ell n}+P_{i+\ell n-1}) - \delta_{i+1,j}P_{i+\ell n} - \delta_{i,j+1}P_{i+\ell n}] \quad (5.19)$$

Here, p_i is assumed to be nonzero only inside the range of the vector.

The second moment of the estimator f, which we will use as an estimator of the variance is then

$$VAR(\hat{f}_i) = \sum_{\ell=0}^{\infty} (P_{i+\ell n} + P_{i+\ell n-1}) \quad (5.20)$$

In order to proceed further we need an approximation for the observation vector. Its mean value is given by

$$P = aG = aTF \quad (5.21)$$

where a is a constant. The estimator is then

$$\hat{F} = T^{-1}aTF = aF \quad (5.22)$$

Thus, the elements are

$$\hat{f}_i = af_i \quad (5.23)$$

$$P_i = a\sum_{\ell=0}^{k} t_{i\ell} f_\ell = a\sum_{\ell=0}^{n-1} f_{i-\ell} \qquad i<\ell \quad \ell>k \quad (5.24)$$

where f_i is zero if $i < \ell$ or $\ell > k$. Then, it might be seen that the variation of $\hat{f}_i$ is given by

$$VAR(\hat{f}_i) = a(f_i + 2\sum_{j=1}^{i-1} f_j) \qquad \text{for } n>1 \quad (5.25)$$

$$VAR(\hat{f}_i) = af_i \qquad \text{for } n=1 \quad (5.26)$$

Equation 5.26 always gives lower variation than equation 5.25. Therefore, the foil thickness should be determined from the stopping power. A thicker foil will, for the same resolution, give the same mean values of the estimate. However, the standard deviation will be deteriorated.

The only way to improve the situation, to get a higher counting rate with preserved accuracy while the foil thickness is increased, is to include some measurement of the proton energy loss in the foil.

5.5 Scintillator foil scatterer

One way to enable the use of a thick scatterer is the use of a scintillator. An organic scintillator contains much hydrogen. Therefore, it may be used as scatterer. The light output from the scintillator may be used as a measure of the energy loss in the scatterer.

The energy loss in an organic scintillator is approximately the same as in polyethylene, 30 to 40 MeV per cm. The resolution of a scintillator is about 10%. Therefore, only a fraction of the energy of the proton is allowed to be absorbed in the scintillator. Half an MeV gives a thickness of about 0.14 mm. This means that the scintillator from the light collection point of view is a foil.

Scintillator foils have been used as start detectors of charged particle time-of-flight experiments {43,44,45,46}. Normally, no energy information is extracted from the signal[1]. However, Muga {46} has investigated the light collection. He recognizes two effects. Light is transported directly to the edge or it is trapped in the foil and transported to the edge by several reflections. Both these effects are highly position-dependent. Muga uses two photomultipliers viewing a foil from opposite directions. The variation of the sum signal was 20% over the central one-third portion of the foil.

Geller et al. {16}[2] use a 5 mm thick trans-stilbene scintillator combined with a semiconductor detector. The 5 mm corresponds to the range of 22.7 MeV protons {41}, the upper limit of the spectrometer. The semiconductor and the scintillator are used in coincidence. Only those protons which emerge from the scintillator back surface and hit the semiconductor will be counted. Therefore, the volume of the active scattering material increases with proton energy, i.e. neutron energy, which gives an efficiency increasing with the neutron energy.

The spectrum of the protons reaching the semiconductor is shown in figure 39. In principle, the distribution should have a cut-off at the highest energy. However, it has a slope caused by the pulse-shape-discriminator used in the scintillator line. It is this part of the distribution which has the best proton-measurement resolution. Therefore, pulse-shape-discrimination must be avoided or improved.

The intrinsic resolution is defined by Geller et al. as the energy spread caused by the detectors. It is calculated to 2.4%, 1% for the semiconductor and 6% for the scintillator[3]. The intrinsic resolution can be improved by making the scintillator thinner. However, then we are again limited by the position-dependence.

Our conclusion is that the foil scintillator technique will give more problems than benefits for our type of instrument.

5.6 Scatterer materials

Polyethylene is the scatterer material used by almost all telescope makers. One exception is Keith Furr and Runyon {23}, who use mylar as an alternative. Table 1 verifies that polyethylene is the proper choice. It has a high relative content of hydrogen and acceptable mechanical properties.

Pure hydrogen should be the best choice if the problems with a gas-scatterer could be overcome. It might be possible to have a special proton detector inside the gas in order to avoid the straggling problems in a window.

---

1) Rather complicated arrangements are needed in order to extract a signal for energy determination. Reflecting tents or special light guides surrounding the scintillator have been used. However, it is difficult to introduce such arrangements in this application.

2) See also paragraph 2.3, »Two scintillators.», page 24 and figure 7 on page 27.

3) Most of the energy is measured by the semiconductor.

Table 1. Stopping power for 14 MeV protons.

Scatterer	% hydrogen	Stopping power, from ref. 41. keV per		
		mg/cm^2	micrometer	$mg\ H/cm^2$
Bakelite	10.6	33.7	3.85	318
Mylar	4.2	30.8	4.15	733
Nylon	9.99	33.2	3.76	332
Polyethylene	14.4	35.8	3.29	247
Polystyrene	7.74	33.0	3.50	426
Polypropylene	14.4	35.8	1.84	247
Anthracene	5.76	32.1	3.99	557
Pilot B	8.45	33.3	3.40	392
Trans-stilbene	4.58	31.7	3.67	692
Water	11.2	32.5	3.25	290
Hydrogen	100	71.8	0.65	71.8
Methane	25.1	40.3	2.89	161

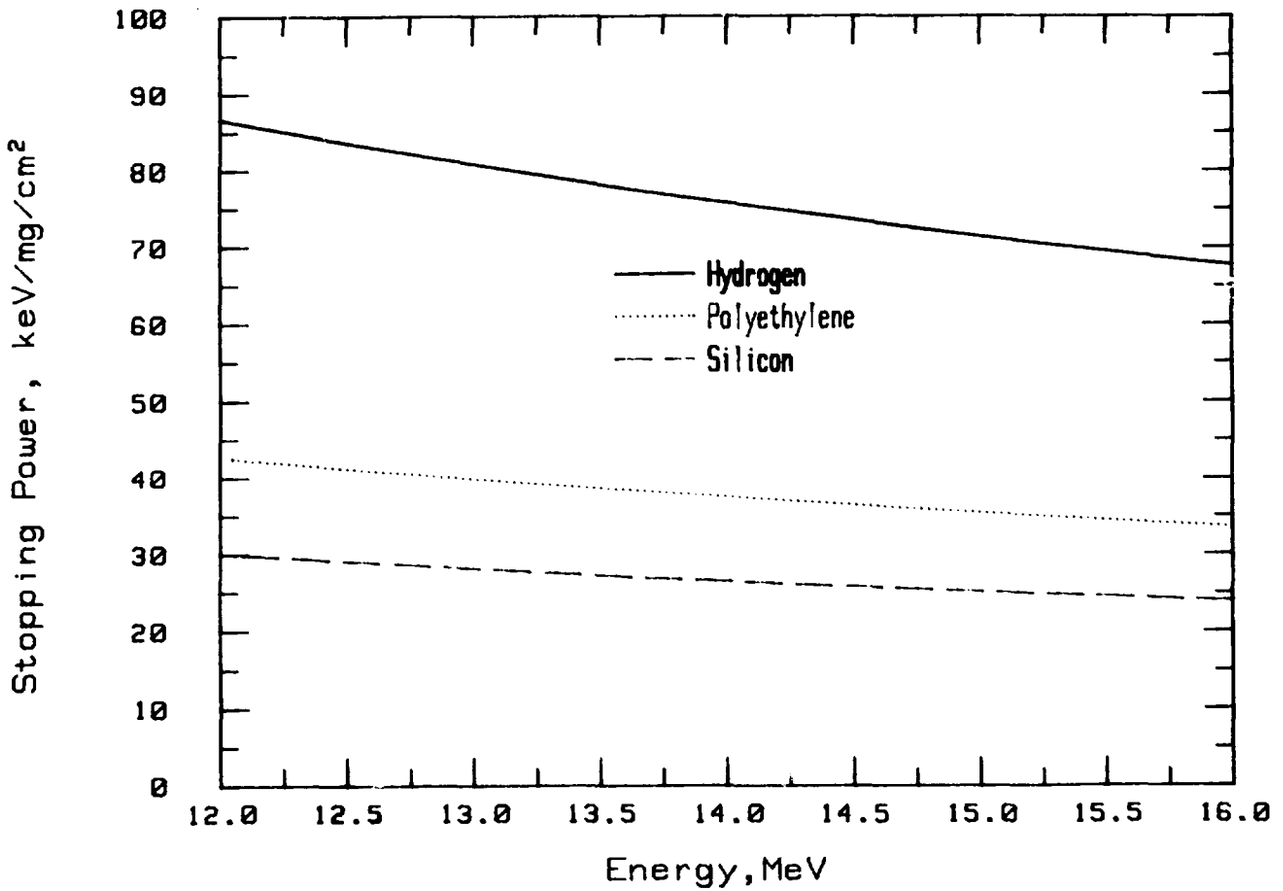

Figure 34. Stopping power.

The stopping power curves are calculated using equation 5.1. They are in agreement with the values given by Janni {41}. An empirical formula is given in the text (eq. 5.2).

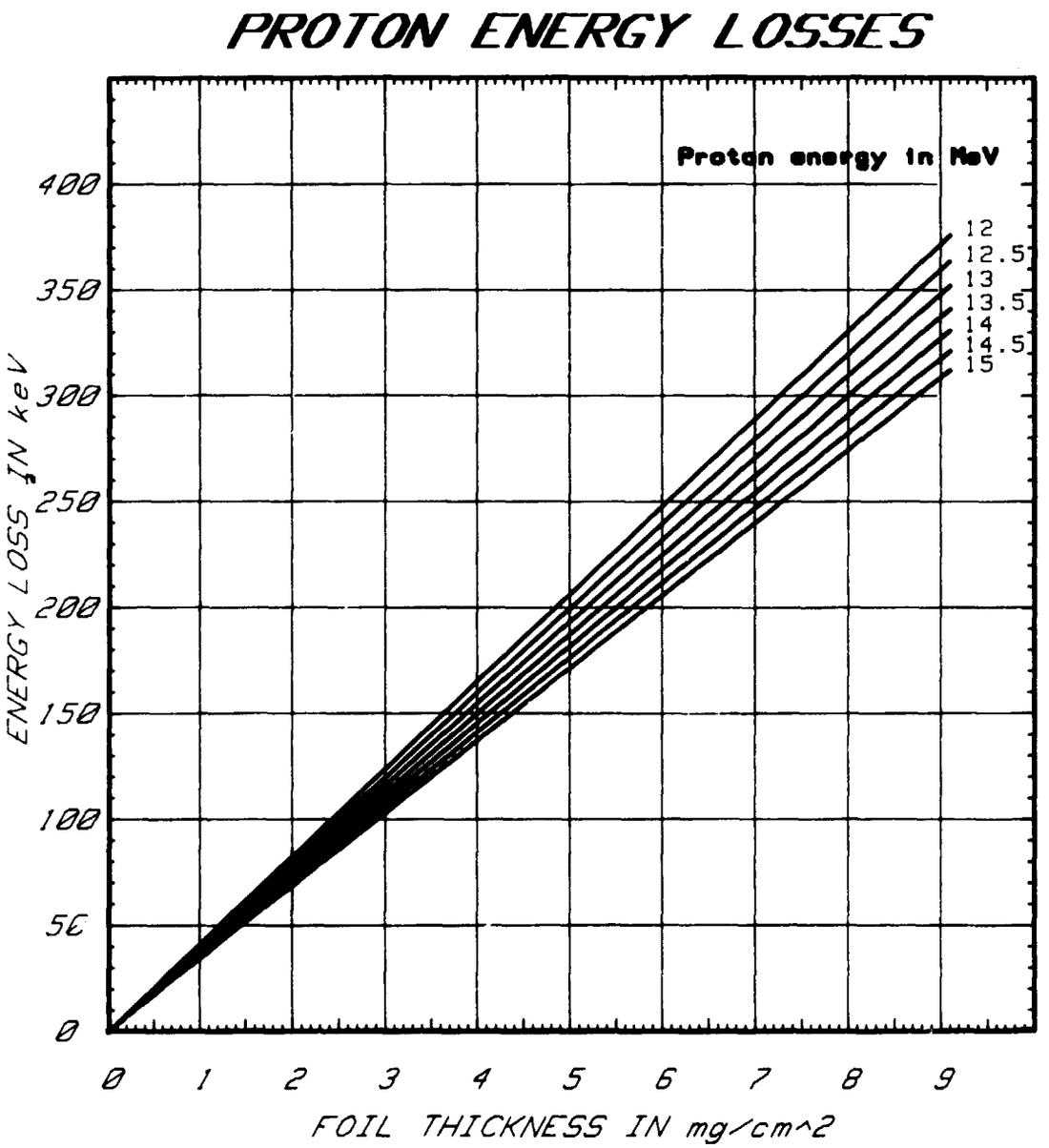

Figure 35. Proton energy loss in polyethylene.

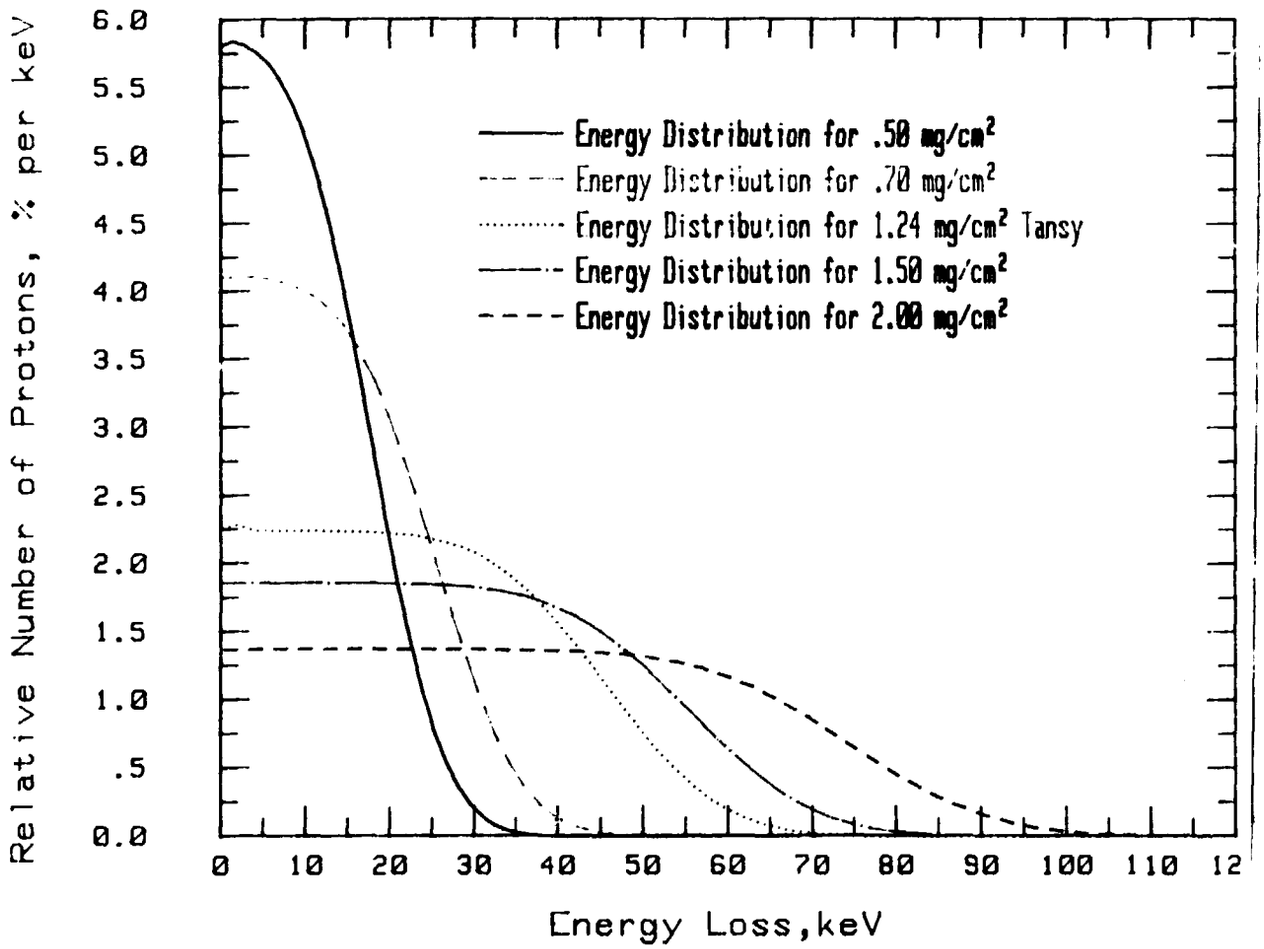

Figure 36. Energy straggling for 14 MeV protons.

The energy loss according to equation 5.2 is 18.8, 26.3, 46.6, 56.4, and 75.2 keV, respectively.

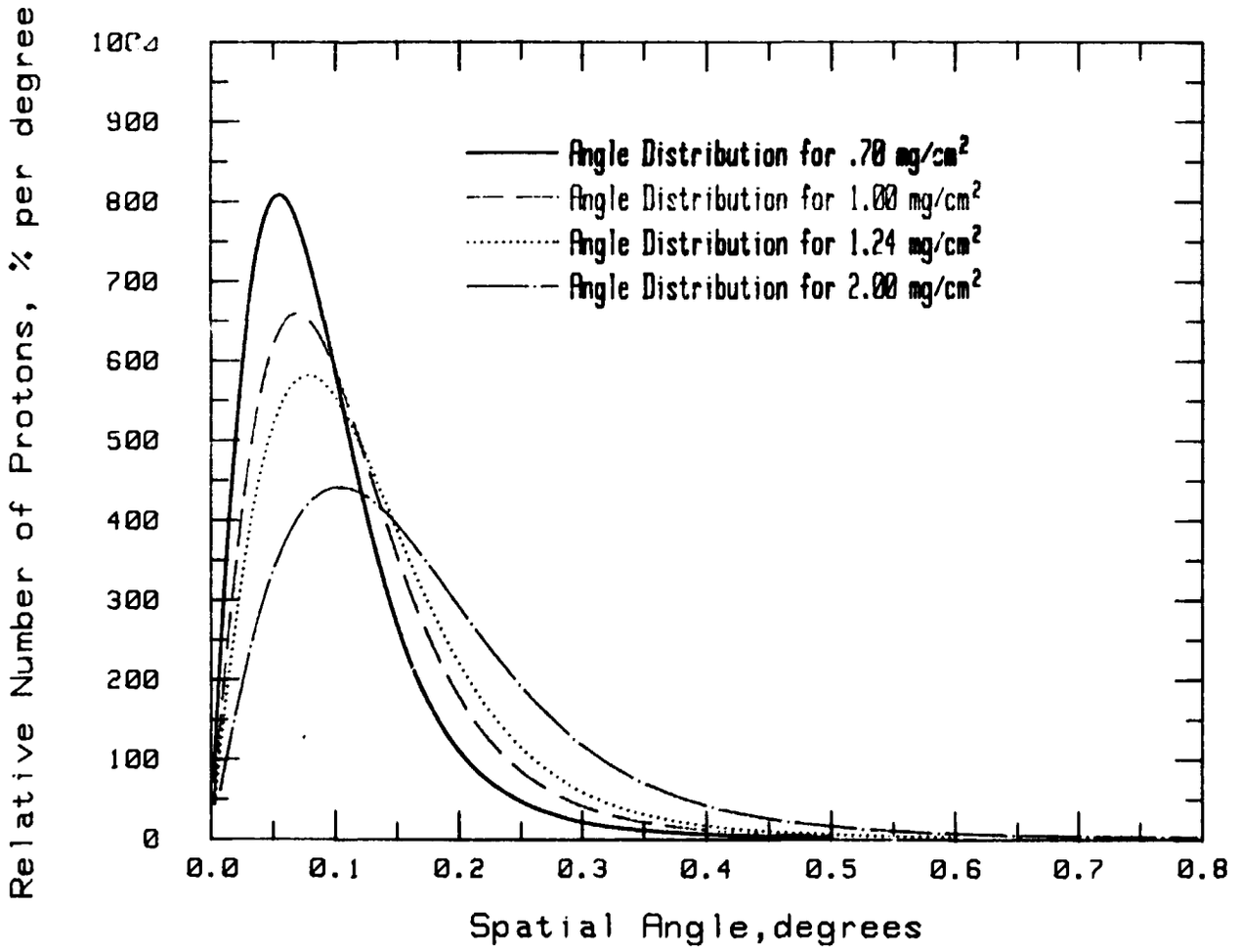

Figure 37. Angle straggling for 14 MeV protons.

The angle straggling calculated from equation 5.8. In TANSY an angle of 0.1 degrees corresponds to about 1 mm at the detector position.

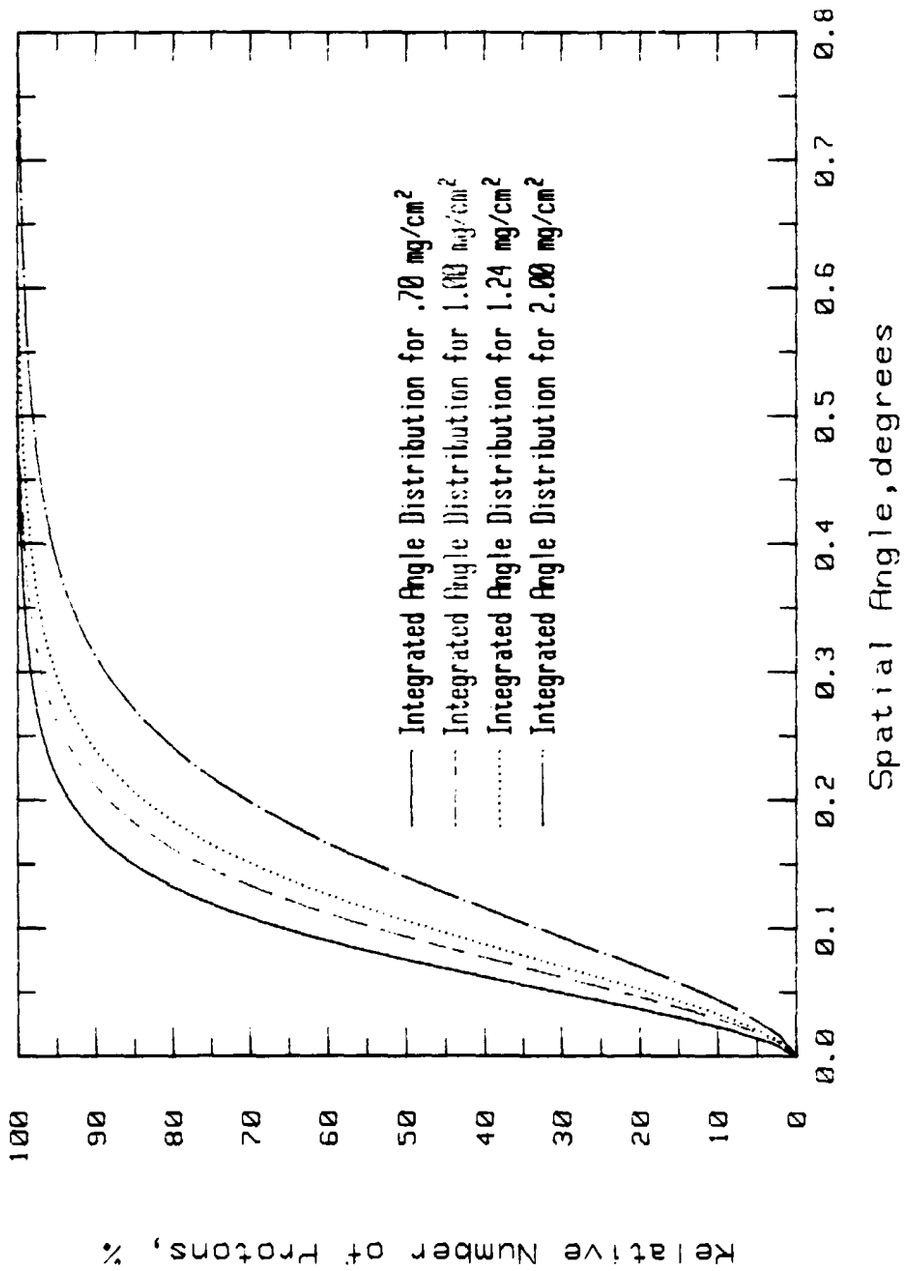

Figure 38. Integrated angle straggling.

Equation 5.8 is integrated from 0 to the given angle. Thus, the figure shows the relative amount of protons inside a given angle.

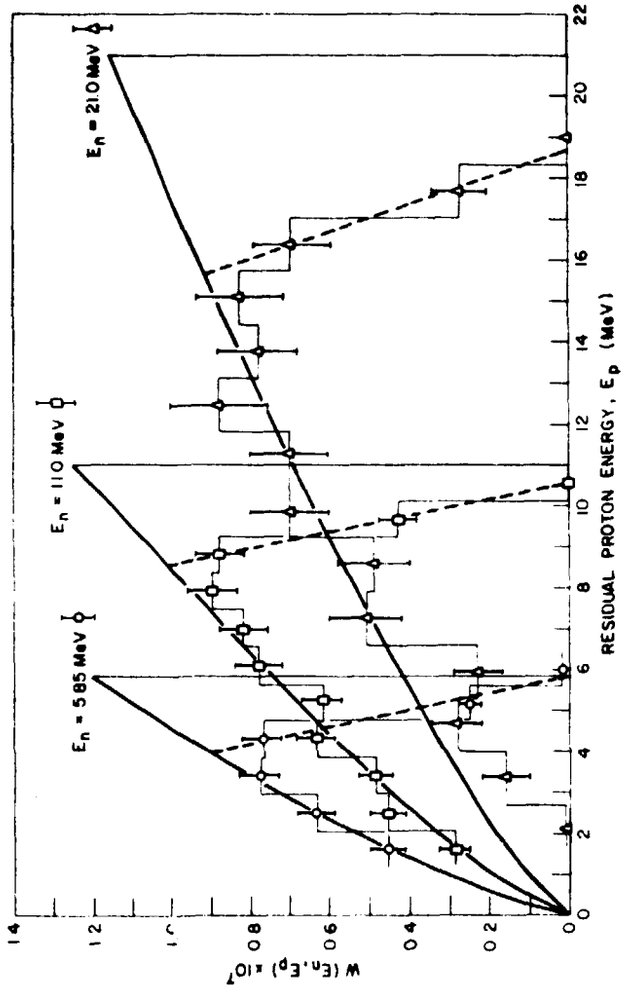

The differential yield data for monoenergetic neutrons at the energies indicated. The experimental yields are normalized to the calculated efficiencies given by the smooth curves. The fall-off in the experimental yields for residual proton energies near the maximum energy is due to the PSD defect.

Figure 39. The energies of protons from a thick scatterer.

Calculated and measured proton distributions for protons emerging from an anthracene scintillator. Reproduced from reference 16.

6 Proton detection

Some of the recoil-protons created in the foil reach the proton-detector and trigger a measurement. The transfer of protons from the foil to the detector depends on the inner and outer radii of the foil, the distance between the foil and the detector, the detector radius, and the scattering function.

The transfer goes from the foil to the detector. However, an equivalent case is the reverse process, transfer from the detector to the foil. Actually, we are looking for all possible transfers between the two items, folded with the differential scattering cross-section.

For a given azimuth angle, the transfer lines to a point on the detector surface are lying on a cone surface. The intercept line between the cone surface and the foil plane forms a circle. The transfer is total if all the cirles from all points of the detector are inside the foil limits. The energy distribution of the detected protons for a given initial-neutron energy is constant within the energy interval for which the condition of total transfer is fulfilled.

Total transfer can only occur if the detector diameter is less than or equal to the foil width. It gives the maximum possible transfer probability for a given set of geometrical parameters. The total transfer probability integrated over the foil area is equal to the detector area divided by the initial-neutron energy.

The energy spread, the difference between the highest and lowest energy divided by the initial-neutron energy, is for large detector-foil distances inversely proportional to the squared distance (equation 6.14). The same is true for the sensitivity (equation 6.16). Therefore, there is a linear relationship between the spread and the sensitivity. From this we find that the proton detection sensitivity for TANSY is ten times higher than a corresponding instrument using only proton detection.

The obvious choice of proton-detector is a totally depleted silicon surface-barrier detector, e.g. a detector from the Ortec B-series[1]. A 2 mm thick silicon detector has a sufficient energy resolution. We are not convinced that it has sufficient timing properties[2]. However, it is always possible to add a thin silicon detector in order to get an improved time signal.

6.1 Angular distribution

The collimated beam from the torus is almost parallel. A 10 cm source at a distance of 15 m gives a divergence of 0.4 degrees. The largest opening is defined by the port at the torus vessel. It has a height of 70 cm, which gives a divergence of 2.7 degrees. However, the angular distribution will be peaked, most of the neutron-paths will be parallel. Therefore, we are justified to use a parallel incoming beam in the calculations of this chapter.

The recoil-proton angular distribution is controlled by the differential scattering cross-section. The same relationship holds for the proton-recoils as well as for the scattered neutrons. The classic equal-mass model gives

$$\sigma_H(\theta, \varphi) = \sigma_0 \frac{1}{4\pi} 4 \cos(\theta) \sin(\theta) \, d\theta \, d\varphi \qquad (6.1)$$

[1] O.N. Jarvis has pointed out that the high rate of low-amplitude pulses from a silicon detector in a neutron field may give problems (see also chapter 11, »Test measurements.», page 145). The rate of low amplitude pulses is much lower in a high purity Ge-detector.

[2] According to G. Sadler, the timing properties of a Si-detector are sufficient for this application.

where

σ_0 = the total microscopic scattering cross-section

θ, φ = the scattering angles.

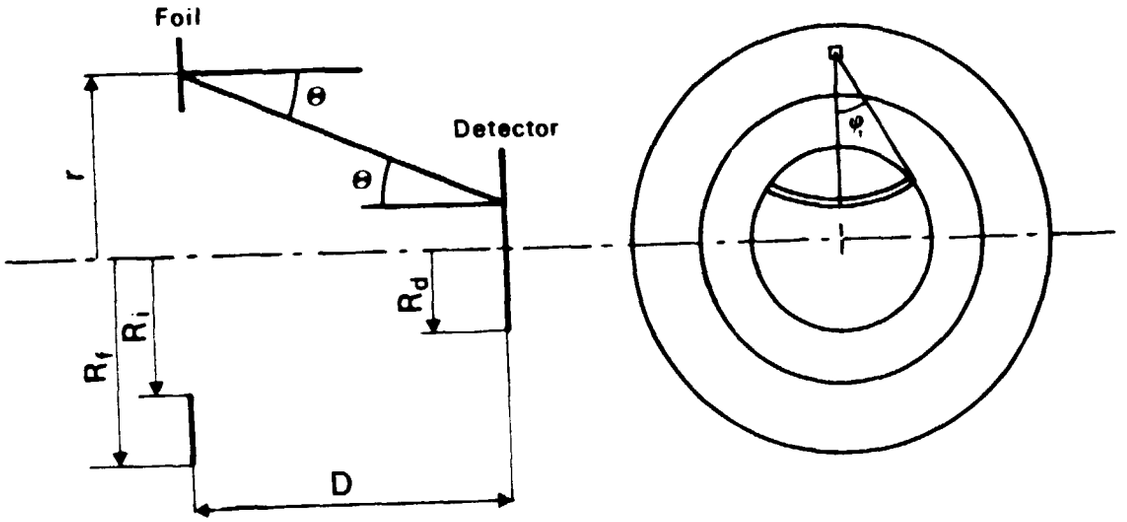

Figure 40. Principles of proton detection.

The angular distribution is given by all the possible different lines we can draw between the foil and the detector, folded with the differential cross-section as defined by equation 6.1. Thus, the angular distribution per unit foil area is

$$P_p(\theta) = \frac{4\cos(\theta)\sin(\theta)}{\pi(R_f^2 - R_i^2)} \int_{R_i}^{R_f} dr\, r\varphi_1(\theta) \qquad (6.2)$$

The geometrical quantities used are defined in figure 40. The arc shown in the figure is

$$\varphi_1(\theta) = \cos^{-1}\left[\frac{r^2 + (D\,tg(\theta))^2 + R_d^2}{2rD\,tg(\theta)}\right] \qquad (6.3)$$

for the interval

$$r - R_d \leq D\,tg(\theta) \leq r + R_d \qquad (6.4)$$

and zero elsewhere.

The integral in equation 6.2 defines an area on the protondetector. This area is limited by the boundaries of the proton-detector or/and the radii of the foil. A special case appears for some angles if the detector diameter is less than or equal to the width of the foil. Then, the limits are only defined by the boundaries of the proton-detector and the integral will be equal to half the area of the proton-detector. Therefore, in this special case we have

$$P_p(\theta)\,d\theta = 2\sin(\theta)\cos(\theta)\,\frac{R_d^2}{R_f^2 - R_i^2} \tag{6.5}$$

which is valid if and only if

$$R_i + R_d \leq D\,tg(\theta) \leq R_f - R_d \tag{6.6}$$

We call this the total transfer. It is total in the respect that, for a given azimuth angle defined by equation 6.6, all the subregions of the proton-detector have a corresponding complete annular subregion on the foil. The partial transfer is defined to be all other cases, i.e. the cases for which the relation 6.6 is not true.

The equations 6.2 to 6.6 are illustrated in figure 41. The total transfer shows up as an envelope to the curves for different distances. The total transfer is independent of the distance between the foil and the detector. I' is the highest transfer probability possible for a given angle as long as the diameter of the detector is less than the width of the foil.

In TANSY, the diameter of the detector is equal to the width of the foil. Therefore, as can be seen in figure 42, only the maximum point of the angular probability curve will be on the envelope.

6.2 Energy distribution

There is a direct connection between the energy and the angle. From equation 4.1 we get

$$dE = -2E_o\cos(\theta)\sin(\theta)\,d\theta \tag{6.7}$$

and

$$tg^2(\theta) = \frac{E_o - E}{E} \tag{6.8}$$

Using these, equation 6.2 can be transformed to energy variables. It takes the form

$$P_p(E) = \frac{2}{E_o\pi(R_f^2 - R_i^2)} \int_{R_i}^{R_f} dr\, r\varphi_1(E) \tag{6.9}$$

The arc function, equation 6.3, goes over to

$$\varphi_1(E) = \cos^{-1}\left[\frac{E(r^2 - R_d^2) + D^2(E_o - E)}{2rD\sqrt{E(E_o - E)}}\right] \tag{6.10}$$

for the energy interval defined by

$$\frac{D^2}{(r+R_d)^2+D^2} \leq \frac{E}{E_o} \leq \frac{D^2}{(r-R_d)^2+D^2} \tag{6.11}$$

and is zero elsewhere.

The total transfer has a very simple distribution. From equation 6.5 we get

$$P_p(E)\,dE = \frac{dE}{E_o}\,\frac{R_d^2}{(R_f^2-R_d^2)} \tag{6.12}$$

which is valid for

$$\frac{D^2}{D^2+(R_i+R_d)^2} \geq \frac{E}{E_o} \geq \frac{D^2}{D^2+(R_f-R_d)^2} \tag{6.13}$$

Equation 6.12 is very important for the understanding of the transfer. It says that the number of transfers per energy unit depends only on the dimension of the proton-detector as long as condition 6.13 is fulfilled. It does not depend on the distance. This is illustrated in figure 43. The distributions have a flat central part, which has a magnitude independent of the distance. This total transfer part is surrounded by the partial transfer parts, which give tails on the distribution. The high energy tail is steeper than the low energy tail.

The flat part disappears if condition 6.13 is not fulfilled. Still, as can be seen in figure 44, the height of the maximum point is independent of the foil-detector distance. The gross behaviour of the distributions in figure 44 is the same as in figure 43. A small foil-detector distance gives a broad distribution. An increased distance makes the distribution more peaked. The maximum amplitude is preserved and the mean value is shifted towards higher energies.

The influence on the energy distribution by a change of the TANSY proton-detector radius is shown in figure 45. Total transfer appears for detector-radii less than 1 cm. The maximum transfer probability is here proportional to the squared radius. Above 1 cm, where the detector diameter is larger than the foil width, the maximum transfer probability will increase more slowly. Already at 1.2 cm the increase is almost proportional to the detector radius.

6.3 Energy spread

The endpoints of the probability distribution are defined by equation 6.4 or 6.11. The inner foil radius defines the upper energy limit and the outer foil radius defines the lower energy limit.

Figure 46 illustrates the effect of a variation of the outer foil radius. The upper energy limit is constant while the lower limit varies. The distribution alters from a very peaked distribution for a foil with small width to a flat distribution for the foil with a large width.

The situation appears to be more complicated when we vary the inner radius, figure 47. The lower energy limit is constant and not very far from the initial-neutron energy. This gives a smaller span for the variation of the upper energy limit than for the lower limit in the previous case. The energy distribution is more peaked for a small foil width. However, the distribution with the maximum transfer probability is not caused by the smallest foil.

We define the energy width as the difference between the highest and lowest energy of the transferred protons, divided by the energy of the initial neutron. Then, from equation 6.11 we have

$$\eta = \frac{E_{max} - E_{min}}{E_o} = \left(\frac{R_+}{D}\right)^2 \frac{1 - \left(\frac{R_-}{R_+}\right)^2}{\left(1 + \left(\frac{R_+}{D}\right)^2\right)\left(1 + \left(\frac{R_-}{D}\right)^2\right)} \quad (6.14)$$

where $R_+ = R_f + R_d$

$R_- = R_i - R_d$

A graph based on equation 6.14 is given in figure 48. For large distances the energy spread is inversely proportional to the distance, i.e. we may control the width by the detector-foil distance. However, simultaneously there will be a shift of the mean energy[1].

The energy spread depends on the detector radius. For TANSY the spread is 6.15%. It increases to 9.15% for a 2 cm detector radius and decreases to 4.6% for a detector radius of half a cm.

6.4 Efficiency and sensitivity

The proton detector gives a signal for all protons impinging on the detector, the sensitivity of the proton detector is 1. Therefore, the sensitivity of the instrument for proton detection is given by an integration of the angle dependent or energy dependent transfer probability, equations 6.2 or 6.9. The proton sensitivity is defined[2] as the number of protons registered per neutron scattered in the foil.

$$S_p = \int_E P_p(E)\, dE \quad (6.15)$$

The sensitivity has been calculated for all distributions presented in this chapter. The result is printed on the respective diagram. In the figures 41, 43, and 44 we see that the sensitivity varies with the distance. Figure 45 shows a variation with the detector radius. However, the variation of the sensitivity with the foil radii is small as can be seen from the figures 46 and 47. Approximately, the sensitivity is equal to the space angle occupied by the proton detector, as seen from the foil, times the scattering cross-section in the forward direction.

$$S_p \approx \left(\frac{R_d}{D}\right)^2 \qquad \left(= \frac{\pi R_d^2}{4\pi D^2}\, 4\right) \quad (6.16)$$

Thus, the sensitivity as well as the energy width, equation 6.14, are asymptotically inversely proportional to the squared foil-detector distance. Therefore, we can express the sensitivity as a function of the energy spread

---

1) See the figures 44 and 43.

2) In analogy with the definitions in paragraph 2.1, page 23.

$$S_p \approx \eta \frac{R_d^2}{(R_+^2 - R_-^2)} \qquad (6.17)$$

The coefficient for TANSY is 0.0156, i.e. a spread of 100 keV gives a sensitivity of 1.11×10^{-4}. The calculated sensitivity in figure 45 is 0.97×10^{-3}, a factor of ten higher[1].

The efficiency is the sensitivity times the foil area. Therefore, it is easy to convert the above sensitivities to efficiencies. However, it is not obvious that the efficiency for constant foil width and energy spread is almost independent of the inner (or outer) foil radius. This property of the proton detection efficiency is seen in figure 49. It is based on equation 6.14 and an approximation to equation 6.15.

6.5 The proton detector

The range of 15 MeV protons in silicon is 1.45 mm {41} and the path length straggling is 0.02 mm. At 17.5 MeV the range has increased to 1.90 mm. Therefore, an adequate silicon layer thickness is 2 mm.

For TANSY we have assumed a detector radius of 1 cm, which gives an area of 314 mm^2. The maximum area for 2 mm silicon detectors listed in the Ortec catalogue is 300 mm^2 (B-020-300-2000). However, we assume that larger detectors may be made on special order[2].

The energy resolution guaranteed for 5.5 MeV alfa-particles is 20 keV. We add 15 keV for preamplifier noise and assume that it is possible to get an energy resolution of 35 keV. However, this is a point which should be tested by a measurement.

The flight time of the proton in the silicon layer is about 40 ps {41}. The charge collection time is proportional to the layer thickness. Ortec gives 200 ns for a 2 mm thick layer. Paulus et al. {49} have shown that it is possible to do subnanosecond timing with surface-barrier detectors. However, it might be necessary to include a thin time-pick-up detector for the time measurement.

Serious damage of surface-barrier detectors occurs at 10^{13} protons/cm^2, 3×10^{11} neutrons/cm^2, or 10^{11} alpha-particles/cm^2 {47}. The neutron flux from the foil is equal to the proton flux. We assume that the 3 cm^2 detector is useful up to 10^{10} n/s and that we have less than 10^5 proton-registrations per shot. Then, a detector should withstand about 10^5 shots.

Several neutron-reactions in silicon give charged particles. However, it is shown in chapter 11, »Test measurements.», that the pulses from the neutron reactions are lower than those from the protons. Therefore, we can easily get rid of them by pulse-height discrimination.

---

1) See chapter 8, »Characteristics of the detection method.», for a further discussion.

2) A question to Ortec has given the answer: »The largest area, 2000 micron thick detector for which we can get high resitivity silicon is 450mm sq. The expected resolution is 25 keV.»,(Telex 24feb83).

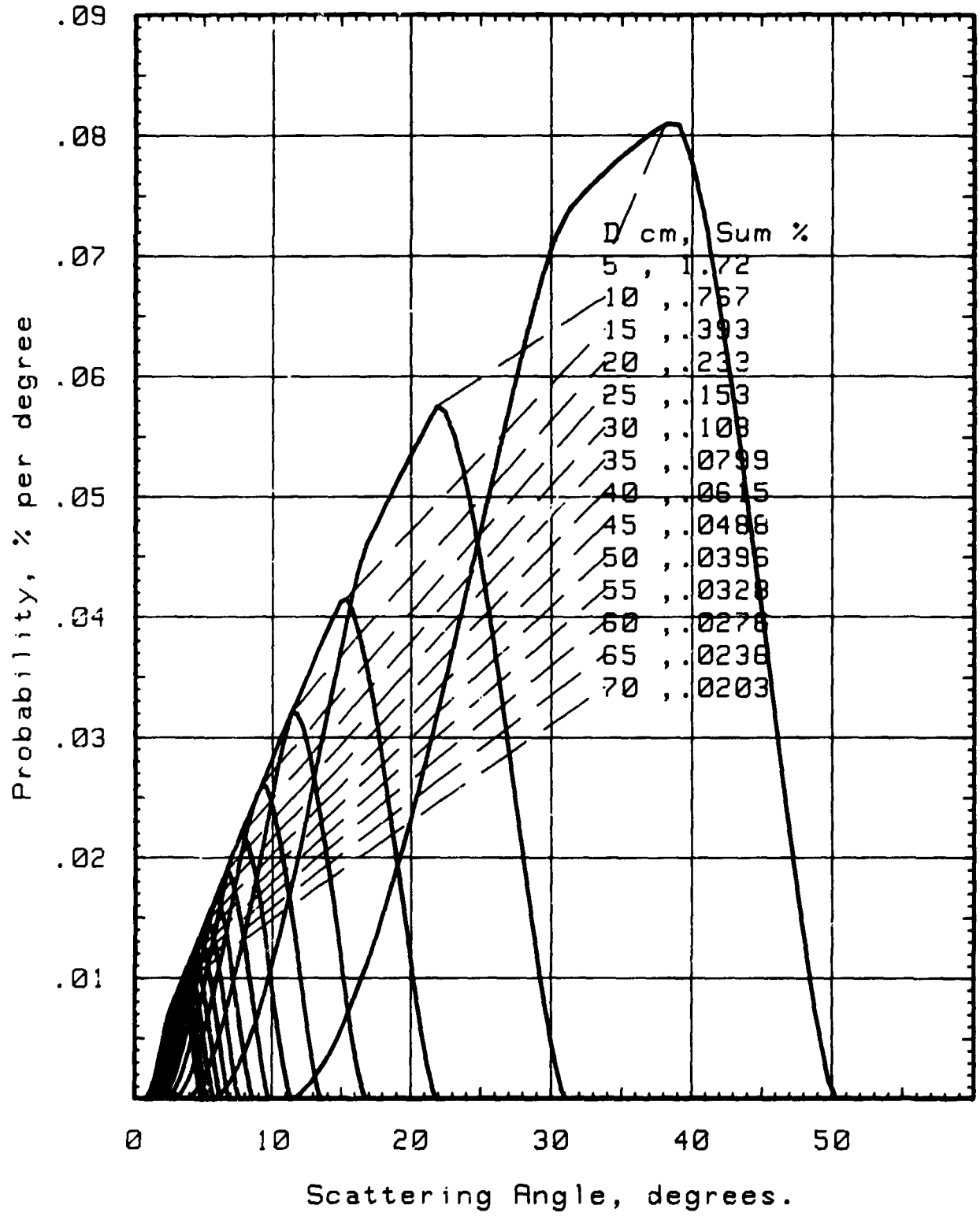

Figure 41. Proton angle distributions.

The angle distribution for different distances. The foil radii are 2 and 5 cm. The detector radius is 1 cm. The envelope of the curves is caused by total transfer.

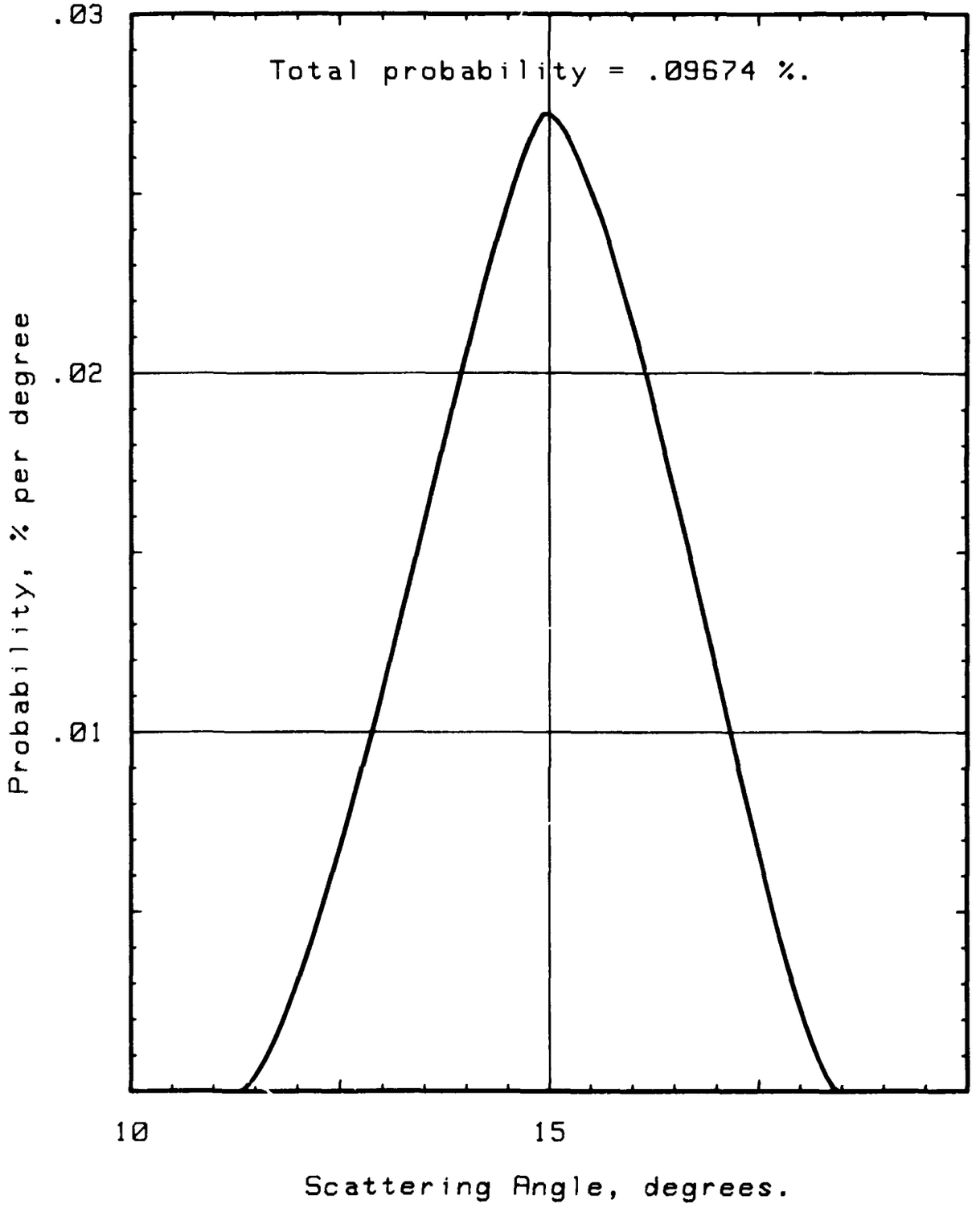

Figure 42. Proton angle distribution for TANSY.

The foil radii are 7 and 9 cm, the detector-foil distance is 30 cm, and the detector radius 1 cm. About 1 per mille of the recoil-protons are registered.

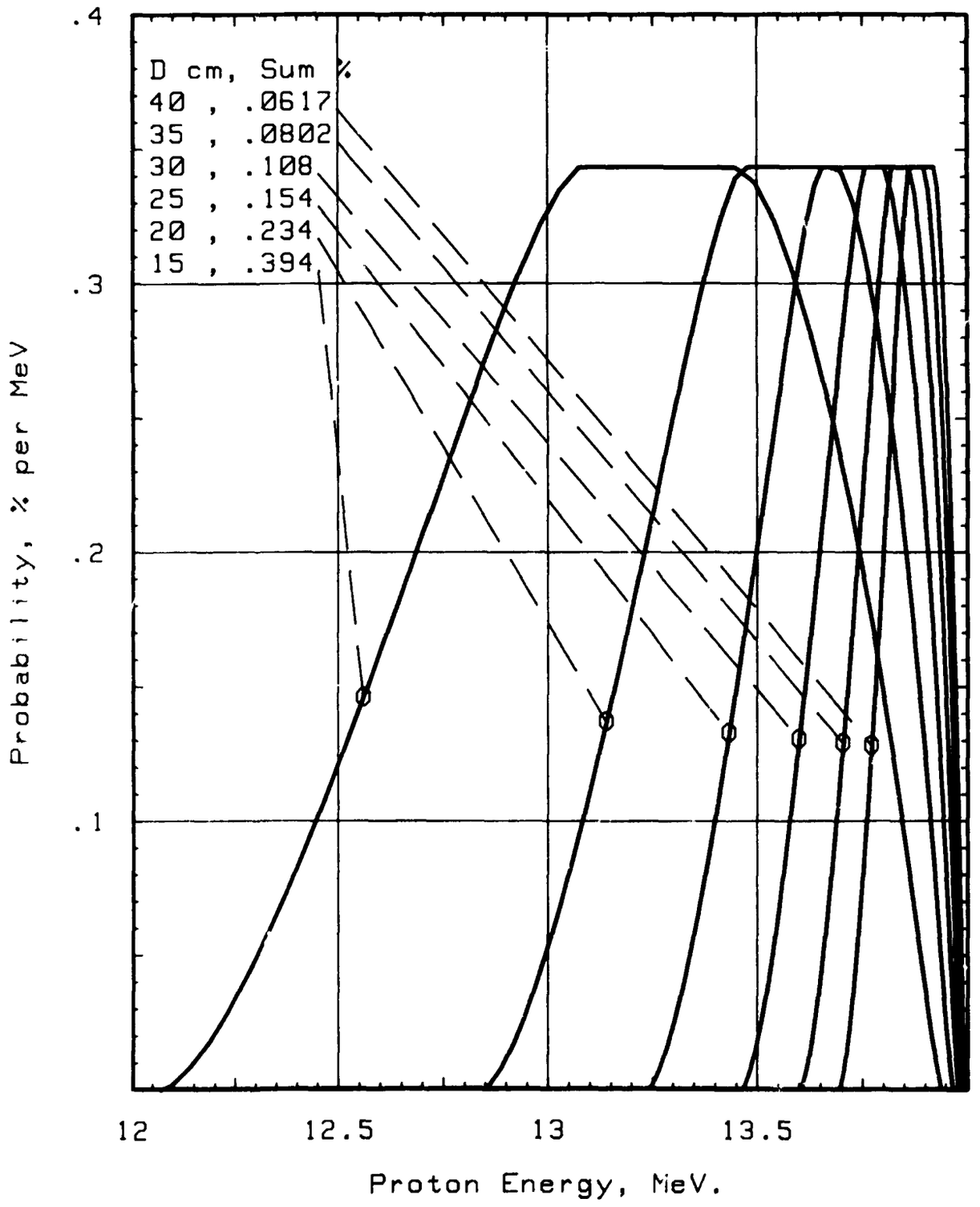

Figure 43. Proton energy distributions.

The energy distribution is given for different foil-detector distances. The foil radii are 2 and 5 cm. The detector radius is 1 cm and the initial-neutron energy is 14 MeV.

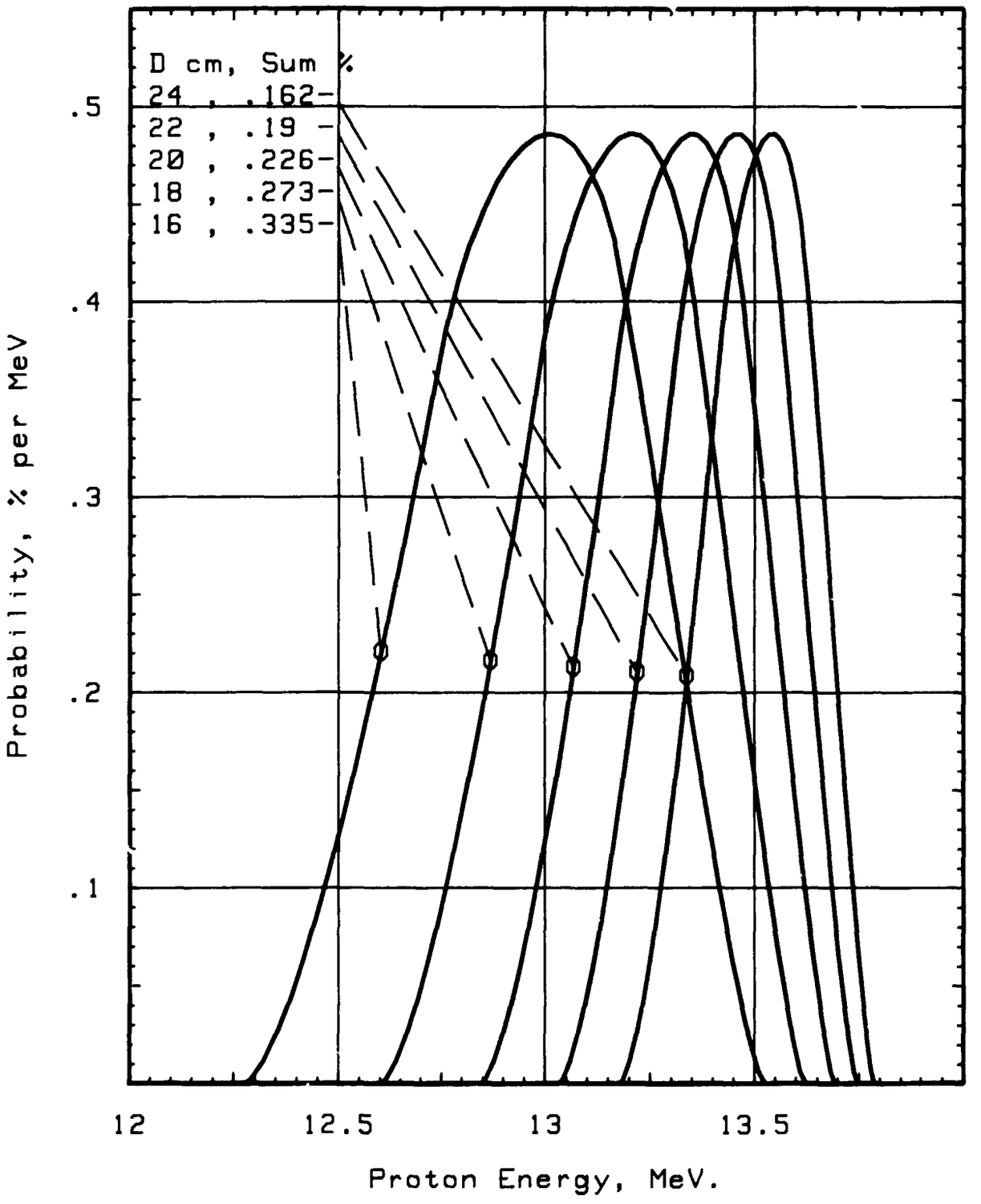

Figure 44. Proton energy distributions for partial transfer.

The energy distribution for different distances. The foil radii are 4 and 5 cm, the detector radius is 1 cm. Thus, the total transfer condition is never fulfilled.

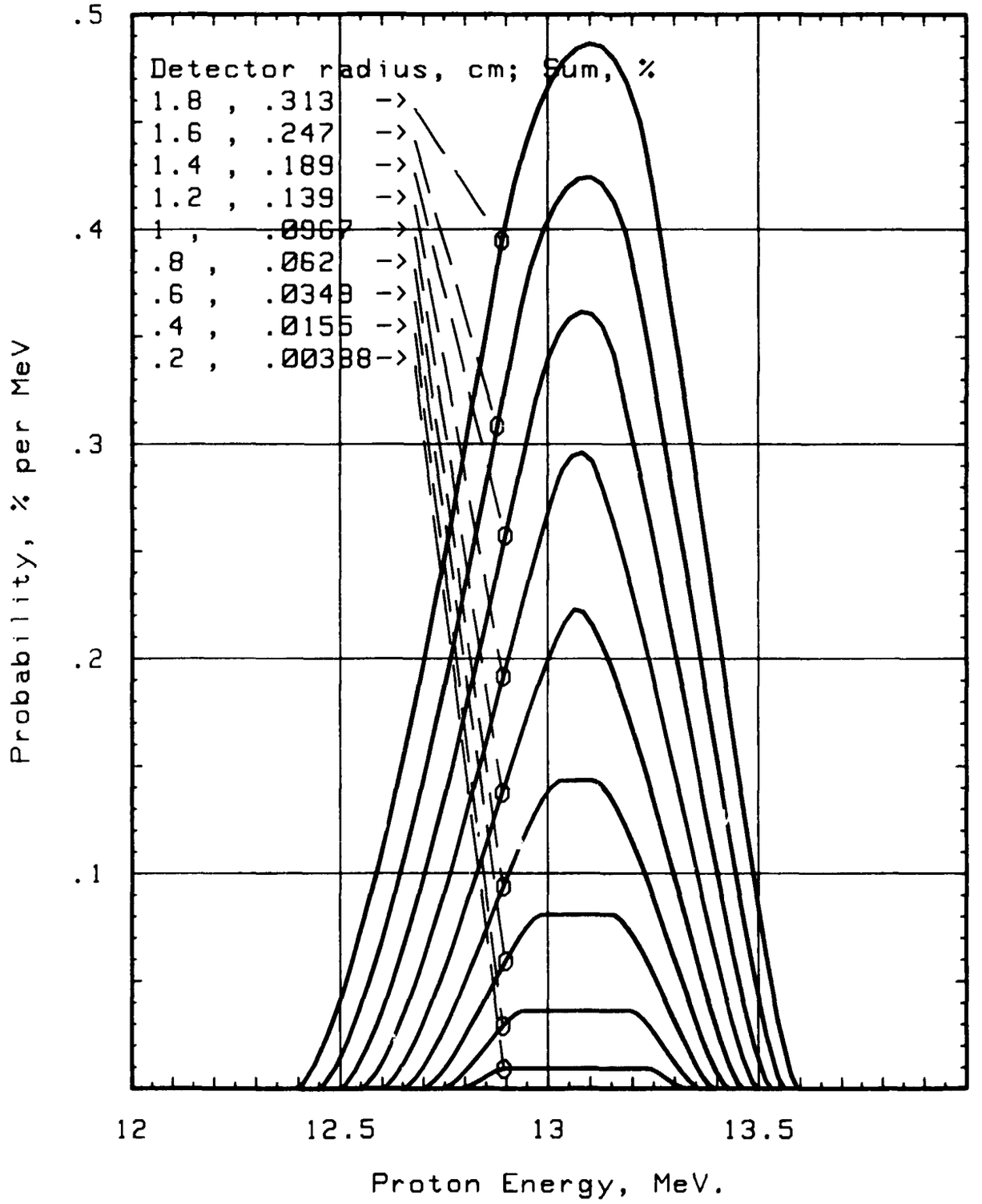

Figure 45. Proton energy distributions for TANSY.

The foil radii are 7 and 9 cm, the foil-detector distance is 30 cm. The maximum transfer probability is proportional to the detector area for radii lower than or equal to 1 cm. It is approximately proportional to the radius for radii above 1.2 cm.

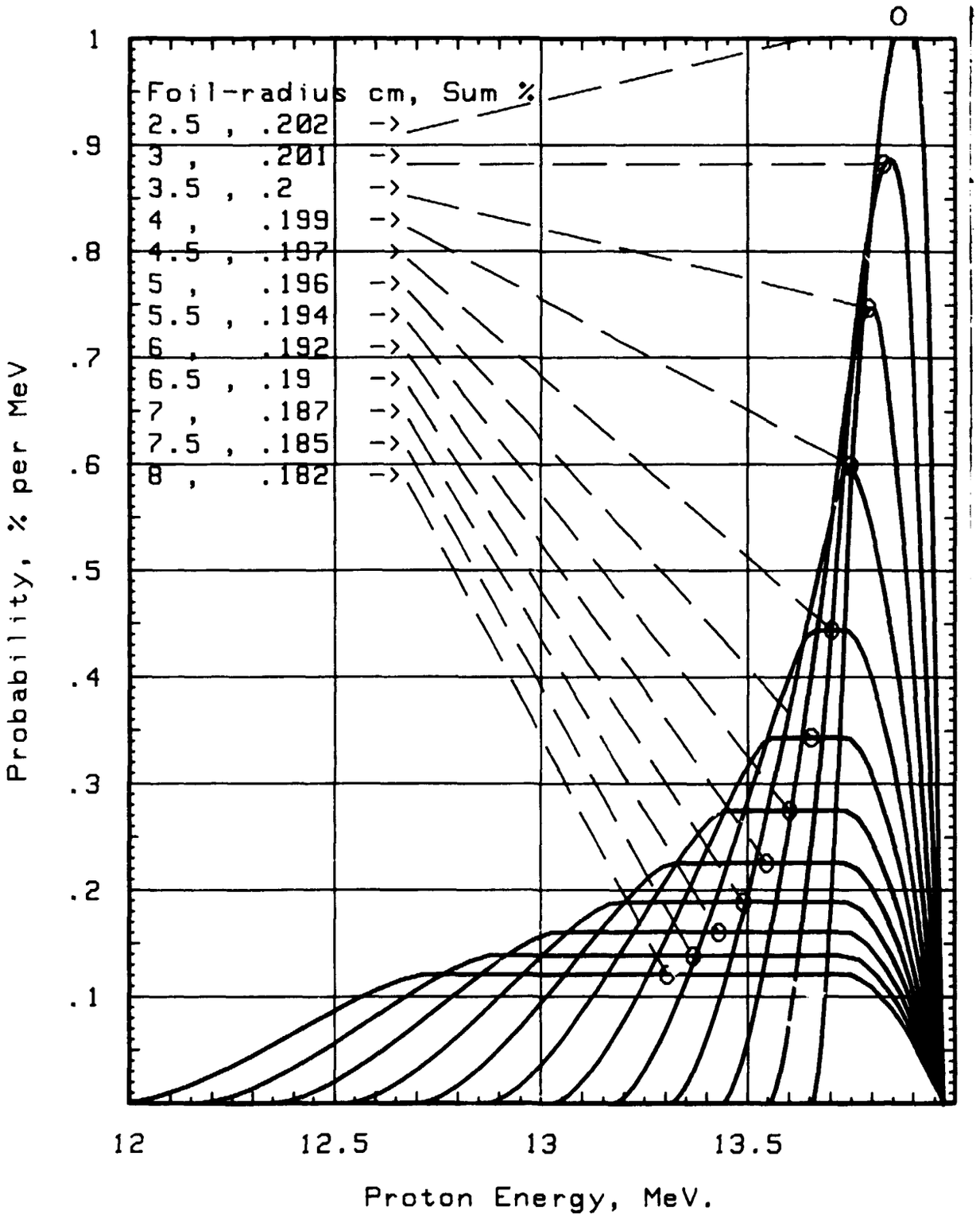

Figure 46. Proton energy distributions, different outer radii.

Inner foil radius is 2 cm, the foil-detector distance is 22 cm, and the detector radius is 1 cm.

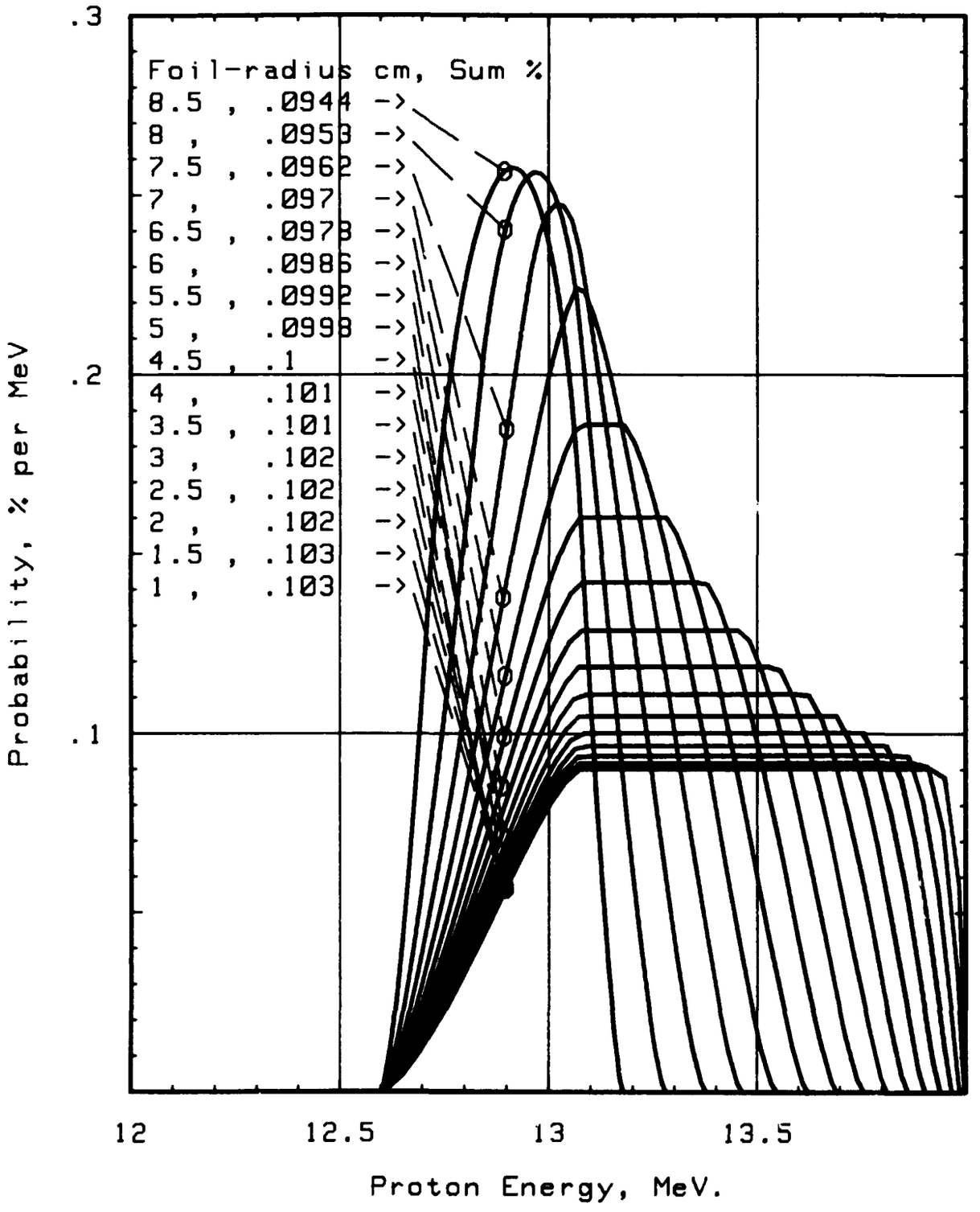

Figure 47. Proton energy distributions, different inner radii.

Outer foil radius is 9 cm, foil-detector distance 30 cm, and detector radius 1 cm.

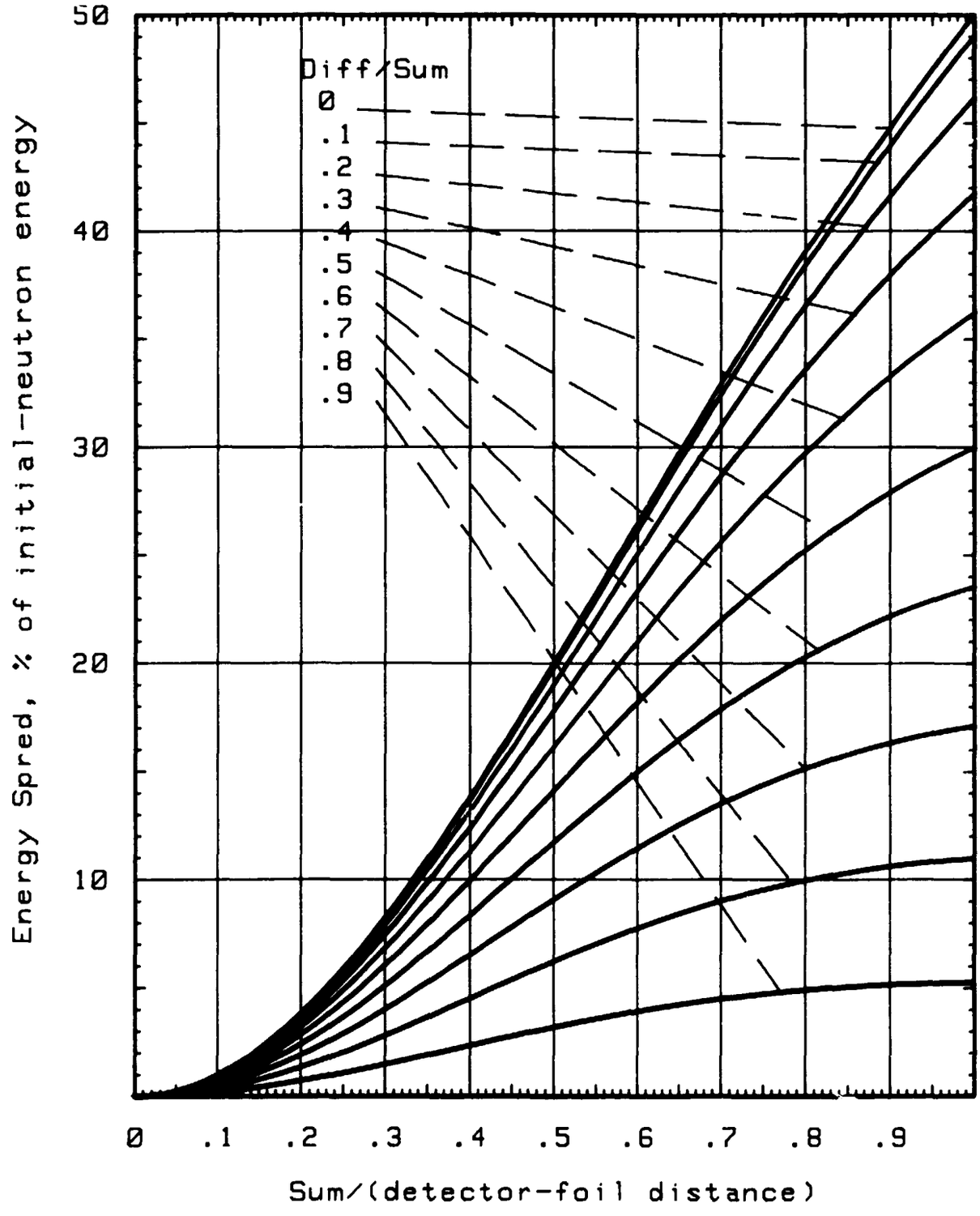

Figure 48. Proton energy spread.

Diff is the difference between the inner foil-radius and the detector-radius. Sum is the sum of the detector radius and the outer foil radius.

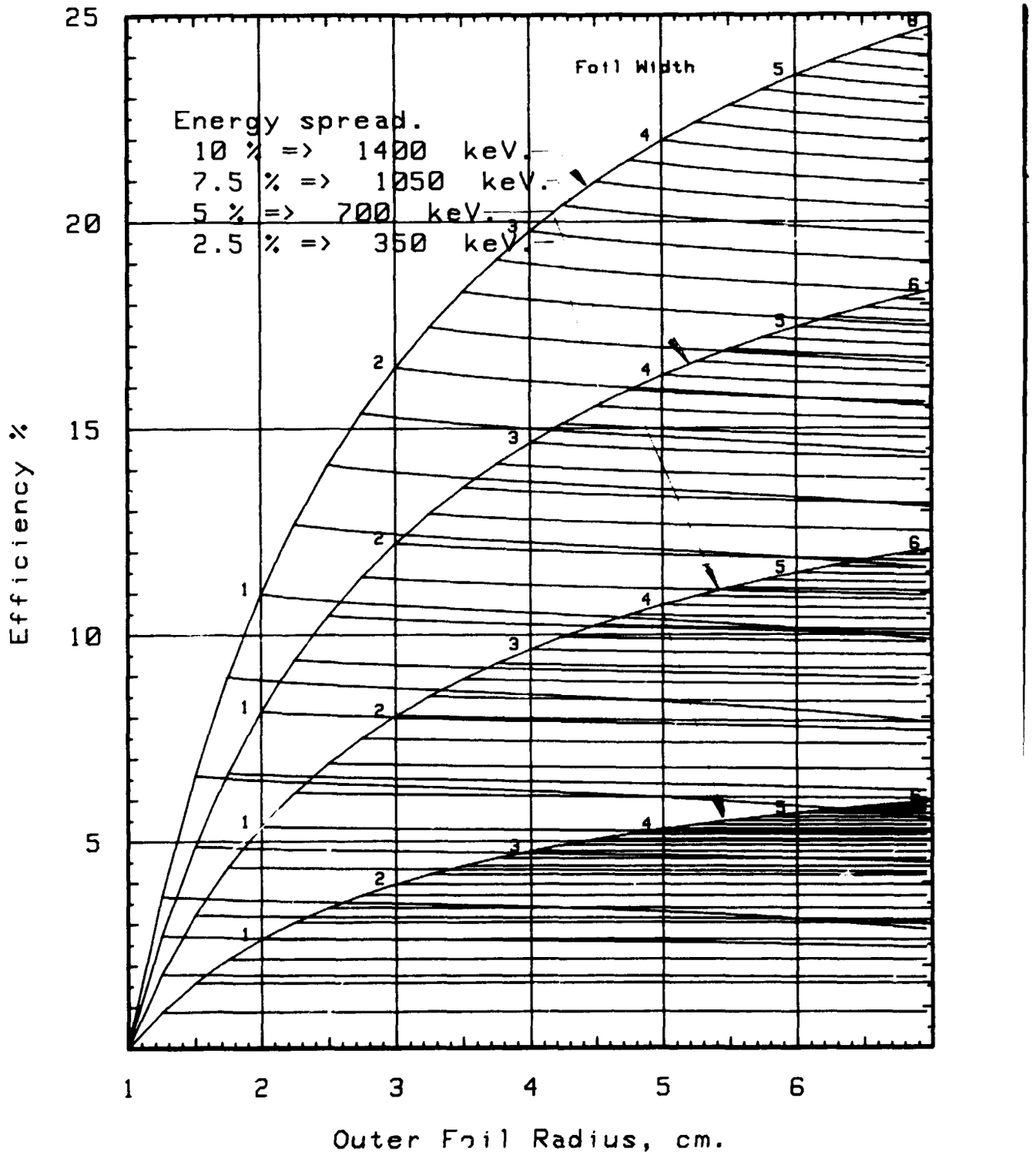

Figure 49. Proton detection efficiency.

The proton detection efficiency is the number of protons detected relative to the number of scatterings per cm^2.

7 Neutron detection

The wanted qualities of the neutron detection system are that it should be fast, it should have a low background sensitivity, and it should have a high sensitivity for neutrons in the low MeV energy-range. Three types of detectors are considered, namely the Li-glass, the liquid scintillator, and the plastic scintillator.

None of these has all the wanted qualities. The best choice seems to be a plastic scintillator. It has good timing properties. The sensitivity is about 20% at 1 MeV for a 2 cm thick detector.

The background sensitivity is estimated at 1000 counts/s per mrem/h for 1 MeV gammas. The total sensitivity is then 1200 counts/s per mrem/h. However, no shielding has been considered. Therefore, the background sensitivity given is an upper value, which may be reduced by a proper shielding.

7.1 Glass scintillators

The Li-6 reaction cross-section is characterized by a peak at 252 keV. The maximum cross section within the peak is about 2.7 barn, a value which makes a Li-loaded glass-scintillator interesting for the neutron detection.

The Li-glass scintillator has been developed by Spowart {50,51,52}. NE912 is one of the most sensitive commercially available glass-scintillators. It contains 7.7% lithium enriched in Li-6 to 95%. The result of an approximate calculation of the sensitivity is given in figure 50. A 2 cm thick scintillator gives a sensitivity of 10% in the peak. However, outside the peak the sensitivity drops to a few per cent.

The light pulse has a fast rise time. It reaches the top value within a few nanoseconds. The decay goes along two exponentials with the decay times 19 and 90 nanoseconds, respectively {52}. Macklin et al. {53} have used a thin glass-scintillator at the ORELA electron linear accelerator. They have found a time resolution better than 2 ns.

7.2 Liquid scintillators

The liquid scintillator NE213 gives a comparatively high sensitivity. It has a decay time of 3.2 ns, which gives good timing properties. The light output is 78% of the light output of anthracene-100.

NE213 gives a possibility to use pulse shape discrimination for background separation. The separation works well above 2 MeV and has been used down to 200 keV. However, great care must be taken in order to achieve a good separation in the low energy range {54}.

The properties of a liquid scintillator and a plastic one are not very different. We will concentrate our analysis on the use of a plastic scintillator. A shift to a liquid one would give somewhat higher sensitivity and the possibility to use pulse shape discrimination. However, the construction would be more complex.

7.3 Plastic scintillators

The protons liberated by recoils in a plastic scintillator have energies ranging from zero to the energy of the neutron. For a given neutron energy the proton energy-distribution is flat, there is equal probability to find a proton at any energy below the neutron energy.

The response of the scintillator, the light output for a given proton energy, has been measured by Madey et al. {55}. They give the response curve for NE102 as

$$E_e = -8.0\,[1 - \exp(-0.10E_p^{0.90})] + 0.95E_p \quad (7.1)$$

where

E_p = the proton energy in MeV and

E_e = the equivalent electron energy in MeV.

The response curve is drawn in figure 51. The proton response is much lower than the electron response. It is very small at 200 keV and rises above that. A reliable light signal can not be expected below a few hundreds of keV.

The sensitivity[1)] of a 2 cm Pilot U scintillator is shown in figure 52. The uppermost curve shows the sensitivity when all protons are detected. However, in order to get rid of the low energy gammas we must use a discriminator, which gives a bias corresponding to the lowest energy detected. The bias gives a cut of the low energy part of the protons, so the sensitivity will be zero below the bias. For energies above the bias the sensitivity is proportional to the total scattering cross-section and the relative amount of energy between the bias and the neutron energy.

$$S_n = \frac{(E - E_b)}{E}\left(1 - e^{-\Sigma_t(E)\,d_n}\right)\frac{\Sigma_r(E)}{\Sigma_t(E)} \quad (7.2)$$

The cross-section decreases with increasing energy. Therefore, the sensitivity rises to a maximum value and then it decreases.

The sensitivity has been measured and calculated by several researchers {56,57,58}. Some attempts have been made in order to use a low threshold. A low bias gives an increased sensitivity in the whole usable energy interval. The problem is the low light output for low proton energies, figure 51 and equation 7.1. Adams et al. {59} have solved the problem by using two photomultipliers in coincidence. The coincidence circuit sorts out noise in the photomultiplier tubes and, therefore, the bias can be set as low as 50 keV. However, gamma-pulses will not be sorted out by this technique.

The plastic scintillators have good timing properties. Cernigio et al. {60} have got a time resolution of 650 ps with a NE110 plastic scintillator, 200 cm long, 15 cm in height, and 5 cm thick. Eight photomultipliers were used, four at each end of the scintillator. The refractive index of the plastic scintillators is 1.58 which gives a velocity of light in the scintillator of 19 cm/ns. Therefore, the time to cross a 8 cm wide scintillator, as that of TANSY, is 0.42 ns. The actual time resolution (in fwhm) will be less than that because of the smearing out effects caused by reflections in the scintillator surfaces. Therefore, the limiting factor of the time measurement is neither the scintillator nor the light collection.

7.4 Background considerations

A plastic scintillator is sensitive to gamma radiation. The detection probability of one of the 32 detectors is given in figure 53. It is calculated for a 313 cm^3 Pilot-U scintillator from the Klein-Nishina formula {62}, taking into account the bias in the same way as we did for the neutrons, equation 7.2. The bias level for 500 keV protons corresponds to 50 keV electrons according to figure 51.

1) The sensitivity is the efficiency per square centimeter.

For the calculation of the count rate we need full knowledge of the energy distribution of the gamma radiation. However, we do not know anything about the energy distribution and very little about the radiation intensity levels. Therefore, this calculation will be limited to an estimate taken in relation to the maximum permissible radiation dose-rate for personnel in radiological work.

We assume that the radiation level at the instrument is 2.5 mrem/h = 25 μSv/h. Furthermore, we assume that all the gammas have an energy of 1 MeV. Then, the gamma flux is $(2.5 \times 10^{-3})/(1.923 \times 10^{-6})$ = 1300 photons/cm^2,s. From figure 53 we get the detection probability to 20 counts per photon/cm^2. Thus, the count rate is 26000 counts/s in each scintillator. Then, the total count rate in the 32 scintillators is 0.86×10^6 counts/s.

This is too high to be acceptable. It may be decreased by shielding, either directly around the scintillators or by an outer shield. A proper calculation of this shielding can not be made without a more detailed knowledge of the radiation level and the gamma energy distribution.

The high count rate gives a large load on the photomultipliers and the amplifier chains. Therefore, separate lines should be used for the multipliers in order to minimize pile-up effects.

7.5 Practical problems

The scintillators should be mounted on a ring with a radius of about 1 m[1]. An indication of the mounting is given in figure 6.

The detailed construction is not a part of this work. However, it should be emphasized that the indicated orientation of the photomultipliers might not be the best one. In figure 6 we have indicated the best solution for maximum light collection and minimum time spread. However, it includes light guides placed in the coincidence-neutron beam. Therefore, neutrons may be scattered back from the light guides. This gives an increased efficiency but the time determination is detoriated. A calculation on the amount of backscattering must be done prior to the final decision about the orientation of the light guides and the photomultipliers.

We have suggested 32 scintillators connected to 32 photomultipliers. The number of photomultipliers may be reduced by the use of a light pipe system. However, then again pile-up effects should be considered.

The suggested type of scintillator is the Pilot-U scintillator from Nuclear Enterprises. An alternative scintillator with comparable properties can be obtained from Bicron. A low cost alternative from Japan is reported by Inagaki and Takashima {61}.

[1] The radius is determined in chapter 8.3, »The resolution-efficiency dilemma.», page 103.

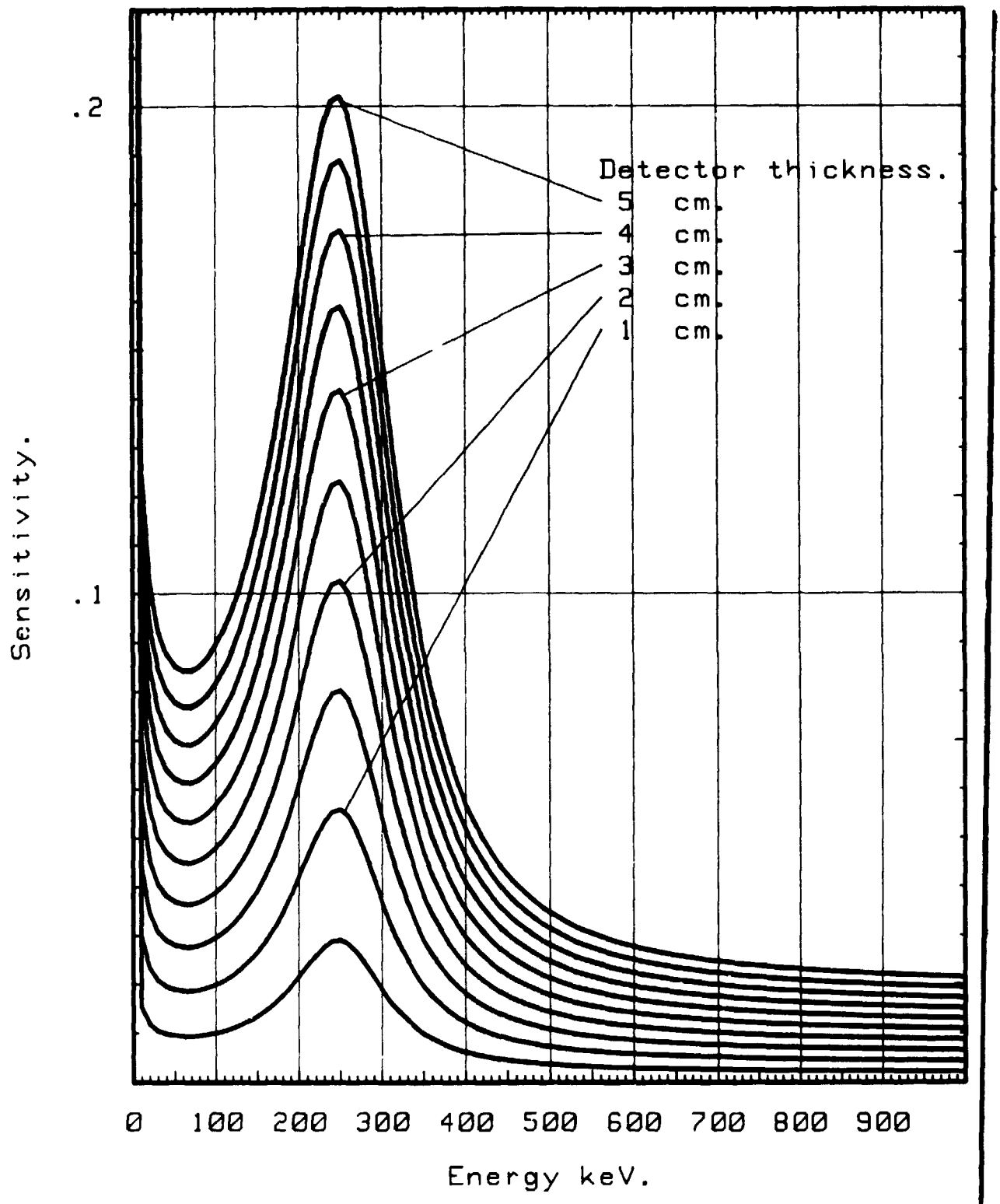

Figure 50. Sensitivity of Li-glass NE912.

The calculation is based on approximate values of the cross-section. It is about 30% too high for energies below the resonance peak.

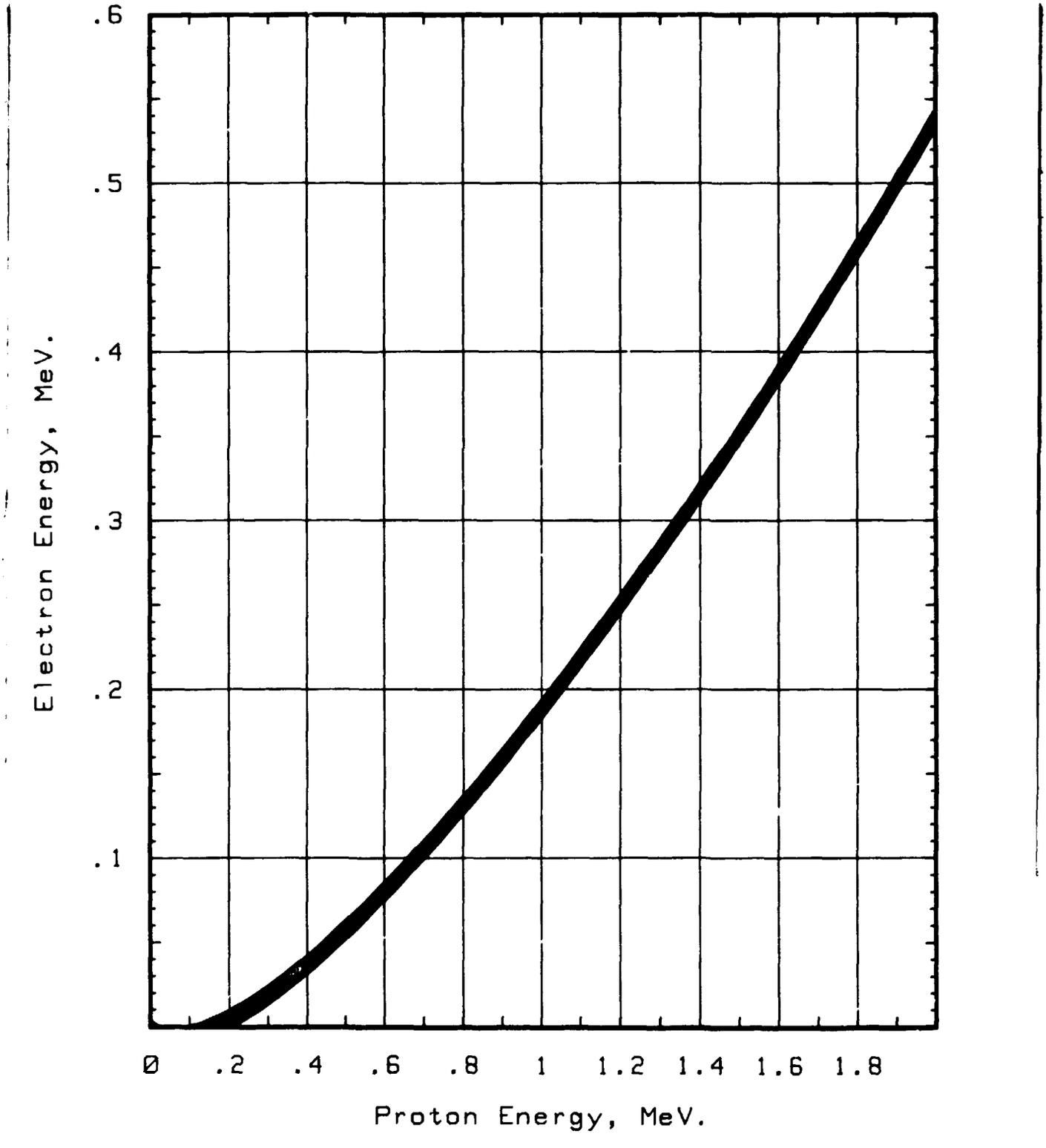

Figure 51. Light response for a plastic scintillator.

The plastics have a low light response for protons. The diagram gives a relation between the proton and the electron response. The electron response is linear and can directly be used for gamma quanta. The diagram shows values for NE102 but the difference between different scintillators of the same type is small. From reference 55.

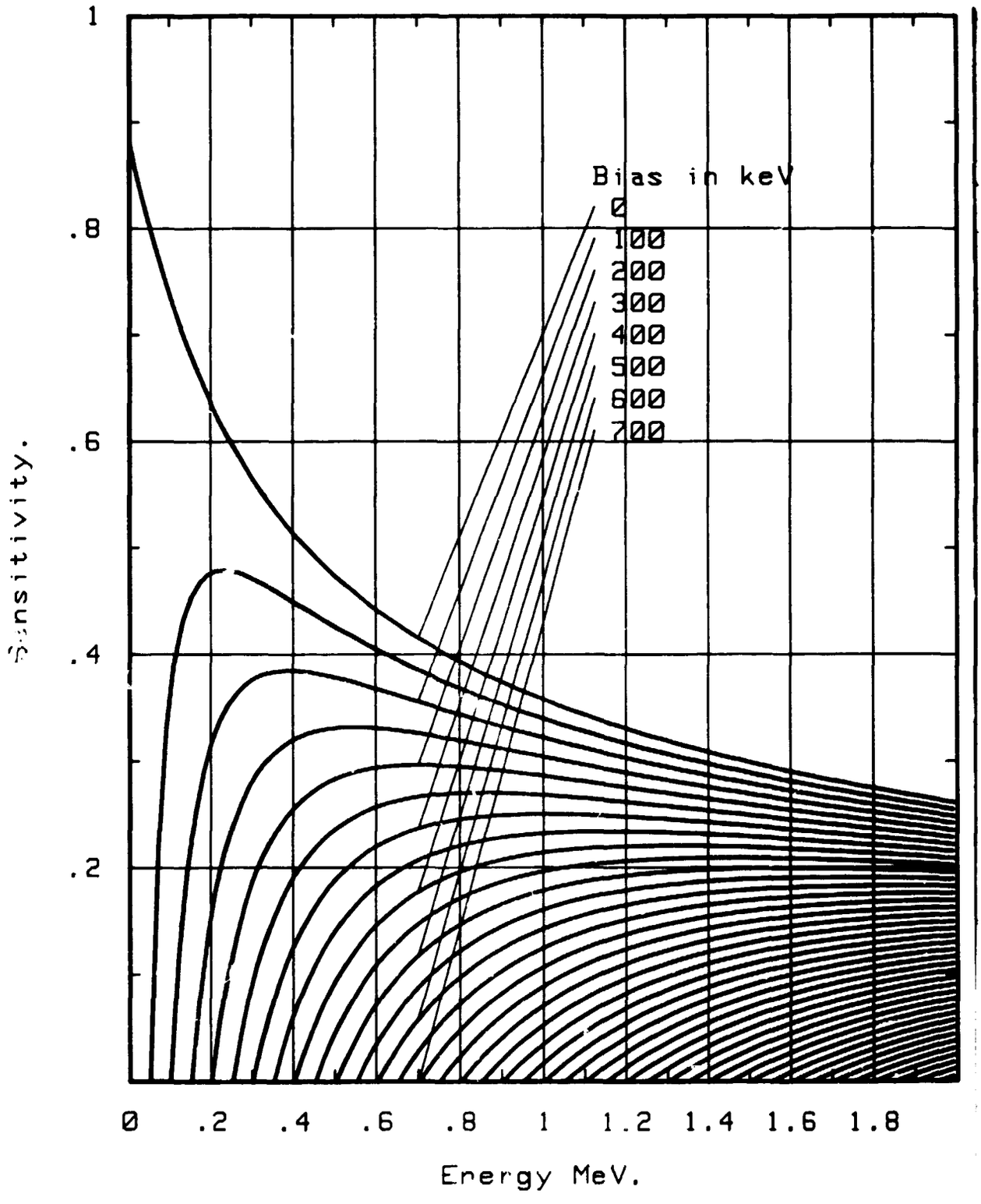

Figure 52. Sensitivity of a Pilot U scintillator.

The neutron detection sensitivity increases with decreasing bias. However, problems arise with photomultiplier noise and gamma radiation in the low energy part. See figure 51.

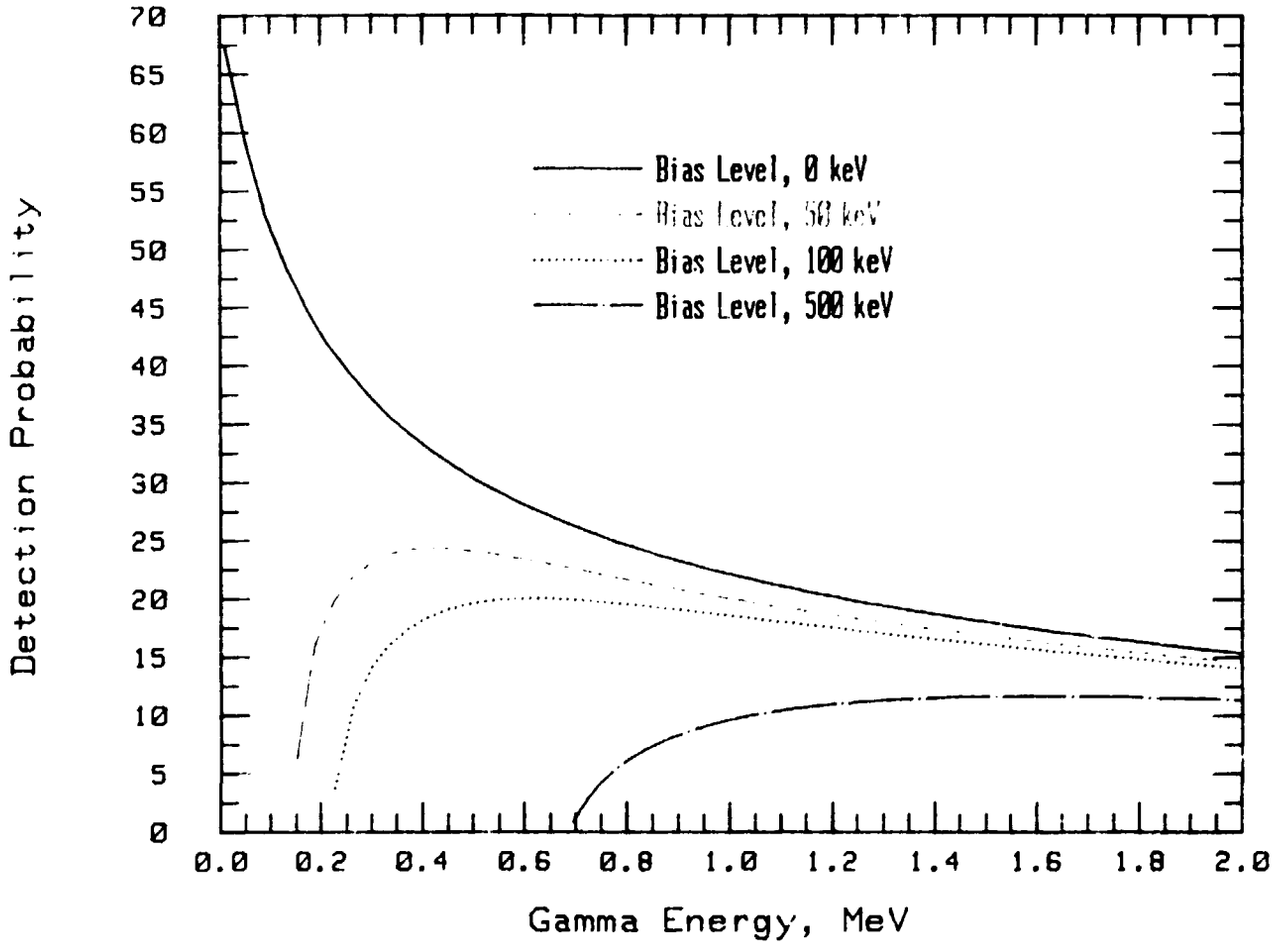

Figure 53. Gamma detection probability.

The number of counts per photon/cm^2 for a 313 cm^3 Pilot U detector. A bias of 50 keV corresponds to 0.5 MeV proton bias. See figure 51.

8 Characteristics of the detection method

The efficiencies of the scattering, the proton detection, and the neutron detection are put together in order to get a total efficiency of the instrument (paragraph 8.1). We find that the plastic scintillator is ten times as efficient as the Li-glass scintillator and that an efficiency of 10^{-6} detected events per neutron flux density unit can be obtained.

The resolution (8.2) increases with increasing scattering angle. We combine the resolution with the results from the efficiency calculations. For most of the parameters we find that an increased efficiency leads to a worse resolution, the efficiency-resolution dilemma (8.3). However, some combinations give a resolution better than 100 keV for a sensitivity higher than 10^{-6}. Among these we search for a solution with a peaked symmetric energy-distribution of the neutrons detected in coincidence with protons in order to obtain an efficient use of the whole neutron detector.

A detection rate of 1000 events per second gives a working range close to the limits of the instrument (8.4). The limit is set by the electronics, mostly the analog-to-digital converter, and the background rate. Considering the fact that we need a high collection rate, the usable dynamic range will be limited to about one decade. From figure 14 we find that the neutron flux density may increase about one decade for a 1 keV increase of the plasma temperature. Therefore, the neutron flow into the detector must be controlled by some outer means, i.e. an aperture in the collimator or in a primary shield[1)].

The efficiency capacity of the neutron-proton detection method applied to plasma diagnostics is considerably higher than an only-proton detection method (8.5). We also gain reliability as the coincidence method is an excellent method for the selection of relevant data out of a flow of irrelevant information.

8.1 Total efficiency

The number of events registered by the spectrometer is given by

$$R = \Phi \varepsilon \tag{8.1}$$

where

Φ = the neutron flux density at the foil and

ε = the total efficiency, see 2.1.

The efficiency can be written as a product of three factors, the scattering probability per square cm times the theoretical probability for coincidences times a loss factor.

$$\varepsilon = S_f \varepsilon_{pn} \Lambda \tag{8.2}$$

The scattering probability is given by

1) See chapter 9, »Neutron beam shaping.», page 131.

$$S_f = \sigma_s(E_o)\, N_f d_f \rho_f \tag{8.3}$$

where

N_f = number of scattering nuclei per area unit,

d_f = foil thickness,

ϱ_f = foil density, 0 93 g/cm^3 for polyethylene,

σ_s = scattering cross section, equation 4.3.

The scattering probability for 14 MeV neutrons in polyethylene is 59.6x10^{-6} scatterings per mg/cm^2, which gives a scattering probability of 71.5x10^{-6} in TANSY.

The theoretical probability for proton-neutron coincidences is given by

$$\varepsilon_{pn} = A_f \int_E P_p(E)\, S_n(E)\, dE \tag{8.4}$$

A_f = the foil area

P_p is given by equation 6.9,

S_n is given by equation 7.2.

The loss factor A is the relative number of losses of neutron-proton coincidences. The losses are caused by straggling (paragraph 5.3), absorption and scattering of neutrons in vacuum chamber walls, air etc, and by non-existent parts of the neutron-detector (paragraph 8.3).

The resonance peak of Li (figure 50) gives an energy selection of neutron-proton coincidences, see figure 55. The peak is thin and, therefore, only a narrow band of energies around 240 keV is used. The highest detection probability occurs when the mean angle is matching the resonance energy. In the example given in figure 55 we have a maximum probability of 1.8x10^{-3} at a foil proton-detector distance of 32 cm.

About ten times higher neutron-proton coincidence probability can be achieved by using a 2 cm thick plastic scintillator instead of Li-glass, see figure 56. Here, the 0.5 MeV bias gives a detection probability, which decreases at low neutron-energies, i.e. large distances[1]. The energy spread increases with decreasing distance, so more high-energy neutrons will be included. These will increase the efficiency. However, the detection sensitivity reaches a maximum and then it decreases with increasing neutron energy, see figure 52. Therefore, it is possible to find a maximum efficiency for the coincidence detection.

The proton detection probability and the neutron detection sensitivity are folded together in an integration, equation 8.4. It is not possible to get an exact solution from a multiplication of two factors, the effects are not separable. However, for large foil to proton-detector distances we may use an approximation such as equation 6.16 for the proton-detection and multiply this with the neutron-sensitivity from 7.2 in order to construct an approximate expression for equation 8.3. Equation 6.16 does not take the angle dependency into account. Including this we get

$$\varepsilon_{pn} \approx \frac{\pi (R_f - R_i)^2 \cos^2(\theta)}{4\pi D^2} \pi R_d^2 \cos(\theta) \cdot 4\cos(\theta)\, S_n \tag{8.5}$$

[1] Compare with the figures 44 and 52.

which is inserted into equation 8.2. Thus we have

$$\varepsilon \approx \Lambda S_f(E_o)\, S_n(E_b, E(\theta)) \frac{2W}{D} \pi R_d^2 \, tg(\theta) \cos^4(\theta) \quad (8.6)$$

where

$$W = R_f - R_i = \text{the foil width.}$$

For a given angle, the efficiency is proportional to the ratio of the width to the distance and to the proton detector area. The angle and bias dependencies, according to equation 8.6, are illustrated in figure 57. It shows that the bias gives a large influence on the efficiency. At 15 degrees the 0.5 MeV bias decreases the efficiency by more than a factor of two. Actually, there is a coupling between the bias and the lowest usable angle. A small angle can only be used together with a low bias.

It must be emphasized that equation 8.6 does not include the energy spread. It is a point model and, therefore, it will give erroneous results if any part of the proton energy distribution is higher than the proton energy defined by the bias. The proton energy limits are defined in equation 6.11.

Equation 8.6 indicates that the efficiency is independent of the foil to proton-detector distance if the foil width over the distance is kept constant. This statement is confirmed, for large distances, by the results of a calculation given account for in figure 58. The asymptotic value is reached at about 30 cm for a width-over-distance ratio of 1/15. The figure shows that the proton-neutron coincidence spectrum at this distance is characterized by an almost symmetrical, well peaked distribution. This means that all parts of the neutron detector are well used.

Equation 8.6 may be used for an estimate of how the total efficiency depends on the initial neutron energy. An inspection of the equation shows for a thin neutron detector an efficiency, which is proportional to the squared scattering cross-section. The efficiency according to equation 8.6 is drawn for TANSY in figure 59. A bias of 0.5 MeV gives an almost constant response. However, the results in figure 59 are obtained using a point model. Therefore, the results should be confirmed by experiments.

8.2 Resolution

We will analyse the resolution by using the concept of the squared sum. According to this the resolution is given by

$$\Delta E_o = \sqrt{\sum_i \left(\frac{\partial E_o}{\partial x_i}\right)^2 (\Delta x_i)^2} = \sqrt{\sum_i Q_i^2} \quad (8.7)$$

where Δx is the fwhm-value of the parameters[1]. The initial-neutron energy is a function of the parameters as given by equation 4.6[2].

The most important sources of errors are:

---

1) The equation can be used for standard deviations as well as for fwhm-values.

2) See paragraph 4.2,»The measurement method.», on page 36.

a. slowing down of the protons in the foil,

b. resolution of the proton-energy measurement,

c. variation of the flight-path-length of the scattered neutron, and

d. resolution of the time measurement.

The first two factors are treated together,

$$Q_{ab}=\Delta E_p\left(1+\frac{D(tg\,\theta)^{3/2}}{L\cos(\theta)}\right) \tag{8.8}$$

ΔE_p is the square root of the squared sum of the proton energy loss in the foil and the resolution of the proton energy measurement[1]. The variation of the measured energy is well represented by a Gaussian distribution. However, that is not true for the energy loss, which gives a distribution as illustrated in figure 36. For TANSY, we will use the fwhm-values 35 keV for the energy measurement and 46 keV for the energy loss. Together, these give 57.8 keV, a value which increases somewhat with the angle, see figure 60.

The variation of the flight-path-length gives an error in the energy-determination of the scattered neutron,

$$Q_c=\frac{2\Delta L}{L}E_o\sin^2(\theta) \tag{8.9}$$

The length uncertainty for small angles is the sum of the neutron detector thickness and the foil width. One may argue about the sum, whether it should be the arithmetic sum or the squared sum. We have taken a pessimistic approach and used the arithmetic sum. An additional path length variation is given by the fact that the foil is annular. Therefore, the scattering does not occur in the centre of the neutron-detector ring. However, a Monte Carlo calculation, figure 61, has shown that most of the neutrons travel along the radius. For TANSY the deviation for the askewest flight paths is estimated at less than 1 mm. Therefore, it is neglected. Equation 8.9 is illustrated in figure 62. We get a value of 75 keV for TANSY.

The last part comes from the uncertainties in the time measurement. It is given by

$$Q_d=2E\,\frac{c\Delta\tau}{L}\sqrt{\frac{2E_o}{m}}\,\sin^3(\theta) \tag{8.10}$$

It increases faster with angle than the flight path error. However, the coefficient is lower as can be seen from figure 63. The value for TANSY is 25 keV.

The total energy-resolution is drawn in figure 64. The dominating parts are from the proton energy measurement and the proton energy loss in the foil at low angles and the flight path length at larger angles.

8.3 The resolution-efficiency dilemma

The main parameters determining the efficiency according to equation 8.6 are

[1] See paragraph 5.2,»Energy straggling.», and 6.5, »The proton detector.».

a. the mean scattering angle,

b. the foil thickness,

c. the neutron detector thickness,

d. the bias,

e. the foil width,

f. the foil to proton-detector distance, and

g. the proton-detector radius.

Most of the parameters appear also in the calculation of the resolution, equation 8.7. One parameter only, the time measurement uncertainty, affects only the resolution.

We are searching for those parameter combinations, which give a resolution of 100 keV or less and an efficiency higher than 10^{-6}. Several solutions exist and other arguments such as background and mechanical design considerations should be taken into account for the final choice of parameters.

One approach is demonstrated in figure 65. It shows the resolution and efficiency for different positions of the neutron- and the proton-detector. The figure indicates that long foil to neutron-detector distances are needed in order to get the wanted resolution.

Another approach is to keep the resolution and the efficiency constant at the given values. Then, a variation of one parameter must be compensated by a variation of another parameter. Figure 66 shows that for each proton-detector position there is a mean foil radius giving a minimum neutron-detector distance. This minimum is connected to the angle. Figure 67 shows that an optimum angle can be found around 13 degrees.

The optimal foil thickness is around 1 mg/cm^2. Figure 68 shows that one should not use more than 2 mg/cm^2.

The conclusion so far is: a foil thickness of about 1 mg/cm^2 and an angle of 15 degrees. This gives some space for the energy spread not taken into account in the formulae.

Equation 8.6 says that the efficiency is independent of the proton detector distance if the foil width is kept proportional to the distance. Then, the resolution would decrease with decreasing distance and one may come to the conclusion that it would be favourable to choose small dimensions. However, the point model used does not take the energy spread into account. The equation indicates that a width over distance ratio of 1/15 gives a sufficient efficiency. The coincidence spectrum for this ratio is shown in figure 58. The spectra are detoriated for small distances and the efficiency is lower than predicted by the asymptotic formula, equation 8.6. A proper choice from the figure is a distance of 30 cm. Consequently, the foil width is 2 cm.

The neutron detector thickness is determined to 2 cm. A 1 cm thick detector would give half the efficiency with a rather small gain in the resolution.

The width of the neutron detector is given by the energy limits, the endpoints of the energy distribution in figure 58. However, we have recommended a somewhat smaller width, 8 cm. The tails of the distribution will then be cut. The loss of coincidences will be small but the background sensitivity will decrease in proportion to the amount of scintillator removed.

Finally, the foil to neutron-detector distance is determined to 100 cm, see figure 69, and the foil thickness is increased to 1.24 mg/cm^2 in order to compensate for angular straggling losses and the removed part of the neutron detector.

The bias is an important parameter. In the discussion above it has implicitly determined the angle. We have used a high value of the bias in order to keep the gamma background sensitivity as low as possible. In the final instrument the angle is fixed but the bias can be adjusted in order to find the proper value. From figure 57 we find that an efficiency gain of two is possible provided the background allows us to do so. However, note that the response curve will be changed, see figure 59.

The found parameters are collected in chapter 1.3, »TANSY, a reference design.». The efficiencies and sensitivities emerging from this parameter set are given in table 2.

Table 2. Efficiency parameters.

Symbol	Value	Dim.	Remark
ε	1.05×10^{-6}	cm^2	Detected events per $n/cm^2,s$ at the foil.
S_f	71.5×10^{-6}	-	Neutron-proton scatterings per cm^2,s and $(n/cm^2,s)$.
S_p	9.72×10^{-4}	-	Detected protons per scattering.
S_n	0.168	-	Detected neutrons per neutron passing the neutron detector.
ε_{pn}	1.63×10^{-2}	cm^2	Coincidences per scattering/cm^2.
S_{pn}	1.63×10^{-4}	-	Coincidences per scattering.
Λ	0.9	-	Loss factor.
η	0.0625	-	Total number of scattered neutrons passing the neutron detector per scattering.
S_{nd}	0.010	-	Total number of neutrons detected per scattering.

8.4 The dynamic range

It is stipulated that the instrument should work in the energy range 12 to 16 MeV. From equation 4.5[1)], we can calculate the corresponding flight times. The result is given in figure 70. The proton flight-time ranges from 5.6 to 6.7 nanoseconds and the neutron flight-time ranges from 64 to 101 nanoseconds. However, the measured quantities are the flight-time difference and the proton energy. These quantities are illustrated in figure 71, which shows a time ranging from 61 to 95 nanoseconds and an energy range from 11.2 to 15.4 MeV. We add a few nanoseconds for transients and get a coincidence detection ranging from 50 to 100 nanoseconds with a midpoint value at 75 nanoseconds.

The main electronic units needed are an analog-to-digital converter (ADC), a time-to-digital converter (TDC), a storage unit, and some interconnecting logic modules. One possible electronic principle-diagram is shown in figure 54.

1) Paragraph 4.2, »The measurement method.», on page 36.

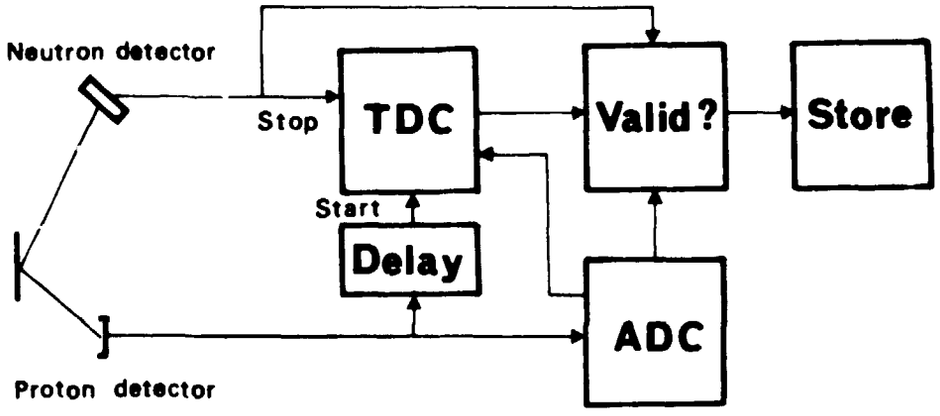

Figure 54. Electronic first principle diagram.

Table 3. Measurement timing.

Time, ns	Event
-6.7 to -5.6	Neutron scattering.
0	Proton recognized.
	Start of cycle.
	Start of ADC.
50	Coincidence possible.
	Start of TDC.
75	Middle of coincidence interval.
100	End of coincidence interval.
100 to 6000	Conversion active.
6000 to 10000	Validation and storage.
10000	End of measurement cycle.

The number of scattering events per time unit in the foil is given by[1)]

$$\dot{n} = S_f \Phi A_f \tag{8.11}$$

We assume that the system is non-paralysable, i.e. it is unaffected by the input during the cycle time. Then, the start rate is given by

$$\dot{n}_s = (S_p \dot{n} + \dot{B}_p) C \tag{8.12}$$

1) See equations 8.1 and 8.2 and table 4.

where

S_p is given by equation 6.15,

$\dot{B}_p$ is the background rate in the proton detector, and

C is the deadtime correction.

The background is partly caused by the neutrons and, therefore, it is related to the scattering rate. However, it is difficult to get a value on the relation factor at this point of the work. The most important part is the neutron-scattering from the collimator walls, the calculation of which is not a part of this work[1].

The deadtime correction is the commonly used correction for non-paralysable systems, i.e.

$$C = (1 + (S_p \dot{n} + \dot{B}_p)\,\tau_c)^{-1} \tag{8.13}$$

where τ_c is the cycle time.

The rate of the true coincidences, the quantity we want to measure, depends on the neutron flight-time spectrum. For this estimate of the dynamic properties we assume that all coincidence neutrons arrive at the midpoint of the time window defined by the TDC. Furthermore, the TDC is assumed to handle only one event for each cycle. Therefore, it might be blocked by a background signal prior to the arrival of the neutron. Thus, the coincidence rate will be given by

$$\dot{n}_c = \dot{n} C S_p S_n \Lambda\, e^{-\frac{\dot{B}_{nd} T_w}{2}} \tag{8.14}$$

$$\dot{B}_{nd} = S_{nd} \dot{n} + \dot{B}_n \tag{8.15}$$

where

T_w is the time window defined by the TDC

$\dot{B}_{nd}$ is the background rate in the neutron detector[2]

S_n is a mean value of the neutron sensitivity, eq. 7.2,

S_{nd} is the total neutron detection sensitivity.

The total sensitivity of the neutron detector for all neutrons scattered by the foil can be estimated by assuming that all scattering occurs in the foil centre[3]. Thus, the sensitivity is given by the relative energy range calculated from the angle range occupied by the neutron detector ring. Or, approximately, using the energy spread defined in paragraph 6.3, page 78

$$S_{nd} = \eta S_n \tag{8.16}$$

The false coincidences appear as an almost constant distribution in the coincidence spectrum. We divide them into two parts, those arriving before and those arriving after the true coincidences. Thus, the false coincidences may be written

---

1) However, see chapter 9, »Neutron beam shaping.».

2) See paragraph 7.4, »Background considerations.», in page 92.

3) An unreachable point in the middle of the collimator.

$$\dot{n}_f = \dot{n} C S_p \left[\left(1 - e^{-\frac{\dot{B}_{nd} T_w}{2}}\right) + e^{-\frac{\dot{B}_{nd} T_w}{2}} (1 - S_n \Lambda) \cdot \right.$$

$$\left. \cdot \left(1 - e^{-\frac{\dot{B}_{nd} T_w}{2}}\right) \right] + \dot{B}_p C \left(1 - e^{-\dot{B}_{nd} T_w}\right) \tag{8.17}$$

which can be simplified to

$$\dot{n}_f = \dot{n}_s \left(1 - e^{-\dot{B}_{nd} T_w}\right) - \dot{n}_c \left(1 - e^{-\frac{\dot{B}_{nd} T_w}{2}}\right) \tag{8.18}$$

The beauty of the coincidence method is, as can be seen from equation 8.15, that we pick up the relevant information from a sea of background events. However, care must be taken that the channels are not overloaded. The limits from the data collection point of view can be expressed by the three criteria:

1. a start frequency less than 10% of the inverse cycle time,
2. a neutron detection signal frequency less than 10% of the inverse window opening time, and
3. a false coincidence detection rate less than 10% of the true coincidence detection rate.

The three criteria can be written

$$T_c (\dot{B}_p + \dot{n} S_p) < 0.1 \tag{8.19}$$

$$T_w (\dot{B}_n + \dot{n} S_{nd}) < 0.1 \tag{8.20}$$

$$\frac{\dot{n}_f}{\dot{n}_c} \approx T_w \dot{B}_{nd} \left(\frac{\dot{n}_s}{\dot{n}_c} - \frac{1}{2} \right) < 0.1 \tag{8.21}$$

The first criterion is the limiting one if the background is zero. For TANSY it gives a scattering rate less than 10^7 s^{-1}. It corresponds to 1.4×10^9 $n/cm^2,s$ (eq. 8.11). The start rate is 10,000 s^{-1} and the coincidence rate 1300 s^{-1}. The ratio between false and true coincidences is 0.04, i.e. criterion 3 is fulfilled. Actually, it gives room for some background. The maximal signal rate from criterion 3 is 2.8×10^5. Of these 1.1×10^5 are used by the neutrons. Therefore, the background limit is 1.7×10^5. In paragraph 7.4 we got a background rate of 0.86×10^6, five times higher than can be accepted. It is possible to work with this background but it is highly recommendable to decrease it by using shielding around the neutron detector.

The dynamics of the instrument is illustrated in four diagrams, 72 to 75. The first shows the background rates when no background is present. It shows that the instrument is usable from zero up to about 10^7 scattering events per second, where the false coincidences begin to appear and the correction for the system cycle time sets in.

The background effects are illustrated in figure 73. The false coincidences dominate both at low and high frequencies. A small band ranging about one decade is usable. This dynamic range is small and other means should be available for the control of the intensity, see chapter 9. In practice, the low frequency part is anyhow not usable because of the short run time of a shot in JET. The background effects are further illustrated in figure 74 and 75.

Table 4. Rates of events at 10^9 n./cm^2,s.

Rate	Text
10^9	Neutron flux density at the foil, n/cm^2,s.
10^{11}	Number of incoming neutrons, 1/s.
7.15×10^6	Scattered neutrons in the foil, 1/s.
6950	Detected protons, start rate, 1/s.
1170	Number of coincidences, 1/s.
1050	Detected number of coincidences, 1/s.

8.5 Proton-neutron or only-proton detection?

Several times in the course of this work the question of the relevancy of the neutron-proton coincidence method has crossed our minds. Is there any meaning with the expensive complications created by the neutron detection?

In paragraph 6.4, using equation 6.17, we found that it is possible to make an only-proton detector with the same resolution as the neutron-proton one. However, the sensitivity was ten times lower. Including the sensitivity of the neutron detector we find that neutron-proton detection is twice as efficient as the only-proton detection for the same energy resolution and foil dimensions. That is not much. It means that a neutron-proton system is equivalent to two only-proton systems or one with twice the area of the foil and the proton detector.

One great advantage of the neutron-proton method is the coincidence selection, which is an efficient identification of the neutron scattering events. An example is given in figure 73. The start rate is equivalent to the only-proton method. The background deteriorates the relation between the proton-detection and the intensity, while the coincidences are almost unaffected.

Another point, however, is the divergence of the incoming beam. The neutron-proton method is insensitive to a small divergence. For the only-proton detection method we have

$$\Delta E = 2E_o \sin(\theta)\cos(\theta)\Delta\theta \tag{8.22}$$

The uncertainty depends on the angle. For a divergence of one degree we have 65 keV at 5, 167 keV at 10, and 244 keV at 15 degrees mean scattering angle. The divergence goes from 0.4 to 2.7 degrees depending on the aperture. Using a 10 degrees mean scattering angle will give an energy spread ranging from 67 to 450 keV. Therefore, only the smallest openings are allowed. From figure 14 we find that this corresponds to a factor of ten in the neutron flux density.

The conclusion is that the proton-neutron coincidence method, as applied to plasma diagnostics, is more reliable and has a capacity of twenty times the capacity of the only-proton method.

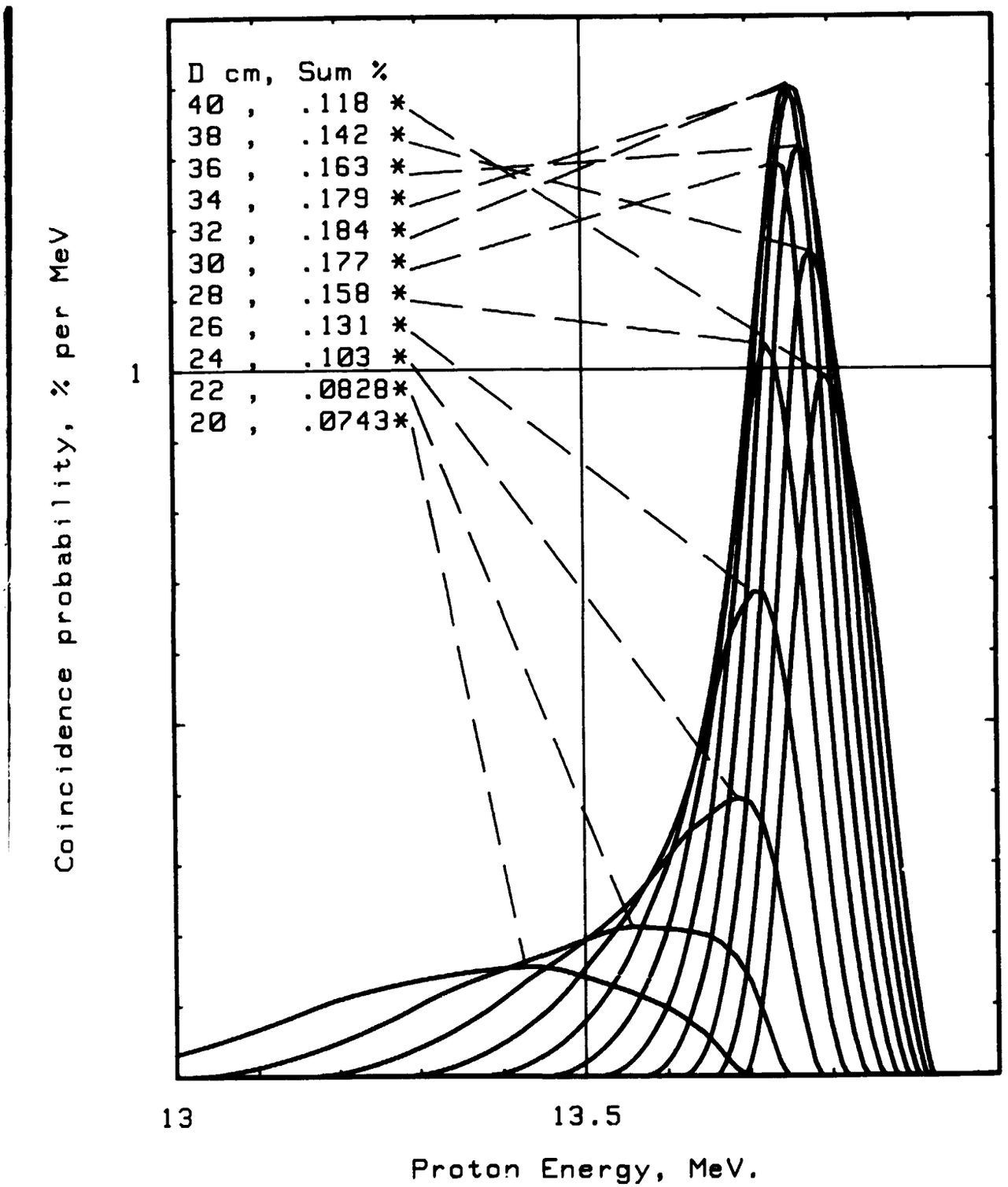

Figure 55. Li-glass coincidence probability.

The peak in the lithium cross-section gives an energy-selection of coincidences. The peak is narrow, only a small part of the energy-range is used. Compare with figure 44. Foil radii: outer 5 cm, inner 4 cm. Neutron detector: 2 cm NE912.

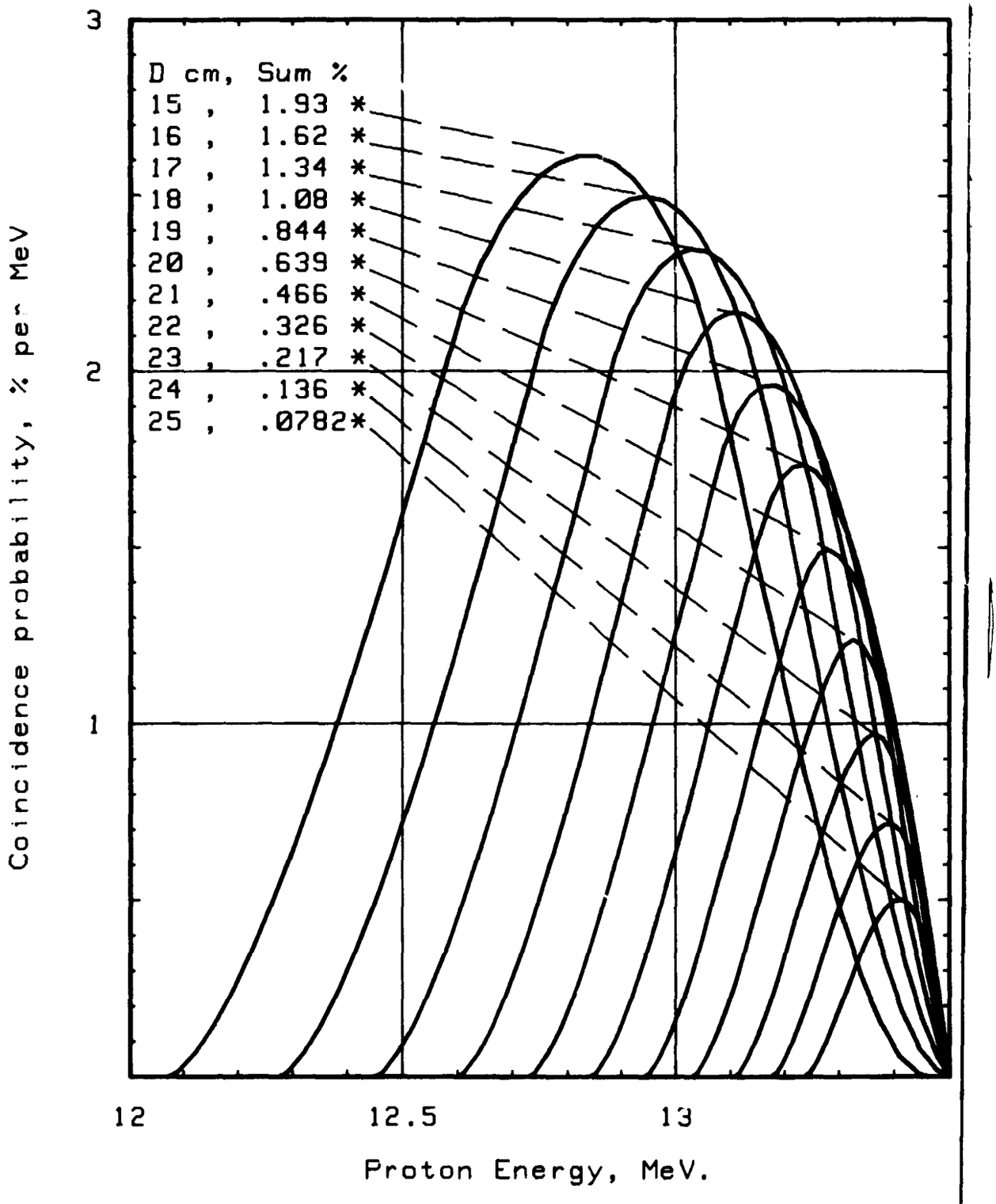

Figure 56. Pilot U coincidence probability.

The 0.5 MeV bias gives a cut-off at 13.5 MeV. Foil radii: inner 4 cm and outer 5 cm. Neutron detector: 2 cm Pilot U.

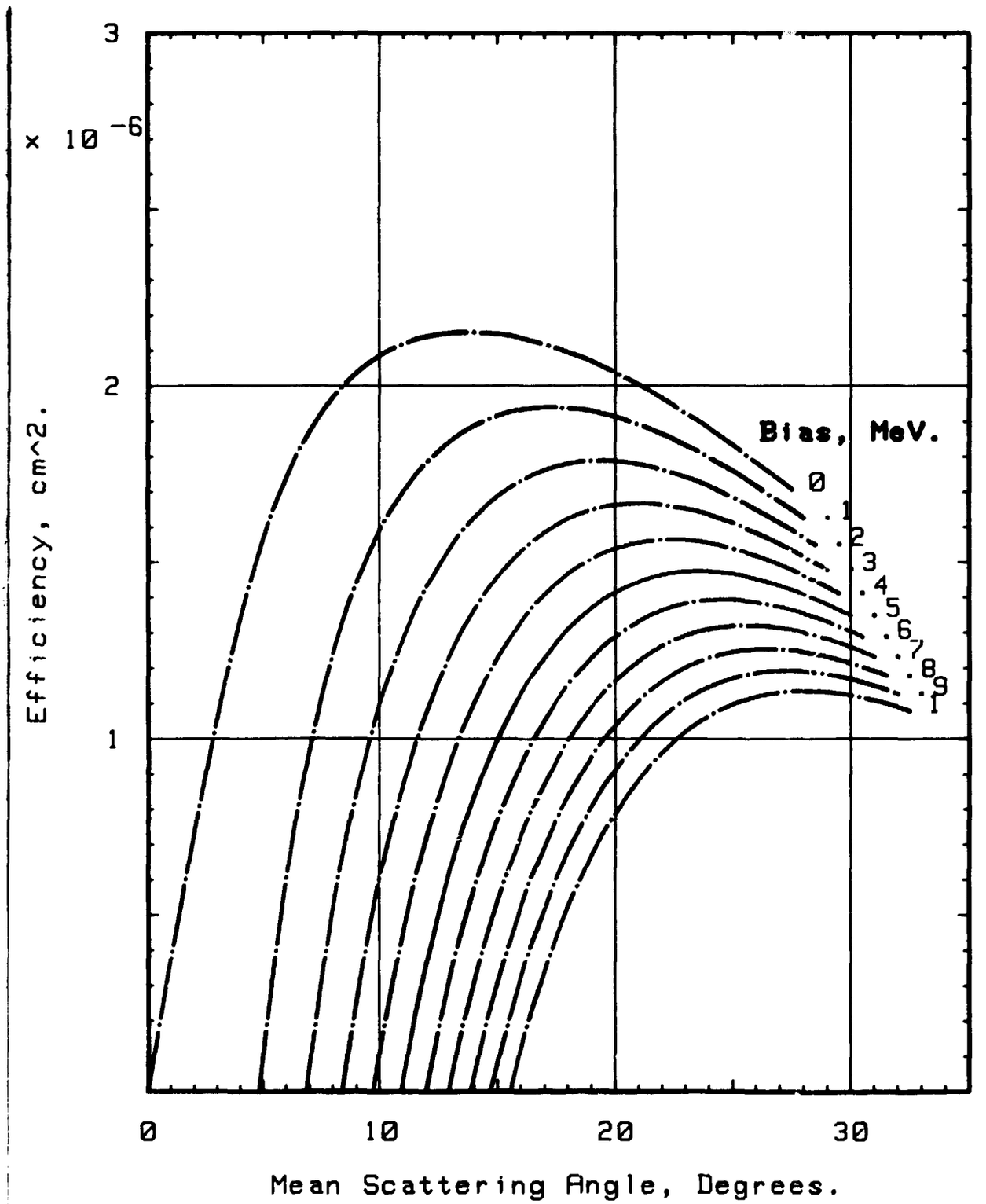

Figure 57. Efficiency for different angles.

The total efficiency for TANSY according to equation 8.5. The efficiency is proportional to the ratio of the foil width to the foil to proton-detector distance, here set to 1/15.

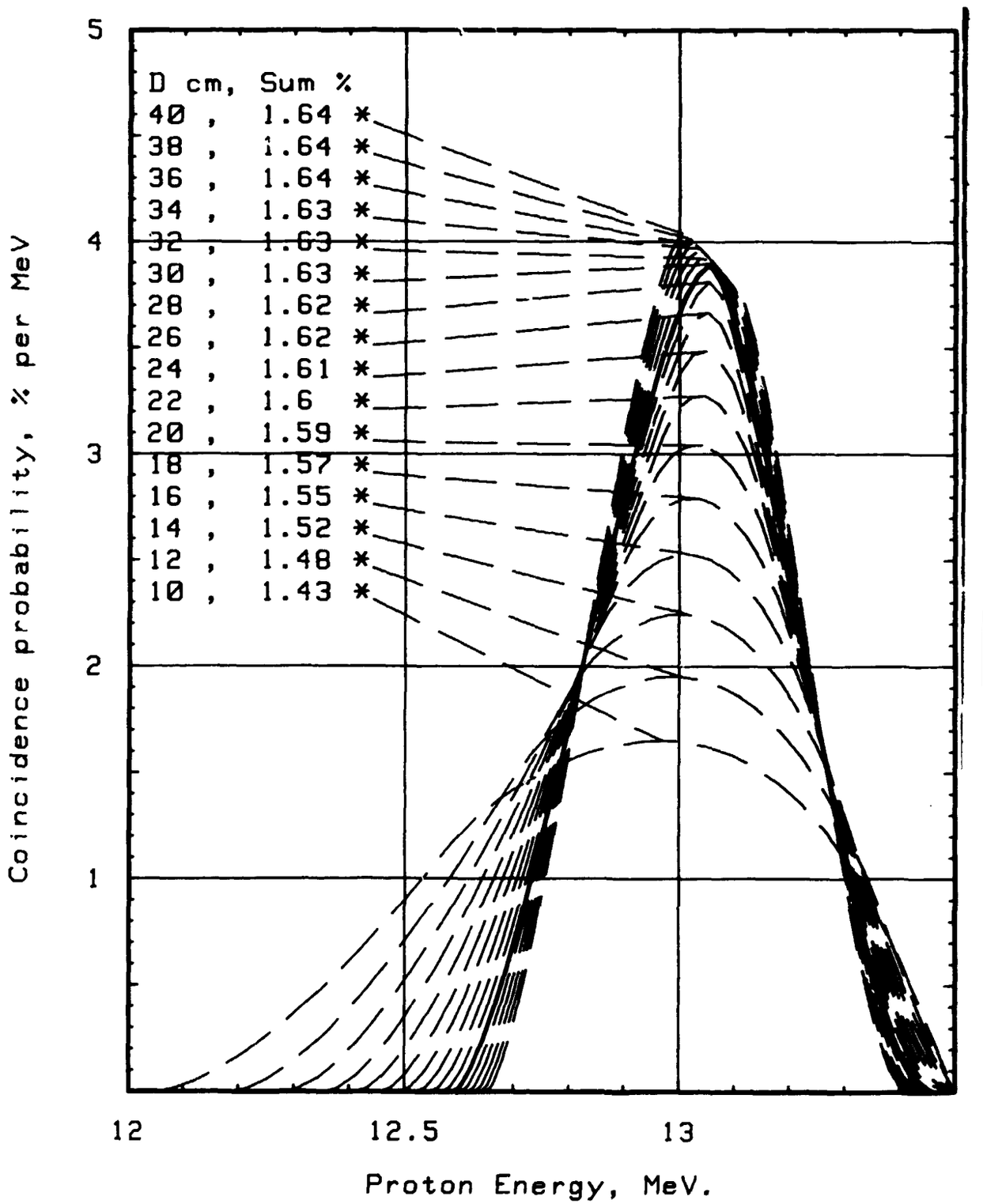

Figure 58. Coincidence probability in TANSY.

The parameters in TANSY are chosen in order to give symmetric energy-distributions of the detected coincidences. The somewhat smaller neutron detector will cut the tails of the distribution at 12.72 and 13.30 MeV.

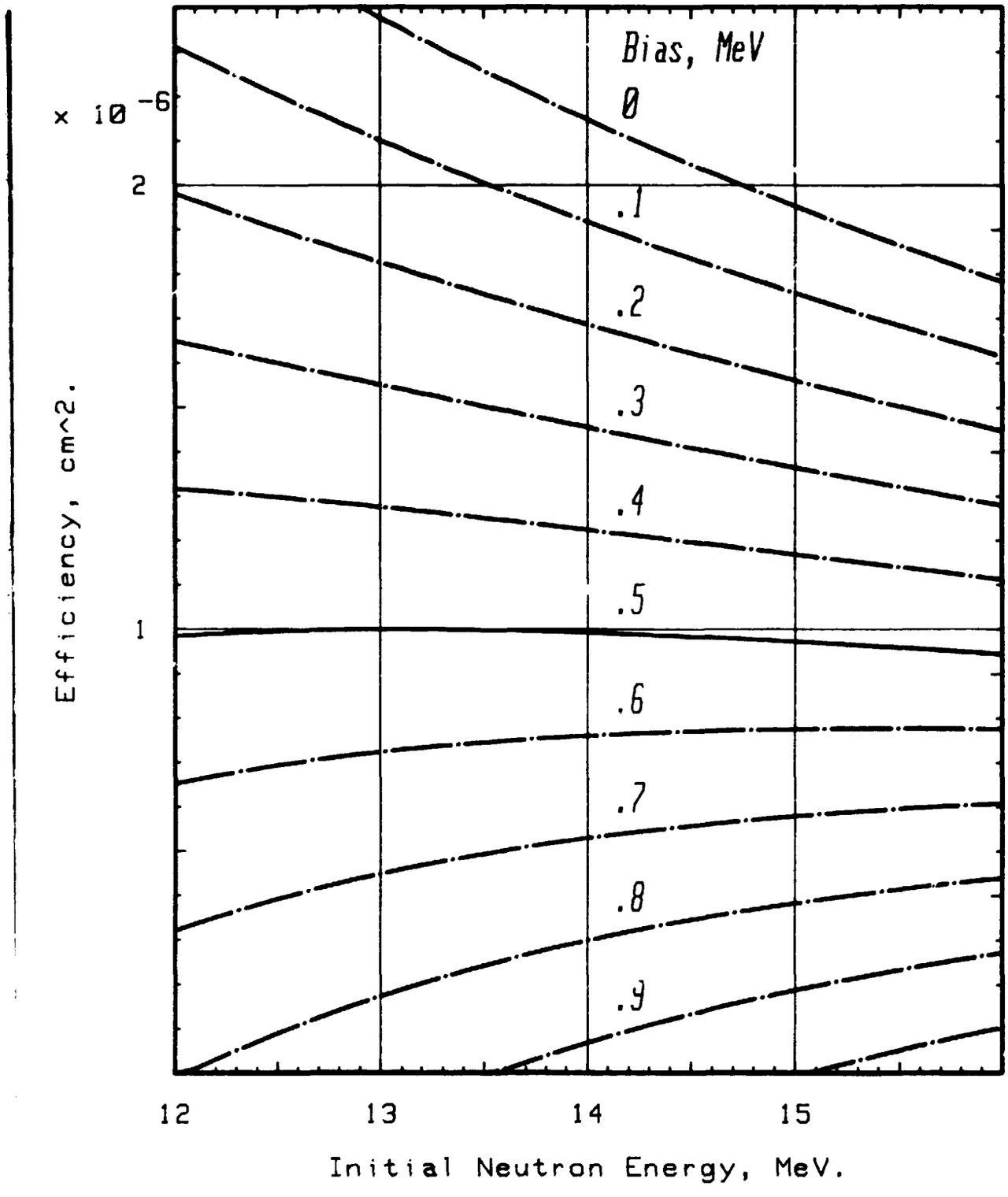

Figure 59. The response curve.

Efficiency as a function of energy of the initial-neutron energy for TANSY.

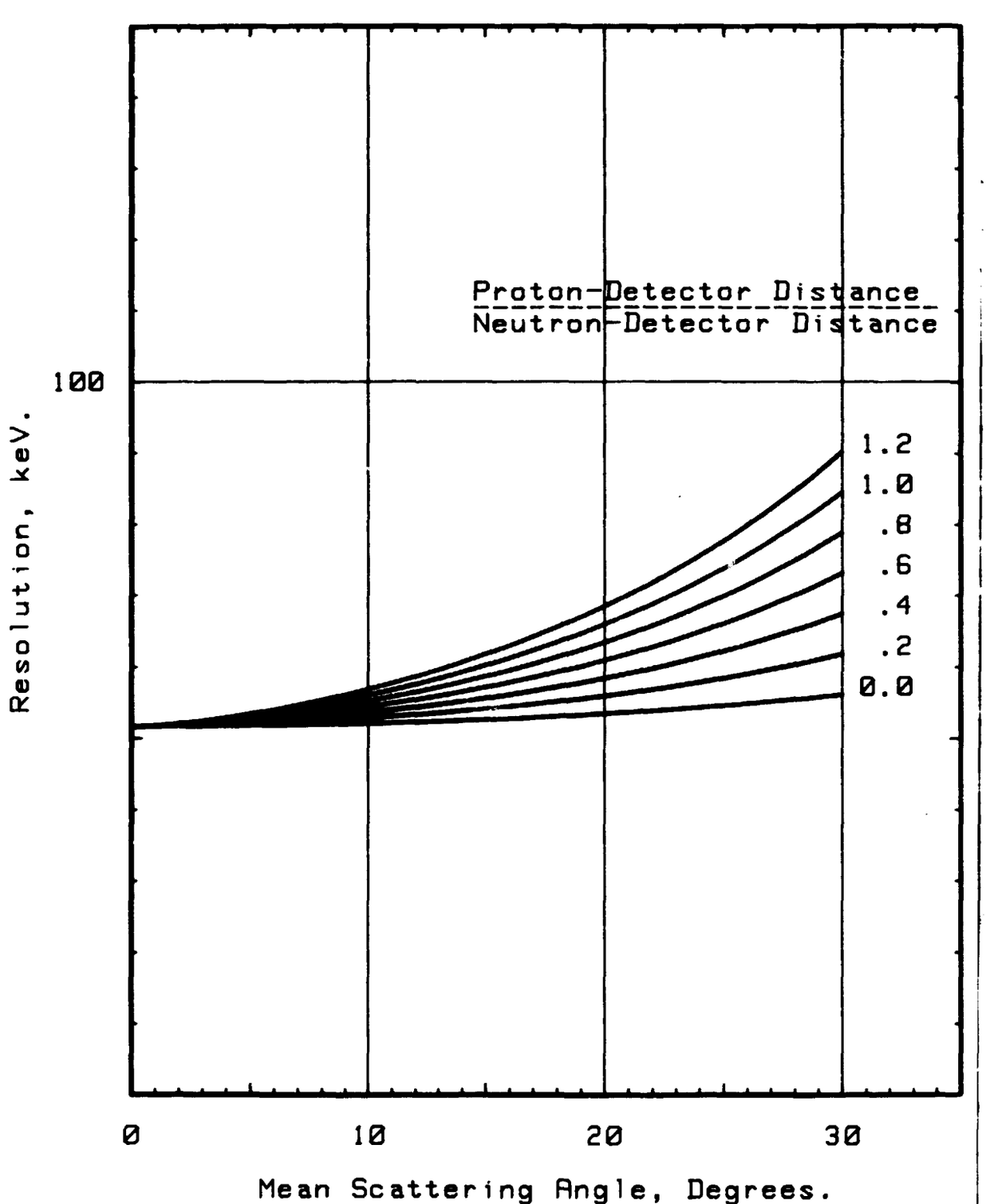

Figure 60. Foil and proton-detector resolution.

The energy-uncertainty due to slowing down in the foil and the proton-detector energy resolution, equation 8.8.

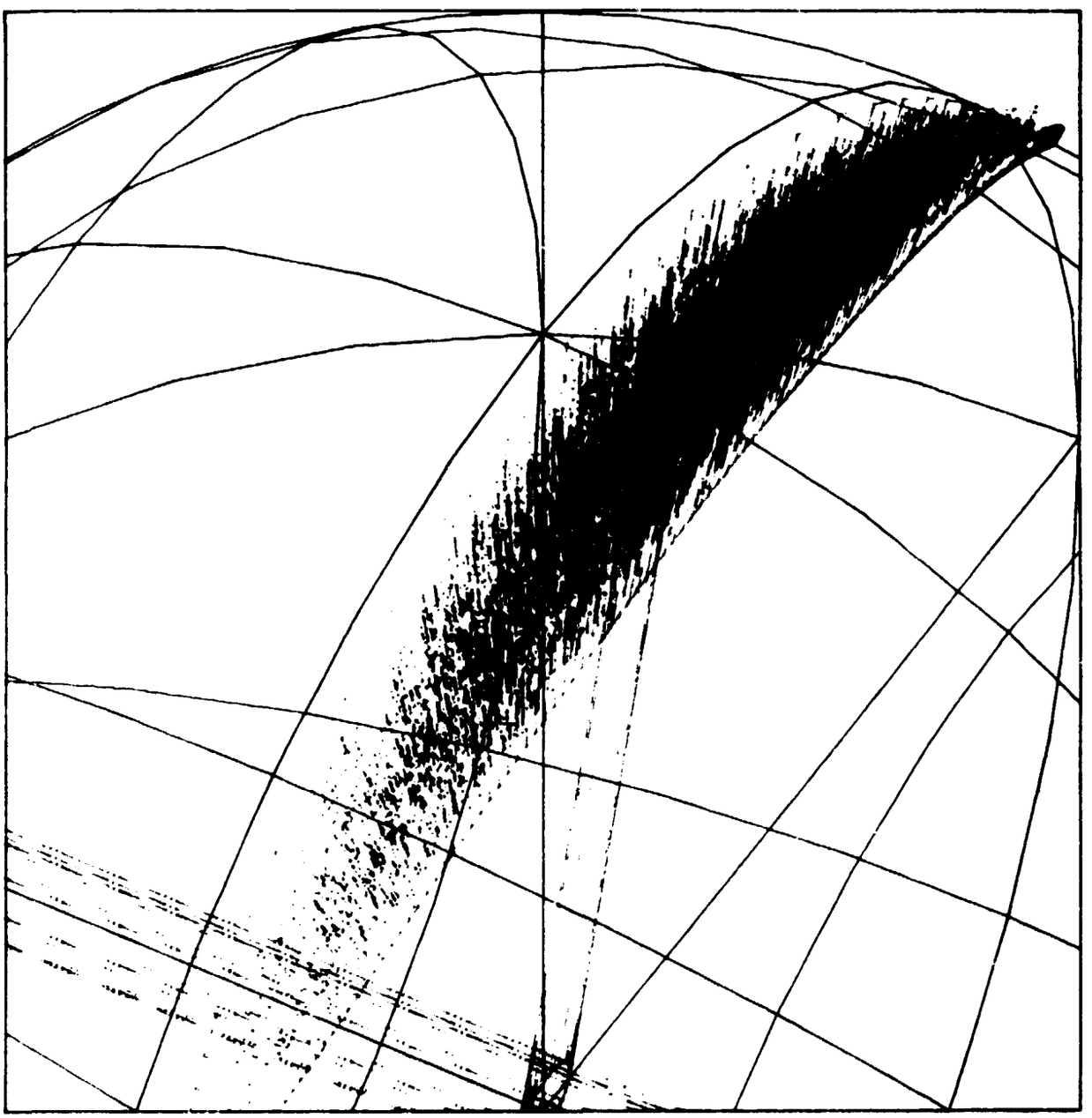

Figure 61. Impacts of coincidence-neutrons.

A Monte Carlo calculation showing the neutron impact positions in the neutron-detector for coincidences from a circular foil and a circular proton detector. Compare with figure 29.

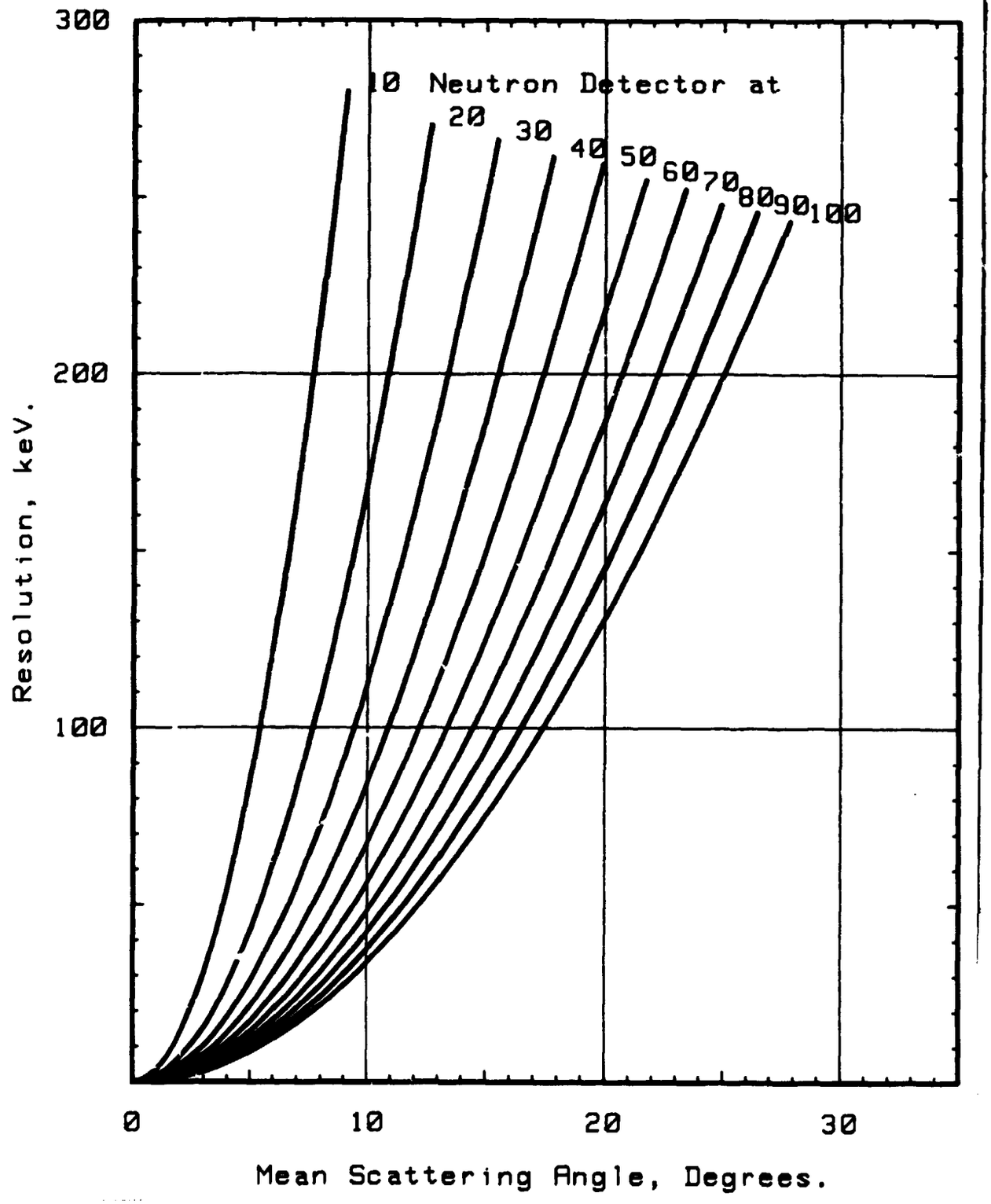

Figure 62. Flight-path energy resolution.

The energy uncertainty due to a flight path variation of 4 cm, 2 cm for the foil and 2 cm for the neutron-detector. The resolution is proportional to the flight path variation. The parameter, the distance between the foil and the neutron-detector, is given in cm.

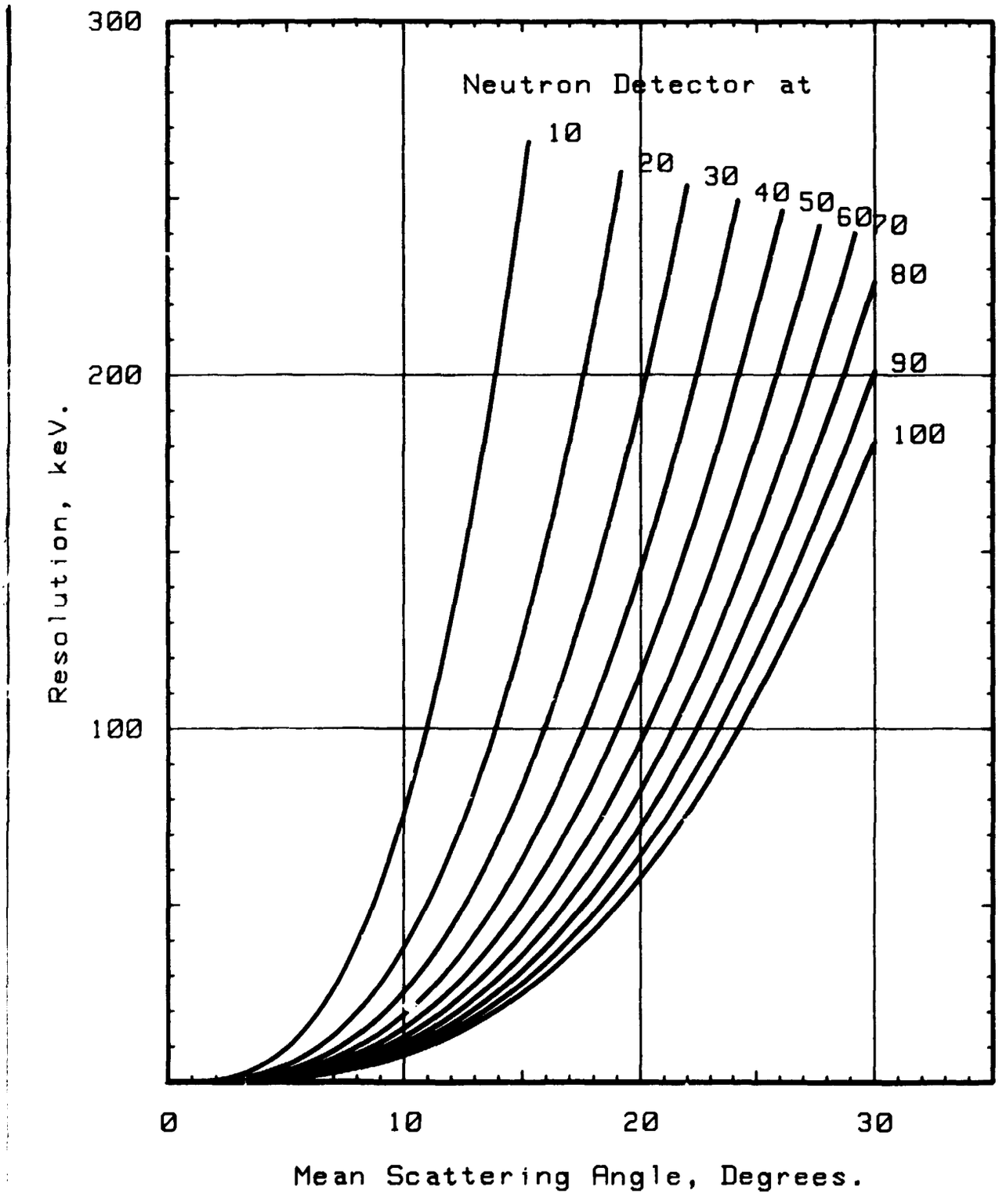

Figure 63. Time measurement energy resolution.

The energy uncertainty due to a time measurement resolution of 1 ns. The parameter, the distance between the foil and the neutron-detector, is given in cm.

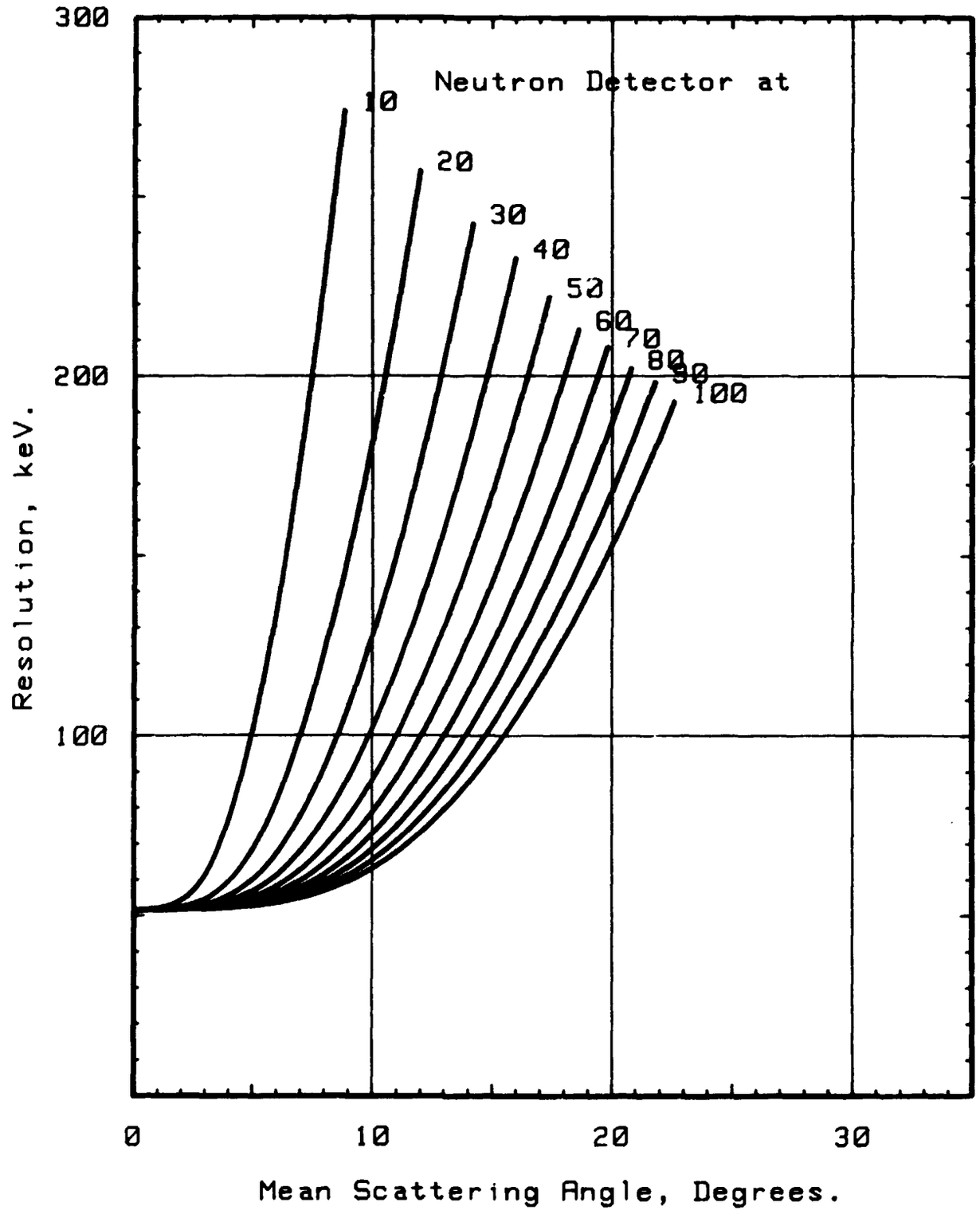

Figure 64. Total energy resolution.

The slowing down energy variation is 46 keV. The proton energy resolution is 35 kev. The flight path of the neutrons is 100 cm and it has a variation of 4 cm. The proton-detector to foil distance is 30 cm and the time resolution is 1 ns. The parameter, the distance between the foil and the neutron-detector, is given in cm.

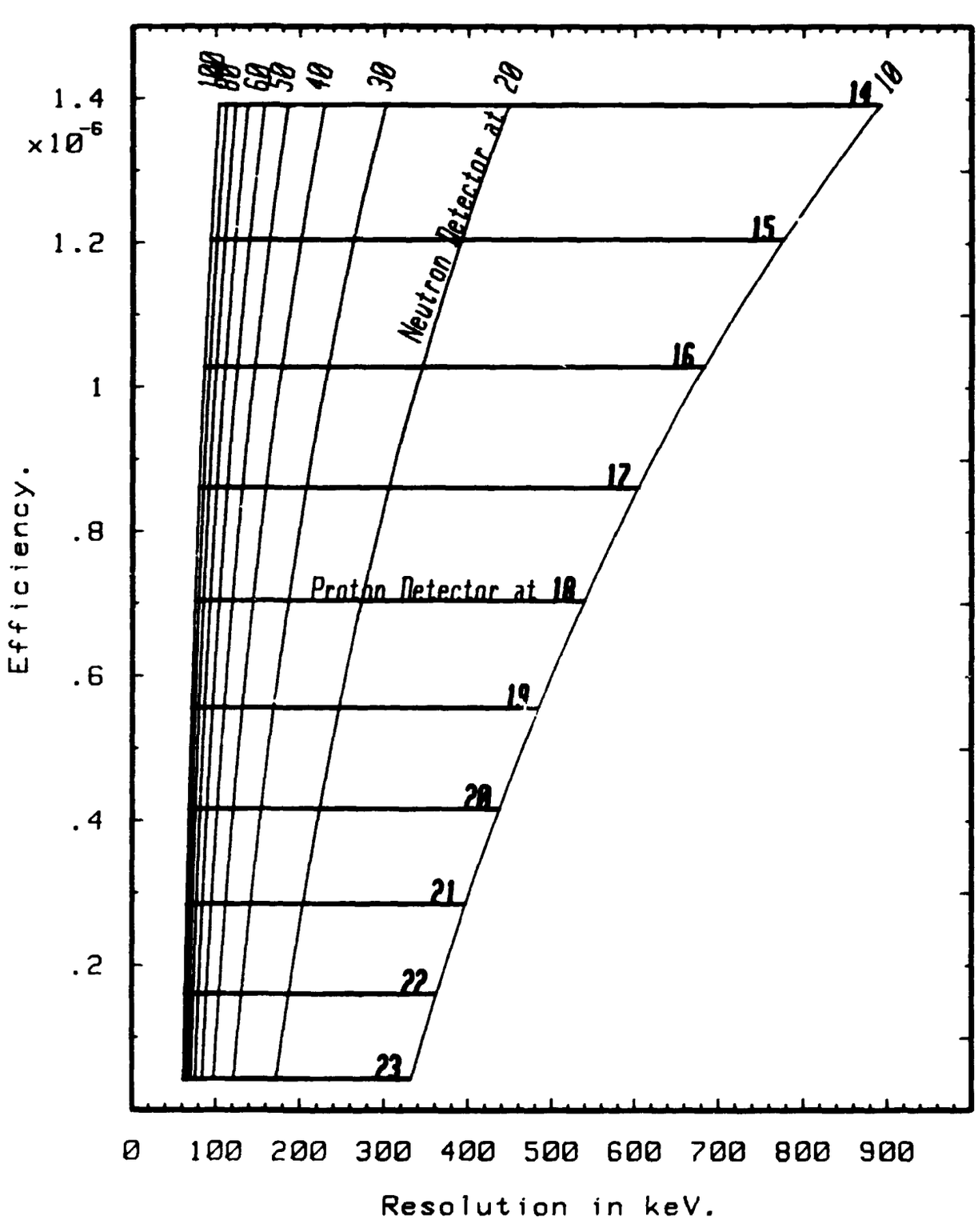

Figure 65. Efficiency-resolution chart.

Resolution: foil 46 keV, proton-detector 35 keV. Detector radius 1 cm, foil radii 4 and 5 cm. Bias 0.5 MeV in a 2 cm Pilot U neutron detector. Distance. in cm.

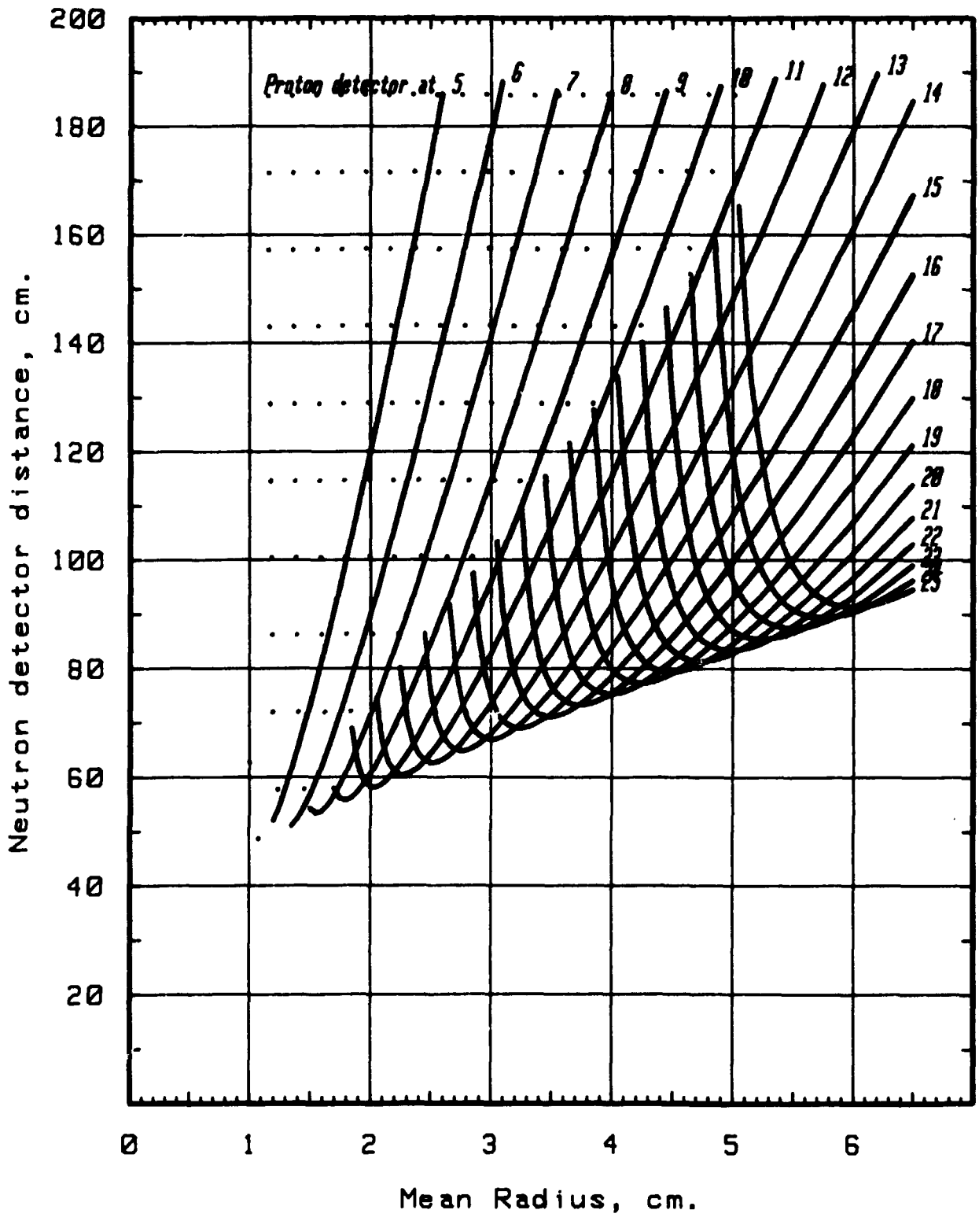

Figure 66. Neutron-detector distance versus foil radius.

Resolution, foil 48 keV, proton detector 50 keV, time 1 ns. Detector radius 1 cm. Total resolution 100 keV. Efficiency 10^{-6} cm^2. Bias 0.3 MeV in a 2 cm thick Pilot U neutron detector. Distances in cm.

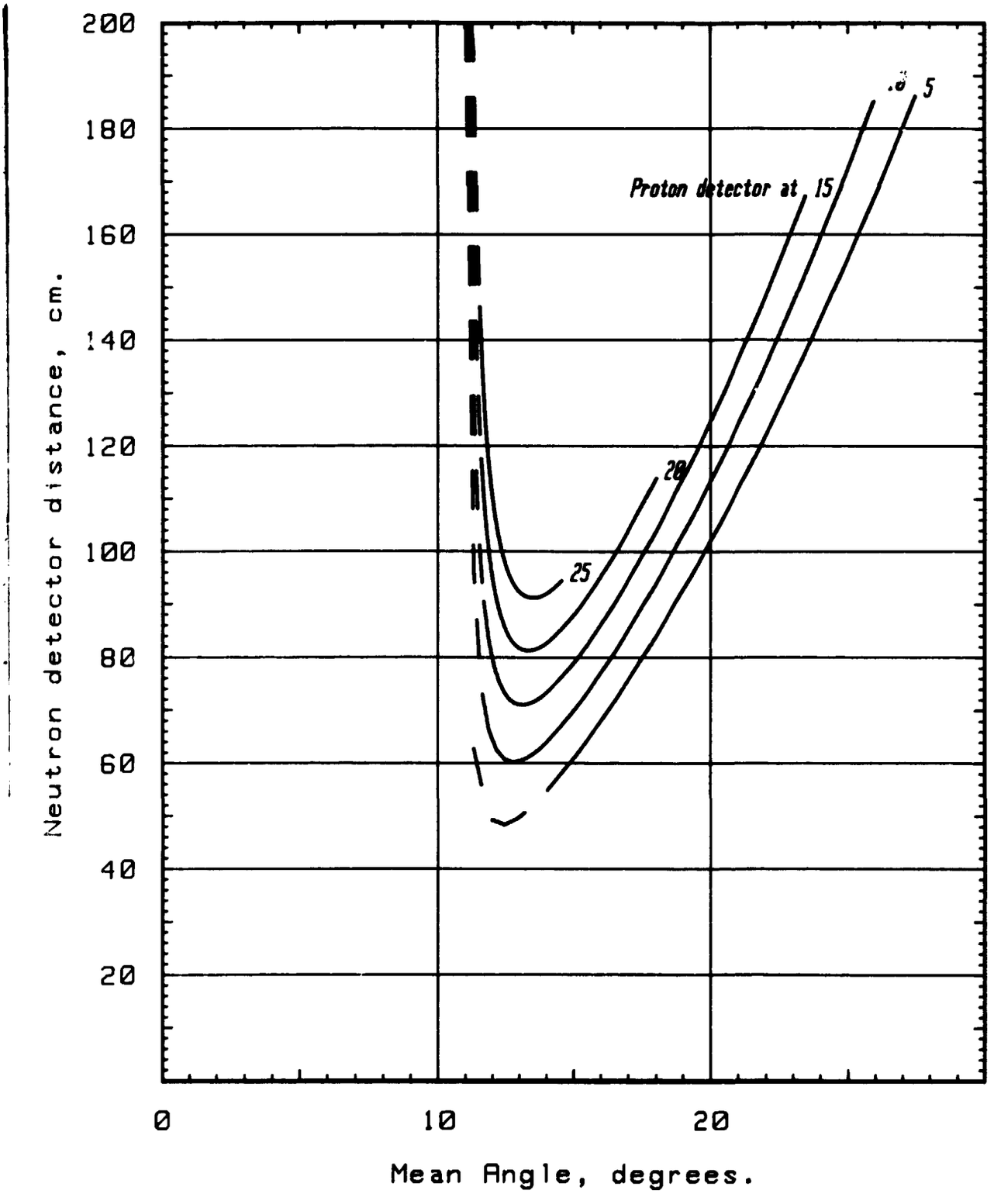

Figure 67. Neutron-detector distance versus scattering angle.

Resolution, foil 48 keV, proton detector 50 keV, time 1 ns. Proton detector radius 1 cm. Total resolution 100 keV. Efficiency 10^{-6} cm^2. Bias 0.5 MeV in a 2 cm thick Pilot U neutron detector. Distances in cm.

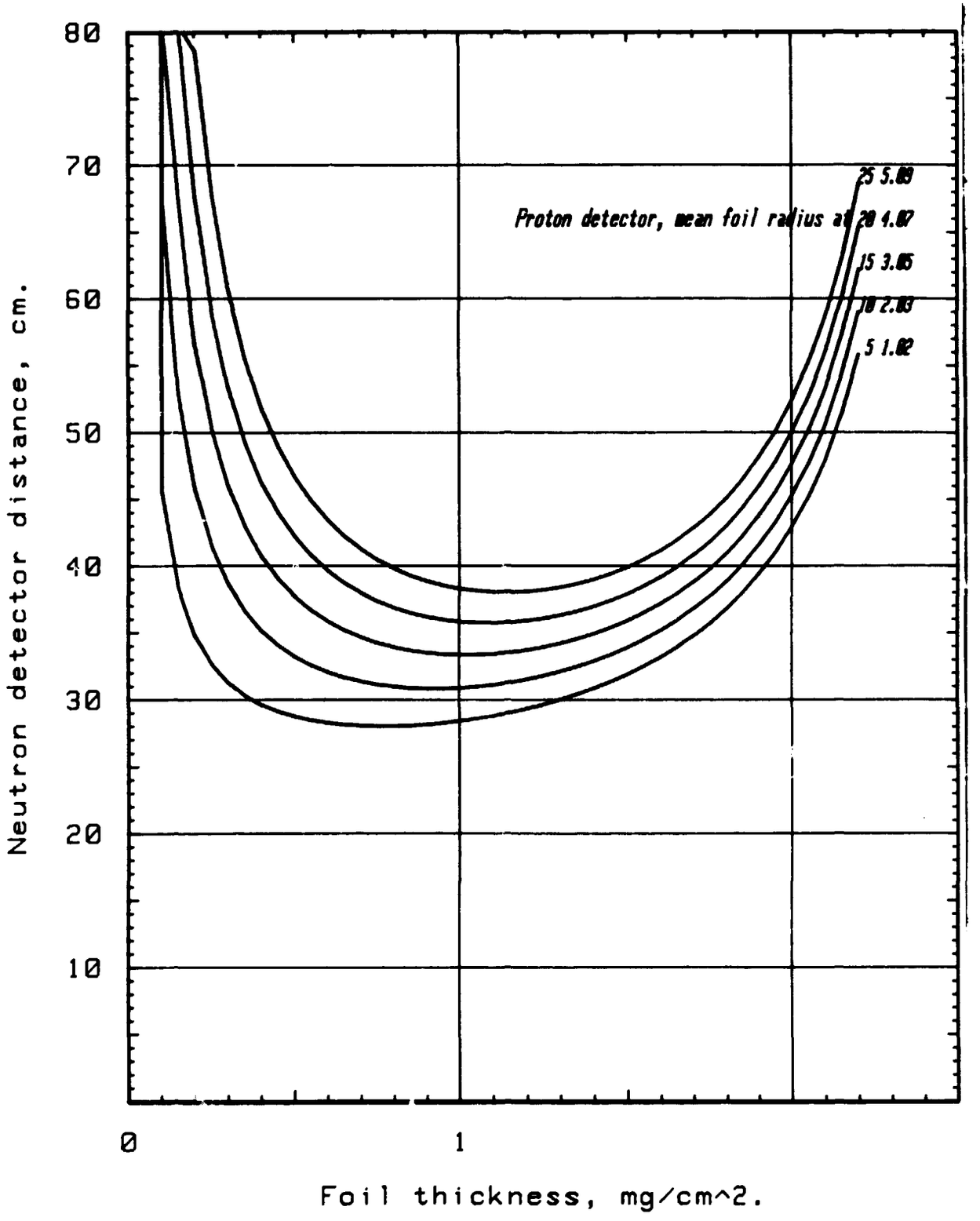

Figure 68. Neutron-detector distance versus foil thickness.

Mean scattering angle 11.5 degrees. Resolution: foil 38 keV/(mg/cm^2),proton detector 35 keV, time 1 ns. Proton detector radius 1 cm. Total resolution 100 keV. Efficiency 10^{-6} cm^2. Bias 0.4 MeV in a 2 cm thick Pilot U neutron detector. The proton-to-detector distance is related to the mean foil radius. Both are given in cm at the curves.

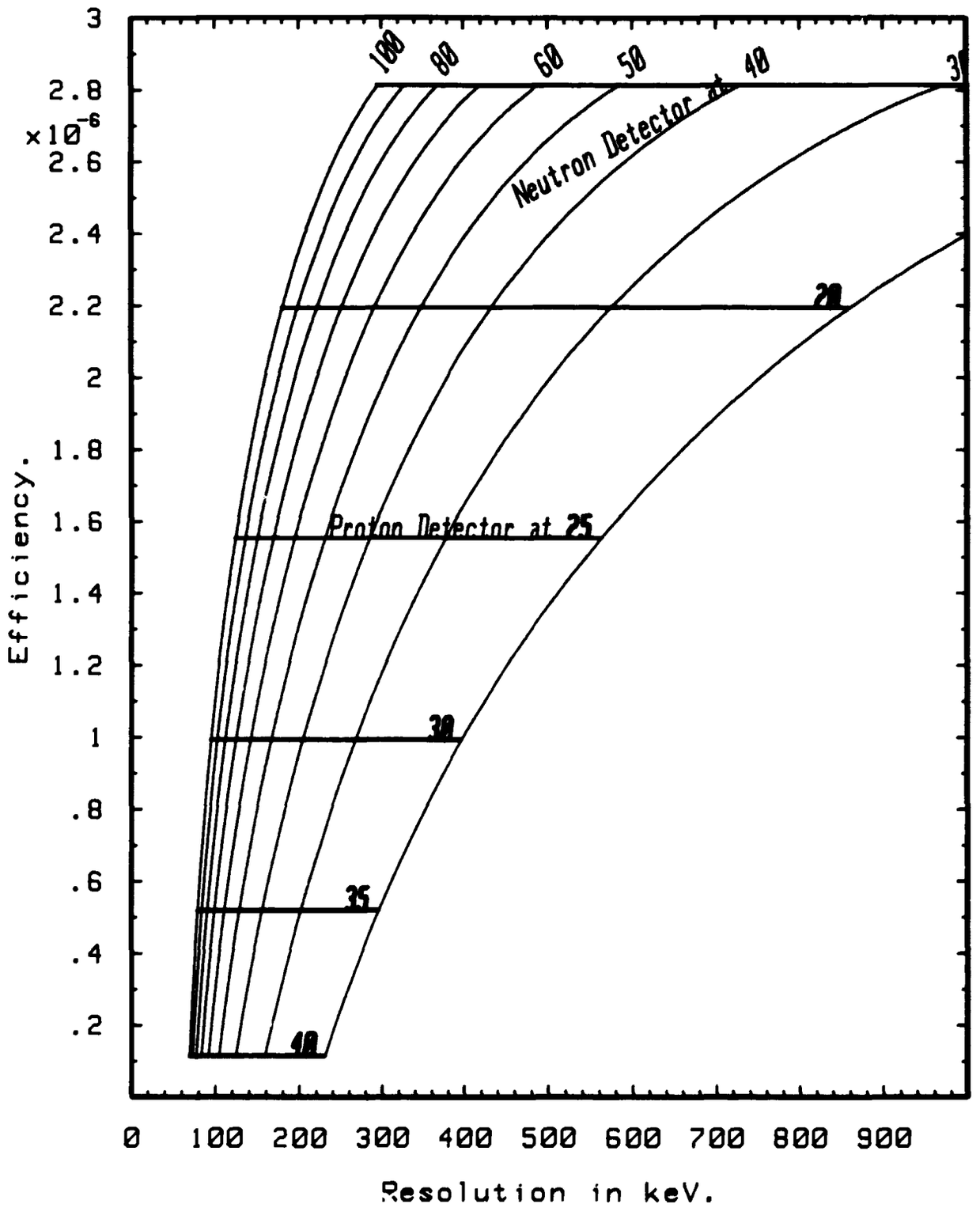

Figure 69. Efficiency-resolution chart for TANSY.

Parameters according to TANSY. Bias 0.5 MeV. Distances in cm.

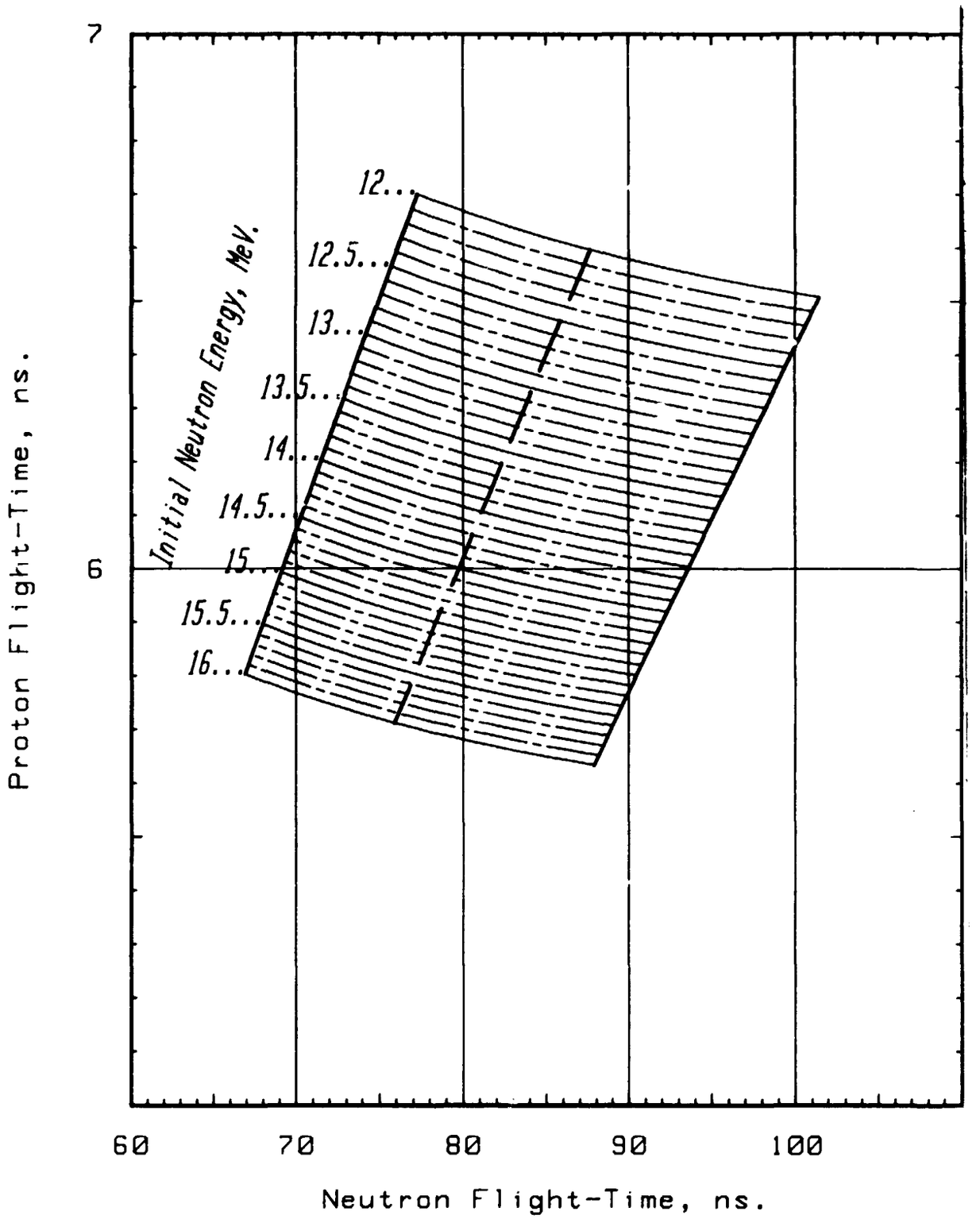

Figure 70. Neutron and proton flight-times.

Flight-times in TANSY. See paragraph 4.2, »The measurement method.».

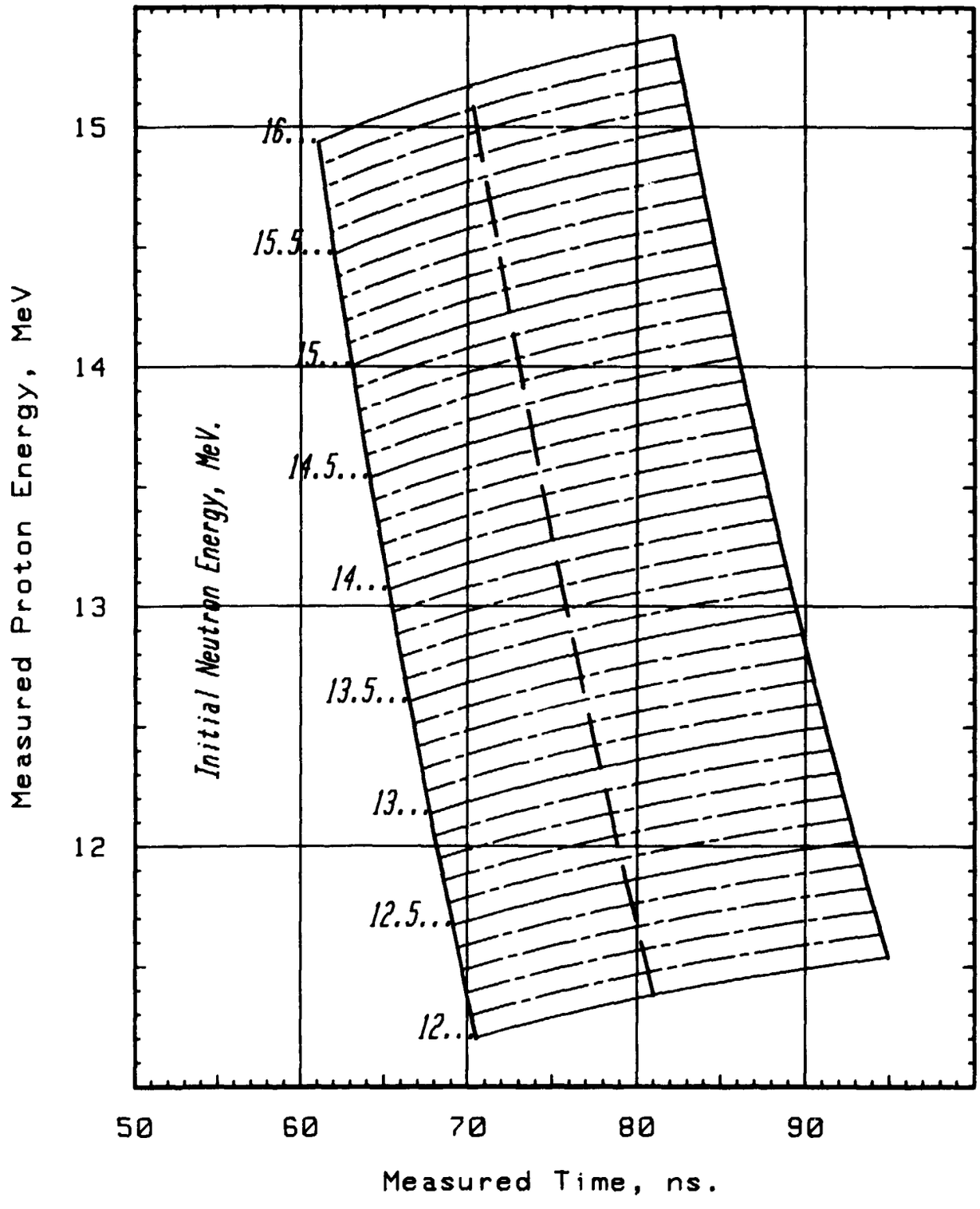

Figure 71. Time-energy chart.

We measure the proton energy and the time difference between the neutron and the proton flight-times, equation 4.5. The corresponding initial-neutron energy can be found from this graph.

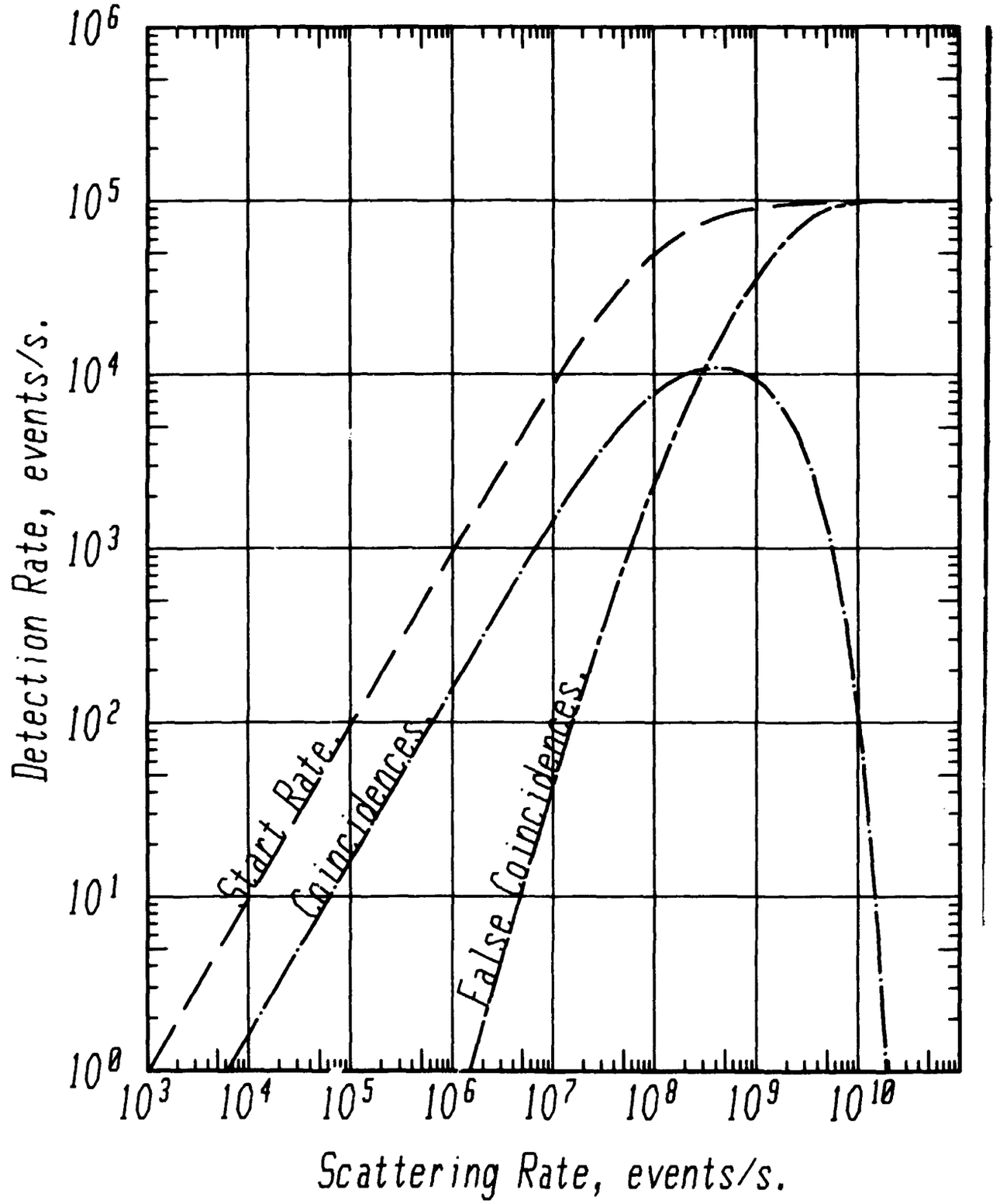

Figure 72. Detection rate, no background.

The scattering rate is equal to the neutron flux density times 7.15×10^{-3}. The time window is 50 nanoseconds and the cycle time 10 microseconds. The instrument is supposed to work in the range of 10^6 to 10^7 scattering events per second.

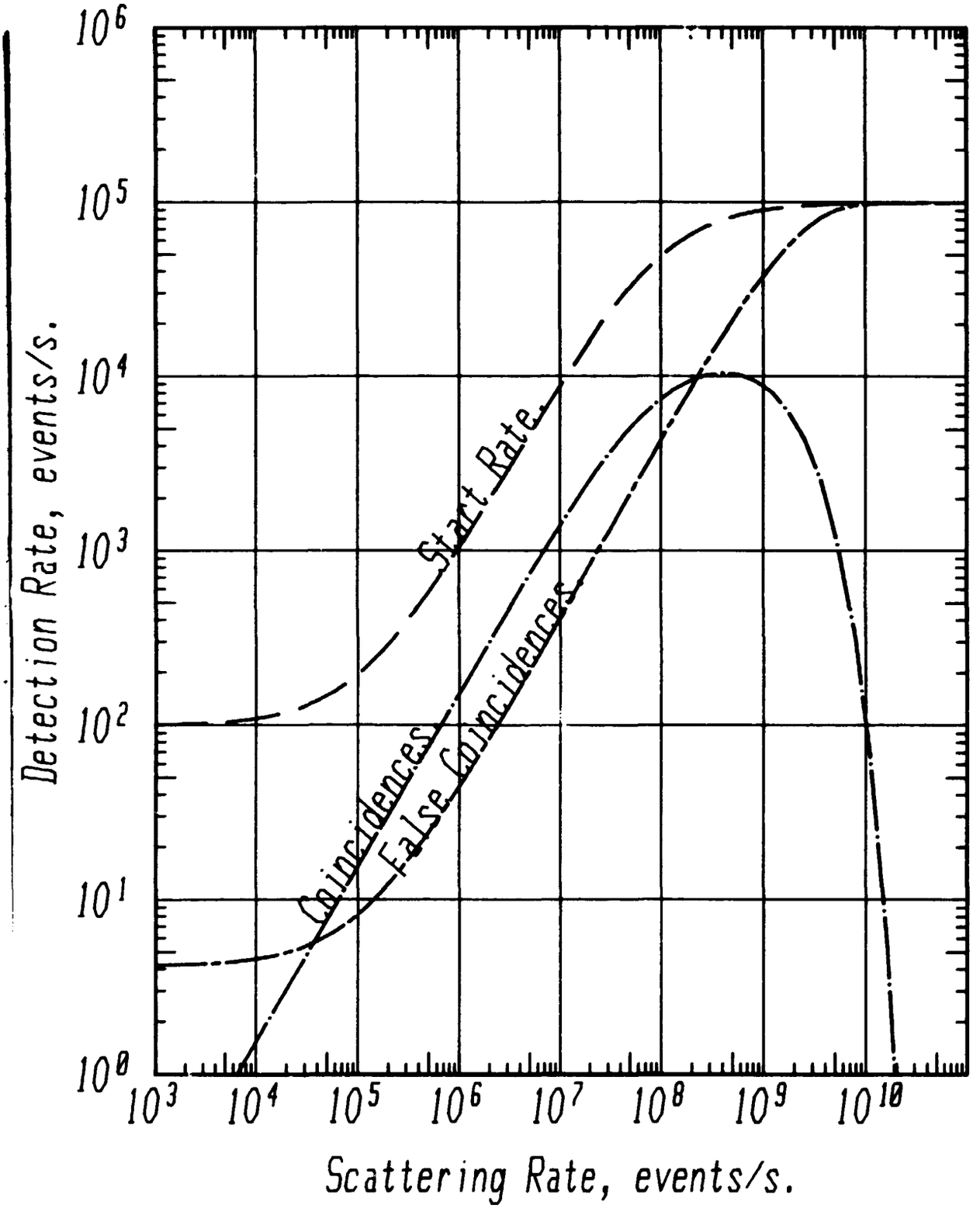

Figure 73. Detection rate, with background.

The background is 100 events/s in the proton-detector and 86,000 events/s in the neutron-detector. See paragraph 7.4, »Background considerations.», for a discussion about the background. The instrument parameters are given in figure 72.

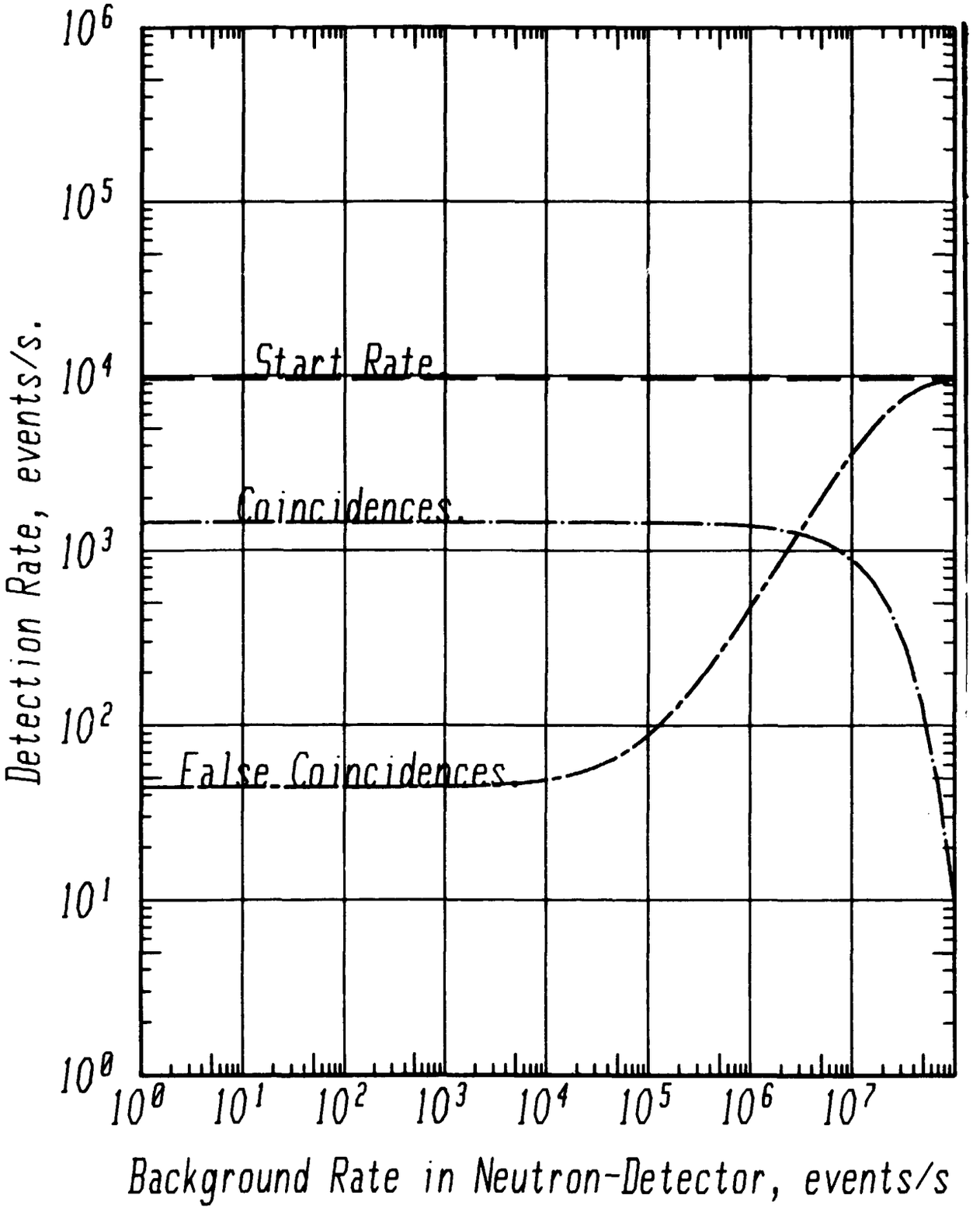

Figure 74. Detection rate versus neutron-detector background.

The scattering rate is 10^7 events/s corresponding to a neutron flux density if 1.4×10^9 n/cm^2,s. The background in the proton-detector is 100 events/s. Other parameters are given in figure 72.

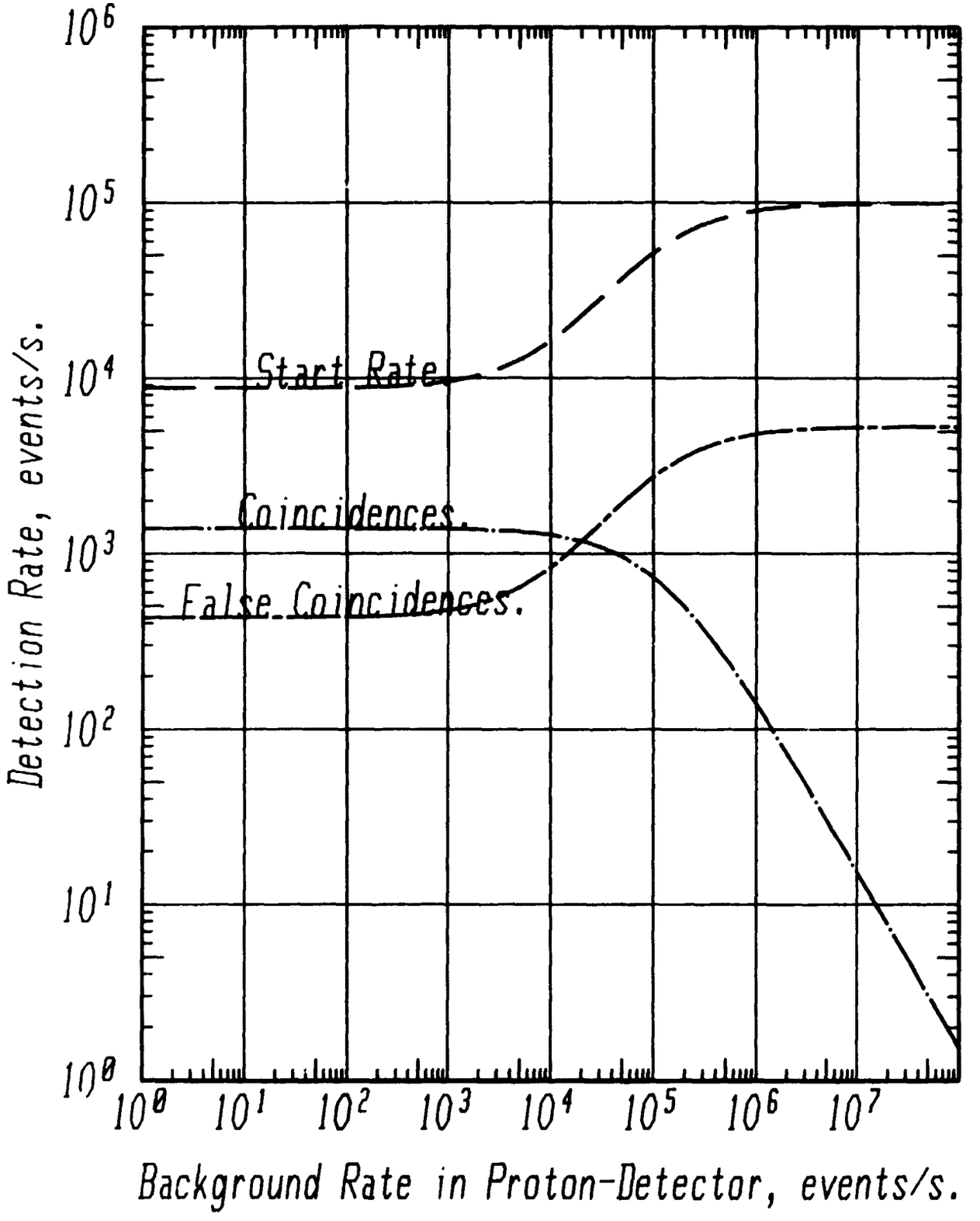

Figure 75. Detection rate versus proton-detector background.

The scattering rate is 10^7 events/s corresponding to a neutron flux density of 1.4×10^9 n/cm^2,s. The background in the neutron-detector is 10^6 events per second. Other parameters are given in figure 72.

9 Neutron beam shaping

The spectrometer is designed for a neutron flux density of 10^9 n/cm^2,s at the foil. The total rate of neutrons passing the foil is 10^{11} n/s. Only about 1000 of these are registered as coincidences per second[1]. It is obvious that great care must be taken in order to avoid disturbances from neutrons scattered by various materials in and around the spectrometer.

The most important reactions caused by 14 MeV neutrons are the elastic scattering and the (n,2n)-reaction. As an example, the total cross section of iron is 2.4 barn. Of this, 1.1 barn is from elastic scattering, 0.8 barn from inelastic scattering, and 0.5 barn from the (n,2n)-reaction. Small angle elastic scattering, which is predominant for the scattering in the beam shaping system, gives a negligible energy loss. Inelastic scattering and the (n,2n) reaction give neutrons of comparably low energy.

The purpose of the beam shaping system is threefold. It shall select neutrons coming from relevant parts of the plasma, it shall shield the spectrometer for neutrons scattered in the torus hall, and it shall take care of the neutron beam passing the instrument. Three components are needed in order to solve these tasks. A primary shield at the window of the plasma vacuum vessel, a diaphragm, selects a suitable part of the neutrons emerging from the plasma. A collimator in the wall between the torus hall and the diagnostic hall provides further selection and shields the instrument for neutrons scattered in the torus hall. A beam catcher serves as a neutron dump.

A careful calculation of the beam shaping system is very complicated. Here, we will only do some rough estimates in order to find out the problems involved and the order of magnitude of the equipment dimensions.

The beam shaping system determines the volume of plasma seen by the instrument scattering foil. In paragraph 8.4, »The dynamic range.», we found that the dynamic range was limited to about one decade. Therefore, the rough total efficiency of the system should be controlled by the beam shaping system. Figure 77 shows a system using the full opening of the vacuum vessel window.

9.1 The diaphragm

The primary selection of the part of the plasma seen by the spectrometer scattering foil is done by the diaphragm. A shield attenuation factor of about 100 is needed. This gives a shield thickness of about 25 cm for a heavy material, see table 5.

The area of the opening has a strong influence on the counting rate of the spectrometer [2]. The largest opening is 70x20 cm^2. It is determined by the vacuum-vessel window, which has a shape that is very inconvenient for the spectrometer. The best opening is a circular one because of the cylindrical geometry of the spectrometer. Therefore, the height-to-width ratio of the smaller openings should be as close to 1 as possible. Suitable plugs should be available for the limitation of the neutron flow. They should be designed so that it is possible to adjust the opening according to the plasma position.

---

1) See table 4, »Rates of events at 10^9 n/cm^2,s.», page 108.

2) See figure 14, page 34.

Table 5. Attenuation of primary 14 MeV neutrons.

Material	Cross-section (cm^{-1})	Thickness (cm) for a transmission of			
		10^{-2}	10^{-6}	10^{-8}	10^{-10}
Steel	0.205	22	67	90	112
Heavy concrete	0.151	30	91	122	152
Lead	0.178	26	78	103	129
Tungsten	0.335	20	41	55	69
Polyethylene	0.103	45	134	179	224
Water	0.103	45	134	179	224

9.2 The collimator

The collimator is composed of two parts. The outer tube limits the area seen by the spectrometer foil. The inner bar protects the semiconductor and the preamplifier. The coarse shape of the collimator is given by the requirement that all parts of the foil shall be able to see all parts of the opening in the primary shield. This criterion has been used for the calculation of the neutron flow, figure 14, and the drawing of the figures 77 and 78.

An estimate of the necessary shielding capacity of the collimator can be obtained from the amount of neutrons reaching the proton detector from scatterings in the foil. The neutron-proton symmetry of the angle distribution gives a ratio of the neutron flux density at the proton-detector to that at the scattering foil of

$$F_s = S_p S_f \frac{A_f}{A_d} \tag{9.1}$$

From table 2, page 103, and the geometrical dimensions of TANSY we get a ratio of 2.2×10^{-6}. This disturbance can never be avoided. Other effects should be lower. However, there is no point in making them much lower. Therefore, we conclude that the shielding capacity of the collimator should be of the order of 10^{-6} or better.

Using steel in the central bar we find a minimum length of 67 cm from table 5. Therefore, the bar indicated in the figures 77 and 78 gives a more than sufficient shadowing effect.

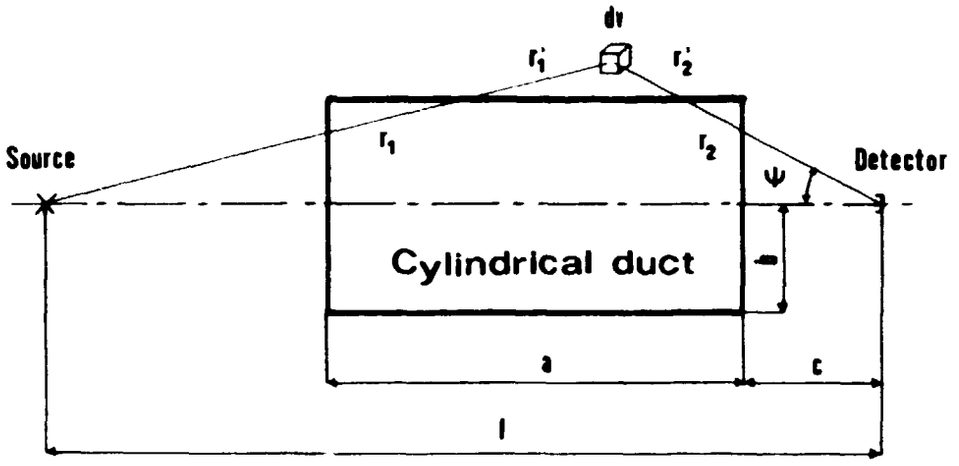

Figure 76. Definitions for the collimator calculations.

The calculation of neutron streaming through ducts is very complicated. We will estimate the ratio of the scattered to the direct flux in a cylindrical duct using a very simplified model. We use an isotropic point source and a plane detector as indicated in figure 76. We consider only single scattering. The error of such an approximation has been estimated at less than a factor of ten for a thin duct {74}. The ratio of the scattered to the direct neutron flux density is

$$F_s = \frac{\Sigma_s l^2}{4\pi} \int_V \frac{1}{r_1^2 r_2^2} e^{-(r_1' + r_2')\Sigma_t} dV \qquad (9.2)$$

The integral should include the entire volume of the scattering material. However, most of the scatterings take place close to the surface. Using this we get, for duct radii much smaller than the length dimensions, the approximation

$$F_s = \frac{\Sigma_s}{\Sigma_t} \frac{b^2}{2l} \left[\frac{1}{\sqrt{c^2+b^2}} - \frac{1}{\sqrt{(a+c)^2+b^2}} \right] \qquad (9.3)$$

The cross-section ratio for steel is about 0.7, the source-detector distance is 11 m, and the duct radius is 9 cm. Using a duct length of 2 m and a duct-to-detector distance of 30 cm we get a ratio of 7×10^{-4}, which is 700 times higher than can be accepted.

Most of the scattered neutrons come from the neighbourhood of the detector. The ratio can be decreased by moving the duct away from the detector. However, for b/c ratios much less than 1 the flux ratio is proportional to the inverse of the detector-to-duct distance. Therefore, we need a much more powerful method to decrease the flux ratio.

The solution is the use of the central bar as a shielding not only for the direct beam but also for the scattered neutrons. It can be seen from the figures 77 and 78 that we can easily obtain penetration lengths greater than 50 cm, which give transmission factors less than 3.5×10^{-5}. Then the flux ratio is decreased to less than 2×10^{-8}, which is lower than required. However, we need a good safety margin because of the simple approximation used.

The main principle for the design of the collimator is that the detector shall never be able to see any surface directly exposed to the direct beam of neutrons. This principle is valuable for the entire beam shaping system. As a consequence of this rule the supports of the central bar must be placed far away from the detector. The cylindrical wall of the vacuum chamber should never be touched upon by the beam. Therefore, the chamber must be larger than indi-

cated in figure 5. The support of the foil should be placed outside the beam. The best support close to the beam is the foil itself.

The neutron exit-window of the vacuum chamber scatters neutrons towards the proton-detector. A shielding is necessary. It can be placed behind the detector in the shadow of the central bar. This shield is also necessary for shielding against neutrons from the beam catcher.

9.3 The beam catcher.

The neutrons scattered in the beam catcher, the neutron dump, can reach the proton detector or the neutron detector. The disturbance at the proton detector can in principle be calculated using equation 9.2. Assuming that there is no absorption in the catcher, that the total number of neutrons catched is defined by the foil area, and that the neutrons are isotropically scattered in one point of the catcher we get

$$F_s = \frac{A_f}{4\pi d^2} \tag{9.4}$$

where d is the distance between the scattering point and the proton detector. The equation gives a flux ratio of 8×10^{-4} for a distance of 1 m and 9×10^{-5} for 3 m. This is too high. It indicates that we need a shield between the proton detector and the catcher. A thickness of 40 cm would give a sufficient shielding. The shield should surround the detector and the preamplifier in order to protect the detector against scattered neutrons from the exit window of the vacuum chamber and other necessary support materials in that area.

The total area of the neutron detector is approximately 5000 cm^2. The number of neutrons reaching the neutron detector from the foil is 6950 per second[1], which gives a neutron flux density of 1.3 $n/cm^2,s$.

The energy distribution of the neutrons leaving a sphere of ordinary concrete with a central isotropic 14 MeV neutron source has been calculated using the ANISN code {75}. The result, shown in figure 79, indicates that about 2 m is needed in order to have a background essentially lower than the neutron flux density caused by the foil.

A special problem is the cables connecting the proton-detector to the instrumentation. The neutron beam forms a cylinder, which shall not be interrupted by any hydrogenous material, such as the insulating material in the cables. Therefore, we suggest that the cables should follow the axis of symmetry through the beam catcher. However, it must be verified that no damage to the cables and no disturbances of the signals are caused by the interactions of the neutrons.

[1] From table 4, page 108.

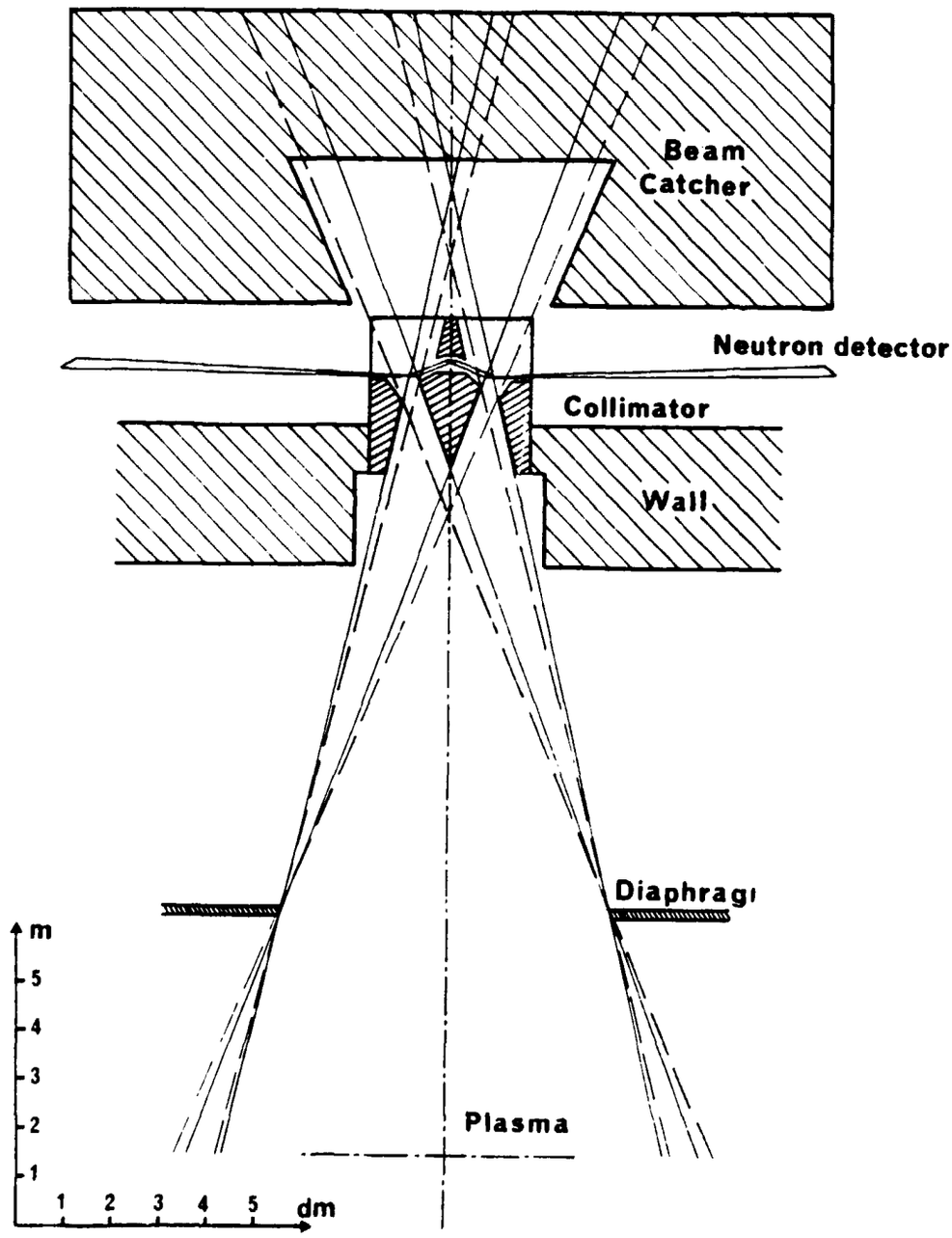

Figure 77. A 1400 cm^2 beam shaping system.

The opening is 20x700 = 1400 cm^2. The figure shows a vertical cut of the system. A horisontal cut gives smaller angles. Therefore, an optimal system has not cylindrical symmetry. Measures from reference 76.

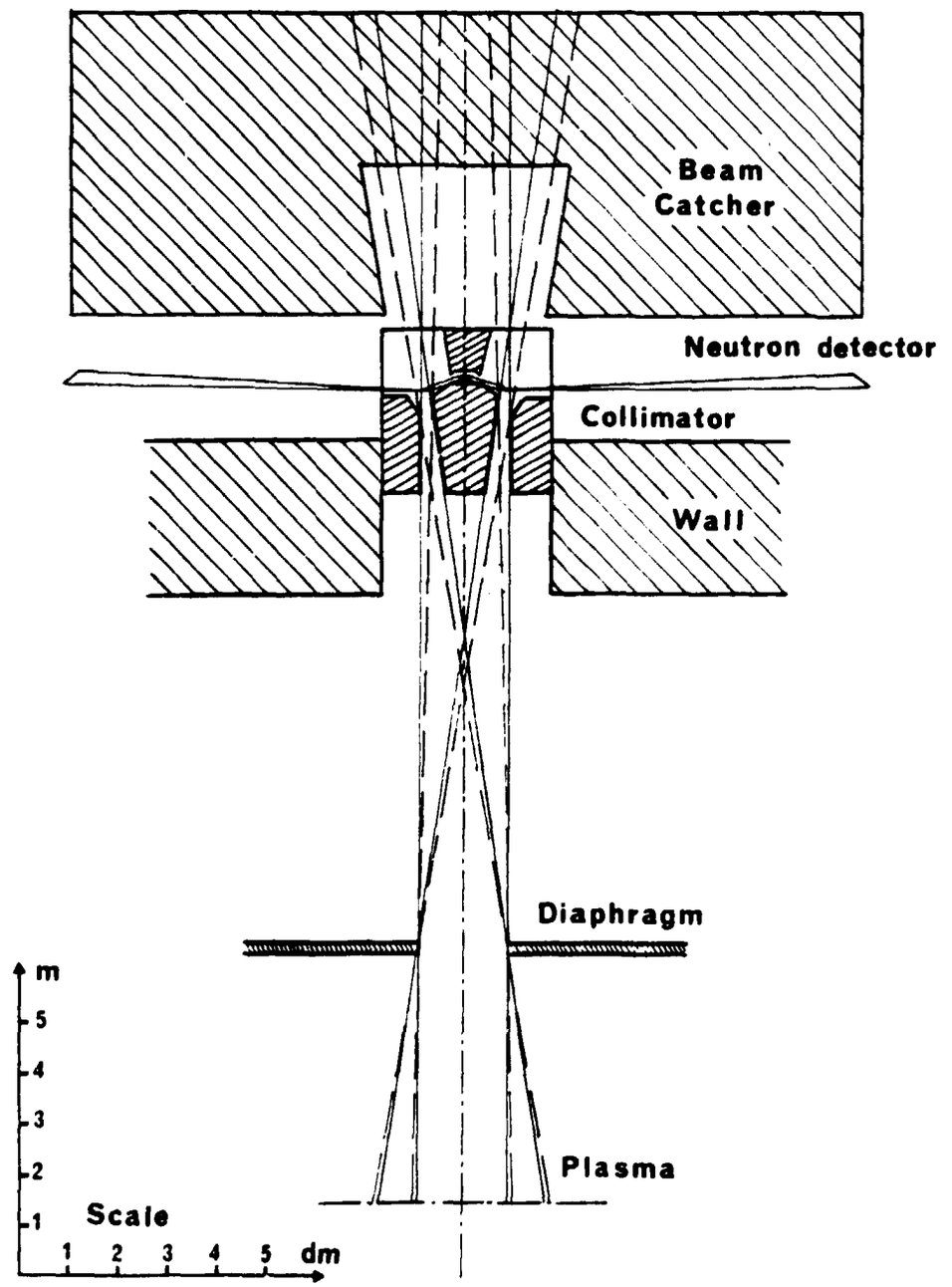

Figure 78. A 324 cm^2 beam shaping system.

The opening in the diaphragm is $18 \times 18 = 324$ cm^2. Cylindrical symmetry is recommended for the whole system. Measures from reference 76.

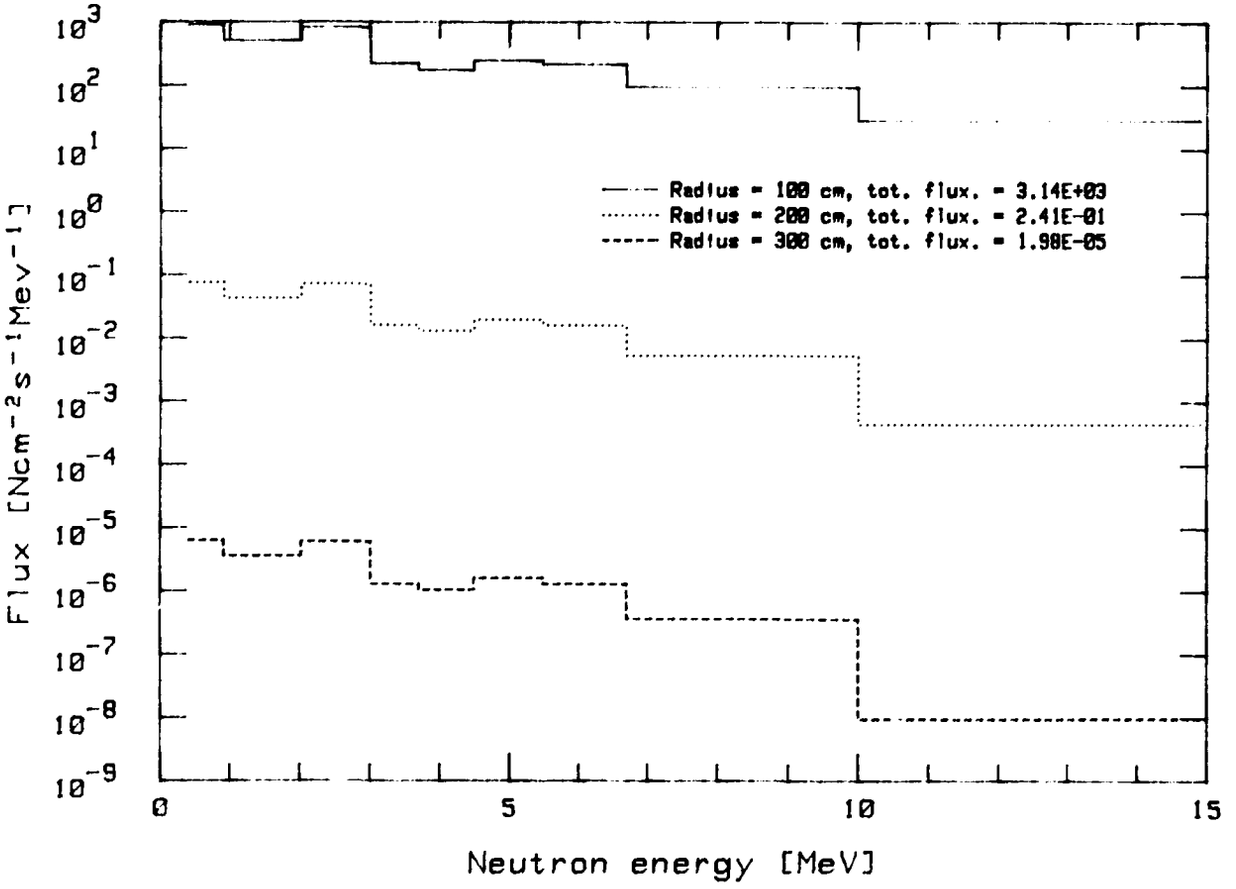

Figure 79. The leakage from a neutron dump.

The leakage from a sphere of ordinary concrete with a central isotropic source of 10^{11} 14-MeV neutrons per second. The calculation was done using an ANISN code {75}.

10 Data acquisition

A careful analysis and a final design of the electronic system including the data acquisition is not a part of this work. However, we will discuss a general lay-out of the system and try to pin-point the most essential problems to be solved in order to obtain a reliable instrument.

10.1 Measurement data

The parameters measured for each coincidence event are the proton energy and the time difference between the interactions in the proton-detector and one of the neutron-detectors. The formulae for these parameters are given in the equations 4.1 and 4.5. The resulting energy of the initial neutron according to equation 4.6 is illustrated in figure 71.

The necessary channel width for the final energy distribution is estimated at 100 keV[1]. The dominating part of equation 4.6 is the proton energy. Therefore, the proton energy-measurement channel-width must be lower than 100 keV. A differentiation of equation 4.6 or an inspection of figure 71 shows that 100 keV corresponds to a time interval of about 5 ns. Therefore, an upper limit for the widths are 100 keV for the energy channels and 5 ns for the time channels. However, this is true only as long as the parameters are separate. The combination of the parameters according to equation 4.6 gives numerical interferences. Therefore, we need a factor of 10 to 100 lower channel widths. Using 8000 channels for the energy and 8000 for the time we obtain an energy channel width of 2 keV and a time channel width of about 10 ps.

The full two-parameter area can not be stored and a data reduction according to equation 4.6 can not be done within the few seconds available. Therefore, the primary data must be stored in a list mode leaving the the data reduction to the instrument computer (ND-100) or the main computer.

The plasma behaviour is different during different parts of the shot. We do not have enough events for the analysis of the time behaviour from a single shot. However, a summing up of the stored data from a number of shots would give information of the mean behaviour of the plasma. Therefore, we suggest that each event is tagged with a time information. The time is running from a reference time defined by a trigger signal for each shot. Time intervals of 0.1 seconds give sufficient accuracy.

A valuable but not necessary information is the neutron detector number responsible for the coincidence. This number contains some information about the position of the plasma. It is also useful for checks of the measurement. The delay line settings can be checked and data from a malfunctioning detector chain can be excluded from the analysis.

In conclusion, we suggest a main data collection of three 16-bit words for each event. The protocol is

byte 0	Time-interval of the shot.
byte 1	Detector number.
byte 2 and 3	Proton energy + coincidence tag.
byte 4 and 5	Flight time + coincidence tag.

A measurement containing 10000 events for a shot gives a minimum storage need of 30 k 16-bit words. To this should be added the storage of two 8 k 24-bit single parameter spectra and space for programs. Therefore, the minimum memory size of the computer at the instrument is estimated at 64 k 16-bit words.

[1] See paragraph 1.2. »Channel width and count rate.», page 12.

The single parameter areas are used for energy spectra. The energy spectrum from the neutron detectors gives information about the background and the energy spectrum from the proton measurement is valuable for proton detector checks. The proton energy measurements are 5 times as frequent as the coincidences. They give a poor energy resolution, but still a rough estimate of the plasma properties can be obtained. For example, it should be possible to distinguish between thermo-nuclear and beam-plasma induced neutrons.

10.2 Calibration

The energy and the energy interval of the proton detector can be calibrated with common methods. An Am-241 source should be included in the vacuum vessel for this purpose. An insertion of the source with remote control would enable checks and recalibrations between the shots. This is motivated by the risk of burn-out of the semiconductor.

The neutron-detectors should be as equal as possible. The energy and the energy-interval can be measured using a proper gamma source. The timing must be equal for all the detectors. A light source giving the possibility of a simultaneous light pulse in all the scintillators should be incorporated. One possibility is the use of a pulsed laser connected to the scintillator by fiber optics[1].

A difficult problem is the synchronization of the proton and neutron time measurement. We have not found any solution for a direct calibration or measurement of this time lag.

An indirect method is the use of the measurement itself. From the equations 4.1 and 4.5 we can get the mean energy in two ways,

$$\bar{E}_o = \frac{m}{2nc^2} \sum_{i=1}^{n} \left(\frac{l_{ni}}{\sin(\theta_i)} + \frac{l_{pi}}{\cos(\theta_i)} \right)^2 \frac{1}{(t_i + t_d)^2} \qquad (10.1)$$

or

$$\bar{E}_o = \frac{1}{n} \sum_{i=1}^{n} \frac{E_{pi}}{\cos^2(\theta_i)} \qquad (10.2)$$

where t_d is the time lag, the difference between the true and the measured flight times. Now, we may approximate the equations 10.1 and 10.2 by replacing the geometrical quantities with their mean values. Then, we can use an iterative process to determine that value of the time lag for which the two equations give the same mean energy. We do not know how good this approximation is. Before use, it should be tested by e.g. a Monte Carlo calculation.

10.3 Electronics

The principles of the electronic system are sketched in figure 80. The symbols used are collected in table 6. The purpose of the diagram is the identification of the necessary functions. No comparisons between modules from different manufacturers have been done. Surely, the number of modules and the cost of the system can be reduced by a skilled electronic engineer. However, it is emphasized that high quality units are needed in order to assure proper measurements. The equipment will work under very hard dynamic conditions.

Most of the solutions indicated in the figure are straight forward. Here, we only will discuss the most essential points.

[1] O.N. Jarvis has suggested the use of a source emitting beta and gamma in coincidence.

The key units are the time detection (FSCA), the time measurement (TAC + ADC), and the proton energy measurement (ADC) units. The use of the single analyser concept as early as possible in the signal chains gives a possibility to ignore non-relevant data and thereby keep the deadtime as low as possible[1]. An alternative choice in the proton detection line is a timing discriminator instead of a timing single channel analyser. However, in the neutron detection lines we have to select the neutron induced events from gamma events, which give both higher and lower amplitudes than the neutron events. We suggest 32 fast single channel analysers, one for each neutron detector. An essential cost reduction can be achieved by using one common fast single channel analyser. However, in that case the analog signals must be mixed. The pile-up effects and the distortion of the analog signals in this mixing unit must be very carefully investigated before such an approach is decided upon.

The photomultiplier bases must be modified or exchanged in order to tackle the problem of large load transients. Zenerdiod stabilization has been used, see chapter 2.

The linear amplifier and data acquisition line using the dynode signal from one or all of the photomultipliers is added for test purposes. It is necessary for the calibration of the fast lines, the adjustment of the high voltage and the discriminators. During the measurement it gives information about the background.

A corresponding line is indicated for the proton detection. This information could be included in the data flow of the coincidence line. However, the use of a separate line with data collection in a histogramming memory saves computer memory space and, which is the most important point, saves deadtime in the coincidence line.

The MIXER contains those parts of the electronics for which we have not found standard commercially available units. It has three functions:

1. An OR-circuit for the derivation of the stop signal to the time-to-amplitude converter. The dynamic of this circuit is very essential. The circuit must be symmetric with respect to all the neutron detector lines. It is possible to include the external delay lines in this circuit. The external delay lines suggested have a time interval setting of 0.5 ns. It should be valuable to decrease this and to include remote control.

2. A converter and a data register for the detector number information.

3. A timer with a register for the measurement of the time from the beginning of the shot.

10.4 Remote control

The calibration and the trimming of the spectrometer are most readily done at the instrument prior to the measurements. It involves movements of the gamma source and settings of several potentiometers; one would need a robot for a complete remote control. Therefore, only the most important parts of the trimming are assumed to be done remotely. We suggest remote controls for:

1. Insertion and removing of the americium calibration source. This enables calibration measurements during the ten minutes period between the shots.

2. The fast single channel analyser in the proton detection line. This presupposes a modification of the unit. Adjustments are required for obtaining the lowest possible number of false starts.

3. High voltage to the photomultipliers. This is easily done using LeCroy high voltage units. The coarse settings are supposed to be done prior to the measurements. Fine adjustments can be done by remote control between the shots.

[1] See Paragraph 8.4, »The dynamic range.», page 104.

Table 6. Electronic units.

Symb.	Qt.	Manu-fact.	Model no.	Name
PMB	32	Ortec	265	Photomultiplier Base
FSCA	33	Ortec	583	Constant Fraction Differential Discriminator
DEL1	8	Ortec	DB463	Delay Box
DEL2	1	Ortec	425A	Nanosecond Delay
ADC	4	LeCroy	3512	Analog-to-Digital Converter, 8 k
HMM	1	LeCroy	3588	Histogramming Memory
TAC	1	Ortec	457	Time-to-Pulse-Height Converter
PAMP	1	Ortec	H242A	Preamplifier
FAMP	1	Ortec	579	Fast Filter Amplifier
LAMP	2	Ortec	572	Spectroscopy Amplifier
LP	32	Ortec	113	Scintillator Preamplifier
LIP	1	Lambda Physik		Light Pulser, Laser
TCAL	1	Ortec	462	Time Calibrator
PG	1	Ortec	458	Research Pulse Generator
BIAS	1	Ortec	428	Bias Supply
HV	1	LeCroy	HV4032A	32 Channel High Voltage System
	32		HV4032IP	including 32 Plug-in Pods
	1		2132	and HV-to-CAMAC Interface
CAMAC	1	LeCroy	1433	CAMAC Crate
NIMBIN	4	Ortec	M400/N	Nimbin
MIXER	1	?	Special	Mixer and Timer
(ND100	1	Nord Data		Computer, Terminal and CAMAC Interface)

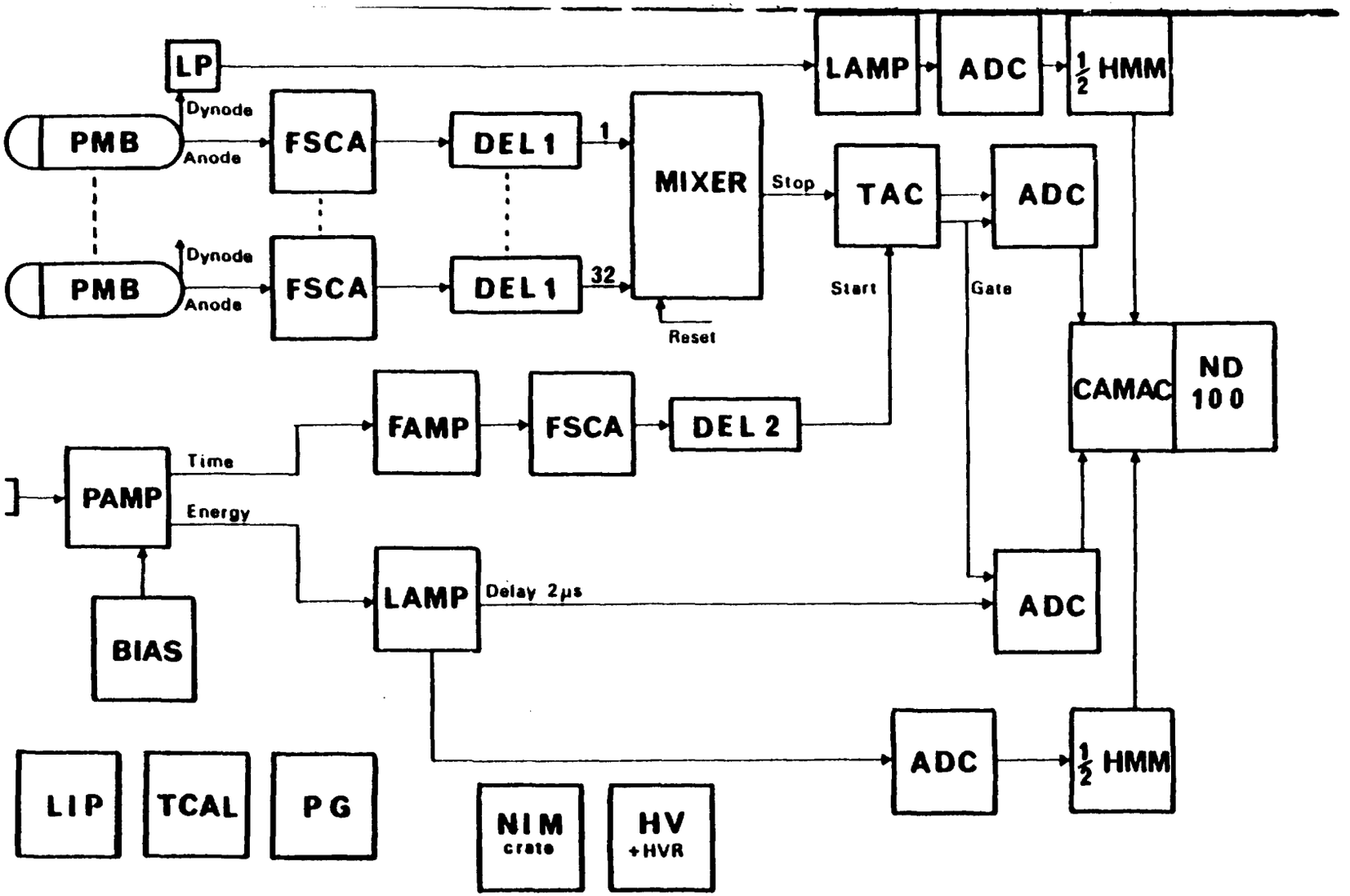

Figure 80. Electronic principle diagram.

The symbols are explained in table 6.

11 Test measurements

The conditions for neutron-spectrometry at a small neutron-generator and at JET are very different. The low neutron intensity at the neutron-generator can be compensated by placing the spectrometer close to the source. However, the proton-detector must be shielded against the neutrons. The shield needs some space. Therefore, the scatterer can not be placed closer to the source than a few tens of centimeters.

The neutron flux density at a neutron generator giving approximately a point source is proportional to the inverse squared distance from the source. At a practically usable distance the neutron flux density is too low for a test with a TANSY-like set-up. Therefore, these tests have been done for only proton detection and with a special scatterer, constructed for an optimal use of the low neutron flux density. In spite of these limitations the tests have given some experiences about the use of a semiconductor for proton-detection in an environment of a severe field of background neutrons.

It was found that the background spectra recorded were mainly due to neutron-induced reactions in the silicon of the detector and that they did not interfere with the proton recoil distribution. The test result emphasizes the importance of keeping a low neutron background in the detector.

11.1 The neutron source

The 400-keV SAMES neutron-generator in Gothenburg produces neutrons by the D-T reaction. The target is disc-shaped with a diameter of 30 mm. The whole area is not used. The radius of the beam impact spot in a normal run is about half a cm. The neutrons are almost isotropically distributed. However, the energies and the spread of the energies vary with the angle between the ion beam and the neutron path. The lowest spread is found at an angle of 100 degrees. The neutron energy at this angle is 14.0 MeV.

The tests were done at the 100 degrees angle. The source intensity was 10^{10} n/s giving running times in the order of half an hour. The runs were monitored and normalized to the same neutron fluence.

11.2 The design used for the tests

Potenza and Rubbino {22} have suggested a special scatterer for spectroscopy with a low-intensity neutron point-source. It is barrel-shaped, see figure 9. In principle it explores the concept of a constant angle between the neutron-paths and the paths of the recoiling protons reaching the detector.

The scatterer topography can be calculated in the following way. We assume a point source and a point detector. Let a circle arc run through the source and the detector. The circle radius is selected in order to achieve the required scattering angle. Let this circle-arc revolve around a central line between the source and the detector. A cigar-shaped surface is generated. Have the »cigar» cut by 30 per cent at each end and the remainder is a barrel-like surface. In our experiments we had to reduce the length of the scatterer even more in order to fit it into the existing vacuum vessel.

The appearance of the apparatus can be seen in figure 81. The distance from the source to the detector is 78 cm. The finite size of the source and the detector gives a variation in the scattering angle. It ranges from 15 to 21 degrees and has a mean value of 17.5 degrees. The scatterer was made of 2 mg/cm^2 polyethylene foil of standard household quality. It is mounted without any inner support, thereby utilizing the whole area of 690 cm^2.

The proton detector is a commercial silicon surface-barrier detector with an area of 0.5 cm^2. It is made of p-doped silicon, 2 mm thick and it was operated at a bias high enough to make it totally depleted. Normally, one uses the n-type silicon detector. However, our detector was considered for use also in a hydrogen atmosphere, see figure 31. According to the manufacturer (Ortec) only a special type of p-doped detector could be protected for use in hydrogen. Protection is done by applying a coating on the rear, gold electrode. It does not affect the incoming particle, nor the resolution of the detector. The resolution, including the amplifier chain, was measured using an americium source. It was better than 30 keV and did not change during the experiments.

During the first experiments, the detector was shielded for direct neutrons by a central rod of lead. The lead was in the later runs replaced by iron. The central shield is essential to assure the detector a resonably long life-time. The surface-barrier detectors are destroyed by a dose of 10^{11} to 10^{12} neutrons/cm^2. The length of the shield is limited in the test set-up. However, at JET the length is practically unlimited.

The vacuum vessel was made of stainless steel except the front end of aluminium. The pressure was less than 10^{-3} torr. The neutron intensity was reduced with 8% by the aluminium front end. An alpha-source was built into the vessel for absolute energy calibration of the detector.

We used common commercial modules for the electronic system. The pre-amplifier was an Ortec 142A. The spectra were collected in a multichannel analyzer using a channel width of 40 keV.

11.3 Efficiency and resolution of the test design

The energy of the protons reaching the detector is calculated using equation 4.1. The mean proton-recoil angle is 17.5 degrees, which gives an energy of 12.7 MeV. However, the slowing down of the protons in the foil gives a shift downwards.

According to the definitions in paragraph 2.1, the efficiency is 1.2×10^{-5} cm^2 and the mean sensitivity 1.7×10^{-8}. A source intensity of 10^{10} neutrons/s gives a mean flux density at the foil of 4.0×10^6 n/cm^2,s. Consequently, the count rate is about 4.8 counts/s.

The energy resolution is estimated at 710 keV fwhm. Three major effects contribute:

a. The neutrons reaching the foil have energies ranging from 13.7 to 14.2 MeV. This depends on the fact that the angles between the ion-beam and source-neutron paths to the scatterer range from 92.5 to 107.5 degrees. We estimate this contribution to the resolution at 250 keV.

b. The variation of the angle between the initial-neutron path and the detected recoil-proton path gives an energy width of 1 MeV.

c. The proton-paths towards the detector exit the scatterer foil with very small angles between the surface and the proton-path. This is most important in the parts of the scatterer most close to the detector. The exit angle goes down to about 5 degrees, which means that the protons pass through ten times as much material as if they exit at right angles. The maximum energy loss in the 2 mg/cm^2 foil is 900 keV.

The square sum of these three contributions gives a total resolution of 710 keV. The energy-losses in the foil give a shift of the peak downwards to 12.3 MeV.

11.4 The tests

Here, we report five of the tests done with the spectrometer. All runs were done with the same fluence and, therefore, the series was automatically normalized. We used a discriminator setting of about 1 MeV in order to avoid the high count-rate at low energies.

The first run was done with the apparatus as shown in figure 81. The second run was done without scatterer in order to observe the background effects. These were further investi-

gated in the three last runs. We replaced the central lead shield by one made of steel and repeated the second run. In the forth run we re-installed the scatterer and shielded the detector with a tantalum foil. Finally, we shielded the detector with a lead shield.

The first spectrum recorded is shown in figures 82 and 83. The proton peak appears between 11.5 and 13 MeV. The peak is extracted by a background subtraction and shown in figure 83. It has a tail on the low-energy side, which probably is caused by imperfections, such as folds in the scatterer foil. The peak appears at the predicted energy of 12.3 MeV. However, the resolution is 820 keV, a value which is somewhat higher than the estimated 710 keV.

11.5 The background spectra

Figures 82 and 83 show a region from 3 to 11.5 MeV with several small but not fully resolved peaks. These are caused by the reactions ^{28}Si(n,alpha)^{25}Mg and ^{28}Si(n,p)^{28}Al, with the Q-values -2.7 and -3.9 MeV, respectively. The complexity of the spectrum is due to several possible excited states of the product nuclei. Mingay et al. {63} have done detailed analyses of such spectra. The peaks have large low-energy tails caused by incomplete energy deposition in the detector and a broad background spectrum of neutrons. Superposition of these tails gives a count-rate increasing with decreasing energy. Therefore, the peaks at lower energy float on a high continuous background distribution.

No peaks can be seen below 3 MeV. The number of counts increases exponentially with decreasing energy. This is probably caused by gamma pile-up and secondary electrons. However, it is difficult to experimentally separate out these effects. They give a worsened resolution in the proton recoil spectrum.

The neutron-induced charged-particle reactions in silicon have negative Q-values. The ground state of ^{25}Mg corresponds to the peak at 11.2 MeV. It is 0.1 MeV lower than the value calculated from the Q-value of -2.7 MeV. The difference is due to the fact that the energy of the recoiling Mg-nucleus is not sensed by the detector.

The interference between the neutron-reaction peaks and the proton peak was small in the tests. However, TANSY covers an energy range from 12 to 16 MeV. Therefore, it may be necessary to adjust the discriminator level according to the measured spectrum. The discriminator should cut the spectrum at 2.8 MeV below the maximum energy of the neutrons reaching the silicon detector.

Natural silicon contains 4.7% ^{29}Si and the reaction ^{29}Si(n,alpha)^{26}Mg has a Q-value of -33 keV for the ground state {63}. As the polyethylene foil also scatters the same number of neutrons as protons into the silicon detector, alphas from this reaction will give false pulses with energies very close to the energies of the proton-recoils. The cross-section is 2.4 mb {63}. In TANSY this gives a false count-rate which is less than 10^{-5}, times the count-rate of the proton-recoils. Another possible interference is the first excited state of ^{26}Mg. It has a Q-value of 1.9 MeV {64}. The cross-section is 7 mb {65}, which gives a count-rate in TANSY less than 10^{-4} times the count-rate of the proton-recoils. Both of these effects are small and will be neglected.

Figure 84 shows the results of the three background runs. The curve noted 1 is the background after removing the scatterer but with no extra shielding of the detector. Curve 2 was recorded with 0.4 mm tantalum in front of the detector. All charged particles produced by reactions in the construction or shielding material will be absorbed in the tantalum foil. The lowest background, curve 3, was recorded with the detector shielded by 5 cm lead in all directions. The lead shield stops all charged particles, 80% of the gammas and 50% of the 14 MeV neutrons. The reduction measured was less than expected. That may be due to neutrons scattered into the detector from the shielding or its supports.

11.6 Experiences achieved

The major contribution to the background in the proton-measurement is neutron-induced charged-particle reactions in silicon. However, most of the background can be avoided by a discriminator setting at 2.8 MeV below the highest energy of the neutrons reaching the proton-detector. The observed real interferences have a very low amplitude and can be neglected.

In the final design there may be problems with the low energy part of the background. It has a high count-rate and may influence the resolution of the proton-energy measurement. Therefore, the background neutrons reaching the detector should be as few as possible.

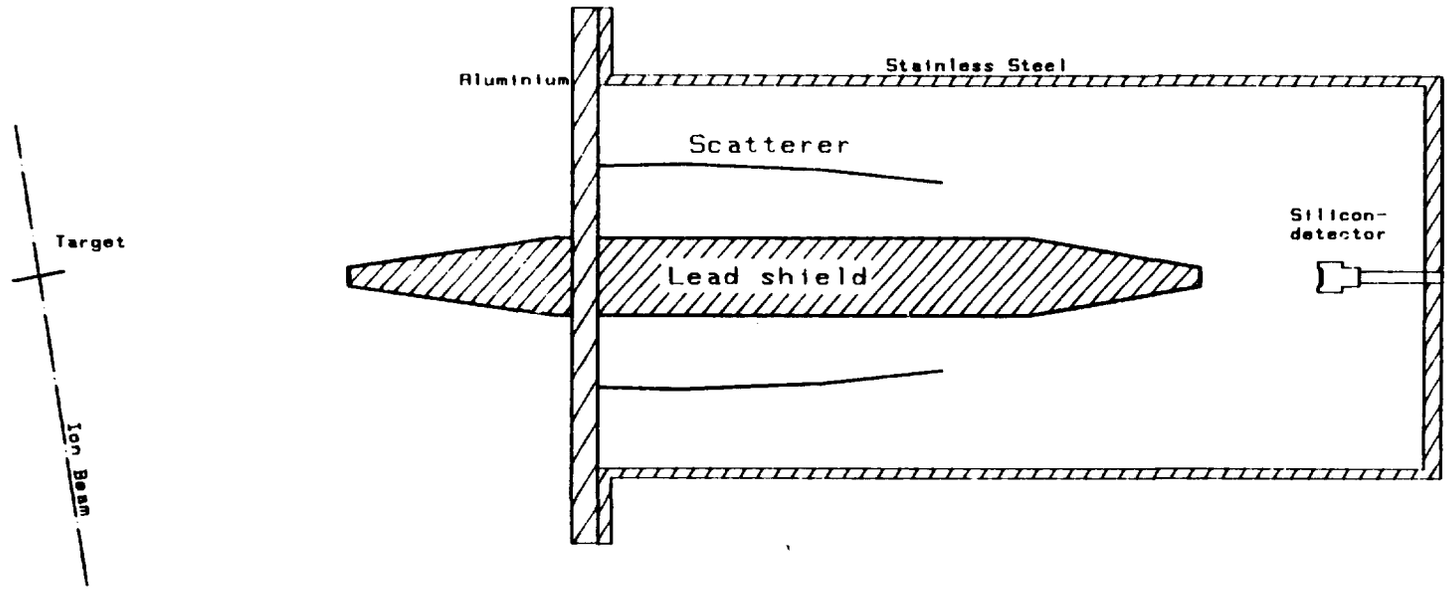

Figure 81. Experimental set-up.

The proton-detector is a 0.5 cm^2 p-type 2 mm thick semiconductor. The foil thickness is 2 mg/cm^2 and the foil area is 690 cm^2. The foil is arranged so that the initial-neutron to recoil-proton angle is as constant as possible.

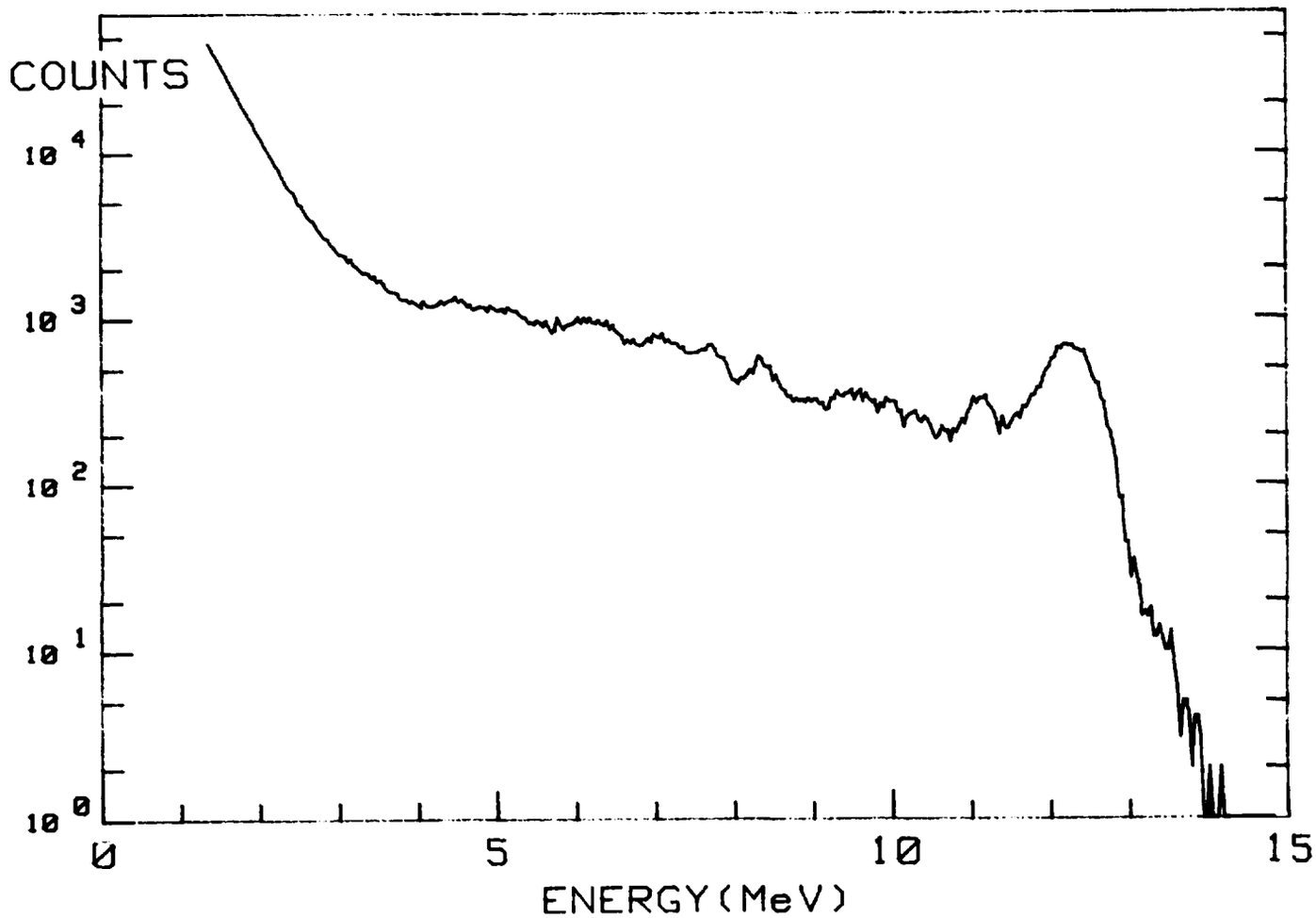

Figure 82. A recorded spectrum in the proton-detector.

Three different types of effects can be seen. The uppermost peak at about 12 MeV is the proton-recoils. The neutron-induced reactions in silicon appear as broad peaks in the 3 to 11 MeV energy range. A very high rate of background appears below 3 MeV.

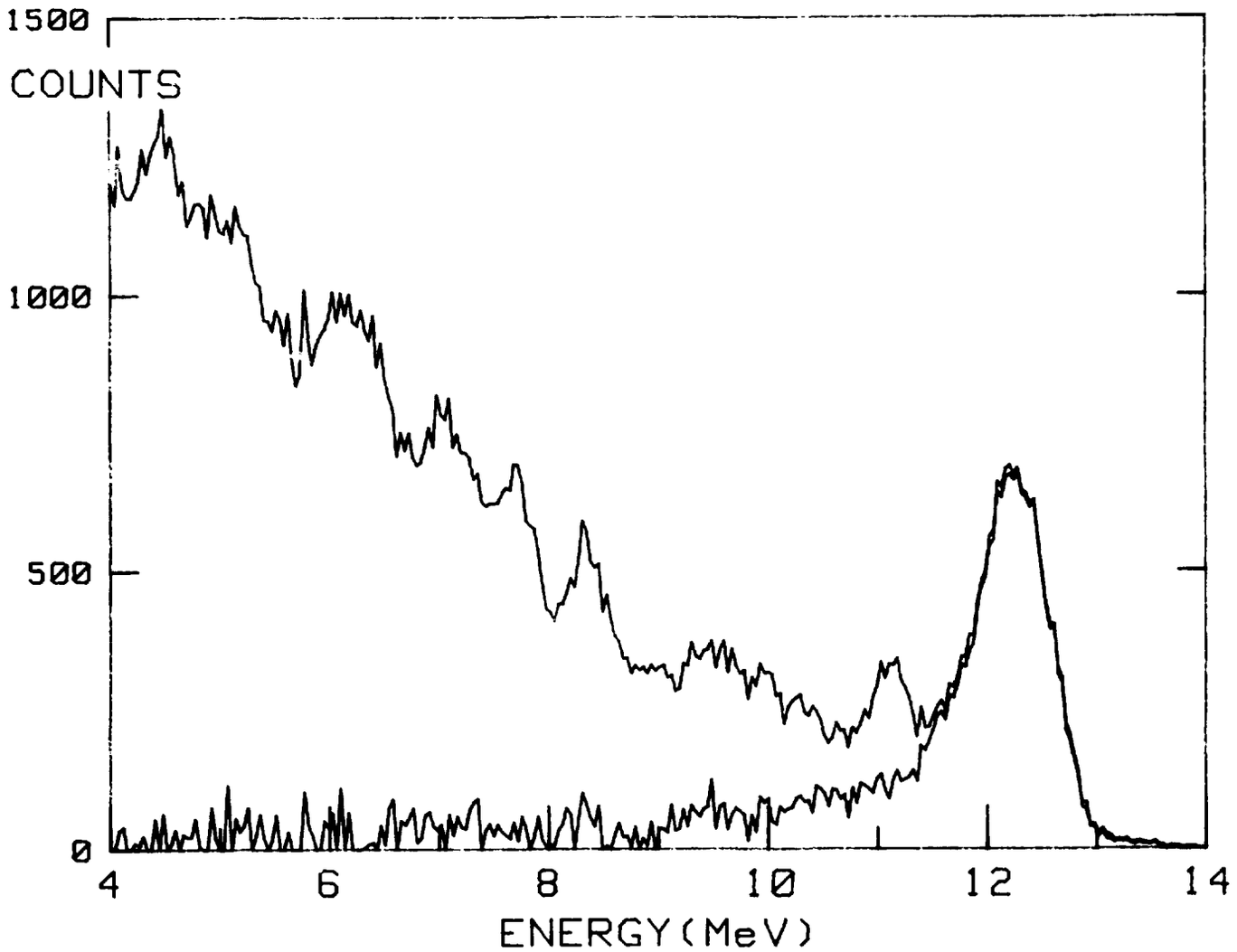

Figure 83. Background subtraction.

The measurements with and without foil were done with the same fluence. Therefore, a direct background subtraction can be done. The lower curve shows the stripped neutron peak, the upper the peak with background. It is clearly demonstrated that the peaks below the neutron-peak do not belong to scatterings in the foil.

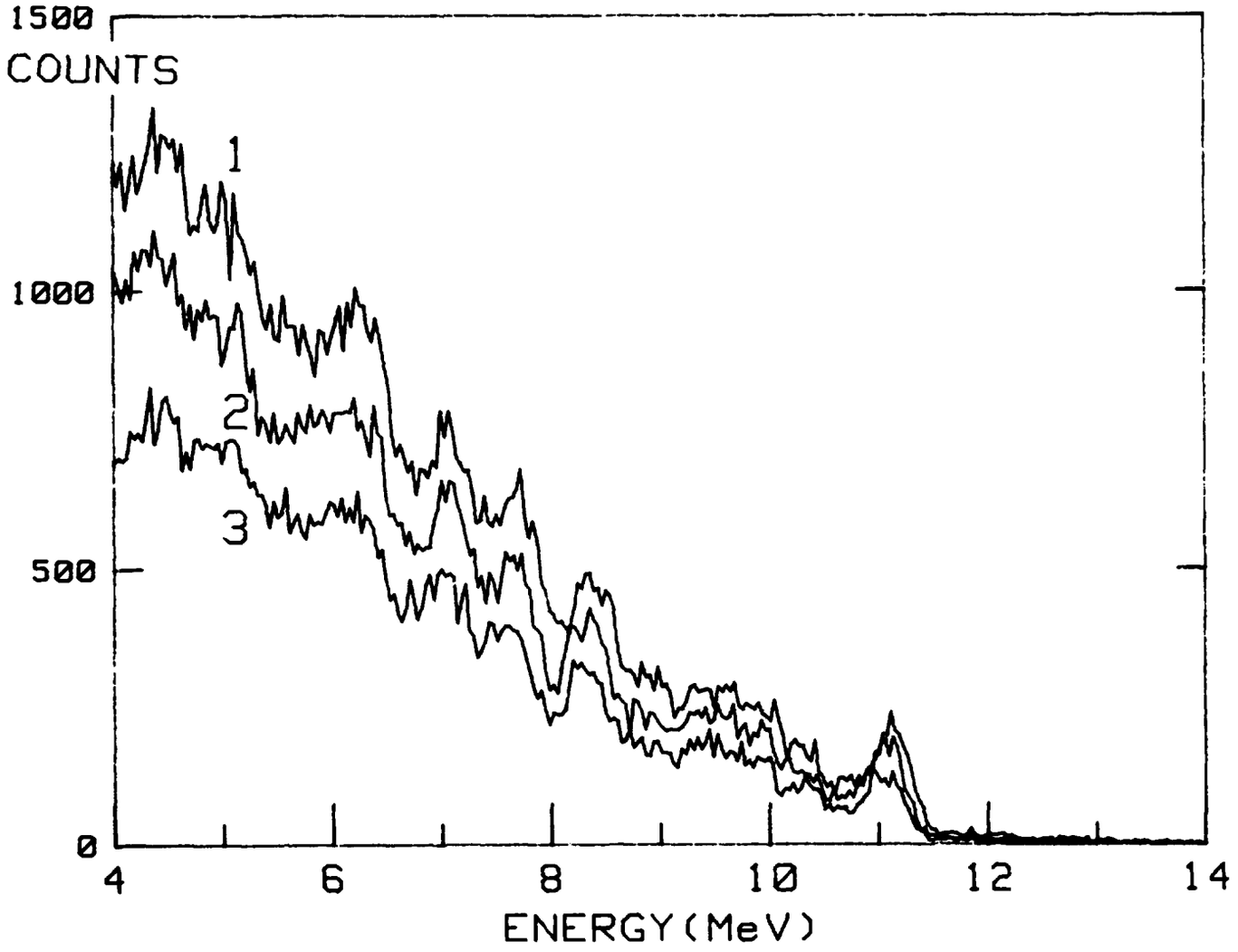

Figure 84. Three background runs.

Curve 1 shows a run without scatterer, curve 2 a run with scatterer and with a 0.4 mm thick tantalum foil in front of the detector, and curve 3 a run with scatterer and a shielding of 5 cm of lead around the detector. Very few events are recorded above 11.5 MeV in all the cases.

12 Cost estimates

We estimate the cost of materials in Swedish currency at 3.4×10^6 SEK corresponding to about 500,000 USD or 300,000 GBP[1]. The cost is summarized in table 7.

[1] 1 USD = 7.5 SEK, 1 GBP = 11.5 SEK.

Table 7. Cost of material.

Qt.	Item	Price 10^3 SEK	Tot. cost 10^3 SEK
Detectors.			
32	PM-tube RCA 8850	9.0	288.0
32	Magnetic shield	0.4	12.8
32	Scint. + Light-Pipe, Pilot U	9.9	316.8
1	Proton Detector	40.0	40.0
	Total for Detectors		657.6
Electronics, see table 6, page 142.			
32	PMB	6.3	201.6
33	FSCA	15.9	524.7
8	DEL1	10.1	80.8
1	DEL2	4.2	4.2
4	ADC	34.9	139.6
1	HMM	26.2	26.1
1	TAC	18.3	18.3
1	PAMP	9.1	9.1
1	FAMP	13.9	13.9
2	LAMP	12.6	25.2
32	LP	2.6	83.2
1	LIP	300.0	300.0
1	TCAL	14.1	14.1
1	PG	20.2	20.2
1	BIAS	8.1	8.1
1	HV	123.7	123.7
1	CAMAC	29.5	29.5
4	NIMBIN	14.9	59.6
1	MIXER	50.0	50.0
	Accessories	150.0	150.0
	Total for Electronics		1881.9
Mechanical parts.			
	Material		40.0
	Manufacture		50.0
	Assemblage		60.0
	Vacuum pump		50.0
	Total for mechanical parts		200.0
Total.			
	Sum		2739.5
	Taxes, delivery		684.9
	Total for material		***3424.4***

13 Developments required

We have tried to find solutions based upon well-known techniques. Therefore, most parts of the system can be designed directly from the ideas presented in this report. However, a few details need a further study. The items to be considered are:

a. Gain shifts.

b. Shielding of the neutron detectors.

c. Time measurements with the proton detector.

d. Energy resolution of the proton detector.

e. Calibration.

f. Beam shaping.

g. Monte Carlo calculation of the entire system.

a) An important problem is the large transients during the plasma ignition phase. The entire system must be designed taking the transients into account. Gain shifts may occur in the photomultipliers and the amplifier chains.

b) The neutron detectors need shielding for gamma radiation. Lead has been used for gas filled proton-recoil chambers[1]. It has been shown that a 5 cm thick lead shield gives an energy displacement of 1-2%. In a detector surrounded by a thin shield the neutron absorption losses are compensated by neutrons gained from elastic scattering. However, the time distortion of a lead shield has not been studied.

c) The timing properties of a 2 mm thick silicon detector must be studied in order to verify that a total time-resolution of less than 1 ns can be obtained. As an alternative we have suggested the use of a thin timing detector followed by a thick one for the energy measurement. However, this solution is electronically more complicated and should be avoided, if possible.

d) The energy resolution of the proton detector is very essential. It might be destroyed by background noise in the system and by burn-out phenomena. We have tested a proton-detector in a low resolution system[2]. However, the behaviour of a silicon detector with a preamplifier in a neutron field should be tested using a high resolution system[3].

e) We have discussed the calibration in paragraph 10.2, page 140. The problem is that we have not found any way to test the complete system prior to the measurements at JET. A comparable neutron source is not available. Therefore, tools must be incorporated for tests and calibrations of parts of the system. We have suggested a laser system for the adjustment of the neutron-detector timing. However, we do not know how such a system will work. Development and experimental verification are necessary.

---

1) See reference 7, page 147.

2) See chapter 11, »Test measurements.», page 145.

3) Paragraph 6.5, »The proton detector.», page 80.

f) The beam shaping system has been sketched using a very simple calculation model. A calculation, taking multiple scattering into account, must be done in connection with the design of the beam shaping system.

g) A Monte-Carlo calculation for the entire system would be very valuable for a final prediction of the behaviour of the system. Excluding the loss factor, which depends on the final design of e.g. the vacuum chamber, we expect the efficiency calculation to be correct within 10%. The resolution, however, is calculated using Gaussian distributions. These are in some cases very far from the true distributions. We expect the fwhm-values to be correct within 50%. However, the distributions are not calculated. They may have a non-Gaussian shape.

14 Conclusions

The main effort put into this work is the foundation of a reliable physical basis for a 12-16 MeV neutron-spectrometer at JET. The essential problem is the amount of scatterer that can be incorporated without losing resolution. We have found two possible methods, the use of a pure hydrogen scatterer and the use of a polyethylene foil scatterer. The pure hydrogen solution gives a very complicated spectrometer with large neutron detectors. The polyethylene solution is limited by the thickness and the width of the foil.

We judge the solution with the polyethylene foil to be the most promising one for a reliable spectrometer. However, a large foil area is needed. This gives a spectrometer design with an annular foil, an annular neutron detection system, and a central proton-detector. An efficiency of 10^{-6} counts/s per n/cm^2,s at the foil can be obtained with a resolution in the order of 100 keV for 14 MeV neutrons.

Following the »General Requirements.» given in the contract of this work {5}, we conclude:

1. The physical basis of the proposed neutron spectrometer is the main task of this work. We have as carefully as possible treated neutron scattering (4), the processes in the foil (5), the proton detection (6), and the neutron detection (7). The conclusion is that an instrument with the desired properties can be made. The instrument is able to give useful information about the plasma from plasma temperatures of about 5 keV (3).

2. The testing and calibration of the system is a problem as no neutron source with qualities comparable to the JET plasma is available. The instrument parts must be tested separately leaving the final adjustments to be done at JET (10.2).

3. Data processing can be done by a minicomputer at the instrument or by the main computer system (10). The data are stored in the list mode in order to enable a flexible processing system.

4. Remote control is necessary for the recalibration of the proton energy measurement (10.4). It is valuable with remote control for the high voltage supply of the photomultipliers, the settings of the single channel analysers, and the delay lines.
The mechanical design has not been included in this work.

5. A diaphragm, a primary shield, is needed as close to the window of the torus vacuum-vessel as possible. No account has been taken of the attenuation of the neutron intensity in the window.

6. Preliminary lay-outs of the system are given in the figures 5, 6, 77, and 78, on the pages 20, 21, 135, and 136, respectively. However, they are only sketches. The final lay-out depends on available space, the diagnostic port used, et cetera.

7. The spectrometer is considered only for the D-T phase of the JET project. It must be located behind the 3 m radiation shielding wall, in the diagnostic area.

Acknowledgements

We are most grateful to Erik Kaffehr and Lennart Norberg. Erik Kaffehr made the calculations for figure 79 and wrote all the equations using a program called SESAM designed by him for this project. Lennart Norberg has given us valuable technical support.

We thank G. Sadler, P. Stott, and O.N. Jarvis for valuable comments and suggestions for this work. Finally, we thank C. Gauffin for his help with the program »Dokf», used for the printing of this document.

References

1) J. Lorenzen, Studsvik Energiteknik AB, *private communication (1981).*

2) T. Elevant, Department of Plasma Physics and Fusion Research, Royal Institute of Technology, S-10044 Stockholm, *private communication (1981).*

3) M.M.R. Williams, A Generalized Energy Exchange Kernel for Inelastic Neutron Scattering and Thermonuclear Reactions., J. Nucl. En. **25**(1971)*489*

4) W.B. Thompson, Thermonuclear Reaction Rates., Proc. Phys. Soc. (London) **B70**(1957)*1*

5) Contract under article 14 of the statutes of the JET joint undertaking between the JET joint undertaking, the European Atomic Energy Community and Euratom-NSBESD Association, *JET contract number JB2/9008.*

6) J.B. Marion and J.L. Fowler, eds., Fast Neutron Physics, Interscience Publ. Inc., New York 1960.

7) G. Grosshoeg, Neutron Ionization Chambers., Nucl. Instr. Meth. **162**(1979)*125*

8) J.A. Harvey and N.W. Hill, Scintillation Detectors for Neutron Physics Research., Nucl. Instr. Meth. **162**(1979)*507*

9) F.W.K. Firk, Neutron Time-of-Flight Spectrometers., Nucl. Instr. Meth. **162**(1979)*539*

10) G.L. Morgan and A.C. England, Measurement of Neutron Flux from a TOKAMAK Plasma Device., Nucl. Instr. Meth. **129**(1975)*1*

11) D.R. Slaughter, Plasma Neutron Diagnostic Techniques with good Spatial and Energy Resolution., IEEE Trans. Nucl. Sci. **NS-26,No1**(1979)*802*

12) M. Chatelier et al., A Fast Neutron Spectrometer for Fusion Experiments., Nucl. Instr. Meth. **190**(1981)*107*

13) R.F. Mozley and F.C. Shoemaker, A Fast Neutron Scintillation Spectrometer., Rev. Sci. Instr. **32**(1952)*569*

14) J.M. Calvert, A.A. Jaffe and E.E. Maslin, An Investigation of the Reaction 19F(d,n)20Ne using a New Fast-Neutron Spectrometer., Proc. Phys. Soc. (London) **68a**(1955)*1017*

15) E.A. Zherebin, L.G. Andreev, and D.V. Timoshuk, A Fast Neutron Spectrometer., (Prib. Tekh. Eksp.) Instr. Exp. Techn. **No5**(1959)*725*

16) K.N. Geller, D. Eccleshall, and T.T. Bardin, Thick Radiator Fast-Neutron Spectrometer., Nucl. Instr. Meth. **69**(1969)*141*

17) C.H. Johnson and C.C. Trail, Proton-Recoil Neutron Spectrometer., Rev. Sci. Instr. **27**(1956)*468*

18) S. Takemoto and Y. Hiratate, Proton Recoil Neutron Spectrometer using a Liquid Hydrogen Radiator and a CsI(Tl)., J. Phys. Soc. (Japan) **17**(1962)*245*

19) M. Cambiaghi, F. Fossati, and T. Pinelli, Fast Neutron Spectrometry with Identification of Recoil Protons., Nucl. Instr. Meth. **82**(1970)*106*

20) T.B. Ryves, A Proton Recoil Telescope for 12-20 MeV Neutrons., Nucl. Instr. Meth. **135**(1976)*455*

21) G.L. Morgan, D.K. Olsen and J.W. McConnell, A Proton-Recoil Telescope for In-Line Absolute Neutron Fluence Measurements., Nucl. Instr. Meth. **157**(1978)*525*

22) R. Potenza and A. Rubbino, Fast Neutron Spectrometer., Nucl. Instr. Meth. **25**(1963)*77*

23) A. Keith Furr and R.S. Runyon, A Fast Neutron Spectrometer for Reactor Flux Measurements., Nucl. Instr. Meth. **27**(1964)*292*

24) A.S. Figuera and C. Milone, A Proton Recoil Fast Neutron Spectrometer with Solid State Detectors., Nucl. Instr. Meth. **27**(1964)*339*

25) G.S. Sidhu and J.B. Czirr, A Neutron-Spectrum Monitor with Annular Radiator and Axial Recoil Detector., Nucl. Instr. Meth. **120**(1974)*251*

26) T. Elevant, A Neutron Spectrometer Suitable for Diagnostics of Extended Fusion Plasmas., Nucl. Instr. Meth. **185**(1981)*313*

27) J.C. Hopkins and G. Breit, The^{1}H(n,n)^{1}H Scattering Observables Required for High-Precision Fast Neutron Measurements, Nucl. Data Tables **A9**(1971)*137*

28) A. Foderaro, The Elements of Neutron Interaction Theory. MIT Press, Cambridge (Mass.), 1970.

29) A.M. Baldin, V.I. Goldanski, and I.L. Rozenthal, Kinematics of Nuclear Reactions. Pergamon Press, Oxford, 1961.

30) V. McLane, Brookhaven National Laboratory.
private communication (1982).

31) R.C. Weast ed., Handbook of Chemistry and Physics, 55th. ed., CRC Press Inc, Cleveland Ohio 1974.

32) G.D. Joanou, A.J. Goodjohn, and N.F. Wikner, Moments Calculations of the Fermi Age in Moderators and Moderator-Metal Mixtures., Nucl. Sci. Eng. **13**(1962)*171*

33) J.B. Marion and F.C. Young, Nuclear Reaction Analysis, Graphs and Tables, North-Holland Publishing Co., Amsterdam 1968.

34) N. Bohr, The Penetration of Atomic Particles Through Matter., Dan. Vid. Selsk. Mat.-Fys. Medd. **18,No8**(1948)*1*

35) J. Lindhard, M. Scharff, and H.E. Shiott, Range Concepts and Heavy Ion Ranges, Notes on Atomic Collisions II,, Dan. Vid. Selsk. Mat.-Fys. Medd. **33,No14**(1963)*1*

36) S.T. Perkins and D.E. Cullen, Elastic Nuclear Plus Interference Cross Sections for Light Charged-Particles., Nucl. Sci. Eng. **77**(1981)*20*

37) H. Bichsel, Charged Particle Interactions. In »Radiation Dosimetry Vol 1» (F.H. Attix et al.,eds.), 2nd ed., Academic Press, New York 1968.

38) U. Fano, Penetration of Protons, Alpha Particles and Mesons., Ann. Rev. Nucl. Sci. **13**(1963)*1*

39) H. Bichsel, Passage of Charged Particles through Matter. In »American Institute of Physics Handbook», (D.E. Gray et al., eds.), 2nd. ed., McGraw-Hill, New York 1957.

40) G. Moliere, Theorie der Streuung schneller geladener Teilchen II, Mehrfach- und Vielfachstreuung., Z. Naturforschg. **3a**(1948)*78*

41) J.F. Janni, Proton Range-Energy Tables, 1 keV - 100 GeV., Atom. Nucl. Data Tables **27**(1982)*147*

42) W.C. Hamilton, Statistics in Physical Science, Ronald Press Company, New York 1964.

43) H. Geissel et al., Energy Loss and Straggling of Alpha Particles in Thin Homogeneous NE-111 Scintillator Foils., Nucl. Instr. Meth. **144**(1977)*465*

44) K. Ettling and W. von Witsch, A Thin-Film Scintillator Detector for Light Ions in Low-Energy Nuclear Physics., Nucl. Instr. Meth. **148**(1978)*299*

45) L. Muga and G. Griffith, Response of Thin Film Scintillator Detector to Light and Heavy Ions., Nucl. Instr. Meth. **109**(1973)*289*

46) L. Muga, Position Sensitive Response of a Thin Film Detector to the Passage of Alpha Particles., Nucl. Instr. Meth. **105**(1972)*61*

47) G.F.Knoll, Radiation Detection and Measurement, John Wiley & Sons, New York 1979.

48) Principles and Applications of Timing Spectroscopy, AN-42 EG&G Ortec, received 1982.

49) T.J.Paulus, R.D. McKnight and T.L. Mayhugh, Experimental Characterization of the Timing Properties of a Detector-Preamplifier System for Charged Particle Detectors using a Laser Pulser., IEEE Trans. Nucl. Sci. **NS-24,No1**(1977)*335*

50) A.R.Spowart, Neutron Scintillating Glasses: Part I., Nucl. Instr. Meth. **135**(1976)*441*

51) A.R. Spowart, Neutron Scintillating Glasses: Part II, Nucl. Instr. Meth. **140**(1977)*19*

52) E.J. Fairley and A.R. Spowart, Neutron Scintillating Glasses: Part III. Pulse Decay Time Measurements at Room Temperature., Nucl. Instr. Meth. **150**(1978)*159*

53) R.L. Macklin, N.W. Hill, and B.J. Allen, Thin^{6}Li(n,alpha)T Transmission Flux Monitor., Nucl. Instr. Meth. **96**(1971)*509*

54) Von P. Schneider-Kuhnle et al., Neutronenspektroskopie im Energiebereich 20 keV bis 16 MeV mit Protonenruckstosszählern., Atomkernenergie **26**(1975)*29*

55) R. Madey et al., The Response of NE-228A, NE-228, NE-224, and NE-102 Scintillators to Protons from 2.43 to 19.55 MeV., Nucl. Instr. Meth. **151**(1978)*445*

56) R. Honecker and H. Grässler, Detection Efficiency of a Plastic Scintillator for Neutrons between 0.2 and 3 MeV., Nucl. Instr. Meth. **46**(1967)*282*

57) L.P. Wishart, R. Plattner, and L. Cranberg, Detector for Neutron Time-of-flight Spectrometry with Improved Response to Low Energy Neutrons., Nucl. Instr. Meth. **57**(1967)*237*

58) S.T. Thornton and J.T. Smith, Measurements and Calculations of Neutron Detector Efficiencies., Nucl. Instr. Meth. **96**(1971)*551*

59) J.M. Adams et al., A Low Threshold Neutron Detector for Nanosecond Time of Flight Spectrometry., Nucl. Instr. Meth. **34**(1965)*21*

60) C. Cernigoi et al., Preliminary Results on the Time Resolution of a Plastic Scintillator Neutron Counter of Large Area for Neutrons of 16 MeV., Nucl. Instr. Meth. **144**(1977)*479*

61) T. Inagaki and R. Takashima, New Types of Plastic Scintillators., Nucl. Instr. Meth. **201**(1982)*511*

62) H. Goldstein, Fundamental Aspects of Reactor Shielding, Addison-Wesley, Reading, Mass. 1959.

63) D.W. Mingay, J.P.F. Sellschop, and P.M. Johnson, Neutron Induced Reactions in Silicon Semiconductor Detectors,, Nucl. Instr. Meth. **94**(1971)*497*

64) R.G. Miller and R.W. Kavanagh, Semiconductor Detector as a Fast Neutron Spectrometer., Nucl. Instr. Meth. **48**(1967)*13*

65) L.I. Klochkova and B.S. Kovrigin, Cross Sections for (n,alpha) Reactions in ^{28}Si and ^{29}Si at a Neutron Energy of 14.1 MeV., Sov. Atom. En. **42**(1977)*158*

66) L.M. Hively, Convenient Computational Forms for Maxwellian Reactivities, Nucl. Fusion. **17**(1977)*873*

67) W.R. Faust and E.G. Harris, Energy Distribution of Neutrons Produced by a Thermonuclear Reaction., Nucl. Fusion. **1**(1960)*62*

68) H. Brysk, Fusion Neutron Energies and Spectra., Plasma Phys. **15**(1973)*611*

69) V.G. Cordey and W.G.F. Core, Energetic Particle Distribution in a Toroidal Plasma with Neutral Injection Heating., Phys. Fluids **17**(1974)*1626*

70) D.L. Jassby and H.H. Towner, Fusion Reactivities and Power Multiplication Factors of Beam-Driven Toroidal Reactors with Both D and T Injection., Nucl. Fusion. **16**(1976)*911*

71) T.H. Stix, Fast-Wave Heating of a Two-Component Plasma., Nucl. Fusion. **15**(1975)*737*

72) H.H. Towner and D.L. Jassby, Energy Spectra of Fusion Neutrons from Plasma Driven by Reacting Ion Beams., Trans. Am. Nucl. Soc. **22**(1975)*74*

73) L.O. Pekkari et al., Enhancement of High Energy Ion Tails in the Presence of Combined Neutral Beam- and ICRF-Heating of a Two Component Plasma. CTH-IEFT/PP-1982-11, Institute for Electromagnetic Field Theory and Plasma Physics, Chalmers University of Technology, Gothenburg 1982. To appear in Nuclear Fusion.

74) J. Kolibal and Long Poe Ku, 14-MeV Neutron Streaming Through Cylindrical Ducts on the TFTR., Trans. Am. Nucl. Soc. **39**(1981)*776*

75) M.A. Etemad, Verification of ANISN-F by Calculating the Neutron Distribution from a Ra-Be Source in Water as well as by Simple Criticality Calculations. CTH-RF-35, Chalmers University of Technology, Gothenburg 1981.

76) O.N. Jarvis, M.T. Svinhoe, and P. Dixon, Proposed Neutron Diagnostic System for JET, *private communication (1982).*

77) E. Heidbreder et al., A Balloon Borne Detector to Determine High Energy Neutrons in Energy and Direction., Nucl. Instr. Meth. **88**(1970)*137*

78) M.K. Chung, Development of a High-Efficiency Solid State Fast Neutron Spectrum Monitor with Tandem Radiation Detector System. IAEA, Vienna. Final report for the period 1 August 1973 - 30 June 1978. **IAEA-R-1652-F** Sep 1978.